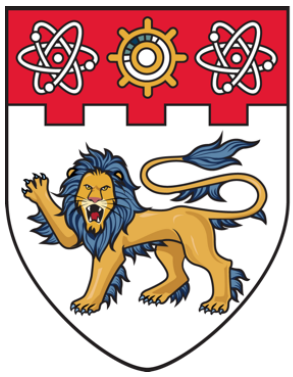

NANYANG TECHNOLOGICAL UNIVERSITY
SINGAPORE

MOLECULAR DYNAMICS STUDY ON THE DEFORMATION AND FRACTURE OF FeCo-BASED ALLOYS

MARIO ARTURO HERNANDEZ MURALLES

SCHOOL OF MATERIALS SCIENCE AND ENGINEERING

2024

MOLECULAR DYNAMICS STUDY ON THE DEFORMATION AND FRACTURE OF FeCo-BASED ALLOYS

MARIO ARTURO HERNANDEZ MURALLES

SCHOOL OF MATERIALS SCIENCE AND ENGINEERING

A thesis submitted to the Nanyang Technological University
in partial fulfilment of the requirement for the degree of
Doctor of Philosophy

2024

Statement of Originality

I hereby certify that the work embodied in this thesis is the result of original research, is free of plagiarised materials, and has not been submitted for a higher degree to any other University or Institution.

05-Jan-2024

. . . . . .

Date

. . . . . .

Mario Arturo Hernandez Muralles

Supervisor Declaration Statement

I have reviewed the content and presentation style of this thesis and declare it is free of plagiarism and of sufficient grammatical clarity to be examined. To the best of my knowledge, the research and writing are those of the candidate except as acknowledged in the Author Attribution Statement. I confirm that the investigations were conducted in accord with the ethics policies and integrity standards of Nanyang Technological University and that the research data are presented honestly and without prejudice.

05-Jan-2024

. . . . . .

Date

. . . . . .

Assoc. Prof. Oh Joo Tien

Authorship Attribution Statement

This thesis contains material from three papers published in the following peer-reviewed journal in which I am listed as an author.

Chapter 4 is published as M. Muralles, J. T. Oh, and Z. Chen. Molecular Dynamics Study of FeCo Phase Transitions and Thermal Properties Based on an Improved 2NN MEAM Potential, J. Mater. Res. Technol. 19, 1102 (2022). DOI: 10.1016/j.jmrt.2022.05.100

Chapter 5 is published as M. Muralles, J.T. Oh, Z. Chen. Influence of V addition on the mechanical properties of FeCo alloys: a molecular dynamics study, Materialia. 27 (2023) 101670. DOI: 10.1016/j.mtla.2022.101670.

Chapter 6 is published as M. Muralles, J.T. Oh, Z. Chen. Modified embedded atom method interatomic potentials for the Fe-Al, Fe-Cu, Fe-Nb, Fe-W, and Co-Nb binary alloys, Comput. Mater. Sci. 230 (2023) 112488. DOI: 10.1016/j.commatsci.2023.112488.

Chapter 7 has been accepted for publication as M. Muralles, J.T. Oh, Z. Chen. Atomistic Investigation of Effect of Alloying on Mechanical Properties and Microstructural Evolution of Ternary FeCo-X (X = V, Nb, Mo, W), Comput. Mater. Sci. 241 (2024) 113030. DOI: 10.1016/j.commatsci.2024.113030.

The contributions of the co-authors are as follows:

- A/Prof. Oh and Prof. Chen conceptualized and provided the initial project direction.
- I co-designed the study with A/Prof. Oh and Prof. Chen.
- I performed the dynamics simulations at the National Supercomputing Centre (NSCC) Singapore. I analyzed and curated the resulting data and subsequently conducted the data evaluation.
- I prepared the manuscript drafts. The manuscript was revised by A/Prof. Oh and Prof. Chen.

05-Jan-2024

. . . . . .

Date

. . . . . .

Mario Arturo Hernandez Muralles

Abstract

In this research, we primarily formulated interatomic potentials for the Fe-Co system using the formalism of the second nearest-neighbor modified embedded-atom method (2NN MEAM). Initially, a potential was meticulously calibrated to accurately reproduce essential thermal phases stability, structural properties, and elasticity. Moreover, point defects were deliberately introduced during the fitting process to enhance thermodynamic characteristics. Employing this refined potential in molecular dynamics (MD) simulations has led to the successful prediction of melting temperatures consistent with experimental data and the revelation of a temperature-induced B2 to L10/hcp transformation. Furthermore, the potential was applied to study the thermal effects of different FeCo phases in both bulk and multilayer films. Nevertheless, during the investigation of deformation mechanisms, the finalized potential exhibited deficiencies.

With a similar approach another interatomic potential was fitted based in an optimized unary potential tailored for mechanical applications. Emphasis was placed on predicting FeCo elastic properties and antiphase boundary (APB) energies to describe the mechanical behaviors accurately. Subsequently, the Fe-Co potential was extended to encompass the Fe-Co-V ternary system by merging it with an adopted Co-V and an in-house developed Fe-V potential. Through simulations, crack nucleation and propagation mechanisms were investigated in nanocrystalline FeCo and FeCo-2V alloys under various degrees of ordering at the grain boundaries (GB) and within the grains. Notably, disordering inside grains was found to significantly impact the ductility of binary FeCo, while the mobility of antiphase domains (APD) inside grains delayed the ultimate tensile strength (UTS) and strain at fracture. The presence of V in the alloy affected the ductility, and its exclusive migration to APBs improved alloy ductility through enhanced mobility of APDs.

Further advancing the study, we developed interatomic potentials for additional binary systems, including Fe-Al, Fe-Cu, Fe-Nb, Fe-W, and Co-Nb, using the 2NN MEAM formalism. These potentials were calibrated to reproduce crucial physical properties, demonstrating agreement with experimental data, CALPHAD evaluations, and first-principles calculations. These potentials were then seamlessly integrated with existing MEAM models, facilitating comprehensive explorations into the physical metallurgy of

FeCo-based alloys and other multicomponent systems, including high entropy alloys (HEA). This comprehensive approach allows for a thorough exploration of the unique mechanical behaviors of these materials at the atomic scale. Considering elements experimentally proven to enhance ductility in FeCo, this study further investigates and compares the effect of V, Nb, Mo, and W on the microstructure of FeCo. Initially, the study delved into the influence on the prevalent slip directions of FeCo, revealing that the solutes have a tendency to decrease the antiphase boundary (APB) energies. Employing a combination of techniques, including Monte Carlo calculations, the study explores solute diffusion in nanocrystalline (NC) models. Notably, a distinct preference for migration towards grain boundaries (GBs) is observed, with the exception of Nb addition. Subsequent straining tests offer valuable insights into deformation behavior. Specifically, the study reveals that the addition of W extends the elastic region before the development of slip bands, while alloys containing Nb and Mo exhibit enhanced resistance to microcrack formation.

In its entirety, this research offers a thorough and systematic exploration of the mechanical characteristics exhibited by both FeCo and FeCo-X (where X = V, Nb, Mo, W) alloys, facilitated by the development of novel interatomic potentials and their application in MD simulations. The findings contribute valuable insights into the behavior of complex multicomponent systems, enhancing our understanding of their mechanical characteristics at the atomic scale and providing guidelines for potential engineering applications.

Lay Summary

Scientists are exploring special metal alloys composed of iron (Fe) and cobalt (Co) with unique magnetic properties that are crucial for advanced applications like high-tech devices and electric engines. However, some of these alloys are brittle and less flexible, particularly at low temperatures. To address this challenge, researchers are experimenting with small amounts of additional metals like vanadium (V), niobium (Nb), molybdenum (Mo), and tungsten (W). Notably, vanadium significantly enhances the alloy's flexibility without severely compromising its magnetic properties.

Understanding why these alloys become brittle and how these added metal elements help make them more flexible is a challenge. Conventiaonally, physical experiments are carried out with different elements and amount of each element but these studies are cost and time consuming. Among computational methods that help design new alloys, ab initio calculations based on quantum theory demand immense computational power and cannot capture a realistic, large-scale view of a material. To bridge this gap, scientists use advanced computer simulations based on Newton's laws to simplify calculations and yet can capture the necessary information to understand the materials behavior. By employing these simulations, we were able to create computer models that closely mimic the behavior of FeCo alloys.

In this study, computer models closely mimicking FeCo alloy behavior were created using these simulations. The models simulated alloy behavior under various conditions, especially when a small quantity (2 at.%) of V, Nb, Mo, and W were separately added. The simulations reveal where these elements prefer to stay within the FeCo systems and how failure begins and proceeds. For V, multiple doping strategies were examined to observe enhancements in ductility. The study also revealed that W contributes to a more significant improvement in ductility before internal cracking occurs. However, simulations involving V highlighted that the extent of improvement also depends on the specific location of the additional element within the alloy.

The findings are significant as they offer a reliable way for scientists and engineers to design new FeCo alloys with enhanced properties. By using this type of simulations,

researchers can save time and resources, bringing us closer to creating stronger, more ductile materials for diverse high-tech applications.

Acknowledgements

This dissertation acknowledges the invaluable support and funding provided by the Agency for Science, Technology & Research (A*STAR) and the Nanyang Technological University (NTU) through the Singapore International Graduate Award (SINGA) program, without which this work would not have been possible. Additionally, I extend my appreciation to the National Supercomputing Centre (NSCC), Singapore (https://www.nscc.sg) for providing computational resources that were instrumental in conducting the computational work for this project.

I extend my heartfelt gratitude to my research project supervisors, Prof. Joo Tien Oh and Prof. Zhong Chen, for granting me the opportunity to be part of their esteemed team. I am immensely grateful for the unwavering support and invaluable guidance they have provided throughout this project. Their profound expertise in the field of metallurgy, coupled with their extensive knowledge across various disciplines, has been instrumental in navigating me through the challenges encountered during this endeavor. I deeply appreciate their contributions to my growth and the success of this research.

I would like to sincerely express my heartfelt gratitude to Dr. Shuzhou Li, Dr. Weiming Huang, and Dr. Kun Zhou for their invaluable contributions to this work. Their insightful comments and suggestions have played a pivotal role in shaping the direction and enhancing the overall quality of this research. Furthermore, I would like to extend my deepest appreciation to Dr. Zhiqiang Li for providing invaluable perspectives on the experimental aspects of this project.

Lastly, I am deeply grateful to my parents and family for their unwavering belief in me and their constant encouragement throughout my endeavors. Their support has been a driving force behind my achievements, and I am forever thankful for their love and guidance.

Table of Contents

Table Captions

Figure Captions

identified representing the GB. (b-d) Atomic representation of different degrees of ordering at the GBs. Green atoms represent Fe and yellow atoms Co, respectively. (e, g) Atomic configuration of different degrees of ordering at the grains, also visualized under the PTM (f, h) where light green atoms belong to the APB.

Figure 5.6 (a) Calculated energies for the Σ3(111) and Σ9(221) GBs types as a function of the degree of order (S), in red and black color respectively. Representation of the B2 symmetric tilted Σ3(111) (b) and Σ9(221) (c) types of GBs.

Figure 5.7 Calculated GSFE curves for FeCo in the {110} (a) and {112} (b) in the <111> slip direction with different LRO ordering degrees (S). In comparison with FP and MD calculations [37,38].

Figure 5.8 Binary FeCo stress-strain curve and dislocation density evolution when disordering is introduced in (a, b) grain boundaries and (c, d) grains.

Figure 5.9 (a, g) Binary FeCo with fully disordered grains before and after the straining process visualized under the PTM. Atoms in turquoise are identified to be on a B2 structure, white atoms are not identified, while light green atoms belong to the APBs. (b-f) Atomic shear distribution during the microcrack nucleation and propagation. Red atoms are under a shear strain > 0.5 GPa.

Figure 5.10 Migration of V atoms in FeCo under the GCMC-MD scheme. (a) Grain configuration visualized under the PTM. Turquoise atoms are in a B2 structure while light green and white atoms represent atoms in the APBs and GBs respectively. Black and red dotted lines present Fe and Co dominated APBs respectively. (b-d) Atomic representation of the evolution of the system. Green atoms represent Fe, yellow atoms Co and purple atoms V, respectively.

[160,167] and MD calculations [129,170].

Figure 6.4 (a) Atomic volume for the bcc solid solution in the Fe-Nb system at 298 K. (b) Enthalpy of mixing for the bcc solid solution (lines) and enthalpy of formation for the principal structures (markers) in the Fe-Nb system at 0 K. (c) Enthalpy of mixing for the liquid solution at 2200 K. In comparison with experimental data [182,188], FP calculations [184], CALPHAD calculations [130,181,187,189], thermodynamic assessments [179,190] and MD calculations [130].

Figure 6.5 (a) Lattice constant, (b) enthalpy of formation and (c) elastic constants for the bcc solid solution in the Fe-W system at 0 K. In comparison with DFT [193] and EAM calculations [198,199]. The reference states are bcc Fe and bcc W.

Figure 6.6 (a) Atomic volume for the Co-rich hcp and the C15-based solid solutions in the Co-Nb system and (b) enthalpy of formation for the experimentally confirmed Co-Nb compounds at 298 K. In comparison with experiments [186,204,213,216–219] and DFT calculations [152,173,212].

Figure 7.1 (a) Lattice constant, (b) enthalpy of formation, (c) elastic constants and (d) elastic moduli for the bcc solid solution in the Fe-W system at 0 K. In comparison with experimental data [228], DFT [193] and EAM calculations [198,199]. The reference states are bcc Fe and bcc W.

Figure 7.2 Variation in FeCo {110} (a) and {112} (b) APB energies in the <111> slip direction due to 4 at.% solute additions. In comparison with FP calculations [37,38].

Figure 7.3 GSFE curves for FeCo in the {110} (a) and {112} (b) in the <111> slip direction due to 4 at.% solute additions. In comparison with FP and MD

calculations [37,38].

Figure 7.3 GSFE curves for FeCo in the {110} (a) and {112} (b) in the <111> slip direction due to 4 at.% solute additions. In comparison with FP and MD calculations [37,38].

Figure 7.4 Calculated energies for the Σ3(111) and Σ9(221) GBs types as a function of the solute additions.

Figure 7.5 (a) Migration of solute atoms to the GBs under the MD-MC scheme. (b) Evolution of the exchange of solute atoms with Fe and Co atoms in the GBs. The MD steps and MC swap attempts throughout the diffusion process are accompanied by their respective multipliers.

Figure 7.6 (a) Representation of the uniaxial straining test over the [001] axis on the NC model and (b) the stress-strain behavior of FeCo containing 2 at.% individual additions of V, Nb, Mo, and W over this direction. (c) Comparative response per alloy when strained in the [100], [010] and [001] directions.

Figure 7.7 Determined averaged values and deviation observed for the elastic moduli: Young's modulus (E), shear modulus (G), Poisson's ratio (ν) and yield strength (YS) compared with the averaged values predicted for the binary FeCo shown as a dotted red line.

Figure 7.8 Sliced view presenting the relaxed model and the evolution of the straining process at various stages under atomic strain analysis for FeCo (a-f), FeCo-2V (g-k), and FeCo-2Nb (l-p). Fe atoms are depicted in cyan, Co in blue, and V and Nb in dark red for the relaxed models. White squares indicate the initial slip and cross-slip development, while circles mark microcrack nucleation.

Figure 7.9 Sliced view featuring the FeCo-2Nb alloy at ~4.6% strain (a) and at ~6%

strain (b), showing slip bands intersecting a compound, highlighted in white lines. (c) Observation of the compound under the PTM analysis, showing bcc, fcc and unidentified atoms in blue, green and white respectively. (d) Representation of the μ-phase ($D8_5$ structure) as observed in the Co-Nb alloys. Fe atoms are represented in cyan and Co in blue, Nb is presented in dark red.

Abbreviations

(ai)REBO	Adaptive Intermolecular Reactive Empirical Bond Order
2NN MEAM	Second Nearest-Neighbor MEAM
A*STAR	Agency for Science, Technology & Research
ACE	Atomic Cluster Expansion
ADP	Anisotropic Displacement Parameters
APB	Antiphase Boundary
APD	Antiphase Domain
ASPIRE	Advanced Supercomputer for Petascale Innovation Research & Enterprise
bcc	Body-Centered Cubic
BOP	Bond-Order Potential
CMC	Canonical Monte Carlo
CNA	Common Neighbor Analysis
DFT	Density Functional Theory
EAM	Embedded-Atom Method
EDR	Enhanced Data Rate
EIM	Effective Interaction Model
EOS	Equation of States
EVI	Electric Vehicle Initiative
fcc	Face-Centered Cubic
FP	First Principles
GB	Grain Boundary
GCMC	Grand Canonical Monte Carlo
GGA	Generalized Gradient Approximation
GPFS	General Parallel File System
GSFE	Generalized stacking fault energy
hcp	Hexagonal Close Packed
HEA	High Entropy Alloys
HPC	High-Performance Computing

LAMMPS	Large-Scale Atomic/Molecular Massively Parallel Simulator
LRO	Long Range Order
MC	Monte Carlo
MD	Molecular Dynamics
MEA	More Electric Aircraft
MEAM	Modified Embedded-Atom Method
MOO	Multi-Objective Optimization
MS	Microcracking Stress
NC	Nanocrystalline
NSCC	National Supercomputing Centre
NTU	Nanyang Technological University
ODT	Order-Disorder Transition
PTM	Polyhedral Template Matching
ReaxFF:	Reactive Force Field
SF	Stacking Fault
SINGA	Singapore International Graduate Award
TIP4P	Transferable Intermolecular Potential with 4 Points
UTS	Ultimate Tensile Strength
VESTA	Visualization for Electronic and Structural Analysis
VMD	Visual Molecular Dynamics
YS	Yield Strength

Chapter 1

Introduction

This chapter serves as an introduction to the underlying premises of the work, aiming to familiarize the reader with the general characteristics of FeCo alloys and emphasize the significance of studying their mechanical behaviors. Additionally, it delves into the practicality of employing molecular dynamics (MD) interatomic potentials to shed light on this subject matter, highlighting their potential utility for future research. Furthermore, the chapter outlines the overall workflow required to conduct this study in the computational field, providing a comprehensive description. Anticipated challenges in the process are identified and discussed, along with potential strategies to address them effectively.

1.1 Problem Statement

FeCo alloys are widely used in inductive applications such as electrical machines and motors. However, their inherent brittleness at low temperatures restricts their range of applications. Previous studies have shown that the addition of small amounts of other metals such as V, Nb, Mo, W can reduce this brittleness, with V being the most effective additive.

Although FeCo alloys have been extensively studied experimentally, the diverse methodologies and conditions employed in these studies have led to some inconclusive results. Controversies surrounding the crystalline structure and its ordering have hindered a comprehensive understanding of the origin of brittleness and deformation mechanisms in these alloys. Based on the existing literature, it is hypothesized that the formation of superdislocations within the ordered structures may underlie the brittleness observed in FeCo alloys. Additionally, it is suggested that the addition of alloying elements induces microstructural effects such as the retardation of order-disorder transformations, the formation of compounds, and the creation of Co-rich regions, ultimately influencing the mechanical behavior of the alloys.

Experimental work has been widely used in the research, however, it could not observe the internal microstructural evolution during testing. To address this limitation, we propose an atomistic approach that can accurately simulate the evolution of FeCo systems at the nano and micro-scale. Molecular Dynamics (MD) simulations offer the opportunity to observe atomic movements under stress through tensile tests. By combining MD simulations with the Monte Carlo (MC) method, valuable insights can be gained regarding the effects of introducing V or other elements into the alloy. Finally, by comparing the critical stresses in binary and ternary alloy systems, we aim to enhance our understanding of how alloying influences the mechanical behavior of FeCo alloys.

1.2 Objectives and Scope

The focus of this research is the development of MD interatomic potentials specifically designed for the study of the mechanical behavior of FeCo alloys. These potentials aim to

accurately capture the energetic, thermal, and elastic properties of FeCo alloys, with a particular emphasis on understanding fracture behavior and the effects of minor alloying elements. By gaining a comprehensive understanding of the mechanical properties, this research seeks to establish design principles that can further enhance the utilization of FeCo alloys. The specific objectives of this research are as follows:

- Develop MD interatomic potentials by utilizing reference fundamental physical properties. Begin by focusing on the binary FeCo alloy, and then extend the development to include ternary additions such as V, Nb, Mo and W.
- Construct nanocrystalline (NC) models with diverse ordering degrees, geometries, and crystal orientations for an approach closer to realistic conditions.
- Employ MD-MC simulations to monitor and analyze the movement of ternary addition atoms within the systems.
- Perform stress-strain tests on the NC models to investigate microstructural evolution. Analyze the tensile behavior and characterize the fracture mechanisms involved.

1.3 Dissertation Overview

This thesis explores and validates the implementation of computational mechanics based on MD to observe the atomistic-level deformation evolution of FeCo-based systems. This thesis is sub-divided into 8 chapters.

Chapter 1 provides a rationale for the research and outlines the goals and scope.

Chapter 2 provides a comprehensive review of the literature on FeCo-based alloys. It delves into the fundamental aspects of these alloys and explores the mechanical properties that have been observed through experimental testing. It further examines the computational studies carried out and the methodologies employed to investigate this family of alloys.

Chapter 3 explores the underlying theories behind the MD methods, elucidating their principles and significance in the context of this research. It provides a comprehensive

review of the Modified Embedded Atom Method (MEAM) and offers insights into the general construction procedures employed to develop the interatomic potentials necessary for the simulations. The chapter presents detailed information on the thermodynamic configurations utilized in the simulations, as well as the generation of the NC models. Additionally, it provides a description of the software and hardware utilized in this project.

Chapter 4 presents the MD simulations and results obtained using an improved interatomic potential designed to accurately reproduce the thermodynamic properties of FeCo. The results encompass the successful replication of phase transformations, melting points, the observation of order-disorder transformations via vacancy diffusion, and the application of the interatomic potential to investigate the stability of metastable thin films.

Chapter 5 focuses on the development of an interatomic potential for the binary FeCo with specific mechanical capabilities, as well as its extension to describe the FeCo-V system. The influence of incorporating V on the microstructure is thoroughly investigated using MD-MC simulations. The results comprise a detailed comparative analysis, examining how different ordering conditions and strategies for incorporating V impact the straining response.

Chapter 6 provides the development of essential interatomic potentials required for the FeCo-X (X = Al, Cu, Nb, and W) ternary alloys. Specifically, interatomic potentials for the Fe-Al, Fe-Cu, Fe-Nb, Fe-W, and Co-Nb binary systems are constructed. The validations encompass a thorough comparison with ab initio and experimental data, assessing the agreement of structural, thermodynamic, and elastic properties.

Chapter 7 explores the effects of V, Nb, Mo and W on the FeCo microstructure. The diffusion and preference of the solutes atoms is explored through MD-MC simulations. Then the evolution of the systems and the impact on the mechanical properties are assessed by performing tensile straining simulations.

Chapter 8 synthesizes the extensive findings from the research project. This section distills

the essence of the research, drawing conclusions about the behavior of the FeCo alloy, as well as the incorporation of low contents of V, Nb, Mo and W. It consolidates the insights gained from the MD and MD-MC simulations, offering a nuanced understanding of atomistic-level deformation evolution in these alloys. Finally, this chapter outlines the implications of these discoveries for materials science and engineering, highlighting potential avenues for future research and practical applications within the realm of materials research and computational mechanics.

1.4 Findings and Outcomes/Originality

This research led to several novel outcomes by:

1. Establishing dedicated FeCo Modified Embedded Atom Method (MEAM) interatomic potentials. These potentials not only encompass fundamental physical properties but also account for point defects and antiphase boundary energies. This approach grants superior control over the mechanical properties of the alloys.
2. Addressing gaps within the MEAM for binary systems missing interatomic potentials, namely Fe-W, Co-Nb, and Co-W. By doing so, we have expanded the scope not only for FeCo alloys but also for other alloys, including these interactions in diverse materials like high entropy alloys (HEA).
3. Developing MEAM interatomic potentials to describe ternary FeCo-X alloys, where X represents V, Nb, Mo, and W. These potentials provide detailed insights into the complex behavior of these ternary alloys, paving the way for targeted material design.
4. Utilizing the Voronoi method, realistic bulk models were meticulously crafted. These models incorporate grains and diverse ordering degrees at grain boundaries and anti-phase domains within grains. This nuanced approach captures the intricate structure of FeCo alloys in a more realistic manner.
5. Performing MD-MC simulations to observe the diffusion patterns and site preferences of alloying elements within the FeCo microstructure.
6. Employing MD tensile straining tests on the bulk models, where the microstructure

evolution during deformation and microcrack formation was observed.

7. Evaluating the simulation results involved a combination of quantitative and qualitative approaches. Quantitative analysis enables to identify trends and data values throughout the material's diffusion and deformation processes. Moreover, qualitative analysis, achieved through detailed graphical observation of the rendered models and supported by advanced structural identification techniques, provides a richer understanding of the material's behavior and structure.

Chapter 2

Literature Review

This chapter provides a comprehensive summary of earlier studies, delving into the fundamental thermo-magnetic structural effects of FeCo-based alloys and placing a particular emphasis on exploring their mechanical properties. Additionally, it highlights the significant advancements made in computational methods, specifically at the atomic and molecular levels, employed to investigate the behavior of these alloys.

2.1 Overview

Magnetic materials have always played an important role in the history of humanity since its first known major application as a compass for navigation purposes. When referring to magnetic materials, people tend to think about hard magnets, which can attract, repel and even magnetize other objects. Soft magnets, distinguished by their ease of magnetization and demagnetization in response to a magnetic field, offer valuable advantages in various inductive applications, spanning electrical machines and electronics [1]. Moreover, these materials exhibit a remarkable capacity to effectively convert electrical energy into magnetic energy and vice versa, while minimizing energy loss in the form of heat. This intrinsic quality assumes paramount importance in the domain of motor applications, as elevated temperatures can adversely affect the electrical and magnetic characteristics of motor components, thereby resulting in a gradual decline in overall operational efficiency. Thus, soft magnetic materials have gained more attention with the Electric Vehicle Initiative (EVI) and the More Electric Aircraft (MEA) initiative, which demands reliable materials with high-power density while aiming to reduce weight, energy consumption and operational costs [1].

Among the soft magnetic materials used for electrical motors, FeCo alloys exhibit the largest magnetic induction in the Slater–Pauling curve. They also possess one of the highest saturation magnetization, good permeability in magnetic fields, and high Curie temperatures among other features [2–4]. These characteristics make FeCo an ideal candidate for a wide range of applications at different scales, from electric engines at the aeronautical industry to magnetic nanoparticles in biomedical fields [5]. For applications under elevated temperatures, the temperature plays an important role on the FeCo crystal structure, which affects the magnetic and mechanical properties. At low temperatures, the alloys presents an ordered B2 structure that maximizes the magnetic properties but at the same time reduces the ductility, which causes difficulty for metal working and/or machining by conventional procedures [2,3,6]. Thus, the most common manufacturing methods include several steps, starting by casting, followed by a heat treatment and finally metal forming which affects the magnetic properties and increases the manufacturing cost [7].

To increase the mechanical capabilities of FeCo the addition of an alloying solute has been considered. The addition of typical alloying elements such as Al, Be, Bo, Cu, Au, Mn, Ag, Si, Ti, and Zr have been studied. It was found that the improvement on the malleability of the alloy is negligible or minimal at best. Conversely, previous studies have revealed that the addition of Cr, Ni, Nb, Mo, Ta, V, and W up to 2 at.% can enhance the ductility of FeCo alloys [8–11]. Among these, V and Nb have been found the most favorable additions due to the positive influence on the magnetic properties of the alloy [3,11–13]. However, V has received the highest level of scrutiny as a solute since it has been proven to massively increase the resistivity by up to 23 times [14] and has shown the capacity to increase the alloy's cold workability by up to 90%, enabling the formation of thin sheets that play a vital role in minimizing eddy currents within motors.

Good soft magnetic properties are observed below a 3% V and at the same time it allows the alloy to be cold workable, hence reducing the economic impact on fabrication [2]. Among the FeCo-V family, the $Fe_{49}Co_{49}V_2$ alloy, widely known as “permendur”, has the best magnetic performance. However, despite the improved mechanical properties compared to the binary alloy, it is still considered brittle. The origin of the brittleness is still not well understood due to the lack of an experimental approach that allows the observation of the deformation mechanisms at the atomic scale. As an alternative, computational methods have become more and more reliable in reproducing material properties and behaviors. Computationally, Density Functional Theory (DFT) based-methods have succeeded in reproducing the Fe-Co interaction and have been used to study the basic structure, ordering and its magnetic effects. However, calculations on the mechanical behavior of alloys using DFT is still unrealistic due to the computationally intensive requirements to process such a heavy load of quantum calculations. An alternative to the DFT approach is the MD method that uses semi-empirical potentials to simulate the behavior of a relatively large system. Therefore, MD is seen as a link between nano- and macro-scale methods. However, up to date, there is no MD approach that studies the FeCo deformation mechanics, especially in the context of alloying insertions. Most past work was focused on the formation of thin multilayers and as a part of multicomponent systems, as will be reviewed in the subsequent sections.

2.1.1 FeCo Alloys Thermal and Mechanical Properties

The properties of FeCo alloys, like many other metals, are strongly influenced by temperature. As the temperature rises, thermal energy affects the arrangement and behavior of atoms within the alloy, leading to increased atomic mobility. This, in turn, brings about structural changes that have significant impact on the mechanical, electrical, and thermal properties of the alloy. The relationship between temperature and these properties in FeCo alloys is complex and requires careful consideration to understand and optimize their performance in various applications. It can be observed in the phase diagram (**Figure 2.1**) that the equiatomic FeCo presents an ordered bcc B2 structure at low temperatures (α_2 phase) and a disordered bcc A2 structure from ~1000 K (α phase). Numerous studies have indicated that ~1258 K, the Curie temperature marks the boundary for the phase transformation of FeCo alloys into a metastable disordered fcc A1 structure (γ phase), which persists until reaching the melting point at ~ 1750 K [2,3,15–17]. However, there is uncertainty regarding an inconsistency observed at ~823 K, also regarded as the "550 ˚C anomaly" which has even been proposed to correspond to a phase transition [3,4].

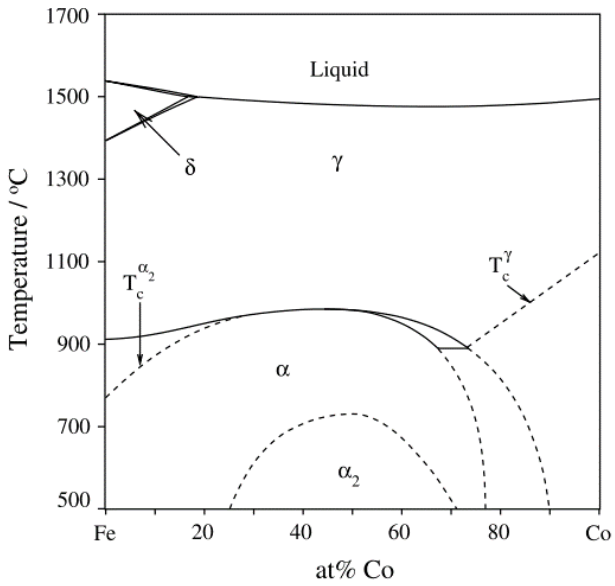

Figure 2.1. The FeCo binary phase diagram as presented by Nishizawa [15]. *No permission is required for thesis purposes.*

The ordering of FeCo alloys, which is temperature-dependent, plays a significant role in determining their magnetic and mechanical properties. The idea behind the disordering in a A-B binary solid solution is that atoms of elements A randomly exchange their lattice site with atoms of element B without distorting the crystalline structure. Thus, the resulting solid solution does not exhibit a predictable arrangement of atoms. To quantify the kinetic ordering evolution, the periodicity of the crystalline structure over large sections is measured through the LRO parameter *S*. Also known as the Bragg-Williams LRO [18], the relationship for a binary bcc alloy is given by the following equation

$$S = 2\left(p - {}^{1}/_{2}\right) \tag{1}$$

where *p* represents the fraction of A atoms occupying B sites. A value of $S = 0$ represents a fully disordered alloy while 1 represents a fully ordered alloy. A simple schematic of ordered and disordered states alongside with the dependance of the *S* parameter with temperature change is shown in **Figure 2.2** [3].

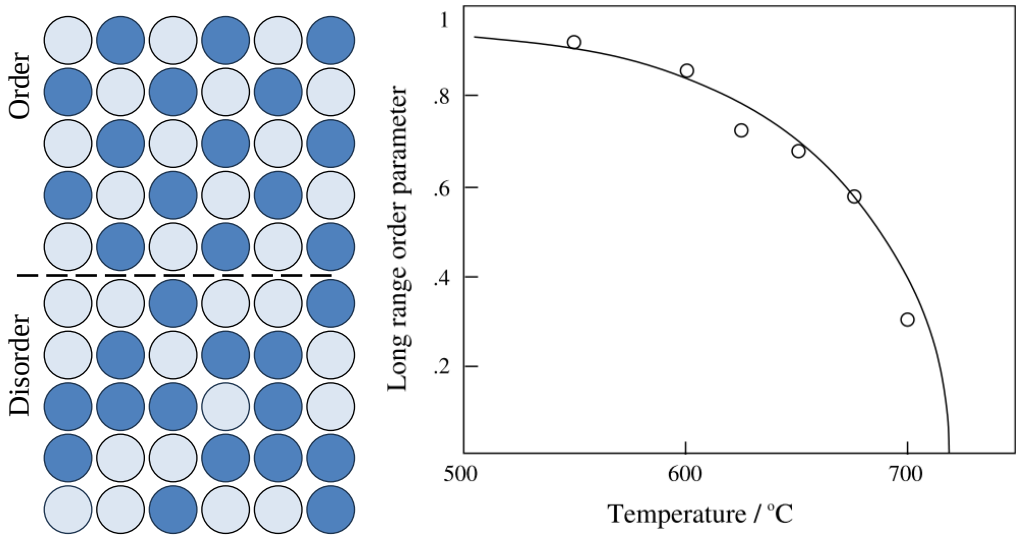

Figure 2.2 Left, schematic of order/disorder. Right, evolution of the FeCo LRO S parameter against temperature as presented by Sourmail [3]. *No permission is required for thesis purposes.*

In terms of magnetic properties, ordering influences the interactions between the magnetic moments of individual atoms. A high degree of ordering promotes the alignment of magnetic moments, resulting in strong magnetic properties. Conversely, disordering leads to a cancellation of magnetic moments due to the random arrangement of atoms. Regarding

mechanical properties, an ordered arrangement of atoms enhances strength and stability. In FeCo alloys, the ordering results in brittle behavior. On the other hand, disordering can reduce strength but can sometimes improve ductility of this material. As a result, low temperatures in FeCo alloys promote ordering, maximizing magnetic properties but adversely affecting ductility [2,3,6].

The poor ductile behavior in FeCo alloys is connected to the low-temperature precipitation of the ordered B2 structure. It has been proposed that the occurrence and behavior of dislocations depend on the value of *S*. It claims that low values of *S* are associated with a single dislocation source, whereas high values of *S* result in paired source dislocations. At low values of *S,* the boundary energy is small enough for superdislocations to disassociate into ordinary dislocations as predicted by the constituents. These dislocations glide leaving anti-phase boundary trails producing hardening. On the other hand, it is assumed that a raise in *S* promotes moderate antiphase boundary (APB) energies which provoke 1/2 <111> dislocations to combine and glide in pairs without creating wrong bonds, leading to superdislocation gliding [8]. The APB energy governs the spacing between 1/2 <111> dislocations. A low APB energy enables dislocations to be widely separated, allowing independent cross-slip for each dislocation. In contrast, a high APB energy prevents the separation of partial dislocations, keeping them coupled and facilitating collective cross-slip. However, moderate energies limit dislocations to intermediate separations that restrict dislocations to slip on the {110} and {112} planes, ultimately suppressing the cross slip of dislocations and leading to a brittle behavior [8–11].

Consequently, FeCo alloys present two types of stress-strain behavior according to their ordering. Disordered FeCo alloys exhibit a deformation flow characterized by a single-stage behavior indicative of internal cross slip. In contrast, ordered FeCo alloys display a three-region behavior that resembles that of fcc alloys [2]. The first region shows a linear response to stress, followed by a small step indicating the transition from elastic to plastic deformation. The second region is characterized by planar slippage of superdislocations, resulting in rapid work hardening. Finally, the third region signifies the breakage of superdislocations into single dislocations, leading to simultaneous cross slip and contributing to fracture [2]. Testing samples treated at various temperatures consistently show that both yield strength and ultimate strength decrease as the heat treatment

temperature rises. At low heat treatment temperatures, FeCo alloys tend to fail primarily through transgranular cleavage. However, as the temperature surpasses the ordering transition, a mixture of transgranular and intergranular failure modes becomes evident. **Figure 2.3** presents the compressive stress-strain curve for the ordered and disordered binary FeCo alloys.

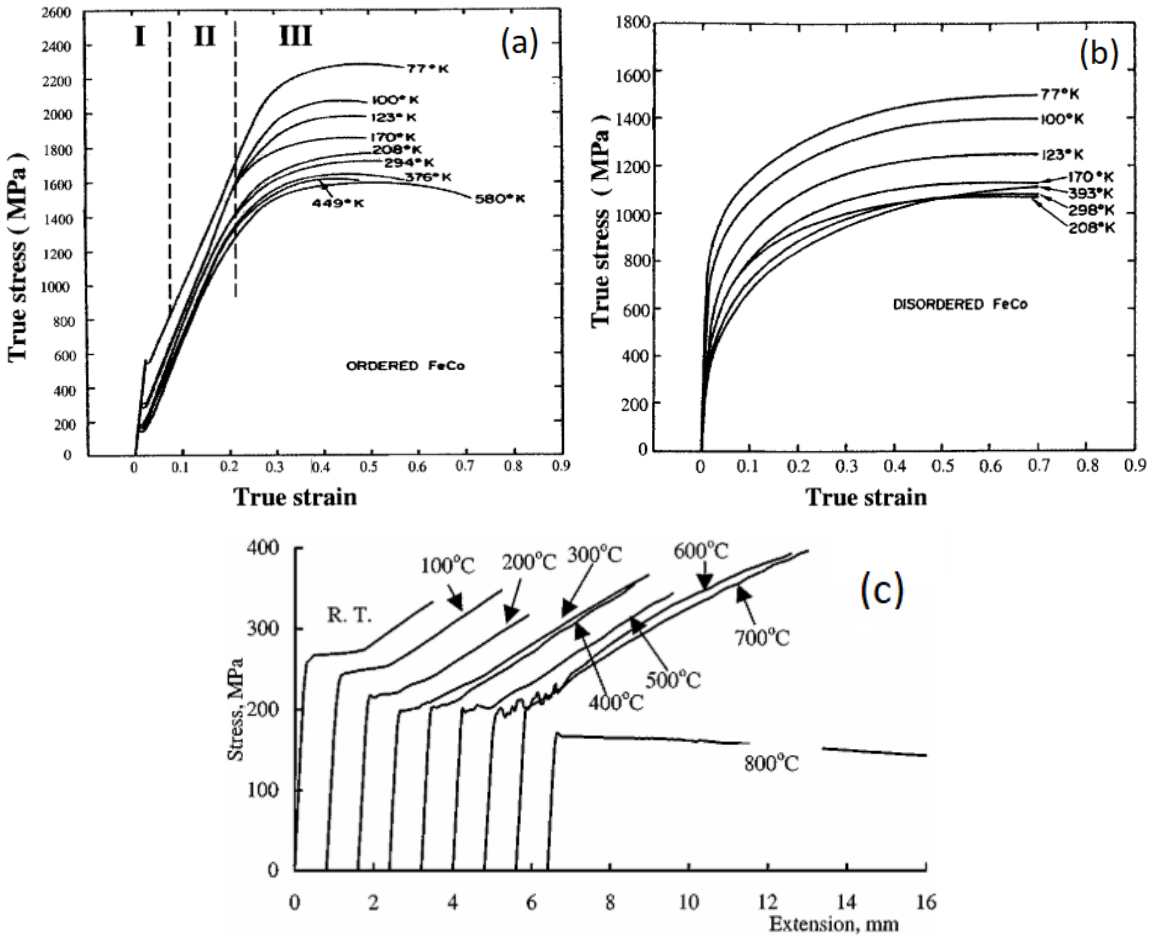

Figure 2.3 Compressive stress-strain behavior for **(a)** ordered and **(b)** disordered FeCo binary alloy under compression, as presented by Fong et al. [19]. **(c)** Tensile stress-strain behavior for the $Fe_{49}CoV_2$ as presented by Ren et al. [20]. *No permission is required for thesis purposes.*

In the literature, it has been consistently shown that the strength of FeCo-based alloys is predominantly governed by the grain size while factors such as solid solution or precipitates have minimal direct influence [3]. These findings emphasize the dominant contribution of grain size in controlling the strength characteristics of FeCo alloys. The strength of FeCo alloys is significantly affected by both the grain size and structure, as explained by the Hall-

Petch relation [21]. This empirical relation describes the connection between the yield strength (σ_y) and the grain size (d), with σ_0 representing the lattice resistance and k representing the Hall-Petch parameter as follows,

$$\sigma_y = \sigma_0 + kd^{-1/2} \quad (2)$$

Studies have shown that both ordered and disordered FeCo alloys adhere to the Hall-Petch relation [3,22]. For larger grain sizes, the disordered structure exhibits inherent strength advantages over the ordered structure. This is attributed to the presence of disassociated unit dislocations that strengthen the material through short-range ordering whereas the ordered structure relies on the glide of superdislocations as previously discussed. However, for smaller grain sizes, grain boundary strengthening effect becomes the dominant factor in determining strength. Fine-grained ordered FeCo alloys can exhibit greater strength compared to their disordered counterparts, presenting significant potential for strength improvements but a decrease in the ductility. Experimental evidence supports this behavior, with ultra-fine-grained FeCo demonstrating higher yield strength values and decreased ductility [22,23]. This is observable in **Figure 2.4** which shows the relationship between applied tensile stress and resulting strain in the FeCo-2V alloy, showcasing the influence of varying grain sizes on the mechanical response.

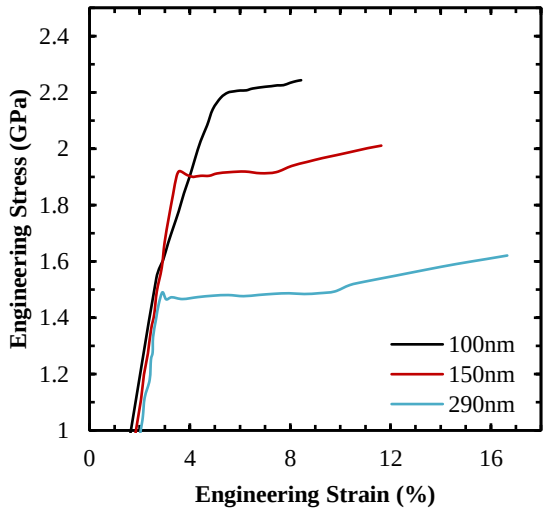

Figure 2.4 Tensile stress-strain behavior for FeCo-2V samples with different grain sizes as presented by Duckham et al. [22]. *No permission is required for thesis purposes.*

2.1.2 Ternary Additions in FeCo Alloys

To enhance ductility while minimizing the adverse effect on magnetic properties, researchers have proposed the addition of small amounts of additional alloying elements. The incorporation of V, Nb, Mo, and W has proven to be effective in enhancing cold workability when coupled with appropriate heat treatment [24]. Among these elements, V stands out as the most favored choice due to its optimal balance, offering enhanced ductility without significantly affecting the magnetic properties. There are varied explanations for the microstructural effect that enhances the ductility of ternary interactions in FeCo alloys. In the case of V, numerous theories have been proposed to explain the increase in ductility attributed to its addition. Initially, it was thought that the retardation of the order-disorder transition temperature was the main cause behind the ductility improvement [25,26]. However, there is no clear indication of this effect, and certain studies have even arrived at opposing conclusions, attributing the observed positive effect to circumstantial evidence [3]. Chen et al. [27] attributed the mechanical improvement to the scavenging effect of V in the bcc microstructure, trapping impurities and allowing a martensitic structure to develop. This theory hinges on the premise that impurities are a significant factor behind the mechanical properties of FeCo alloys. Thus, elements like Al, Si, Mn, and Zr, known for their strong scavenging capabilities and potential formation of second phases, should improve the ductility. Previous studies have explored the impact of commonly utilized elements like Al, Be, Bo, Cu, Au, Mn, Ag, Si, Ti, and Zr on the mechanical properties. However, it has been consistently observed that these elements generally exert minimal or negligible influence on the mechanical characteristics of the FeCo alloys [24]. This rules out the scavenging effect on the mechanical properties and gives way to belief that impurities might only play a secondary role in this matter.

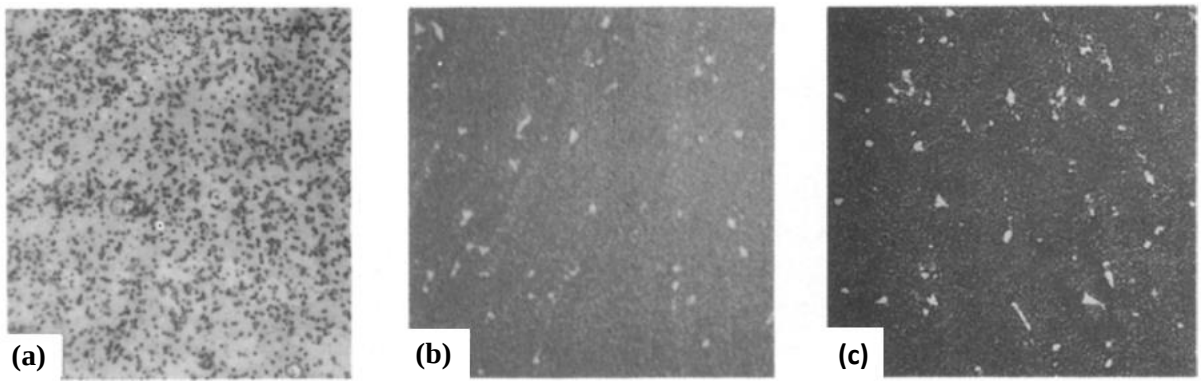

Figure 2.5 Light micrographs **(a)** and back-scattered electron micrographs **(b, c)**, showing γ_2 precipitates in the quenched **(a, b)** and furnace-cooled **(c)** FeCo-2Nb alloy, as presented by Persiano et al. [14]. *No permission is required for thesis purposes.*

After experimental observations of the formation of Co-rich compounds, Kawahara et al. [24] proposed that the formation of Co_3X (fcc - γ_2 precipitates) promotes small concentration of disordered regions around Co_3X (X = V, Nb, Mo, and W) clusters, which, after cold working, becomes uniformly distributed causing a mixture of phases [3,28]. It has been observed that these stable paramagnetic fcc compounds (γ_2-phase) are retained at low temperatures as shown in **Figure 2.5**, contributing to improved ductility in the alloy [14]. Nonetheless, the different conditions of the experiments including heat treatments and cold work applied to the alloys make the results hardly conclusive. Controversially, additive V particles in the ordered bcc phase (α-phase) have been found to have a slight detrimental effect in the magnetic moment in FeCo-V alloys [29,30]. Nonetheless, the addition of up to 2 wt.% V in FeCo presents a major improvement in the electrical resistivity by up to 23 times, substantially increasing the efficiency by reducing the losses due to eddy current [31].

Compared to the binary FeCo alloy, stress strain testing on $Fe_{49}Co\text{-}V_2$ denotes a larger "plateau" introduced by yielding followed by work hardening as can be seen in **Figure 2.3 (c)**. In this case the yielding occurrence happens up to a temperature of 600 ˚C. Intermediate temperatures reveal an anomalous strengthening which has also been observed in other bcc-based alloys [20]. The impact of the order-disorder transition becomes evident as the strain drops beyond 800 ˚C, highlighting the complex behavior of these alloys.

2.1.3 FeCo Alloys in Computational Mechanics

To present days, a few investigations have succeeded in reproducing FeCo nanoparticles properties by ab initio calculations using DFT [11,12,32–36] and Monte Carlo (MC) simulations [12,13]. The focus of these investigations has primarily been on examining the fundamental structural and magnetic properties of the ground states, as well as studying the order-disorder transformations induced by thermal effects. Neumayer et al. [32] and Mizuno et al. [34] conducted ab initio calculations to examine the influence of magnetism in the stability of the B2 structure, along with the behavior of typical vacancy and substitutional point defects. Similarly, Fu et al. [11] provided insights into the order-disorder and phase stability, suggesting that a B2-$L1_0$ transition can be achieved by scaled-down dimensions or the application of mechanical force. Additionally, the study constitutes the first computational exploration of the APB energies, showing low energies in the {110} and {112} slip planes.

To date, two ab initio studies have explored the effect of solutes in the FeCo alloys. Aykol et al. [37] studied the introduction and diffusion of V in FeCo. They found that V atoms tend to cluster linearly in {110} planes where the FeCo B2 structure is known to glide, as shown in **Figure 2.6**. The clustering phenomenon promotes a reduction in the APB energy, which is believed to facilitate a higher degree of independent movement for partial dislocations. This effect would ultimately enhance the ductility of FeCo-V alloys.

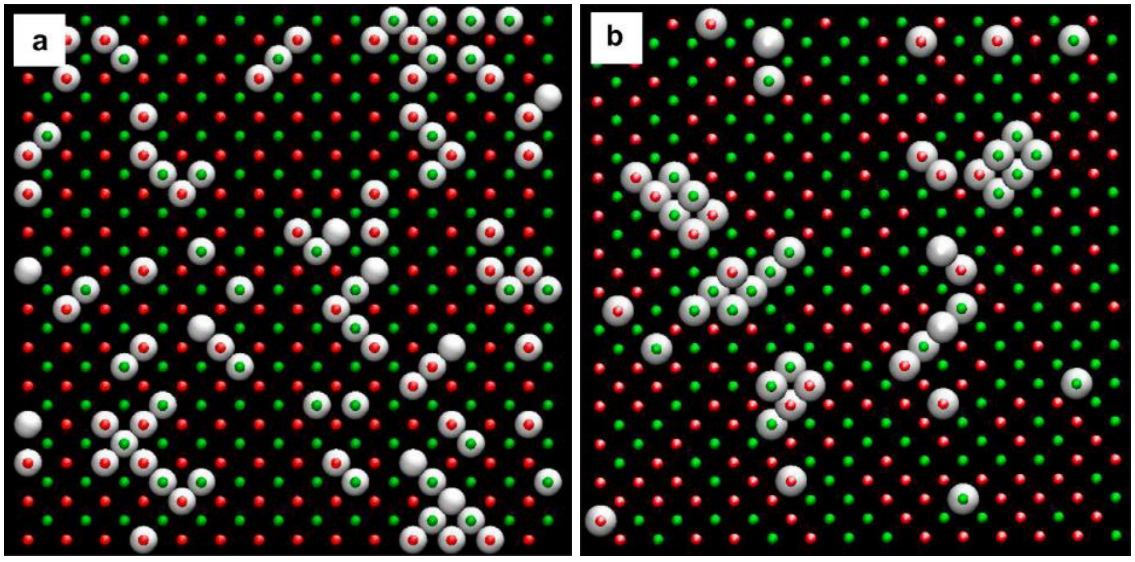

Figure 2.6 Clustering in FeCo-2V in ordered **(a)** and disordered **(b)** superlattice observed from the [001] direction, as presented by Aykol et al. [37]. Green, red and white dots represent Fe, Co and V respectively. *No permission is required for thesis purposes.*

On the effect of ternary additions, recently Li et al. [38] conducted a study investigating the influence of various elements, including V, Nb, Ta, Mo, and W, on the ordering degree of the FeCo alloy. Their findings concluded that Nb and Ta are particularly effective in slowing down the ordering kinetics. This investigation also considered the effects in the antiphase boundary (APB), where the incorporation of these alloying elements led to a reduction in energy associated with APBs in both {110} and {112} planes. The decreased energy values is expected to promote smoother dislocation mobility, thereby improving ductility in the alloy [37–39]. The impact of these additions on the FeCo APB energies can be observed in **Figure 2.7**. Interestingly, these results suggest the V and W additions exhibit the lower energies and thus should be more suitable for enhancing the ductility in FeCo alloys.

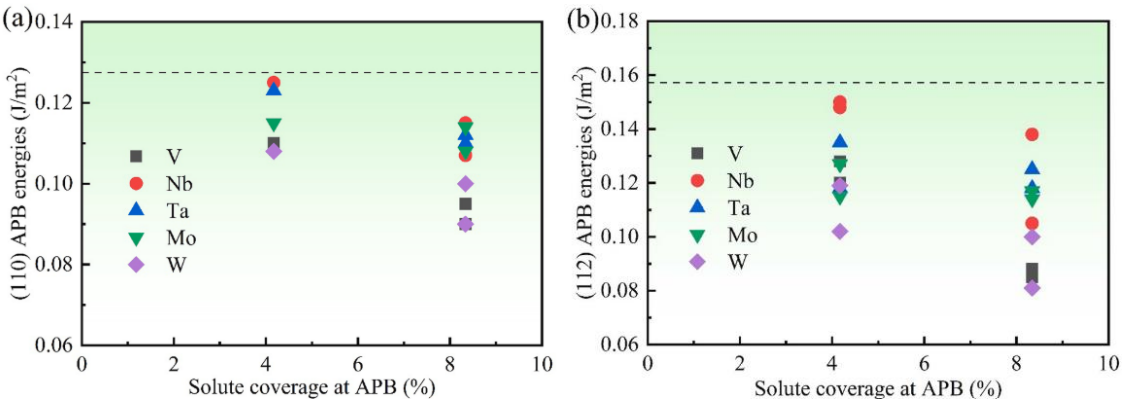

Figure 2.7 APB energies for the **(a)** (110) and **(b)** (112) common slip systems of FeCo (dotted line) vs solute coverage. As presented by Li et al. [38]. *No permission is required for thesis purposes.*

Moving on to the MD field, FeCo systems have been explored using different methods including the embedded-atom method (EAM) [40] and the enhanced version, the modified embedded atom method (MEAM) [41] to study the thermal-structural properties. Up to this date, in the available literature there are two EAM potentials containing FeCo interactions. In 2001, Zhou and Wadley et al. [42,43] developed normalized potentials that provides a

general approach for combinations of 15 metallic unary systems including Fe and Co. The potential was used by its developers to study growth mechanisms and their control on thin multilayer films composed of CoFe/NiFe/Cu, aiming to explore and improve manufacturing processes to maximize the giant magnetoresistance effect. In subsequent studies, Meng et al. [44,45] utilized this potential to investigate the nanostructures of Fe-Co and the thermally induced transitions at varying concentrations of Co. Their research involved the examination of FeCo tendency and mechanisms to form a Fe-shelled structure using nanospheres as samples. Additionally, they explored the structural stability and evolution during annealing and quenching processes. Notably, a favorable transition temperature to the bcc structure was observed during cooling. However, the formation of intermediate phases, such as fcc or hcp structures, was not observed in either process. Instead, a liquid-like icosahedral type structure was observed at high temperatures. With a similar approach Yalcin et al. [12] implemented the EAM potential developed by Zhou et al. [32,33] in a MC-MD combined study. The order-disorder evolution induced by temperature was investigated using MC calculations on nanoparticles featuring different geometries and sizes, demonstrating behaviors that align well with experimental findings. Following, MD simulations were employed to examine the thermal transition structures during melting and quenching processes. The simulations revealed low melting points and the absence of an intermediate fcc phase.

Farkas and Caro [46] developed an EAM potential to describe the Fe-Ni-Cr-Co-Cu high entropy alloy (HEA), thus theoretically capable of describing the FeCo interactions. Nonetheless, as the authors claim this potential was tuned specifically for HEA study, it was not tuned for other alloys, including the binary interaction in discussion. Li et al. [47] focused their research on the FeCo alloy and improved the EAM interatomic potential developed by Zhou et al. [32,33] to examine its mechanical properties. In their study, they went beyond considering just the basic properties of the B2 structure and incorporated the APB energies for the common FeCo slip planes in their fitting procedure, namely {110} and {112}. The resulting interatomic potential was then utilized to investigate the tensile behavior of large models containing grains. The researchers introduced different ordering degrees in nanocrystalline (NC) models at the grain boundaries (GB), observing the GB motion and the formation of microcracks depending on the ordering degree as can be

observed in **Figure 2.8**. However, despite applying a significant strain of 30%, none of the simulations resulted in complete fracture, surpassing the limits observed in experimental studies. This can be considered the first MD attempt to study the deformation mechanics of FeCo, but due to the nature of the EAM, this potential cannot be extended to describe other Fe-Co based systems such as FeCo-V. Subsequently, Li et al. [48] employed the interatomic potential to examine crack propagation in models featuring diverse Fe-Co compositions and microstructure configurations. In this investigation, microcracks were strategically embedded in the grain boundaries of the systems, addressing challenges associated with observing crack formation and thereby facilitating a clearer observation of crack propagation.

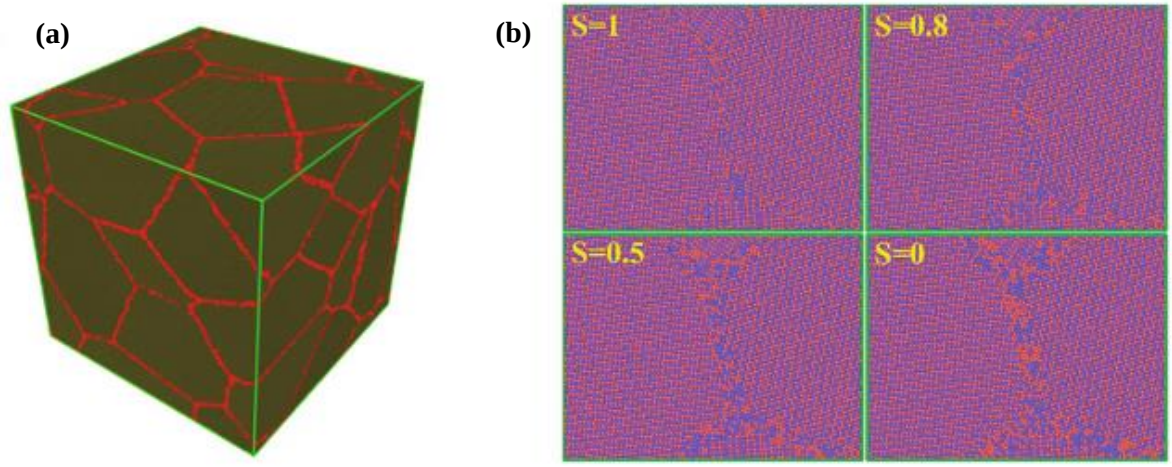

Figure 2.8 **(a)** Diagram of the NC model, highlighting GB atoms in red. **(b)** GBs displaying configurations based on various ordering degrees *S*, as illustrated by Li et al. [47]. *No permission is required for thesis purposes.*

Relying on the MEAM, Choi et al. [49] developed different binary potentials, including Fe-Co, aiming to merge them to describe a multicomponent system. The potential demonstrated a good capability to reproduce FeCo basic properties such as the energies of formation and elastic constants with good agreement with first principles calculations, correctly reproducing the stability of the low temperature phases, namely the ordered B2 and the disordered bcc. However, some overestimation was reported on the stability of FeCo high temperature phases, namely fcc and liquid. The potential was later merged to study a HEA conformed by Co-Cr-Fe-Mn-Ni [50]. Firdosy et al. [51] applied this potential

to examine the tensile strength variation with the composition of additively manufactured (AM) joints, specifically those comprised of FeCo-2V and 316L stainless steel. The graded materials were represented in a polycrystalline nanorod by altering the alloy composition from FeCo to $Fe_{69}Cr_{17}Ni_{12}Mn_2$ (equivalent to 316L steel). Subsequently, the nanorod underwent tensile strength testing. Despite the omission of V interactions in MD calculations, the authors observed a substantial structural and mechanical correlation with experimental trends. However, disparities in strength values were noted, aligning with expectations inherent to such simulations.

Wang et al. [52] completed a Co-Cr-Fe-Ni-Al-Mo-V septenary interatomic potential to investigate two distinct HEAs. Although their study doesn't specifically target the FeCo alloy, they identified limitations with the FeCo potential crafted by Choi et al. [49]. This arises from the inherent deficiencies of the unary Fe potential upon which it is constructed, mainly stemming from the core instability of the bcc structure. To solve this problem the authors highly modified the binary FeCo and FeV potentials to control the screening effects of the nearest neighbors on the bcc structures.

In a different realm of MD methods, Li et al. [53] recently utilized machine learning techniques by incorporating first principles data to formulate an interatomic potential within the atomic cluster expansion (ACE) framework. The primary emphasis of their research was on investigating the melting and solidification points in small FeCo system. The ACE method, although more detailed, is also computationally demanding, typically reserved for the study of smaller systems due to its intricacy. In a novel approach, Egorov et al. [54] introduced an innovative analytic bond-order potential (BOP) that incorporates explicit modeling of magnetism. This potential was designed with a broad scope in mind; however, its current implementation is somewhat constrained. Although it demonstrates notable improvements in describing both ferromagnetic and nonmagnetic structures, its ability to accurately reproduce elastic properties remains limited.

The use of MD simulations has been instrumental in investigating FeCo alloys, specifically in understanding their thermal and ordering characteristics. However, the exploration of other important aspects of the alloy's behavior has been limited. As a result, a comprehensive understanding of the mechanical behavior leading to fracture is still lacking. Moreover, there has been a notable absence of computational studies aimed at reproducing

the properties of FeCoV alloys or other FeCo-based alloys. Further research in computational approaches is necessary to bridge these gaps in knowledge.

2.2 Questions to Answer Based on Literature

Based on existing research, there are several key questions to be addressed:

- How does the ordering of FeCo alloys impact their mechanical properties and behavior?
- What role does grain boundary motion play in determining the strength and ductility of FeCo alloys?
- What are the fundamental mechanisms contributing to ultimate fracture in FeCo alloys, and what types of fractures do they typically induce?
- What microstructural effects does the addition of V have on FeCo alloys, and how do these effects influence ductility and overall mechanical properties?
- What is the typical diffusion behavior of V within the FeCo alloy?
- How do various alloying elements, such as V, Nb, Mo, and W, known for improving ductility, impact the microstructure and deformation behavior of FeCo alloys?
- To what extent do different interatomic potentials and computational methods affect the accuracy of studying FeCo alloys and predicting their properties?

2.3 Summary and Research Gap

Despite extensive research efforts devoted to FeCo alloys, critical questions persist concerning their microstructural behavior and its correlation with mechanical properties. A central inquiry revolves around the impact of ordering on mechanical behavior, believed to be the primary factor defining alloy ductility. Additionally, certain alloying elements in FeCo alloys have been noted to enhance ductility. For instance, the presence of V leads to an improved ductility and a shift in fracture mode from intergranular to a combined transgranular-intergranular manner, as indicated by some studies. However, the roles of these alloying elements and the diffusion patterns within FeCo alloys remain enigmatic, necessitating a comprehensive exploration of the diffusion process.

Traditional experiments often fall short in delving deep into microstructures, and computational methods based on density functional theory (DFT) are impractical for studying large realistic systems. In this context, MD simulations play a pivotal role in bridging the gap between theoretical predictions and experimental observations. However, owing to the semi-empirical nature of MD calculations, specific interatomic potentials must be tailored depending on the application. Despite the extensive computational research conducted on FeCo alloys, there is a notable absence of interatomic potentials capable of providing accurate insights into their deformation mechanisms, especially concerning the impact of added elements. This research initiative is primarily focused on developing customized interatomic potentials with enhanced mechanical capabilities to precisely describe the behavior of FeCo alloys. Subsequently, the objective is to conduct atomistic simulations on large, realistic systems to unravel the diffusion of solutes and deformation processes in these alloys. Addressing these fundamental questions not only advances our understanding but also paves the way for innovations, enabling the comprehensive design of FeCo alloys with diverse characteristics.

Chapter 3

Computational Methodology

This section provides an overview of various computational methods for materials study, highligthing their differences and capabilities. Special focus is dedicated to Molecular Dynamics (MD) and the theoretical underpinnings of the Modified Embedded Atom Method (MEAM) and the combination of MD simulations with Monte Carlo (MC) calculations. The multi-objective optimization (MOO) technique is elucidated as a general procedure for constructing interatomic potentials in this study. The most common thermodynamic ensembles employed in MD are reviewed. Lastly, the computational tools, encompassing both software and hardware, necessary for the successful execution of atomistic simulations are discussed.

3.1 Rationale for Selection of Methods

The first approaches to computational simulations in materials science began nearly five decades ago, marking the beginning of a remarkable journey in the field. Over the years, these methods, along with the advancements in computational power, have undergone significant evolution. What was once only achievable with high-performance computing clusters is now accessible on inexpensive personal computers and even smartphones, enabling researchers to perform atomistic simulations and closely replicate experimental values. These computational simulations were initially developed with the primary goal of unraveling the origins of various material properties. The fundamental nature of these properties can be understood by examining the interactions between the outer layer electrons of atoms and their counterparts in neighboring atoms. Describing these properties relies on nothing more than quantifying the energies associated with these electron interactions.

However, a thorough understanding of the energy of a system poses a considerable challenge, as obtaining exact solutions using only a few atoms is nearly impossible. In response to this challenge, Density Functional Theory (DFT) emerged as a powerful theoretical framework. DFT introduces the concept of electron density potentials, effectively replacing the computationally demanding task of directly simulating the interactions between electrons. Instead, reliable functionals with approximations for the exchange-correlation energies are employed, allowing for efficient calculations of material properties. Despite these advancements, the current state-of-the-art computational equipment still faces limitations in terms of system size. The high demand for computing resources restricts simulations to only a few tens of atoms.

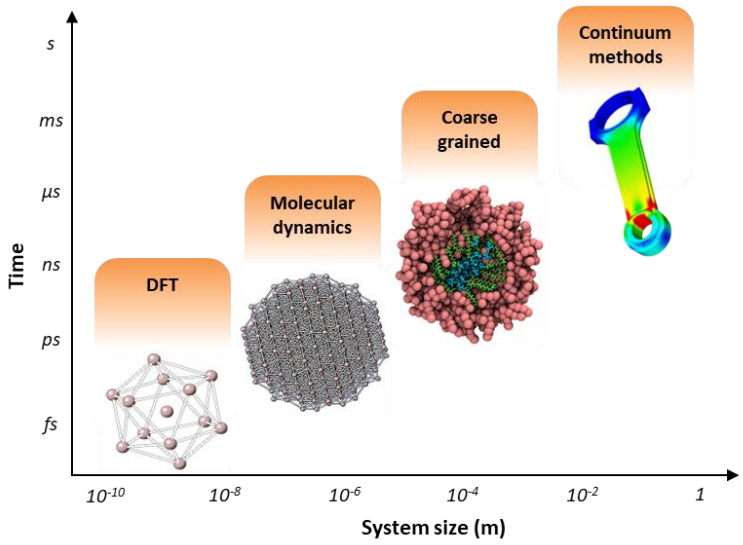

Figure 3.1 Time scale vs length scale of different modeling methods. Adapted from Goel et al. [55]. *No permission is required for thesis purposes.*

Alternatively, molecular dynamics (MD) simulations relying on classical mechanics can accurately reproduce the development of atomistic systems on nano and micro-scales. MD methods open the possibility to create reduced predictive models that can be implemented in methods based on continuum mechanics [56,57]. A comparative overview of different methods, showcasing their respective time and size capabilities are illustrated in **Figure 3.1**. Atomistic simulations rely on the position of the atoms to evaluate the energy of a system and the involved interatomic forces. There is a diverse array of MD methods available, each tailored to suit specific applications. Depending on the intended use or the material under investigation, researchers can choose from a wide range of MD techniques that cater to different scenarios and research objectives. A flowchart of a brief MD process is presented in **Figure 3.2** whereas a diagram showing some of the most popular methods is shown in **Figure 3.3**.

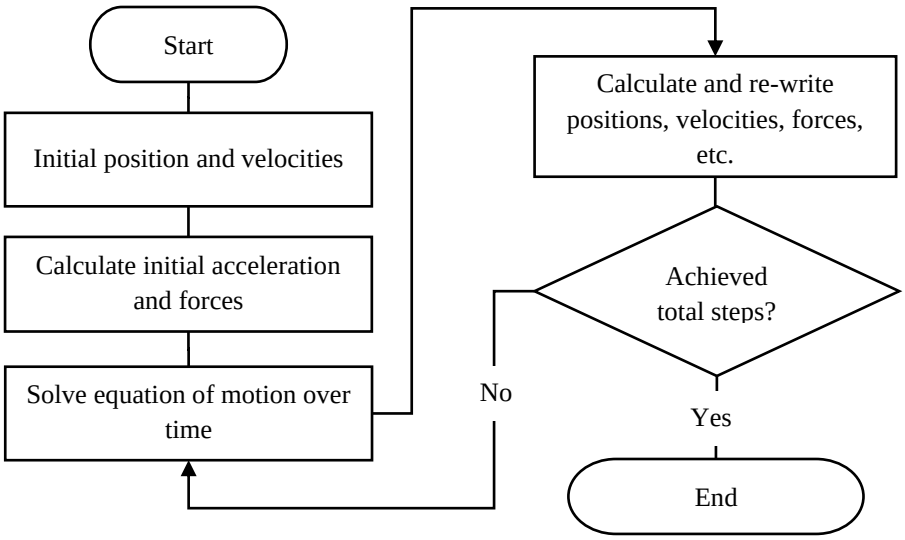

Figure 3.2 Flowchart of molecular dynamics simulation procedures.

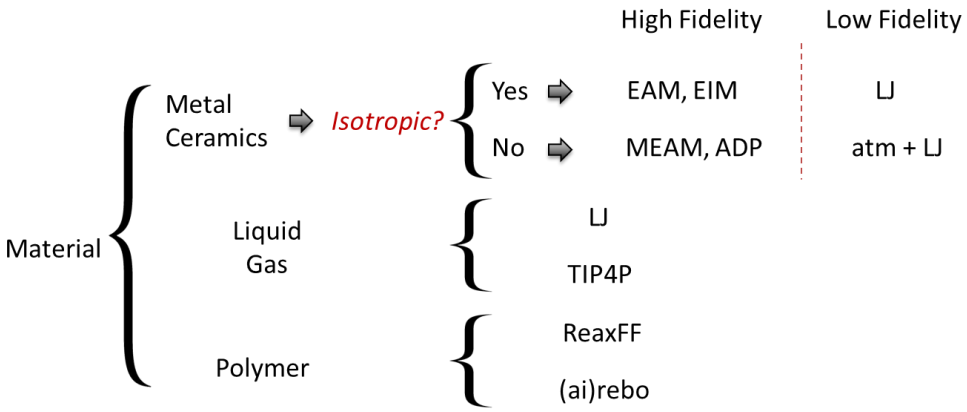

Figure 3.3 Popular MD methods depending on the targeted material of study: EIM (Effective Interaction Model), ADP (Anisotropic Displacement Parameters), TIP4P (Transferable Intermolecular Potential with 4 Points), ReaxFF (Reactive Force Field), and (ai)REBO (Adaptive Intermolecular Reactive Empirical Bond Order). As partially discussed by Harrison et al. [58].

One of the most popular methods nowadays to study alloys is based in the semi-empirical many-body EAM developed by Daw and Baskes [40], constructed as an extension of the Lennard-Jones potential to include metallic bonding. Thus, capable of describing the interactions between atoms and calculating a wide range of properties in metallic systems. The EAM takes the background electron density as a linear superposition of the electron densities with a spherical symmetry therefore being accurate for symmetric structures but increasingly inaccurate for complex atomic configurations and low symmetry systems. Taking this into account, Baskes improved the formalism and presented the MEAM [59].

This version introduces a novel concept by incorporating directionality into electron bonding. By addressing the limitations of the EAM, this method presents a significant advancement in accurately describing various atomic structures. It overcomes the challenges associated with accurately representing complex structures, making it a versatile formalism that can be applied beyond simple systems and opens up new possibilities for studying alloys, semiconductors, and diatomic gases. Later, the Second Nearest Neighbor (2NN) MEAM was introduced in the 2000's by Lee and Baskes [41], to overcome the shortcomings of the original MEAM, particularly concerning the structural stability of bcc metals, as well as for certain fcc and hcp materials. This version incorporates directional shielding capable of including more neighbors and limiting the influence exerted by the atoms. A basic illustration denoting the main differences between the EAM-based series of potentials is shown in **Figure 3.4**.

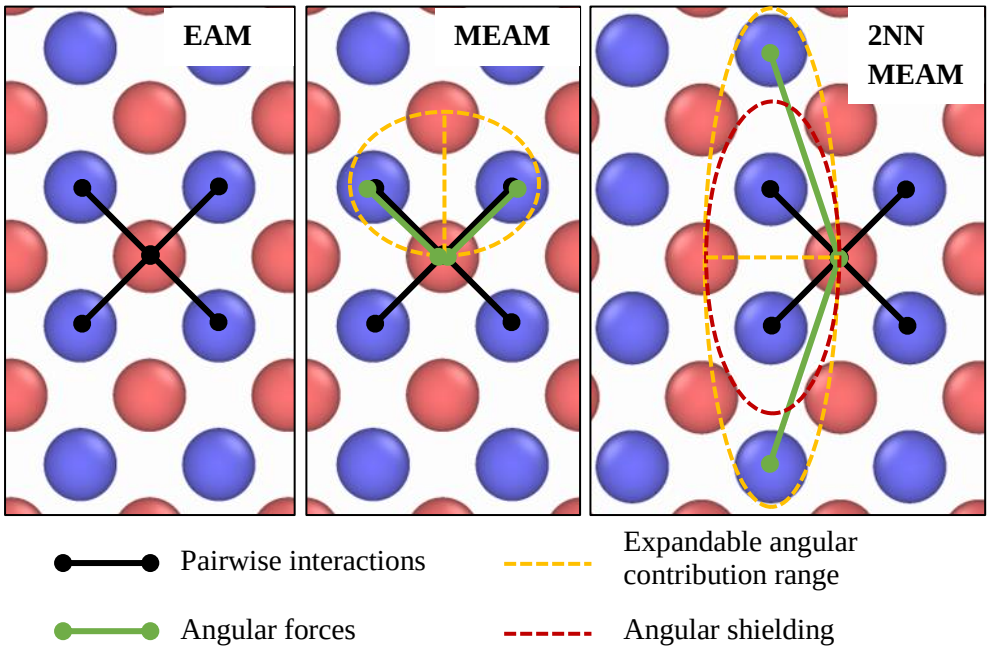

Figure 3.4 Simple ilustration of the differences between the EAM, MEAM and 2NN MEAM.

The construction procedure of a 2NN MEAM interatomic potential involves the fitting of multiple parameters in addition to initial reference data obtained preferably from experimental results and ab initio calculations. The usual procedure consists of reproducing a handful of properties in a reference structure and testing it in different systems. If the

potential is not satisfactory, it will be returned to the first step and modify the initial parameters. This method works eventually in many cases but can become tedious and time-consuming [60]. Thus, we have adopted a MOO based on the force-matching method which allows a weighted margin of error combined with a mesh type search to reduce the optimization time. Once a satisfactory potential is constructed, we are able to create custom atomic systems with specific conditions to perform different physical tests such as melting and tensile tests. Given the versatility of atomistic simulations, atomic systems of different sizes and shapes with different compositions may be fabricated such as thin layers, nanowires and even complex larger structures containing grain boundaries. Moreover, the universality of the interatomic potentials makes it simpler to incorporate other elements into a multisystem to explore new materials.

3.2 Fundamentals of MD Simulations

3.2.1 Modified Embedded Atom Method

The foundation of atomistic simulations lies in the evaluation of system energy and interatomic forces as a function of atomic positions. Some of the most popular methods nowadays are based in the semi-empirical many-body Embedded Atom Method (EAM) developed by Daw and Baskes [40] in 1983. This method effectively captures interatomic energies and computes various properties in metallic systems. However, its accuracy diminishes when dealing with intricate atomic configurations and systems lacking symmetry due to its spherical symmetry-based treatment of background electron density.

To address the importance of directionality in electron bonding, Baskes introduced the Modified Embedded-Atom Method (MEAM) [61] in 1987 as an enhancement to the original EAM. The MEAM accounts for realistic shear behaviors by incorporating partial angular directions in the background electron density function, accommodating local symmetry variations. This modification extends the applicability of MEAM to encompass alloys, semiconductors, and diatomic gases [37], while addressing certain limitations of the EAM. It stands as the first formalism capable of describing a broad range of elements and alloys. In the 2000s, Lee and Baskes [41] introduced the Second Nearest Neighbor (2NN)

MEAM to overcome specific shortcomings of the original MEAM, particularly with regards to bcc metals, further enhancing the accuracy and applicability of the MEAM framework.

For the MEAM and the 2NN MEAM, directionality is provided by interatomic shielding. The main difference between the two methods reside in the consideration of neighbors for the energy contributions. The MEAM considers only the first nearest neighbor whereas in the 2NN MEAM the range can be extended to a second and further neighbors. This expands the method to be applicable to a wide range of structures and alloys, including face-centered cubic (fcc), body-centered cubic (bcc), hexagonal close packed (hcp), diamond structures and their alloys among others. Both methods describe the general energy *E* with the same expression, which can be written as:

$$E = \sum_i \left[F_i(\bar{\rho}_i) + \frac{1}{2} \sum_{j \neq i} S_{ij} \varphi_{ij}(R_{ij}) \right] \tag{3}$$

The embedded function F_i represents the energy of an atom core when it is "embedded" in the electron cloud constructed as a superposition of contributions from neighboring atoms. Based on the Equation of States (EOS) [62], the pair potential φ_{ij} embodies the electrostatic core-core repulsion of two atoms separated by the distance R_{ij}. The improvement of the 2NN MEAM over its predecessors is given by the term S_{ij}, which determines the degree of screening between the atoms i, j and the neighboring atoms limiting the interaction range in different directions by a minimum (C_{min}) and maximum (C_{max}) screening parameters. The embedding function is given by,

$$F(\bar{\rho}_i) = AE_c \left(\frac{\bar{\rho}_i}{\bar{\rho}^0} \right) ln \left(\frac{\bar{\rho}_i}{\bar{\rho}^0} \right) \tag{4}$$

where *A* functions as an adjustable parameter, E_c represents the cohesive energy, $\bar{\rho}_i$ being the background electron density and $\bar{\rho}^0$ the background electron density of a reference structure in equilibrium. The term for the background electron density is given by,

$$\overline{\rho}_i = \rho_i^{(0)} = \sum_{j \neq i} \rho_j^{a(0)}(R_{ij}) + angular\_contributions \tag{5}$$

where R_{ij}represents the distance between atoms i and j atom that will be evaluated by the function $\rho_j^{a(0)}$ to obtain the atomic electron density. The *angular contributions* generated by partial electron densities are defined by the next expressions,

$$(\rho_i^{(0)})^2 = \left[\sum_{j\neq i} \rho_j^{a(0)}(R_{ij})\right]^2 \tag{5.1}$$

$$(\rho_i^{(1)})^2 = \sum_{\alpha}\left[\sum_{j\neq i} \frac{R_{ij}^{\alpha}}{R_{ij}} \rho_j^{a(1)}(R_{ij})\right]^2 \tag{5.2}$$

$$(\rho_i^{(2)})^2 = \sum_{\alpha,\beta}\left[\sum_{j\neq i} \frac{R_{ij}^{\alpha}R_{ij}^{\beta}}{R_{ij}^2} \rho_j^{a(2)}(R_{ij})\right]^2 - \frac{1}{3}\left[\sum_{j\neq i} \rho_j^{a(2)}(R_{ij})\right]^2 \tag{5.3}$$

$$(\rho_i^{(3)})^2 = \sum_{\alpha,\beta,\gamma}\left[\sum_{j\neq i} \frac{R_{ij}^{\alpha}R_{ij}^{\beta}R_{ij}^{\gamma}}{R_{ij}^3} \rho_j^{a(3)}(R_{ij})\right]^2 - \frac{3}{5}\sum_{\alpha}\left[\sum_{j\neq i} \frac{R_{ij}^{\alpha}}{R_{ij}} \rho_j^{a(3)}(R_{ij})\right]^2 \tag{5.4}$$

where R_{ij} with components α, β and γ represent the component *x*, *y* or *z* of a distance vector between *j* and *i* atoms. The partial electron densities are combined without a numerical error by the following expression,

$$\overline{\rho}_i = \rho_i^{(0)} G(\Gamma) \tag{6}$$

where

$$G(\Gamma) = \frac{2}{1+e^{-\Gamma}} \tag{7}$$

then

$$\Gamma = \sum_{h=1}^{3} t_i^{(h)} \left[\frac{\rho_i^{(h)}}{\rho_i^{(0)}}\right]^2 \tag{8}$$

$t_i^{(h)}$ works as adjustable weighting factors for the atomic densities. The atomic electron density is given by,

$$\rho^{a(h)}(R) = \rho_0\, exp\left[-\beta^{(h)}(R/r_e - 1)\right] \tag{9}$$

where $\beta^{(h)}$ is an adjustable parameter governing the exponential decay factors associated with atomic densities. The equilibrium reference structure is characterized by the nearest neighbor distance, denoted as r_e. The parameter ρ_0 is a scaling factor affecting calculations on alloys, this value has no impact on unary systems.

Following the universal equation of state defined by Rose [62] characterized as a function of the nearest neighbor distance denoted by R,

$$F(\bar{\rho}^o(R)) + \frac{1}{2}\sum \varphi(R) = E^u(R) \\ = -E_c(1 + a^*)e^{-a^*} \quad (10)$$

where $E^u(r)$ embodies the universal function governing a consistent expansion or contraction within the reference structure, then

$$a^* = \alpha(R/r_e - 1) \quad (11)$$

and

$$\alpha = \left(\frac{9B\Omega}{E_c}\right)^{1/2} \quad (12)$$

B is referred to the bulk modulus whereas Ω represents the equilibrium atomic volume. These parameters serve as a reference and are usually extracted from either ab initio or experimental results. Finally, the pair potential for an element can be defined as

$$\varphi(R) = \frac{2}{Z_1}[E^u(R) - F(\bar{\rho}^o(R))] \quad (13)$$

Where the number of nearest neighbor atoms is defined by Z_1.

The basic idea of the screening is that a neighborhood is created by the atoms *i* and *j* and delimited by two ellipses defined by C_{max} and C_{min} that reduce or shield the electron density contribution and pair interaction. If an atom *k* remains outside this neighborhood, it is assumed that it does not have any effect on the other atoms. On the other hand, if *k* lies inside then it is presumed that it completely screens in the interaction. **Figure 3.5** depicts a the interaction between the i, j and k atoms with the $C_{min/max}$ ellipses.

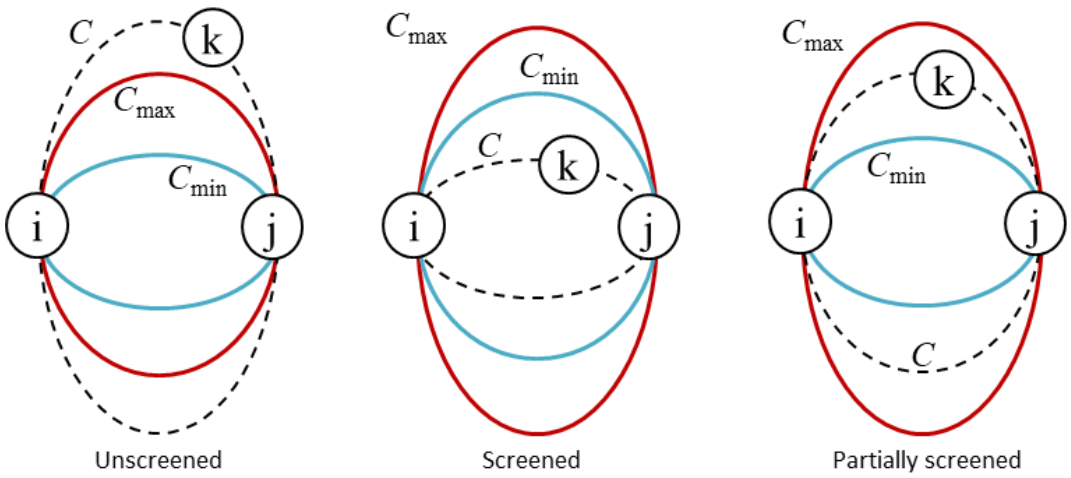

Figure 3.5 Screening function diagram.

The formalism that describes the many body screening function between atoms *i* and *j* is

$$S_{ij} = \prod_{k \neq i,j} S_{ikj} \tag{14}$$

being S_{ij} a product of the screening factors S_{ikj}, these are defined by distances delimited by ellipses. as the next equation shows,

$$x^2 + \frac{1}{C} y^2 = \left(\frac{1}{2} R_{ij}\right)^2 \tag{15}$$

here, the major axis of the ellipse is oriented along the *y*-direction determining the screening range, while the minor axis *x* represents the line segment connecting atoms *i* and *j*. In this context, C is defined by

$$C = \frac{2(X_{ik} + X_{kj}) - (X_{ik} - X_{kj})^2 - 1}{1 - (X_{ik} - X_{kj})^2} \tag{16}$$

where

$$X_{\mathrm{ik}} = (R_{\mathrm{ik}}/\mathrm{R_{ij}})^2 \tag{17}$$

and

$$X_{\mathrm{kj}} = (R_{\mathrm{kj}}/\mathrm{R_{ij}})^2 \tag{18}$$

then the screening factor can be defined as a function of C,

$$S_{ikj} = f_c\left[\frac{C - C_{min}}{C_{max} - C_{min}}\right] \tag{19}$$

where C_{min} and C_{max} are the values that are going to delimit the screening. In the case of unary systems containing A atoms of an element the interaction between *i-j-k* is given by

(*A,A,A*). According to the possible relationships between atoms of different elements A and B, the screening interactions for a binary alloy are defined in four directions (*A,A,B*), (*B,B,A*), (*A,B,A*) and (*A,B,B*). Then the smooth cutoff function will be defined by,

$$f_c(x) = \begin{cases} 1 & x \geq 1 \\ \left[1-(1-x)^4\right]^2 & 0 < x < 1 \\ 0 & x \leq 0 \end{cases} \quad (20)$$

Due to this numerical procedure *Sij*=1 and *Sij*=0 defining that the interaction between atoms can be completely unscreened or screened respectively and defining $f_c(x)$ as a smooth factor for partial screening. Computationally speaking a radial cutoff distance is also implemented to save time in simulations developing neighbor lists as shown by

$$f_c = [(r_c\text{-R})/\Delta r] \quad (21)$$

where r_c is the radius cutoff distance. Δr symbolizes the cutoff region, which limits the electron density and the pair potential. After defining the screening functions and combining them with the previous formalisms we need to redefine the following equations for alloy systems, first the contribution of the electron density is modified to

$$\bar{\rho}^0(R) = Z_1\rho^{a(0)}(R) + Z_2 S\rho^{a(0)}(aR) \quad (22)$$

where Z_2 denotes the count of atoms situated as second nearest neighbors in the reference structure, and a is a ratio between the distance of the first and second nearest neighbors. Then another pair potential appears defining the formula for the expansion/contraction as

$$E^u(R) = F(\bar{\rho}^0(R)) + (Z_1/2)\psi(R) \quad (23)$$

where a second pair potential is defined by

$$\psi(R) = \varphi(R) + (Z_2 S/2)\varphi(aR) \quad (24)$$

finally modifying the main pair potential function as

$$\varphi(R) = \psi(R) + \sum_{n=1}(-1)^n(Z_2 S/Z_1)^n\psi(a^n R) \quad (25)$$

this equation is used as a relationship between both potentials. Despite of having already define the parameters of each individual element of the alloy and to rule the independent elements as a whole system we need to define some parameters of the entire system, usually these are extracted from experiments and first principles calculations as required in **Equation 12**.

3.2.2 Monte Carlo Optimization

Although MD has gained widespread popularity as a valuable tool for conducting computational statistical mechanics, it does have certain limitations. Processes characterized by slow relaxations, such as diffusion, impurity drag effects, and precipitate nucleation, present challenges since they occur on timescales beyond the reach of MD simulations. To address these slow processes, the Monte Carlo (MC) method has been employed in previous studies [63].

The MC method is a mathematical technique used to predict potential outcomes of uncertain events. However, it yields results that are disconnected from the statistical ensemble of the system and fails to capture the effects of the resultant changes. This limitation means that the effects of resultant changes and dynamic processes may not be fully captured. To overcome this limitation and enhance the predictive capabilities, a combined approach that integrates MD simulations with MC simulations has been developed. This hybrid approach offers several advantages, including accelerated sampling of the system and a more comprehensive exploration of its behavior and properties. This integration allows for a more comprehensive exploration of the system's behavior and properties, bridging the gap between MD's accuracy and MC's ability to capture slow processes.

Hybrid MD+MC simulations can be performed by alternating the two types of simulations on the same system using regular time integration displacements. This will allow atom exchanges with a proper stabilized thermodynamic description. A simple MD+MC simulation employing the isobaric-isothermal ensemble (constant number of particles, pressure, and temperature - NPT) combined with atom swapping evaluates the energy and the phase space probability of the system. Atom swaps are attempted between randomly chosen candidates of different species, with equal probability. A general sketch of this process goes as follows, randomly choosing a particle i and performing a trial swap between two atoms $\vec{r_i} \rightarrow \vec{r_i'}$. The energy difference is calculated between the initial and the trial configuration as follows,

$$\Delta U = U\left(\vec{r_i'}\right) + U(\vec{r_i}) \tag{26}$$

following, the acceptance or rejection is measured by the probability

$$P^{swap} = \min\{1, exp^{-\beta\Delta U}\} \quad (27)$$

where β is the inverse of the temperature (T) multiplied by the Boltzmann(k) constant. These basic steps are repeated several times. Then a trial in the volume change is performed by the form $V \rightarrow V' = V + \Delta V$, this change scales the particle coordinates thus changing the energy of ΔU. Following, the change in the enthalpy is given by

$$\Delta H = \Delta U + P\,\Delta V - kT\,N \ln\left(\frac{V'}{V}\right) \quad (28)$$

finally, once again the acceptance or rejection is evaluated by the probability in **Equation 27**. Once a specified number of MC exchanges or exchange attempts is reached, the system undergoes stabilization for a specific number of MD timesteps before the process is repeated. This iterative procedure continues until convergence is achieved or the specified limit of MD timesteps is reached.

3.2.3 Thermodynamic Ensembles and Simulation Conditions

Thermodynamic ensembles play a crucial role in the field of MD, providing a framework for studying the behavior of molecular systems at the macroscopic level. The use of these ensembles in MD aims to replicate the usual conditions observed in experiments and translate them to simulations. To connect MD simulations to macroscopic thermodynamic quantities, such as temperature, pressure, and free energy, the concept of ensembles becomes indispensable. Ensembles represent different possible distributions of particles in a given system which cannot be precisely known in a deterministic manner due to the uncertainty principle between position and momentum [64]. The usual statistical ensembles utilized in MD are described in the following text and illustrated in **Figure 3.6**.

- NVT Ensemble (Canonical Ensemble): used to simulate systems at constant number of particles (N), volume (V), and temperature (T). This ensemble represents a system in contact with a heat bath that maintains the desired temperature. This ensemble is often achieved by applying a thermostat, which adjusts the velocities of the particles to maintain the specified temperature.
- NPT Ensemble (Isobaric-Isothermal Ensemble): used to simulate systems at constant number of particles (N), pressure (P), and temperature (T). Within this ensemble, the

system is in contact with both a heat bath and a pressure bath. The heat bath maintains the desired temperature, while the pressure bath adjusts the system's volume to maintain the specified pressure.

- NVE Ensemble (Microcanonical Ensemble): used to simulate systems at constant number of particles (N), volume (V), and total energy (E). Within this ensemble, the system remains isolated, with no exchange of energy or particles occurring with its surroundings. The NVE ensemble is useful for studying closed systems that are energetically conserved and have a well-defined total energy.

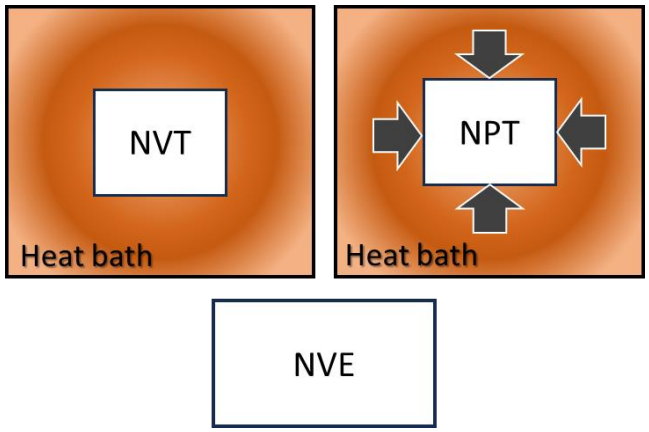

Figure 3.6 Usual statistical ensembles utilized in MD.

The choice of ensemble depends on the specific research questions, the properties of interest, and the experimental conditions being simulated. Given the objectives of this research to study ordering and deformation, mainly the NVT and NPT ensembles were used.

3.3 Interatomic Potential Development

3.3.1 Multi Objective Optimization

In engineering most of the optimization problems require the simultaneous optimization of different objective functions. In line with the force-matching method, a multi objective optimization (MOO) procedure was developed and implemented to fit a MEAM potential

for the magnesium system by Kim et al. [60]. As it is realistically unlikely to obtain a perfect optimization some tradeoffs between the objectives is expected to ensure an overall satisfactory design. One of the targets of this method is to reduce the global error of the objective functions, producing a well-balanced set of parameters avoiding the dominance of a function. The procedure is basically formulated as

$$\min J(x) \text{ such that } x \in S$$

where

$$J = [J_1(x) \dots J_m(x)]^T \tag{29}$$

$$x = [x_1 \dots x_n]^T \tag{30}$$

being m the objectives that defines the vector J, the vectors x belongs to the domain S and define the individual objectives. Given the multitude of objectives in the 2NN MEAM method, it is impractical to expect a set of parameters to optimize all objectives simultaneously. As a solution, scalarization with weighting factors is incorporated to minimize all elements and prevent the dominance of any single objective, implemented as

$$J(x) = \sum_{i=1}^{m} w_i J_i(x) \tag{31}$$

Here, the effect of each parameter can be adjusted by w_i, which allows to increase or decrease the influence of each objective according to the required solution. Each objective function is formulated by considering the disparities between the results and the target values, the following expression is implemented to measure and normalize these differences.

$$J_i(x) = \left[\frac{Q_i(x) - Q_i^0}{Q_i^0}\right]^2 \tag{32}$$

Where Q_i^0 represents the reference value and Q_i signifies the value predicted by the tested potential. This iteration continues until the minimum achievable error is reached.

3.3.2 Fitting Procedure

In total, the 2NN MEAM relies on 14 independent parameters to evaluate the energy function for a binary compound. Three of these parameters are extracted from experimental and/or first principles calculations. They are the cohesive energy E_c, the equilibrium

nearest-neighbor distance r_e, and the bulk modulus B, from these α is calculated representing the exponential decay factor to satisfy the EOS as shown in **Equation 12**. Depending on the source we need to calculate some values. The equilibrium atomic volume, calculated by the formula

$$\Omega = \frac{V}{\mathrm{N_o}} \tag{33}$$

here, V is the volume of the unit cell, and N_o the number of atoms contained unit cell [65]. B is calculated using the elastic constants C using the Voight's average [66] as follows

$$9B = (\mathrm{C_{11}} + C_{22} + C_{33}) + \frac{1}{2}(\mathrm{C_{12}} + C_{23} + C_{31}) \tag{34}$$

because of the similarity, a B2 structure such as the one present in the FeCo alloy can be taken as a cubic structure, where $C_{11}=C_{22}=C_{33}$ and $C_{12}=C_{23}=C_{31}$ simplifying the equation to

$$B = \frac{\mathrm{C_{11}} + 2\mathrm{C_{12}}}{3} \tag{35}$$

These set of equations are valid for cubic structures, for more complex structures or systems such as polycrystal the Voight-Reuss-Hill averages are used as described in the literature [66]. The rest of parameters are determined by fitting to the desired material properties, such are: the pressure derivative of bulk modulus adjustable to attractive or repulsive interactions, d^+ and d^- respectively, a scaling factor for the atomic electron density $\rho 0$ (ρ_0^A/ρ_0^B) and the screening parameters C_{min} and C_{max}. The screening interactions for a binary alloy are defined in four directions *(A,A,B)*, *(B,B,A)*, *(A,B,A)* and *(A,B,B)*, where *A* and *B* correspond to an atom of each element [41,59,67].

On the fitting procedure, individual C_{min}/C_{max} directionality was tested and proven that the directions *(A,B,A)* and *(A,B,B)* usually have a lower impact depending on the reference structure. Thus, *(A,A,B)* and *(B,B,A)* were initially included in the fitting and later *(A,B,A)* and *(A,B,B)* included as refining parameters. The range of screening parameters can vary depending on the specific material system being studied. There is no fixed universal range for these parameters. However, a commonly used range for the C_{min} parameter is from 0 to approximately 2.0 Å, while for the C_{max} parameter, it is typically from approximately 2.0 to 2.8 Å. These ranges allow for the inclusion of the nearest neighbor shells around each atom, ensuring that the immediate local environment is accounted for in the potential.

Moreover, these values are chosen to be large enough to incorporate the desired range of interactions, but not so large as to significantly impact computational efficiency.

On the simulations, first the total energy and internal forces are minimized from the initial unit cell using the Conjugate Gradient method [68] until reaching a ground state form. Several sets are tested following the MOO procedure until reaching convergence with a minimum error. Given the objectives of this study, there is a strong emphasis on evaluating the elastic constants, as they play a vital role in potential fitting. Elastic properties are particularly significant for understanding mechanical behavior, especially in the absence of magnetism. Transferability is tested using different sized systems and compositions along the stoichiometric range. Hypothetical structures are included to validate the stability of our potential for a wide stoichiometric range. Additionally, the averaged results of several random bcc-based supercells containing thousands of atoms are included in this study to simulate the properties of different disordered compositional phases. Ultimately, the finest binary potentials are employed to assess the system's response to stress and temperature. These simulations require additional time as they are conducted on a macroscopic scale, minimizing size-related artifacts by simulating large bulk systems rather than unit cells. Consequently, optimal parameter sets are carefully chosen, and if needed, a final refinement is performed on the most precise set. A general overview of the procedure is presented in **Figure 3.7**.

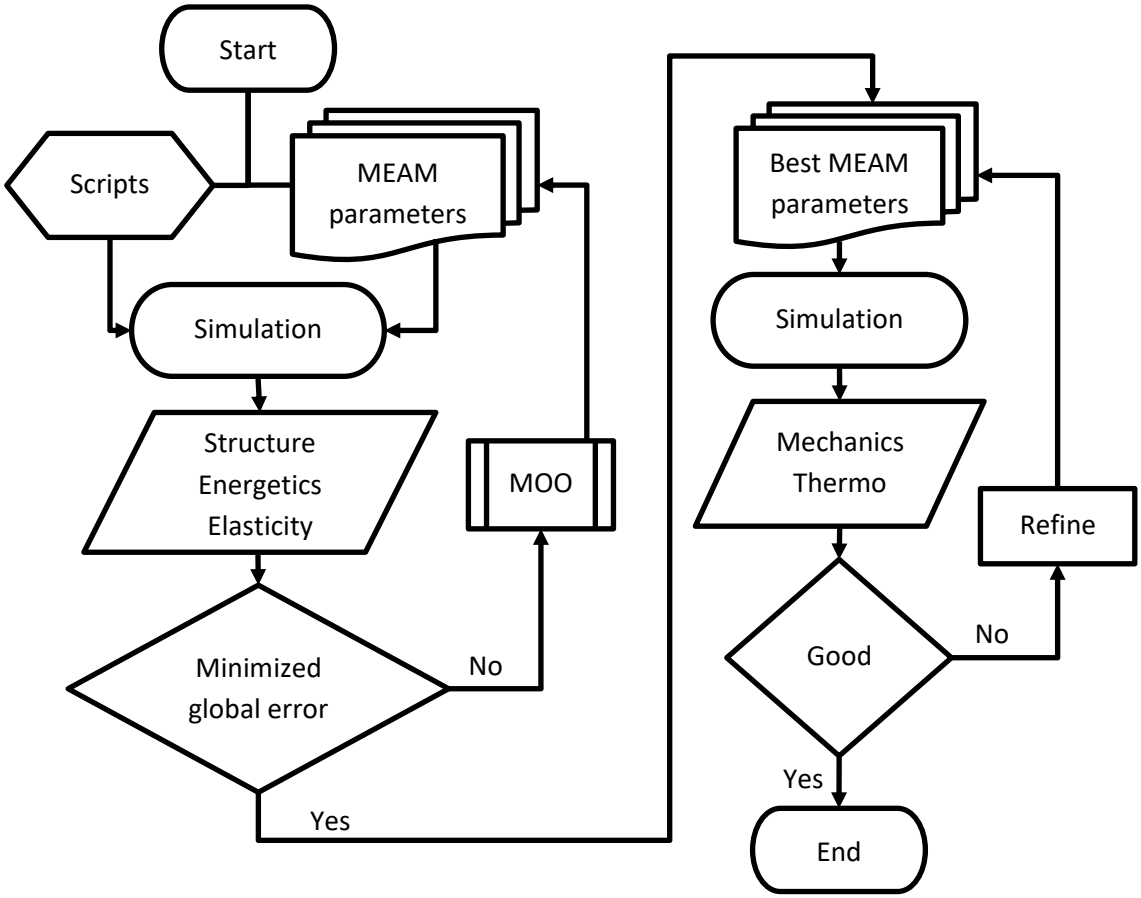

Figure 3.7 Flowchart of the general fitting procedure for a binary MEAM interatomic potential.

For a ternary system, the MEAM potential is derived by integrating both unary and binary interactions. Ternary systems require six more screening parameters, since including a *C* element adds three C_{min} and three C_{max} in the directions (*A*-*B*-*C*), (*A*-*C*-*B*) and (*B*-*A*-*C*). However, measurements of basic physical properties of ternary systems are usually scarce and it is not easy to determine the ternary screening values [69]. Thus, the usual procedure to describe the ternary screening parameters is by assuming that if two of the elements (A, B) are structurally akin to each other compared to the third element (C), it is possible to assume an averaging approach over the binary parameters. Thus, the interaction between atoms of A and B elements screening an atom of a C element [C_{min} / C_{max} (*A*-*C*-*B*)] can be taken as an average of the A-A screening C [C_{min} / C_{max} (*A*-*C*-*A*)] and B-B screening C [C_{min} / C_{max} (*B*-*C*-*B*)]. This approach has been implemented by other studies to describe ternary systems with satisfactory results [70–72].

3.4 Simulation Infrastructure: Hardware and Software Requirements

3.4.1 Hardware Consideration

Timing in MD simulations depends primarily on the MD method, system size, conditions, and available hardware for performing the calculations. While small basic calculations in small systems like unit-cells can be completed in seconds on a typical modern computer, simulations involving millions of atoms require powerful hardware to achieve time efficiency. In this research, large MD calculations were conducted at the National Singaporean Computing Center (NSCC) using Singapore's first national petascale facility for high-performance computing (HPC) known as ASPIRE (Advanced Supercomputer for Petascale Innovation Research & Enterprise). ASPIRE1, introduced in 2015, was the initial supercomputer utilized, and ASPIRE2, introduced in 2021 as an upgrade, was used for the final calculations of this project.

ASPIRE1 boasted an impressive configuration with 1160 nodes, totaling 31,320 cores and providing a compute capacity of 1 petaflop. Each node was equipped with dual Intel E5-2690v3 processors (2.60GHz, 12 cores) and 128GB DDR4 memory. Utilizing cutting-edge enhanced data rate (EDR) interconnect technology with a speed of 100Gbps, ASPIRE1 facilitated high-throughput and low-latency communication between nodes. The storage system of ASPIRE1 offered a total capacity of 14 PBytes, with an I/O bandwidth management capability of up to 500 GB/s. ASPIRE1 operated on the Linux operating system.

ASPIRE2 represents a significant improvement, as it extends the total computing capacity to 10 petaflops. This supercomputer consists of 768 nodes based on AMD HPE Cray EX 2x EPYC Millan 7713 processors, providing 128 cores per node. Each node is supported by 512 GB DDR4 memory. The storage system utilizes a General Parallel File System (GPFS) with a total capacity of 25 PBytes. The operating system utilized on ASPIRE2 is Red Hat Enterprise Linux 8. These advancements in ASPIRE's hardware and computing capabilities have significantly contributed to the efficiency and speed of the MD simulations conducted in this research project.

3.4.2 Software Consideration

The successful execution of simulations in computational research relies not only on the robustness of the computational power provided by the hardware but also on the efficiency and compatibility of the chosen software tools. Selecting appropriate simulation software is a crucial aspect of any computational study, influencing the accuracy, speed, and overall success of the research endeavor. In this section, we delve into the key considerations and software choices that underpin the computational framework. The more important and consistently used software in this study are described in the following sections.

3.3.3.1 Atomsk

Atomsk is a powerful and versatile command-line software designed for the manipulation and conversion of atomic systems. It offers a wide range of functionalities related to atomistic simulations and materials analysis. It provides extensive capabilities for manipulating atomic positions and cell parameters, allowing translations, rotations, and modifications of atomic coordinates, making it convenient for adjusting or transforming structures. One of the key features of Atomsk is its ability to generate crystal structures and periodic systems based on specified lattice parameters and space groups. The functionality expands to include operations such as superimposing structures and merging multiple configurations, enabling the creation of twins and polycrystals, among others.

In this work, Atomsk was utilized to construct polycrystals exploiting the built-in capability to implement the Voronoi tessellation method. This allowed the generation of large systems containing grains with different crystal orientations, which proved useful for performing more realistic simulations.

3.3.3.2 LAMMPS

LAMMPS, the Large-scale Atomic/Molecular Massively Parallel Simulator, is an extensively utilized open-source software package designed for MD simulations. This versatile tool provides a comprehensive set of features to explore and understand material behavior at the atomic and molecular level. With its wide range of simulation capabilities, LAMMPS supports diverse systems, including atomic, polymeric, biological, and granular

materials. Being an MD package, it employs various interatomic potentials and force fields to accurately model interactions between atoms and molecules, allowing for the investigation of a wide array of materials and phenomena.

In addition to MD simulations, LAMMPS offers the flexibility to incorporate other methods, such as MC and density functional theory (DFT) based calculations, through additional packages. This integration expands the software's capabilities and allows for hybrid simulations that combine multiple computational techniques. LAMMPS is optimized for parallel computing, enabling efficient simulations on high-performance computing systems. This scalability makes it well-suited for studying large-scale systems consisting of millions to billions of particles, facilitating in-depth analyses of complex materials.

Within the scope of this research, LAMMPS played a central role as the primary tool for conducting atomistic simulations. It facilitated critical procedures including system minimization and relaxation, thermal ramping, diffusion analysis, and strain testing among others.

3.3.3.3 MATLAB

MATLAB is a powerful and widely used software environment for numerical computation, data analysis, and visualization. This software is able to perform complex mathematical calculations, manipulate matrices and vectors, and solve equations and systems of equations efficiently. It offers a vast library of built-in functions and algorithms for tasks such as optimization, signal processing, image processing, and more. Additionally, MATLAB supports scripting and the creation of custom functions and algorithms, enabling to tailor codes for specific research or engineering requirements. The compatibility with other programming languages and software tools, enables interoperability and facilitates data exchange with external applications. It supports various file formats for importing and exporting data, making it versatile and compatible with different research workflows.

Its rich features, user-friendly interface, and extensive library of functions make it a valuable tool for various disciplines, including mathematics, engineering, physics, biology, and beyond. In this work MATLAB served as the main tool to generate the massive combination of parameters for the interatomic potentials, to analyze the data generated by

LAMMPS and to perform the MOO procedure to generate the most accurate interatomic potentials.

3.3.3.4 Notepad

Notepad is a versatile and user-friendly text editor that supports various file formats, including plain text files, making it compatible with the requirements of LAMMPS input file specifications. Notepad supports code indentation and formatting, aiding in maintaining a well-structured and visually appealing layout of the input script. The program is commonly used to create and edit text-based input scripts. In this work the generated scripts served as instructions for batch files, generation of crystal systems in Atomsk and to set up simulations in LAMMPS.

3.3.3.5 OVITO

Ovito is a dedicated software developed for the analysis and visualization of atomistic and particle-based simulation data. It enables the importation of simulation data from various file formats, presenting it in both 2D and 3D visual representations. With a range of visualization techniques at its disposal, including atomistic rendering, particle tracing, and isosurfaces, it provides valuable insights into the structure, dynamics, and properties of simulated systems. The user-friendly interface and robust architecture make it suitable for visualizing and analyzing large, complex systems such as the ones presented in this work. In this investigation, Ovito played a pivotal role in both generating and analyzing the atomic systems. The software incorporates inherent techniques, including Common Neighbor Analysis (CNA) and polyhedral template matching (PTM), facilitating the identification and separation of grains and grain boundaries, thus enabling targeted modifications within specific regions. Additionally, the included analysis methods, such as atomic strain calculations and the ability to observe trajectory lines, proved essential for investigating post-simulation features of the systems.

3.3.3.6 VESTA

Visualization for Electronic and Structural Analysis [73] (VESTA) is a software primarily utilized for crystallographic analysis and the visualization of crystal structures. The

software offers a wide range of features to explore and manipulate crystal structures in 2 and 3 dimensions. It includes capabilities for symmetry analysis, such as identifying symmetric elements, determining space groups, and visualizing crystallographic symmetry operations. Furthermore, Vesta supports the creation of supercells, allowing the generation of larger crystal structures by replicating unit cells in different directions. This feature is particularly helpful when studying defects, interfaces, or investigating the influence of size and shape on crystal properties. Overall, Vesta provides a powerful and intuitive platform for visualizing, analyzing, and manipulating crystal structures, aiding researchers in their exploration and understanding of crystalline materials. In this work Vesta was mainly implemented to generate the initial configuration of unit cells and supercells used in the interatomic potential fitting phase.

3.5 Overview of Methodologies

This chapter has presented a comprehensive overview of the diverse methodologies and computational tools employed in our study of FeCo alloys. The atomistic insights derived from MD simulations and the probabilistic modeling through MC calculations have each contributed a distinct dimension to our comprehension of material behaviors. The synergistic application of these robust methods, coupled with advanced hardware and software capabilities, establishes a powerful platform for materials research. Through the collective utilization of these tools, our study extensively investigates the mechanical, thermal, and structural aspects of FeCo alloys, offering a holistic understanding of their properties within the realm of MD scales.

Chapter 4

Molecular Dynamics Study of FeCo Phase Transitions and Thermal Properties Based on An Improved 2NN MEAM Potential

A semi-empirical potential in line with the second nearest-neighbor modified embedded-atom method (2NN MEAM) formalism has been improved for the Fe-Co interactions intended to reproduce the different thermal phases stability. Fundamental structural and elastic properties are correctly reproduced. Point defects have been included in the fitting to improve the thermodynamic characteristics. Molecular dynamics (MD) simulations using this potential predict melting temperatures which aligns with experimental data and is the first potential showing a temperature induced B2 to L10/hcp transformation. A disorder transformation is observed by diffusing vacancies at different temperatures and quantified by the long-range order parameter. The potential is also applied to thin films of the metastable L10 structure by using a face-centered cubic buffer, which can predict the good stability and energetical results comparable to ab initio calculations. The potential proves useful to study the thermal effects of different FeCo phases in bulk and multilayer films.

**This section is published substantially in Journal of Materials Research and Technology, 2022. https://doi.org/10.1016/j.jmrt.2022.05.100. Reprint with permission.

4.1 Introduction

FeCo alloys have gained interest by different industries because of its magnetic properties at low temperatures, presenting a B2 structure with intrinsic soft magnetic properties . However, a rise in temperature induces structural disorder in FeCo alloys, leading to a shift in physical properties that is not yet fully comprehended. Following, a phase transformation to a disordered face-centered cubic (fcc) (A1) marks the Curie temperature. At nano scale, it has been found that FeCo can be stabilized to a metastable ordered face-centered cubic (fcc) ($L1_0$) structure by growing up to 6 monoatomic layers on a fcc buffer layer [74]. The $L1_0$ configuration presents large magnetic anisotropy and large magnetic moment, making it a promising hard magnetic material without the need of rare-earth elements [11,74,75]. Under the molecular dynamics (MD) scope, there is no dedicated potential capable of predicting an intermediate phase transition with a correct melting point. Moreover, there has been no attempt to study the $L1_0$ phase stability nor its properties through MD. In this chapter we present a second nearest neighbor modified embedded atom method (2NN MEAM) interatomic potential applicable to FeCo alloys with a focus on the stability of the phases near stoichiometric compositions. The binary parameters were defined by fitting to ab initio and experimental results. Reliability and transferability of the potential are assessed by comparing fundamental properties of non-stoichiometric solid solutions equilibrated through Canonical Monte Carlo (CMC) simulations with the literature. Then, the potential is applied to artificially induce order-disorder through vacancies generated using the Grand Canonical Monte Carlo (GCMC) scheme. Finally, the potential is used to stabilize $L1_0$ monolayers on a neutral fcc substrate, the measured energetics are compared with experimental observations.

4.2 Potential Development

The 2NN MEAM for binary systems is mainly based on unary interactions. We have adopted previously developed and extensively tested single-element interatomic potentials for the Fe [41] and Co [76] systems, shown in **Table 4.1**. These potentials have been previously used to describe a FeCo potential as presented by Choi et al. [49]. Thus, this

work is regarded as an improvement of this binary potential. In comparison, in this study we added the thermal description and the energetics of the point defects in the fitting procedure. The potential fitting is performed using the force matching method combined the weighted sum method where the weighting factors were adjusted to avoid the dominance of an objective in the solution, as implemented by Kim et al. [60].

Table 4.1 MEAM potential parameters for unary systems. E_c is given in eV, B is given in 10^{12} dyn/cm^2 while r_e and C_{min}/C_{max} are given in Å; the rest is unitless.

	E_c	r_e	B	A	$\beta^{(0)}$	$\beta^{(1)}$	$\beta^{(2)}$	$\beta^{(3)}$	$t^{(1)}$	$t^{(2)}$	$t^{(3)}$	C_{min}	C_{max}	d
Fe [41]	4.29	2.48	1.73	0.56	4.15	1.00	1.00	1.00	2.60	1.80	-7.20	0.36	2.80	0.05
Co [76]	4.41	2.50	1.948	0.90	3.50	0.00	0.00	4.00	3.00	5.00	-1.00	0.49	2.00	0.00

On the fitting procedure, the reference structure is set to the CsCl-type body-centered cubic (bcc) ordered B2. Additionally, the properties of the fcc $L1_0$-type structure were also measured following the existing phases observed in experimental and CALPHAD phase diagrams [15–17]. The fitted 2NN MEAM parameters for the Fe-Co binary alloys are shown in **Table 4.2**.

Table 4.2 MEAM potential parameters for the FeCo system. The screening parameters C_{min}/C_{max} relations are given for Co (A) and Fe (B) atoms. E_c is given in eV, r_e and C_{min}/C_{max} are given in Å; the rest is unitless.

E_c	r_e	α	$d+$	$d-$	$\rho 0$	C_{min} (AAB)	C_{min} (BBA)	C_{min} (ABA)	C_{min} (ABB)	C_{max} (AAB)	C_{max} (BBA)	C_{max} (ABA)	C_{max} (ABB)
4.44	2.46	5.224	0.055	0.025	1:1	0.45	1.2	0.15	0.2	2.35	2.1	2.95	2.75

4.3 Results and Discussion

The calculated physical properties for the reference B2 FeCo are detailed in **Table 4.3**. Transferability (ability to predict properties outside the fitting range) of the fitted potential is tested by computing the properties of FeCo in the whole stoichiometric range. Bcc solid solutions at low temperature (298 K) were minimized using CMC atom swapping, showing a strong tendency for ordering. At higher temperatures (1050 K) the alloy presents a

disordered state that cannot be achieved through CMC. Instead, we utilized as a reference the Bragg-Williams long range order (LRO) parameter as a guideline to create bcc disordered solid solutions with a more realistic approach, as discussed in **Section 2.1.1**. The obtained results for the structural, elastic, energetical and thermal properties are discussed in the following sections.

4.3.1 Structural and Elastic Properties

The predicted lattice constant for the FeCo in the cubic B2 is in excellent agreement with ab initio calculations as can be observed in **Table 4.3**. Same as predicted by the present potential, most DFT calculations predicted a B2 lattice constant close to 2.840 Å while Diaz et al. [77] obtained 2.868 Å. The authors attributed this discrepancy to the overestimation of the magnetic energy in DFT generalized gradient approximation (GGA) functionals. This explains the gap between the calculated atomic volumes with the ones predicted by ab initio calculations as shown in **Figure 4.1**. The obtained $L1_0$ structure presents a lattice constant of 3.577 Å, in close agreement with the 3.58 Å observed in ab initio calculations [78]. Moreover, the resulting *c / a* lattice ratios perfectly reproduce the 0.71 and 1 for bcc (B2) and fcc ($L1_0$) respectively.

Table 4.3 Calculated physical properties of B2-FeCo using the present 2NN MEAM potential compared with references. The cohesive energy E_c (eV), the lattice parameter a (Å), the elastic constants C_{11}, C_{12}, C_{44} and the bulk modulus B (GPa). The cohesive energy in $L1_0$ relative to B2 $\Delta E_{B2\text{-}L10}$ (eV), the enthalpy of mixing ΔH (KJ/mol). The formation energies (eV) for anti-site Fe atoms on the β sublattice E_{Fe}^{β}, anti-site Co atoms on the α sublattice E_{Co}^{α} and vacancies on either sublattice E_v^{α} and E_v^{β}. The melting point T_m (K) and the thermal expansion coefficient ε (10^{-6}/K) between 0 and 800 K.

	This Work	Experimental	First-Principles	Other calculations
E_c	-4.44			-4.44 [49], -4.30 [46]
a	2.840	2.857 [79]	2.843 [80], 2.840 [81], 2.843 [32]	2.839 [49], 2.850 [46]
C_{11}	261		259 [80], 263 [81]	225 [49], 125 [46]
C_{12}	151		154 [80], 152 [81]	168 [49], 174 [46]

C_{44}	127		130 [80], 108 [81]	136 [49], 161 [46]
B	188	165 [79]	189 [80], 189 [81], 196 [32]	187 [49]
$\Delta E_{B2\text{-}L10}$	-0.032		-0.049 [82], -0.115 [35]	
ΔH	-11.04		-8.30 [16], -12.51 [77]	-11.61 [16], -9.79 [49]
E_v^{α}	1.69	1.15 [34]	1.65 [32], 1.61* [32], 1.78 [11], 1.35 [34]	
E_v^{β}	1.88	1.15 [34]	1.75 [32], 1.78* [32], 1.78 [11], 1.32 [34]	
E_{Fe}^{β}	0.11		0.7 [32], 0.15* [32], 0.17 [11]	
E_{Co}^{α}	0.054		0.7[26], 0*[26], 0.17 [11]	
T_m	~1700	1713 [83],1750 [15], 1725 [84]		1688 [16]
ε	10.01	9.60 [4]	10.17[72]	

Elastic constants are near perfectly reproduced compared with DFT calculations [80,81]. However, references for stiffness constants are scarce and small discrepancies exist among themselves. Nevertheless, most of the references are consistent regarding the bulk modulus, which is in excellent agreement with the present results. A lower bulk moduli was experimentally observed by Belousov and Palii [79], which is expected due to environmental factors, existence of imperfections, and polycrystalline portions in samples.

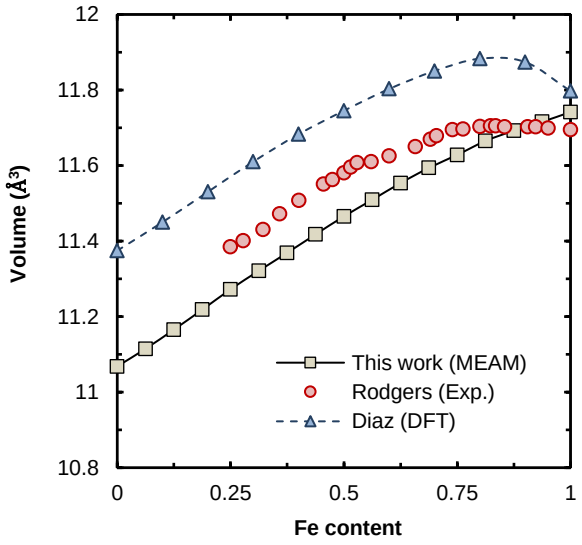

Figure 4.1 Evolution of the atomic volume of bcc solid solutions as a function of the Fe content at 0 K. Compared with experimental measurements by Rodgers et al. [85] and ab initio calculations by Diaz et al. [86].

Shrinking upon ordering is a natural behavior of binary alloys. However, FeCo alloys show a subtle expansion on the near-equiatomic region reaching a maximum at the fully ordered equiatomic configuration [87,88]. This is attributed mainly to magnetic forces [86]. Despite the lack of magnetic interactions, the developed potential describes a similar but softer expansion near stoichiometry. In the MEAM, the equilibrium radius is defined independently for unary and binary systems, in this case Co-Co interactions denote a shorter atomic radius than Fe-Co and Fe-Fe, suggesting that concentrated Co regions will reduce and ordered regions will slightly expand the overall volume. The magnetic momentum affects mostly the Fe-rich area, reaching a maximum at ~80% Fe concentration [86,89]. This creates a concave peak in the trend described by the atomic volume. Such effect is not entirely reproduceable by the present method, which shows a closer approach to a Vegard's behavior. Overall, the developed potential shows a maximum volumetric deviation of ~0.3 $Å^3$ and ~0.15 $Å^3$ from ab initio and experimental results, respectively.

4.3.2 Enthalpies

The $L1_0$ structure yields a less negative enthalpy of formation than the B2, the difference of energy between both structures ($\Delta E_{B2\text{-}L10}$) is slightly lower compared to the references as observed in **Table 4.3**. The compositional dependence of the formation energies was measured for the bcc phases at two temperatures, 475 and 1050 K, representing the ordered and disordered states as mentioned in **Section 4.3**, the predicted convex hulls are presented in **Figure 4.2**. The developed potential appropriately captures a negative miscibility gap to Vegard's law, characteristic of a tendency for ordering. As expected, high temperature disordered systems present a less negative enthalpy of formation than low temperature more-ordered systems. Asymmetry on the convex hull with a deviation towards the Fe-rich region was observed in the present calculations, which agrees with the references.

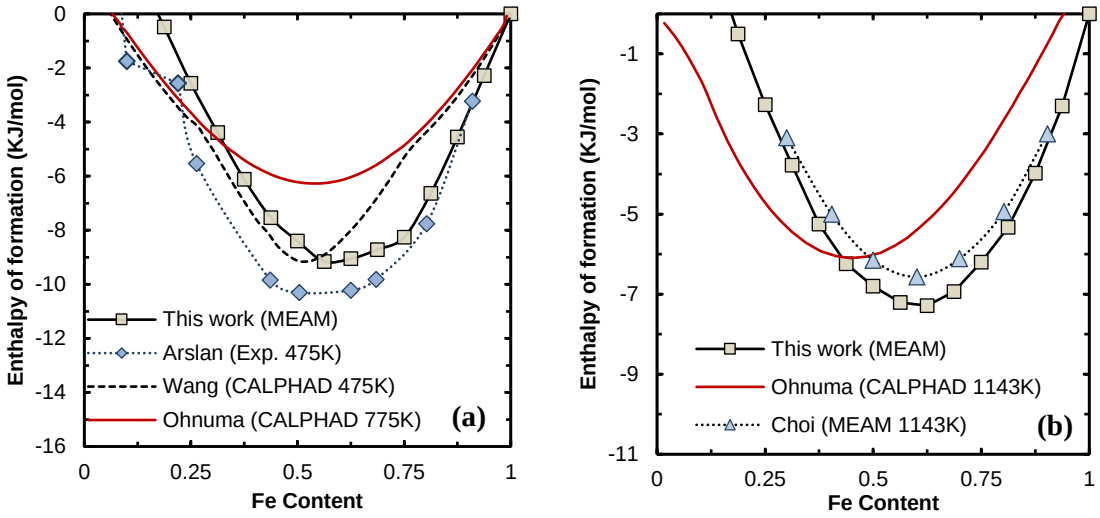

Figure 4.2 Enthalpy of formation of bcc solid solutions at **(a)** 475 K and **(b)** 1050 K. Compared with results presented by Arslan et al. [90], Wang et al. [16], Ohnuma et al. [91] and Choi et al. [49].

4.3.3 Substitutional Point Defects

Diffusion and ordering are closely related to impurities and other point defects unavoidable in a material. In Fe-Co alloys, the magnetic moment is proportional to the ordering parameter which correlates inversely to the number of anti-site atoms and vacancies [92]. Considering the ordered B2 crystal structure, Fe and Co atoms reside on their own sublattices, α and β respectively. Hence, there are four substitutional type point defects: anti-site Fe atoms on the β sublattice (E_{Fe}^{β}), anti-site Co atoms on the α sublattice (E_{Co}^{α}) and vacancies on either sublattice (E_{v}^{α}, E_{v}^{β}). Previous first principles [16] and experimental [92] studies have determined that the type of point defects in the B2 FeCo are mainly anti-site defects while vacancies have a lesser impact due to their low concentrations. Here, we estimate the different formation energies for the different point defects. Calculations were performed in B2 supercells containing 1,024 sites. We replaced or removed an individual atom to generate a substitution or vacancy, respectively. The energy difference was measured for the original and the modified systems. Results are shown and compared in **Table 4.3**. The obtained vacancy formation energy in the α sublattice (E_{v}^{α}) is in the range observed by the references whereas in the β sublattice (E_{v}^{β}) a slightly higher energy was obtained. First principles calculations predict the same formation energy for Fe and Co

anti-site atoms at stoichiometry. The present potential predicted different energies for each anti-site, nevertheless still positive for both substitutions. The obtained substitutional energies are closer to predicted by non-equiatomic results, yielding closer values to FeCo on the Fe-rich side. Differences between our potential and the references are believed to be due to the stabilization of the B2 by FeCo magnetic momentum as explained by Neumayer et al. [32].

4.3.4 Thermal Properties

According to several studies [2,3,15–17], the equiatomic FeCo presents a B2 structure at low temperatures (α_1' phase) which undergoes a second order order-disorder transformation to an A2 structure starting at ~1000 K (α_1 phase). A martensitic transformation takes place at ~1258 K, which changes the A2 into a metastable fcc A1 structure (γ phase). Finally, the solid-liquid transformation occurs at ~1750 K. To examine the thermal applicability of the present potential, different sized supercells up to 30 × 30 × 30 B2 unit cells were constructed. The isothermal-isobaric (NPT) ensemble and periodic boundaries were applied using the interface/NPT method [93]. The systems were initially equilibrated at 1 K and heated up to 2500 K at a rate of 0.5 K/ps. The positive ramp of temperature yielded a lattice parameter increase similar to that observed in DFT and experimental calculations, shown in **Figure 4.3**. The predicted lattice thermal expansion coefficient ε for a temperature window from 0 to 800 K is 10.01×10^{-6} K^{-1}, being in excellent agreement with ab initio calculations and experimental (600 to 800 K) observations, which are 10.17×10^{-6} and 9.60×10^{-6} K^{-1}, respectively [4,81].

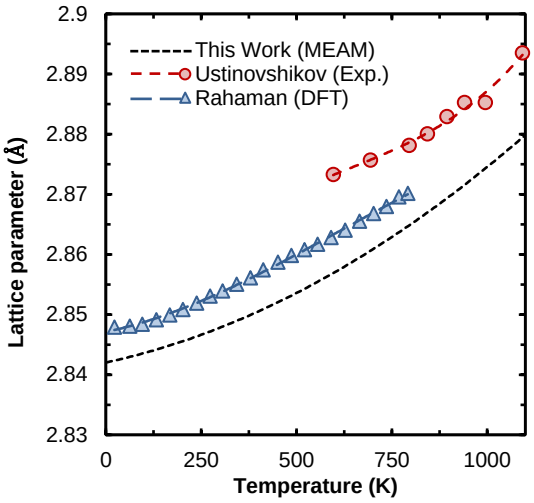

Figure 4.3 Evolution of FeCo lattice parameter at low temperatures compared with experimental measurements by Ustinovshikov and Tresheva [4] and ab initio calculations by Rahaman [81].

The FeCo order-disorder transition is closely related with magnetic effects which are outside the scope of the present potential model. Consequently, order-disorder transformations were not observed. However, in lack of disordering the present potential predicted a B2-to-$L1_0$ martensitic transformation on the heating process. This is reasonable since the counterpart of a disordered fcc binary structure is the ordered $L1_0$. This transformation was found to be slightly affected by the model size, converting the B2 to $L1_0$ or to a majority of $L1_0$ with intercalated layers of hcp along the {110} planes. The transformation took place at ~1125 K, below of the 1250 K observed by the references [15,16]. The melting point was reached at ~1700 K, close to experimental observations and CALPHAD assessments [15,16,83,84]. As a reference, the melting temperatures of the unary systems were also calculated obtaining ~2100 and ~2000 K for Fe and Co respectively, without observing intermediate phases. The temperature induced evolution of the entropy was recorded following the implementation by Piaggi and Parrinello [94], this approximates the entropy as a function of the system's density and the radial distribution function. **Figure 4.4 (a)** shows two upsurges in the entropy, the first denoting the martensitic phase transition and the second the solid-liquid transformation.

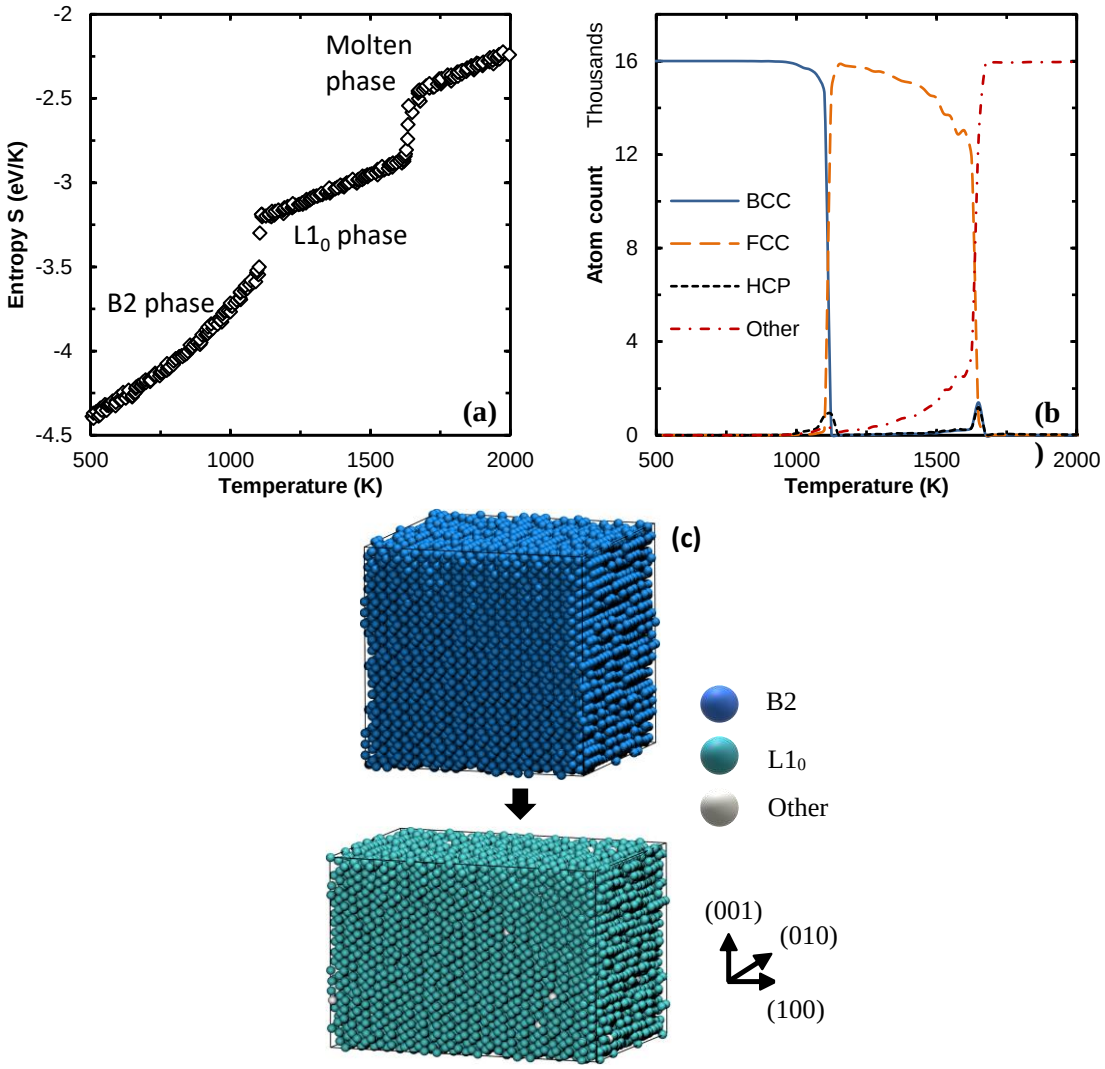

Figure 4.4 Heating process evolution of a 16,000 atoms system. **(a)** Entropy dependence calculated by the present 2NN MEAM potential, **(b)** CNA identified structural ordering, **(c)** PTM identification of the system at 300 K (upper) and 1300 K (bottom).

The involved structural phases were characterized using the common neighbor analysis (CNA), and the polyhedral template matching (PTM). The first method relies on interatomic distances to identify an atomic structure whereas the PTM classifies a structure based on its topology, making it capable of classifying ordered alloys. **Figure 4.4 (b)** displays the atom count according to the crystalline configuration using the CNA method during the heating process. A schematic of the supercell under the PTM identification is

shown in **Figure 4.4 (c)**, showing an initial B2 structure and the final $L1_0$ obtained after the phase transformation.

4.4 Ordering

The magnetic and mechanical properties in near equiatomic FeCo alloys are defined by the temperature driven microstructural ordering. A second order phase transition in FeCo is known to begin at ~775 K and complete at ~1000 K, transforming the ordered bcc (B2) to a disordered bcc (A2). It has been found that ferromagnetism is the main driving factor that of the A2 to B2 transformation [95]. However, ordering is also linked with the thermal equilibrium vacancy concentration and the diffusion rates. In the past, it has been theorized that quenched vacancies remain in FeCo after heat treatment [2]. Consequently, a change in temperature activates these vacancies creating disordering through a vacancy mechanism [96]. Following these assumptions, in this study we introduced vacancies into a system to observe a disordering transition. Vacancies were expected to migrate leaving trails of antisites generating atomic disordering. For the MD simulations, the initial system consisted in a bulk containing a total of 6,750 atoms in a B2 arrangement. The system was equilibrated using the NPT ensemble at different temperatures ranging from 500 to 1050 K for 1 ns. Then, we implemented the GCMC scheme to test several random trial points to check for atoms eligible for deletion. One identified atom of each element was deleted creating two vacancies to maintain the compositional equilibrium. The systems were left to evolve using the canonical (NVT) ensemble for 4 ns which was enough for high-temperature systems to reach a near disordered state.

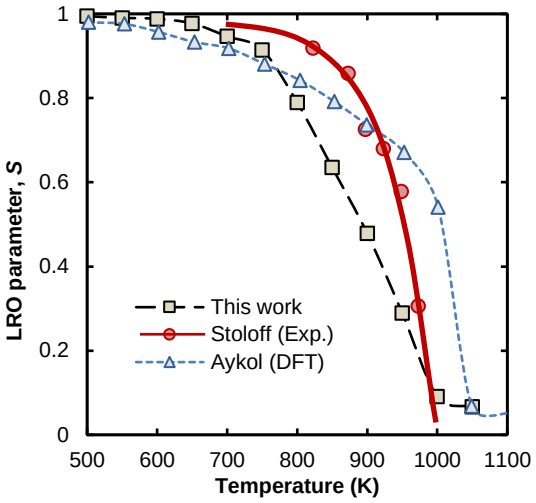

Figure 4.5 LRO parameter S as a function of temperature.

The evolution of the kinetic disordering is analyzed using the periodicity of the crystalline structure over large sections, quantified through the Bragg-Williams LRO parameter *S* as explained in **Section 4.3**. The Wigner-Seitz defect analysis was used to count the number of antisites and calculate the *S* parameter, the results are plotted against the temperature in **Figure 4.5**. Low temperatures show minimal diffusion rates being able to maintain ordering. After ~750 K the diffusion rate increases marked by a drop in the curve, in experiments the same effect occurs at ~820 K with a higher disordering rate. At ~1000 K the alloy reaches a near disordered state converging with the experimental trendline followed by a decrease in the diffusion rate. A schematic of the evolution of the system at ~950 K can be observed in **Figure 4.6**. The initial structure contains 2 vacancies, each replacing one Fe and one Co atom, respectively, to maintain the equiatomic ratio. These vacancies gradually diffuse across the ordered system, inducing disordering in the form of the A2 phase. Atoms neighboring the vacancies often remain non-identified due to the disruption of bonds. Additionally, this representation illustrates the evolution of a high-temperature state, characterized by vigorous atomic vibrations, which occasionally leads to the presence of unidentified atoms. The potential proved useful to recreate disordered systems by vacancy migration without altering the bcc structure. Moreover, systems with specific LRO *S* parameters can be achieved using different MD running times.

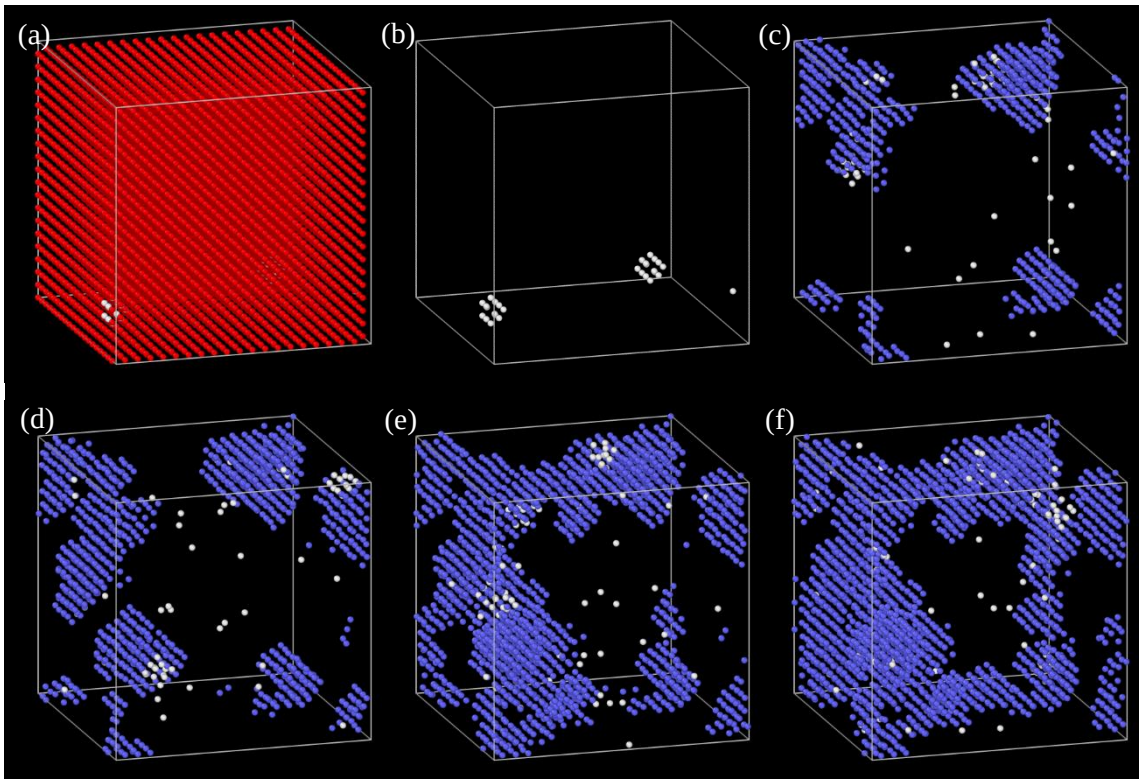

Figure 4.6 Evolution of the system with vacancies at approximately 950 K. Red atoms denote those present in the B2 structure, shown only in **(a)** for reference. White atoms indicate unidentified atoms, while blue atoms represent atoms within the A2 structure. The snapshots were taken at **(a, b)** 0 ns, **(c)** 1 ns, **(d)** 2 ns, **(e)** 3 ns and **(f)** 4 ns.

4.5 Stability of $L1_0$ Thin Films

FeCo presents a metastable fcc phase on high temperatures. However, an ordered fcc $L1_0$ phase has been experimentally stabilized at low temperatures [74]. It has been achieved by growing monoatomic layers of FeCo $L1_0$ over a buffer layer made of a third element presenting an fcc structure. Elements like Ni and Cu have a small mismatch between their fcc lattices (3.55 Å and 3.61 Å respectively) and FeCo $L1_0$ interfaces (~3.58 Å). This difference on the lattices induces a stress through a lattice mismatch which prevents the transition to the B2 structure up to certain extent. A maximum of six $L1_0$ monolayers has been stabilized experimentally over these materials [74]. After this point, surface roughening occurs and magnetic effects convert the $L1_0$ into a more stable B2 structure [11,78]. The performance of the potential stabilizing FeCo $L1_0$ thin films is

assessed by simulating a system where three fixed fcc monolayers act as a buffer to stabilize the subsequent slabs as it has proven to be sufficient by experiments [74]. The system replicates a ~20 nm (55 unit-cells) buffer layer surrounded by vacuum similar as in experiments. The forces were set to zero in the buffer layers to fix the fcc configuration. Then, Fe and Co layers were stacked alternately to form the $L1_0$ structure. In total three different versions of the systems were prepared, with slabs containing three, five and seven monolayers each with Fe and Co terminated (100) surfaces. A schematic of the system and the stacked monolayers is represented in **Figure 4.7 (a)**.

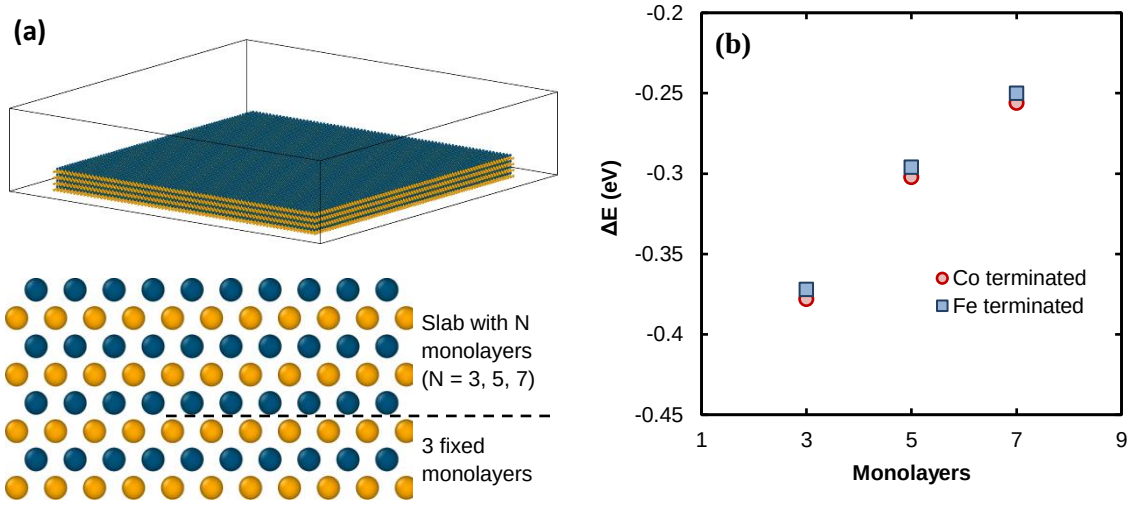

Figure 4.7 **(a)** Representation of system B and a schematic of the stacked monolayers. **(b)** Energy difference described by the reference B2 bulk and the $L1_0$ slab ($\Delta E = E_{B2} - E_{Slab}$) as a function of staked atomic monolayers in Fe-terminated and Co-terminated slabs.

The energy of the systems was minimized to reach a ground state form. The potential predicted a high stability of the stacked $L1_0$ layers for all the systems without noticeable surface roughening. The energy per atom calculated denote that Co terminated layers are slightly less negative as observable in **Figure 4.7 (b)** agreeing with ab initio results [78]. The energy difference depending on the number of monolayers is -0.052 and -0.128 eV between 3-5 and 3-7 monolayers respectively, close with -0.05 and -0.15 eV reported by ab initio calculations [78].

4.6 Conclusions

In this study, we have improved the thermal description of a second nearest-neighbor modified embedded-atom method (2NN MEAM) potential for FeCo alloys. The potential reproduces a large frame of fundamental properties as observed in ab initio and experimental studies. The predicted thermal properties and the ability to predict a phase transformation and melting point present a great advantage compared with other developed potentials. A temperature induced B2 to $L1_0$ or to $L1_0$ with intercalated hcp regions was observed in different scale systems due to a lack of disordering. Despite efforts, a reverse transformation liquid-fcc-bcc was not observed without heavily sacrificing other properties. The order-disorder transformation was induced by introducing vacancies. Using the same simulation time at different temperatures resulted in a long-range order (LRO) behavior similar as described by references. The vacancy diffusion rate increases at ~750 K and a disordered state was achieved at ~1000 K in agreement with the available phase diagrams. By using a fcc buffer layer the potential is capable of stabilizing $L1_0$ nano-films, the ground state of the Co- and Fe-terminated slabs showed similar energetical differences as predicted by ab initio calculations. Discrepancies in the overall behaviors are mainly attributed to the neglect of magnetic interactions, mainly reflected in the compositional lattice expansion and the stabilization of point defect energies. The potential can be easily coupled with other potentials to describe multi-component FeCo-based systems to investigate the thermal and ordering effects with a good general approach to investigate nano-films and the development of new alloys.

Chapter 5

Influence of V Addition on The Mechanical Properties of FeCo Alloys: A Molecular Dynamics Study

Fe-Co and Fe-V interatomic potentials are developed based on an enhanced mechanical Fe potential, are merged to describe the Fe-Co-V ternary system. Emphasis has been placed on the prediction of FeCo elastic properties and antiphase boundary (APB) energies for proper description of the mechanical behaviors. The potentials are used to analyze the crack nucleation and propagation mechanisms in nanocrystalline FeCo and FeCo-2V alloys under different ordering degrees at grain boundaries (GB) and within the grains.

Results show that disordering inside grains has a larger impact on the ductility of the binary FeCo. Antiphase domains (APD) mobility delays the ultimate tensile strength (UTS) and fracture point. Fracture procedure shows that triple junctions of GBs serve as the focal points of stresses concentration, promoting crack nucleation and crack propagation, leading to an intergranular fracture in ordered and disordered binary alloys. Effects of adding 2 at. % V to the FeCo alloy reveals V migrating to GBs in an ordered state, and GBs and APBs in a disordered state. Ordered FeCo-2V displays a decreased UTS and loss of ductility. Introducing V exclusively to the APBs enhances APD mobility boosting the ductility of the alloy.

**This section is published substantially in Materialia, 2023.
https://doi.org/10.1016/j.mtla.2022.101670. Reprint with permission. Copyright 2023 Elsevier.

5.1 Introduction

The binary FeCo alloy has an order-disorder transition (ODT) around 1003 K, at which the B2 ordered bcc structure (B2) transforms into a disordered bcc structure (A2) [3]. The disordering degree in the region below ODT can be partially retained through rapid quenching. This avoids a complete recrystallization leaving grains possibly containing stable antiphase domains (APD) [3,9]. Disordered states may slightly compromise the magnetic properties, but it can improve the ductility. Extensive research has been done regarding the ODT and it has been found that ferromagnetism is the main driving factor [95]. However, the origin of brittleness is still puzzling due to controversies regarding the B2 structure [3,11–13].

Experimentally, it was found that the addition of up to a 2.5 wt.% V in FeCo increases the ductility while minimizing the detrimental effect on the soft magnetic properties and improving the electrical resistivity by up to 23 times [3]. It is well established that V retards the ODT but the microstructural effects of V in the alloy still remain elusive [3,11–13].

In this chapter, we analyze the FeCo mechanical behavior from a molecular dynamics (MD) perspective. We studied the effects of ordering and the introduction of V in theoretical scenarios where these two factors are introduced at grain boundaries (GB) and APBs separately as well as simultaneously. To begin with, a correct description of the interaction between atoms is critical. Here, we propose a 2NN MEAM dedicated interatomic potential for FeCo-V, incorporating the development of the binary parameterizations based on the energetical, elastic and structural properties as described by experimental observations and first principles (FP) calculations. In addition, the APB energies of FeCo alloy for the common slip systems were included to ensure proper prediction of the mechanical behaviors.

5.2 Potential Optimization

In this work, to maintain the universality of the multibody potentials, the unary elements have been adopted from previous publications. It is worth noting that the adopted Fe potential is based on a widely used first nearest neighbor MEAM (1NN-MEAM)

potential [41], later improved by the same author [21]. The new version predicts that screw dislocations have a non-degenerate core in the bcc structure and the phase stability has been enhanced compensating for the lack of magnetic effects, making it suitable to study mechanical behaviors. The Co and V potentials have been widely tested and used to describe other multicomponent systems. Such is the case of the adopted Co-V binary interaction [97]. The MEAM parameters for Fe [98] (regarded as MEAM-T in the reference), Co [76] and V [41] are presented in **Table 5.1**.

Table 5.1 Sets of MEAM parameters of Fe, Co and V unary systems. E_c is given in eV, r_e and C_{min}/C_{max} are given in Å; the rest is unitless.

	E_c	r_e	α	A	$\beta^{(0)}$	$\beta^{(1)}$	$\beta^{(2)}$	$\beta^{(3)}$	$t^{(1)}$	$t^{(2)}$	$t^{(3)}$	C_{min}	C_{max}	$d+/d-$
Fe [98]	-4.28	2.469	5.027	0.585	3.80	2.0	0.9	0.0	-0.8	12.3	2.0	0.63	1.9	*0.0/0.3*
Co [76]	-4.41	2.500	5.235	0.900	3.50	0.0	0.0	4.0	3.5	5.0	-1.0	0.49	2.0	*0.0/0.0*
V [41]	-5.30	2.625	4.813	0.730	4.74	1.0	2.5	1.0	3.3	3.2	-2.0	0.49	2.8	*0.0/0.0*

The compatibility among multicomponent systems in MEAM relies on utilizing the same unary potentials. This means that a new Fe-V potential is needed based on the adopted Fe potential. Thus, the remaining work is to develop the Fe-Co and Fe-V interactions and merge them with the Co-V interaction to describe the Fe-Co-V alloy. A well-rounded potential should be capable to closely reproduce the energies of formation, structural properties, and elastic constants. To ensure the proper mechanical description of FeCo alloy, we have included the APB energies for the preferred slip planes, namely the {110} and {112}, as well as the point defect formation energies. The fitted MEAM parameters for the binary and ternary interactions are presented in **Table 5.2** and **Table 5.3**.

Table 5.2 MEAM potential parameters for the binary systems. The cohesive energy E_c is given in eV, the equilibrium nearest neighbor distance r_e and the screening C_{min}/C_{max} are given in Å; the rest is unitless.

Alloy (A-B)	Fe-Co	Fe-V	Co-V [97]
Ref. Structure	B2	B2	$L1_2$ (Co_3V)
Ec	-4.44	-4.90	-4.77

r_e	2.46	2.51	2.51
α	5.235	5.112	4.941
C_{min} *(A-A-B)*	1.50	0.50	0.14
C_{min} *(B-B-A)*	1.30	0.05	1.20
C_{min} *(A-B-A)*	1.10	0.80	0.20
C_{min} *(A-B-B)*	1.00	0.80	0.49
C_{max} *(A-A-B)*	1.95	2.40	2.80
C_{max} *(B-B-A)*	2.05	1.90	2.80
C_{max} *(A-B-A)*	1.90	2.20	1.96
C_{max} *(A-B-B)*	2.80	2.20	2.80
d+	0.0	0.10	0.00
d-	0.075	0.02	0.00
ρ_0^A: ρ_0^B	1:1	1:1	1:1

Table 5.3 MEAM potential parameters for the Fe-Co-V ternary system. The screening parameters C_{min}/C_{max} are given in Å.

Screening direction	Parameter
C_{min} (Fe-V-Co)	$0.29\ ([0.5(C_{min}^{\text{Fe-V-Fe}})^{1/2} + 0.5(C_{min}^{\text{Co-V-Co}})^{1/2}]^2)$
C_{min} (V-Fe-Co)	$0.46\ ([0.5(C_{min}^{\text{V-Fe-V}})^{1/2} + 0.5(C_{min}^{\text{Co-Fe-Co}})^{1/2}]^2)$
C_{min} (V-Co-Fe)	$1.34\ ([0.5(C_{min}^{\text{V-Co-V}})^{1/2} + 0.5(C_{min}^{\text{Fe-Co-Fe}})^{1/2}]^2)$
C_{max} (Fe-V-Co)	$2.59\ ([0.5(C_{max}^{\text{Fe-V-Fe}})^{1/2} + 0.5(C_{max}^{\text{Co-V-Co}})^{1/2}]^2)$
C_{max} (V-Fe-Co)	$1.97\ ([0.5(C_{max}^{\text{V-Fe-V}})^{1/2} + 0.5(C_{max}^{\text{Co-Fe-Co}})^{1/2}]^2)$
C_{max} (V-Co-Fe)	$2.35\ ([0.5(C_{max}^{\text{V-Co-V}})^{1/2} + 0.5(C_{max}^{\text{Fe-Co-Fe}})^{1/2}]^2)$

5.3 Calculation of Physical Properties

Equiatomic FeCo presents a B2 structure at low temperatures while the rest of the composition range presents a mixed B2-bcc solid solution without any other stable compound [91]. Fe-V alloys present two main phases at low temperatures. On the Fe- and V-rich regions a bcc solid solution is predominant. In the near equiatomic region, the FeV alloy displays a highly complex structure designated as σ-phase. Similar with the FeCr alloy [99], a single unit cell involves five different sublattices with high coordination numbers and lack of stoichiometry [16]. In this investigation the focus was on the bcc-based structure because of the low V content on the FeCo-2V alloy. However, the stability of the FeV σ-phase was also explored. Initially, the lattice parameters, energy of formation,

and elastic constants of the FeCo and FeV B2 structures at 0 K were examined to assess the quality of the potential fitting. Then, the enthalpies of mixing of random solid solutions were utilized to examine the thermodynamic properties and the transferability of the potentials to other compositions. All MD calculations were performed using the Large-scale Atomic/Molecular Massively Parallel Simulator (LAMMPS) [100] and software OVITO [101] was used for post-simulation analysis and visualization.

5.3.1 Calculated Properties of The Fe-Co Binary System

The development of the Fe-Co interaction potentials was given a priority due to the strong interest in the study of $Fe_{49}Co_{49}V_2$ alloy. The calculated properties of the B2 structure include the basic structural, energetical and elastic properties, these are compared with the literature in **Table 5.4**. The lattice parameter is well reproduced while the enthalpy of formation falls within the range reported in the literature. Moderate deviation in the calculated elastic constants is unavoidable since some contributions from the second-nearest neighbors were unscreened to reduce vibrations in the bcc structure. This was done to maintain the description of the mechanical properties delimited by the Fe unary potential [98]. Nonetheless, the predicted elastic constants present a difference of less than 11% compared with the ab initio calculations. For an easier comparison with experimental values, the bulk modulus (*B*) and the Young's modulus (*E*) were calculated via the Voigt-Reuss-Hill equations [66].

The thermodynamic capabilities are assessed by comparing the enthalpies of mixing at 298 and 1050 K for the compositional bcc phases. **Figure 5.1** shows the calculated enthalpy curves, displaying a negative miscibility gap to Vergard's law showing a tendency towards ordering in the alloy at both temperatures. At 1050 K, the potential predicts a slightly less-negative mixing enthalpies in the Co-rich region. This difference becomes smaller when approaching the other end of the composition.

The deformation behavior in FeCo is affected by the promotion of planar slip and the easiness to cross slip, which are directly linked to the APB energies. The present potential closely reproduces the low APB energies, at 141 and 176 mJ/m^2 for the preferred <111>

(110) and (112) slip systems, close to the 120-169 mJ/m^2 limits with a lower <111> (110) APB as observed in the ab initio and experimental studies [2,10,11,37].

In a FeCo B2 structure, Fe and Co atoms reside on their own sublattices, α and β, respectively. Thus, primarily four different point defect formation energies are expected in the binary alloy: anti-site Fe atoms on the β sublattice (E_{Fe}^{β}), anti-site Co atoms on the α sublattice (E_{Co}^{α}) and vacancies on either sublattice (E_v^{α}, E_v^{β}). It is believed that the magnetic momentum is responsible for the stability of the FeCo B2 structure, which is reflected in the same formation energy for both anti-sites according to ab initio calculations [32]. Although not equal, the predicted E_{Fe}^{β} and E_{Co}^{α} are comparable to the references. Vacancy formation energies for both sublattices E_v^{α} and E_v^{β} are overestimated by ~10% compared to the literature. However, given the low vacancy concentration in metals, especially at nanoscale, the predicted error is acceptable.

Table 5.4 Calculated physical properties of the ground state B2 FeCo using the present 2NN MEAM potential compared with references: the lattice parameter *a* (Å), the elastic constants C_{11}, C_{12}, C_{44}, the bulk modulus *B*, the Young's modulus *E* (GPa), the enthalpy of formation ΔH (kJ/mol), APB energies (mJ/m^2) and the formation energies (eV) for anti-site atoms (E_{Fe}^{β}, E_{Co}^{α}) and vacancies (E_v^{α}, E_v^{β}).

	This Work	Exp.	FP	MD/MC
a	2.840	2.857 [79]	2.843 [32,80], 2.840 [81]	2.839 [49] , 2.826 [47]
C_{11}	232		259 [80], 263 [81]	226 [49] , 231 [47]
C_{12}	167		154 [80], 152 [81]	168 [49] , 179 [47]
C_{44}	144		130 [80], 108 [81]	136 [49] , 138 [47]
B	189	165 [79]	189 [80,81], 196 [32]	196 [47]
E	211	197 [79]	235 [80]	
ΔH	-11.04		-8.30 [16], -12.51 [77]	-9.79 [49], -11.61 [16]
$\gamma_{APB}^{(110)}$	141	120-160 [10]	129 [11], 126 [38]	128 [37], 127 [47]
$\gamma_{APB}^{(112)}$	176		169 [11], 157 [38]	159 [37], 140 [47]
E_{Fe}^{β}	0.14		0.7 [32], 0.17 [11]	
E_{Co}^{α}	0.23		0.7 [32], 0.17 [11]	
E_v^{α}	1.95	1.15 [34]	1.65 [32], 1.78 [11]	1.65 [47]

E_v^{β}	2.05	1.15 [34]	1.75 [32], 1.78 [11]	1.65 [47]

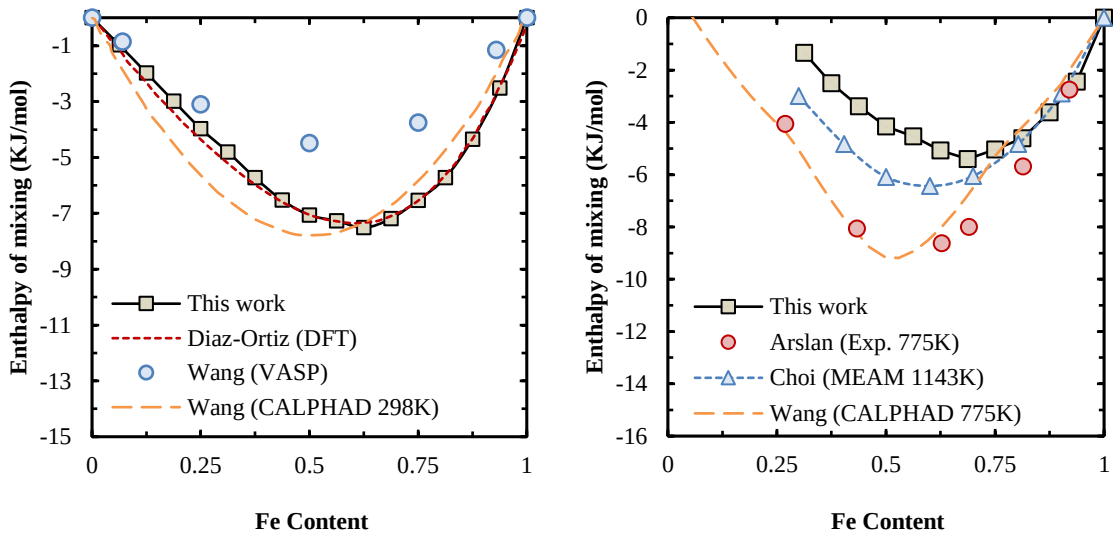

Figure 5.1 FeCo enthalpy of mixing of bcc solid solutions at 298 K (left), and at 1050 K (right) with bcc-Fe and hcp-Co as reference states.

5.3.2 Calculated Properties of The Fe-V Binary System

The predicted lattice constant for the metastable B2 structure agrees with experimental observations and ab initio calculations as listed in **Table 5.5**. The basic elastic parameters are within the range of the ab initio calculations with a margin of error less than 10%. The compositional dependence of the formation energies was measured for the bcc phases at 298 and 1400 K. The enthalpies of mixing follow the trend shown by the literature as shown in **Figure 5.2**, predicting the stability of the bcc phase at both temperatures.

Table 5.5 Ground state FeV physical properties calculated for the B2 and σ-phase using the present 2NN MEAM potential: the lattice parameter a (Å), the elastic constants C_{11}, C_{12}, C_{44}, the bulk modulus B (GPa), the enthalpy of formation ΔH (kJ/mol), and the unit cell volume Vol (Å^3).

	This Work	Exp.	FP	MD/MC
B2 str.				
a	2.898	2.899 [102]	2.87 [103], 2.88 [80]	2.93 [104]
C_{11}	244		267 [103], 260 [80]	248 [104]
C_{12}	159		153 [103], 164 [80]	124 [104]

C_{44}	79		69 [103], 72 [80]	81 [104]
B	188	163 [105]	191 [103], 196 [80]	165 [104]
ΔH	-11.69		-12.43 [80]	-11.37 [104]
σ-phase				
ΔH_σ	-1.66		-4.913 to -0.57 [106]	
Vol_σ	377		371 [107]	

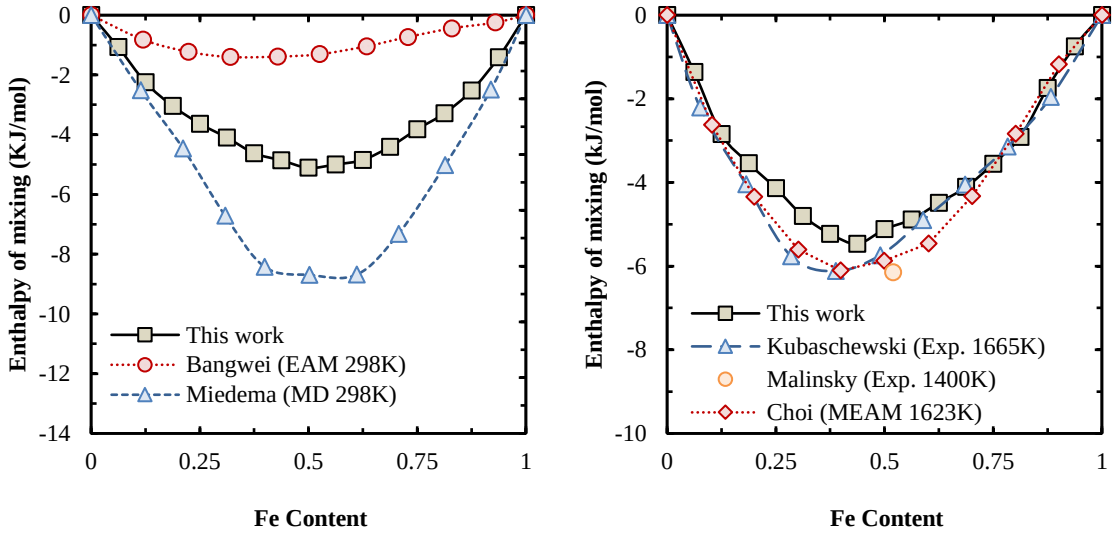

Figure 5.2 Fe-V enthalpy of mixing of bcc solid solutions at 298 K (left), and 1050 K (right).

The FeV alloy presents a complex σ-phase with closed packed structure defined by a tetragonal unit cell that contains 30 atoms distributed in five nonequivalent sublattices, space group $D^{14}{}_4$ h –P42/mnm also referred as $D8_b$. The occupation fraction of Fe and V in each sublattice is compositionally dependent as described by the references [99,108]. To observe the transferability of the potential to study the σ-phase, a unit cell was constructed using a probable configuration for the equiatomic state. A representation of the unit cell utilized to simulate one of the configurations for the σ-phase can be observed in **Figure 5.3**.

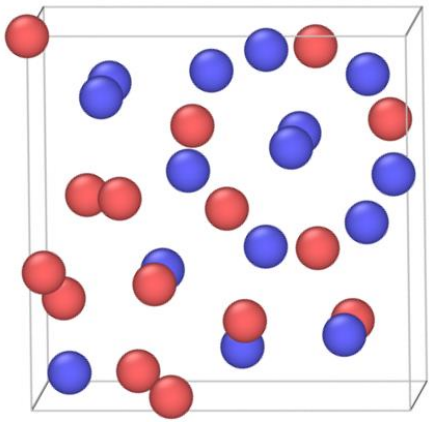

Figure 5.3 Unit cell of the σ-phase with an equiatomic distribution of Fe and V atoms, represented by red and blue spheres respectively.

Our calculations predicted structural stability at 0 K with a unit cell volume 377 $Å^3$, slightly larger than the experimentally observed 371 $Å^3$ [107]. The formation energy of our system was found to be -1.66 kJ/mol, which falls within the range of -0.57 to -4.913 kJ/mol for several possible configurations calculated through ab initio studies [106]. Under finite temperatures, a phase transformation between bcc and σ-phase was not observed, preserving the stability of the starting structure at low temperatures.

5.4 Mechanical Behavior

To understand the FeCo alloys' mechanical response under tensile strain, a cubic nanocrystalline (NC) model containing 8 grains with random crystallographic orientations was generated using the Poisson-Voronoi tessellation method [109]. The length of each side was 300 Å, containing ~2.4×10^6 atoms with an average grain size of ~15 nm. Ordering conditions in this manuscript are from the perspective of the long-range order (LRO), incorporated by adjusting the Bragg-Williams LRO parameter *S* [18,110]. Where a value of $S = 0$ denotes complete disorder while $S = 1$ a fully ordered alloy [18,110]. To independently modify the degree of ordering in both GBs and grains, the generated model underwent initial analysis using polyhedral template matching (PTM). This facilitated the identification of regions characterized by long-range atomic order, akin to those found in

grains, as well as regions featuring short-range atomic disorder, typical of GBs. An illustration showcasing the utilized initial model is presented in **Figure 5.4**.

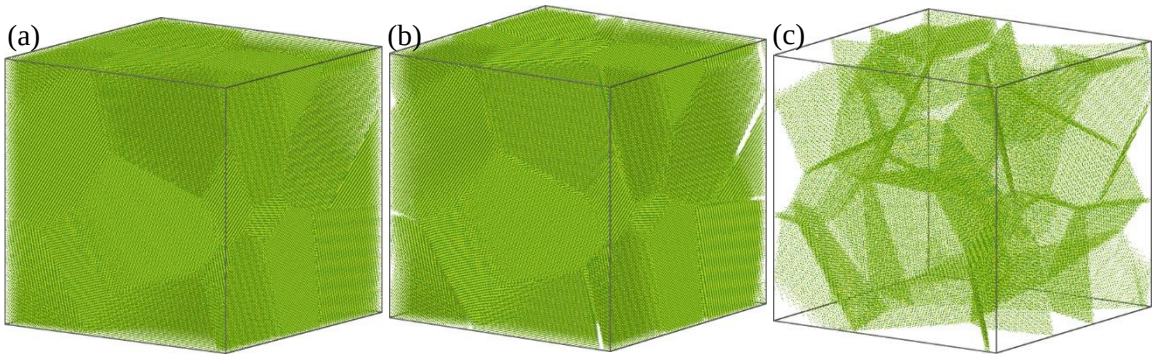

Figure 5.4 **(a)** NC model used in this study. Exploited view of **(b)** grains and **(c)** GBs.

Models with ordering degree *S* of 1, 0.5 and 0 were constructed. The ordering degree was incorporated in GBs and grains separately. In the case of GBs, disorder was introduced by replacing Fe and Co atoms in pairs, promoting Fe and Co rich zones. Performing the PTM analysis after the introduction of disorder reveals that the disordered GB grew by ~20%. Some atoms in the GB borders are now identified to be in a disordered bcc or unmatched structure instead of B2. Disordering within grains was introduced by exchanging Fe and Co atoms in focalized regions within each grain following the S parameter. This would simulate antiphase domains (APD) and consequently antiphase boundaries (APB) within the grains as has been observed experimentally [3,9]. A visualization of the NC model with different *S* degrees at GBs and grains can be observed in **Figure 5.5**. The influence of V is studied by incorporating 2 at. % V in the models. V was inserted randomly replacing Fe and Co atoms in pairs to maintain the equiatomic ratio. Subsequently, hybrid grand canonical Monte Carlo–molecular dynamics (GCMC-MD) simulations were performed to observe the formation of compounds and segregation. In addition, V was introduced into the APBs delimiting the APDs of the models containing disordering in grains. For the tensile test, all the NC models were equilibrated under zero pressure for 1 ns using the isobaric-isothermal (NPT) ensemble while the model temperature was controlled using the Nose-Hoover thermostat. After which, uniaxial elongation was applied at a strain rate of 4×10^9 s^{-1} for a total of 10% strain or failure. The tensile straining was applied on the Z direction while the X and Y directions were allowed to respond to the tensile strain

dynamically under zero pressure. All strain tests were performed using periodic boundary conditions at room temperature (298 K). For convenience, the straining axis is aligned with the vertical direction of the related figures.

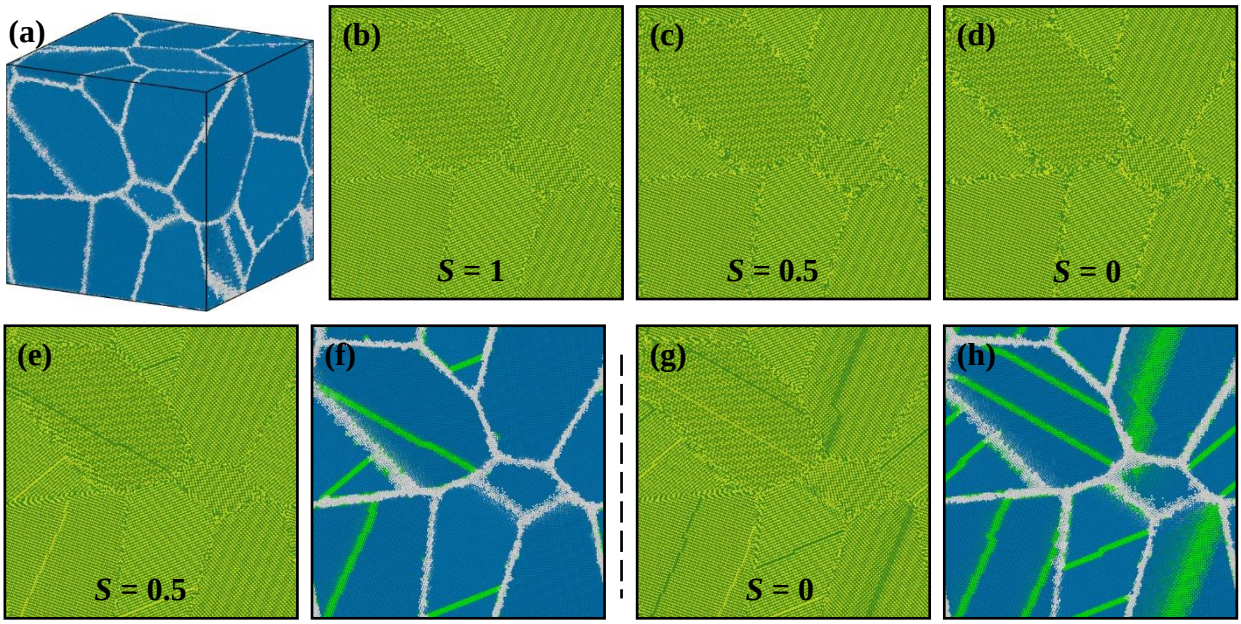

Figure 5.5 **(a)** Grain configuration in the NC model under the PTM visualization. Atoms in blue are identified to be in the B2 structure whereas white atoms are not identified representing the GB. **(b-d)** Atomic representation of different degrees of ordering at the GBs. Green atoms represent Fe and yellow atoms Co, respectively. **(e, g)** Atomic configuration of different degrees of ordering at the grains, also visualized under the PTM **(f, h)** where light green atoms belong to the APB.

5.4.1 FeCo Binary Alloy

The mechanical behavior of FeCo alloys is closely related to the temperature-ordering effects. Poor ductility is connected to the low-temperature precipitation of B2. It has been proposed that the dislocation and fracture behavior changes with the degree of ordering. Disordering in the GBs has been proposed to facilitate the slip transfer across the grain boundaries [111]. To observe the influence of the ordering on the fracture behavior, we initially evaluated the effect of disordering on grain boundary (GB) energies. Specifically, we focused on symmetric tilted Σ3(111) and Σ9(221) types of GBs in this investigation. The Σ3 and Σ9 GB types have been observed experimentally [112], and have been assesed

to constitute a significant proportion of GBs in FeCo alloys, accounting for approximately 60% and 10%, respectively, based on misorientation distributions at temperatures below the ODT [113]. In our calculations, the energy related to the Σ3(111) displayed a lower value than the Σ9(221), indicating a higher ability by Σ3 GBs to form, which is consistent with the distribution observed in experiments. Boundaries with higher energies may lead to decreased mechanical strength as these can act as preferential sites for crack initiation and propagation, contributing to reduced ductility and fracture resistance. As can be observed in **Figure 5.6**, the introduction of disorder reduces the GBs energies, which should in turn provide a higher ductility.

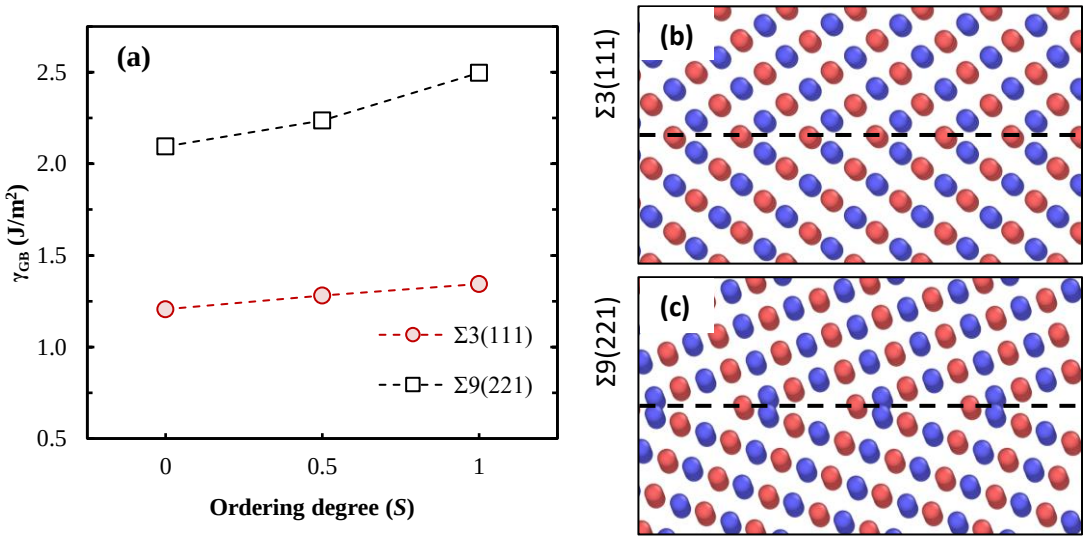

Figure 5.6 **(a)** Calculated energies for the Σ3(111) and Σ9(221) GBs types as a function of the degree of order (*S*), in red and black color respectively. Representation of the B2 symmetric tilted Σ3(111) **(b)** and Σ9(221) **(c)** types of GBs.

The variation of the stacking fault energies as the system undergoes shear displacement is represented by the generalized stacking fault energy (GSFE) curves, as depicted in **Figure 5.7**. In this study, the GSFE curves were calculated by varying the distances relative to the Burgers vector for the binary FeCo alloy in the <111> {110} and <111> {112} slip systems. The curves were evaluated for the ordered (S = 1), partially ordered (S = 0.5) and disordered (S = 0) systems. The ordering effects on the unstable stacking fault (γ_{usf}), the intrinsic stacking fault (γ_{isf}), and the unstable twin fault (γ_{utf}) energies were drawn. Due to the

structural configuration of the B2 in the evaluated slip systems, γ_{isf} is equivalent to the APB energy [48,114]. As observable in **Figure 5.7**, introducing disordering to the alloy reduce the energy barriers that need to be overcome to move dislocations or to create stacking faults within the crystal. Compared to the references, the curve for the ordered alloy aligns well with the FP calculations in the central region, near the γ_{isf} [48,114]. The interatomic potential overestimates the energy barriers to develop unstable faults, the increase in γ_{usf} and γ_{utf} could hinder the movement and slipping of dislocations in the crystal lattice, potentially increasing the stability of the B2 structure and the subequent brittleness of the alloy as observed in further sections.

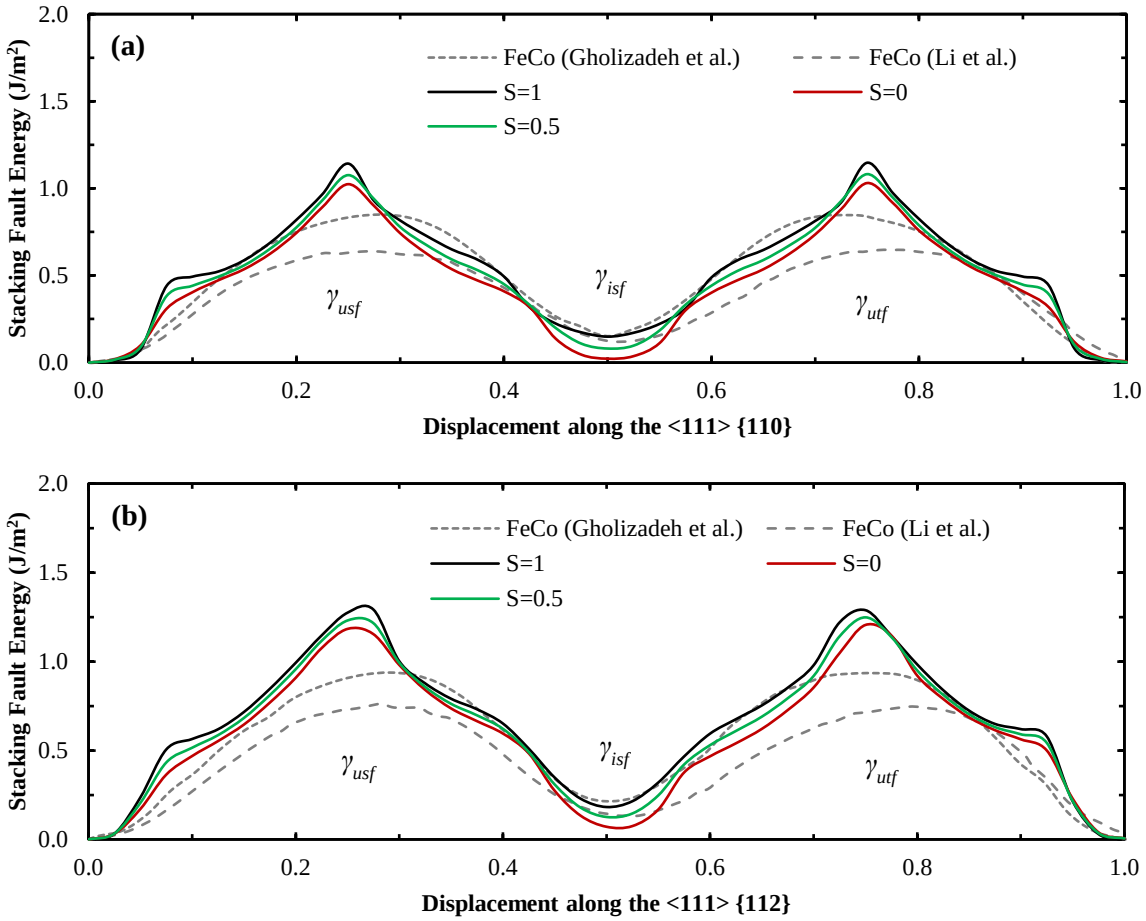

Figure 5.7 Calculated GSFE curves for FeCo in the {110} **(a)** and {112} **(b)** in the <111> slip direction with different LRO ordering degrees (*S*). In comparison with FP and MD calculations [37,38].

Straining tests were performed on NC models displaying disordering in GBs and grains separately. **Figure 5.8 (a)** shows the tensile behavior when different ordering degrees is introduced in the GBs. Regardless of the ordering, the straining curves followed an almost linear response showing yielding at ~4% strain. The Young's modulus was calculated to be ~170 GPa, lower than the 197 GPa presented by Belousov and Palii [79] but in closer agreement with the ~167 GPa obtained by Baco et al. on FeCo thin films [115]. The ultimate tensile strength (UTS) for the different models was achieved at a similar strain of ~6.9%. However, the UTS marginally decreased with an increasing disordering.

Contrary to the majority of literature that reports an extremely brittle behavior without a plastic region, our observations in this work present a different perspective. Duckham et al. [22] observed a development of a plastic flow behavior with ultra-fine grained FeCo alloys at a grain size of 100 nm. Considering that our simulations feature an average grain size of ~15 nm, we anticipated a limited plastic region to manifest since the load is primarily borne by the grain boundaries rather than the grains themselves. This situation compels the microstructure to adapt through grain rotation and grain boundary sliding. This expectation is consistent with the results obtained from atomistic simulations conducted by Li et al. [47], where FeCo shows an extended plastic deformation. However, the authors observed crack formation at ~9% strain but without observing fracture below 30% strain. This contradicts the experimental findings by Duckham et al. [22] where smaller grains tend to reach the fracture point earlierdespite demonstrating a softer elastic-plastic transition. The higher plasticity in conventional MD simulations is associated to the high strain rates used (10^7 to 10^{12} s^{-1}). Such rapid straining limits the time for dislocation nucleation, leading to reduced crack propagation.

In our simulations, introducing disordering into the GBs slightly improved the fracture strain. This is associated with a minor increase of grain mobility allowed by small clusters of the constituent elements at the GBs. The initial $S = 1$ system reached complete failure at ~7.5% while the models with $S = 0.5$ and $S = 0$ failed at ~7.6% and ~7.8%, respectively. Thus, introducing disordering at the GBs has an almost neglectable impact on the UTS and the fracture strain. This supports the theory that ordering at grains may have a dominant effect on the mechanical behavior. In **Figure 5.8 (b)** it is observable that reducing the

ordering in the GBs initially slows down the increase of the dislocation density. This means that the dislocation densities are accommodated within the GBs. Disordering in GBs is known to increase the resistance of dislocations from moving in a continuous slip plane. However, once the initial stresses have been accommodated the dislocations increase denoting a curve with a logarithmical growth behavior until reaching the fracture point.

Figure 5.8 (c) illustrates the straining curves when disordering is introduced in the grains. The tensile stress increases similarly for the different ordered models up to the yielding point at ~5% strain. It was observed that disorder in grains slightly retarded the UTS in contrast with the one in disordered GBs, where the UTS occurs at similar strains as in the binary alloy. This indicates that there is higher mobility at the APBs than at the GBs accommodating the initial stresses in the plastic regime. However, fracture strain of the models with disordering at GBs and grains are similar, and they differ only in the fracture strengths. This suggests that stresses after UTS are better accommodated by disordered GBs. Introducing a fully disordered state to grains or GBs led to ~7% strain increase in the fracture strain compared to the fully ordered alloy. **Figure 5.8 (d)** shows the initial accommodation of stresses in the GB followed by a softened curve, indicating that the stresses are accommodated by slipping in the APBs. Despite this accommodation and the reduction of the dislocation density, the fracture points are marginally increased.

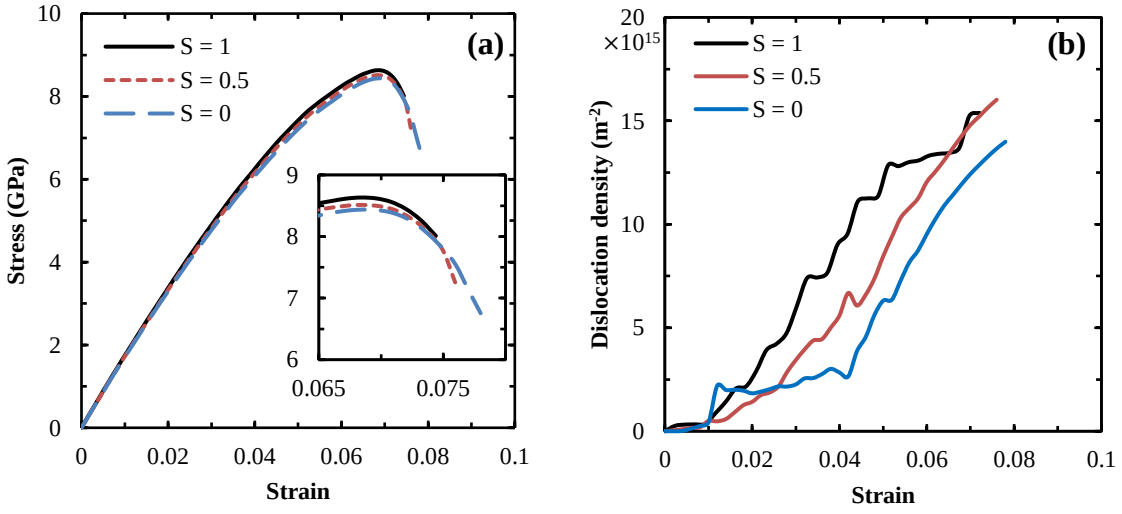

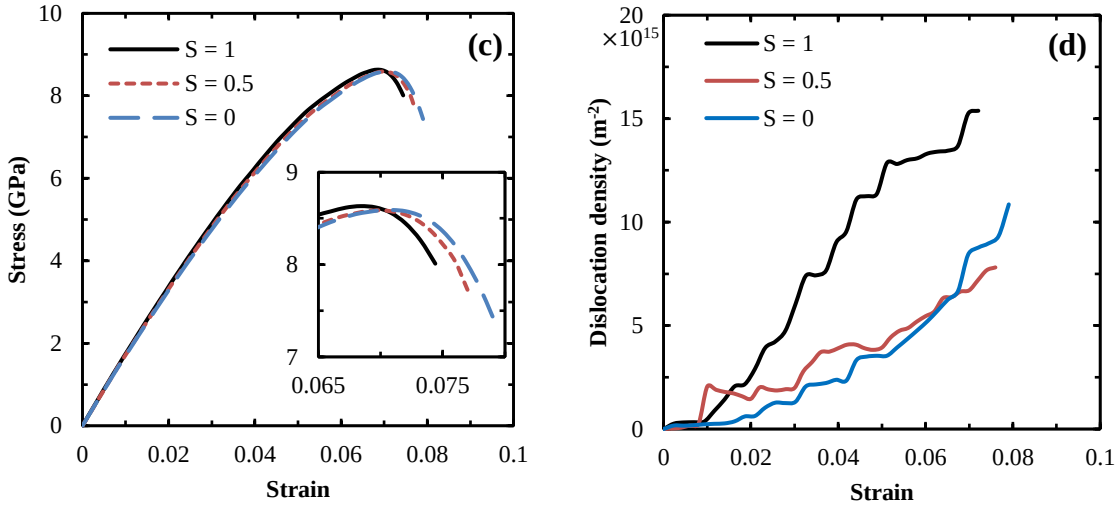

Figure 5.8 Binary FeCo stress-strain curve and dislocation density evolution when disordering is introduced in **(a, b)** grain boundaries and **(c, d)** grains.

A representation of the evolution of the straining and failure in the binary alloy is shown in **Figure 5.9**. The stress builds up on the grain boundaries without observing major signs of intragranular stresses. Stresses concentrate at the triple junctions of the grain boundaries followed by the nucleation of microcracks. These microcracks grow and propagate along low-angle grain boundaries leading to an intergranular fracture. Despite the ordering differences, the atomistic evolution of the straining replicated this behavior. In the model with disordered grains, a major concentration of stresses or slippage at the APB was not observed. This means that, for all models, the concentration of stresses occurred primarily at the GBs. Disorder in the GBs slightly facilitates the grain mobility delaying the crack nucleation and propagation. Our tensile simulations confirm that the stoichiometric FeCo alloy fails primarily by intergranular fracture in ordered and disordered conditions [2].

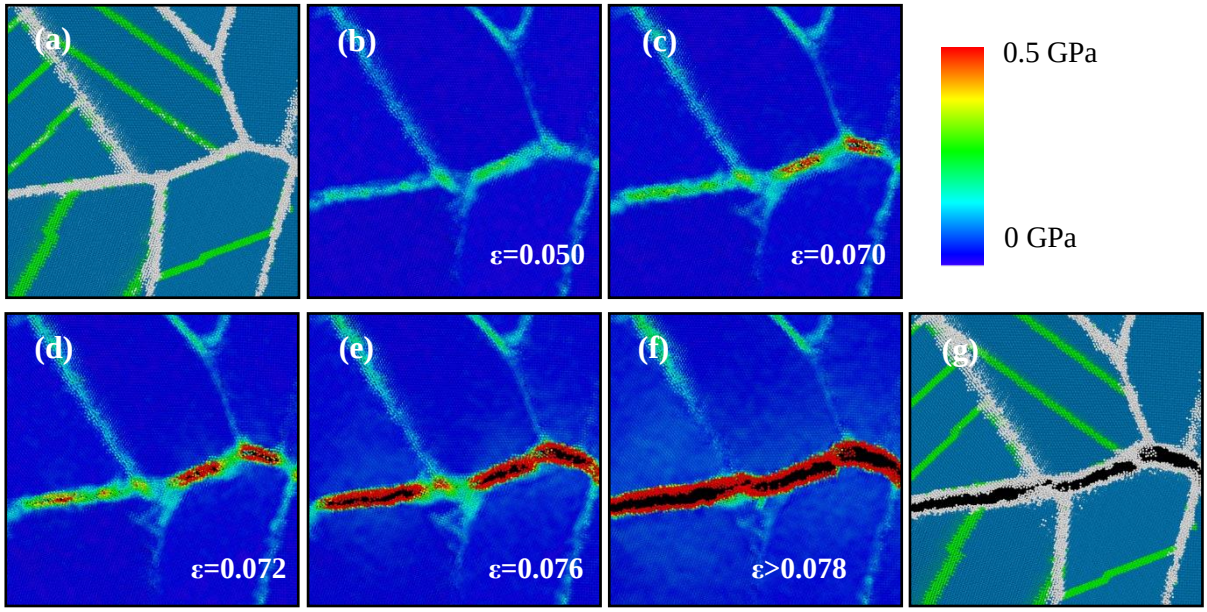

Figure 5.9 **(a, g)** Binary FeCo with fully disordered grains before and after the straining process visualized under the PTM. Atoms in turquoise are identified to be on a B2 structure, white atoms are not identified, while light green atoms belong to the APBs. **(b-f)** Atomic shear distribution during the microcrack nucleation and propagation. Red atoms are under a shear strain > 0.5 GPa.

5.4.2 Influence of V on FeCo

The addition of up to 3% at wt. V into FeCo is known to improve the ductility with a small impact in the magnetic properties. There are different explanations of the microstructural effect of V in FeCo alloys. The most accepted one is that it promotes the formation of precipitates causing a mixture of phases at low temperatures [9]. To observe the preferred configuration of V in a FeCo NC system, 2 at. % V was incorporated. To observe the migration of V we employed GCMC-MD simulations as implemented in LAMMPS [116,117]. In this approach, relaxations are accounted for by MD while a general MC implementation performs site exchanges of atoms with an imaginary ideal gas reservoir. The swap of atoms is performed according to a MC probability based on the interchange energies of atomic pairs from the MD calculations. This allows an accelerated equilibration of systems with different crystal mixtures and slow diffusion rates such as metal alloys. In total, the number of steps to reach equilibrium was ~4×10^6. Atoms in GB

usually present much weaker atomic bonding compared to grains. Thus, alloying elements are energetically attracted to and segregate at GBs. This was observed in the present work, where ~98% of V atoms are concentrated at the GBs after the GCMC-MD minimization. This reveals that V prefers to migrate to the GBs instead of forming compounds inside the grains. APBs are considered a planar crystallographic defect, which are expected to have relatively higher energies. Thus, when V was introduced to FeCo presenting disordering in grains, ~91% V migrated to GBs while ~7% V migrated to the vicinity of APBs. These effects have been observed experimentally, where V segregated to APBs during some stages of aging [2]. A representation of the migration of V for the model with S=0.5 in grains can be observed in **Figure 5.10**.

Site occupancy of V in FeCo has been discussed in the literature without reaching an agreement. From a spectroscopic point of view, it has been proposed that V prefers to reside in the Fe sublattice due to the size and electronegativity [31]. On the other hand, from a magnetic point of view, it has been suggested that the substitution of Co with V atoms is energetically favorable [118]. In this work we observed that V segregates to the GBs or APBs favoring a substitution of Fe atoms in the vicinity of Co-Co interactions. The migration decreased the initial quantity of Fe and Co present in the GBs by ~20% and ~3%, respectively. In this case, the Co-V potential predicts an enthalpy of mixing for equiatomic solid solutions of -14.1 kJ/mol [97] whereas the ones for Fe-Co and Fe-V interactions are -7.06 and -5.10 kJ/mol, respectively. Thus, replacing Fe with V atoms in the vicinity of Co-Co interactions is favorable as it reduces the total energy of the system.

According to MC-Ising model calculations, the addition of V increases the APB energy in the {112} and decreases the energy in the {110} for the <111> slip direction, bringing them to similar values at 139 and 136 mJ/m^2, respectively [37]. It is theorized that this facilitates the ability to cross slip thus improving the ductility. In contrast, recent FP calculations showed that V reduces both APB energies to a range of 84-128 mJ/m^2 in the {112} and 94-109 mJ/m^2 in the {110} [38]. The reduction of the APB energies promotes an easier dislocation slip and thus facilitates ductile behavior. Our MD calculations agree with the FP results revealing that both energies decrease, lowering the energy from 176 to 169

mJ/m^2 in the {112} and from 141 to 129 mJ/m^2 in the {110}. These values are slightly higher than the ones presented by the references but still maintaining the relationship $\gamma_{APB}^{(112)} > \gamma_{APB}^{(110)}$. We attribute this difference to the lack of magnetic effects in this type of semi-empirical potential. The magnetic forces are intrinsic of FP calculations and were incorporated in the previously mentioned work by the addition of the Ising model, which takes into account the atomic spin to describe ferromagnetic phenomena.

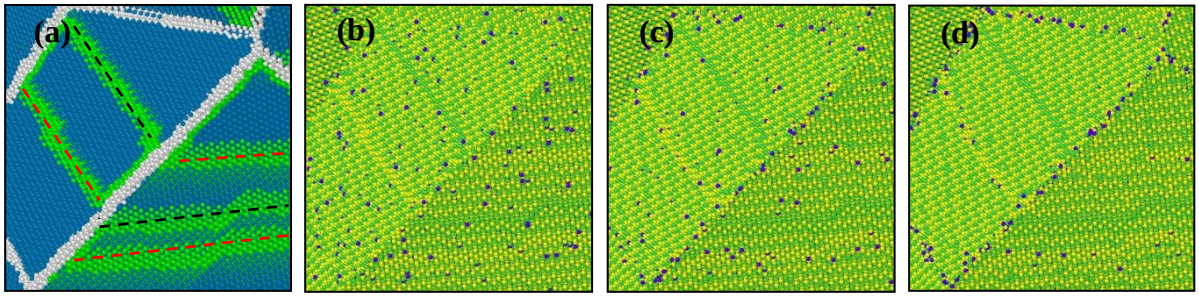

Figure 5.10 Migration of V atoms in FeCo under the GCMC-MD scheme. **(a)** Grain configuration visualized under the PTM. Turquoise atoms are in a B2 structure while light green and white atoms represent atoms in the APBs and GBs respectively. Black and red dotted lines present Fe and Co dominated APBs respectively. **(b-d)** Atomic representation of the evolution of the system. Green atoms represent Fe, yellow atoms Co and purple atoms V, respectively.

The stress-strain response of FeCo-2V is assessed by applying tensile strain to NC models. Initially, a model based on the previous GCMC-MD simulations, where V was segregated into the GBs, was tested. In **Figure 5.11 (a)**, the stress builds up following an almost linear response softly yielding at ~5% strain. After that, the UTS is reduced by almost 10% compared to the binary FeCo. Under the atomic strain analysis, no intragranular stresses were observed. Primarily, stresses concentrate in the vicinity of the GBs with a more perpendicular alignment to the strain direction. Then, the accumulation of local stresses causes a crack initiation. The crack rapidly propagates throughout the GBs leading to an intergranular fracture at ~6.8% strain. The duration of the plastic region is reduced leading to fracture ~8% sooner than the binary alloy. Thus, our simulations revealed that the brittleness of the alloy when V segregates to the GB is stronger compared to the binary alloy. This confirms the observations by the literature, where the introduction of ordering in FeCo-2V alloys resulted in ductility loss at room temperature [28]. As a comparison, V was introduced exclusively in the grains of the fully ordered FeCo. The straining curve

depicts yielding at ~4% strain. The UTS is slightly reduced and delayed compared to the other models. Consequently, the fracture point was greatly delayed by ~15% denoting an increase in the ductility. Kawahara et al. [119] proposed that the formation of Co_3V compounds would result in local concentrated disordered regions that would impart ductility to the alloy. In this model, the incorporation of V randomly substitutes Fe and Co atoms in the ordered matrix. Thus, the observed increase in the ductility occurs due to the formation of cubic V-based compounds. In **Figure 5.11 (b)**, it can be observed that both models with V accommodate a larger number of dislocations than the binary alloy. However, V enhances the embrittlement of the GB increasing the dislocation rate whereas V in grains enhances the motion of V-based compounds spread in the grains which are susceptible to form localized dislocations.

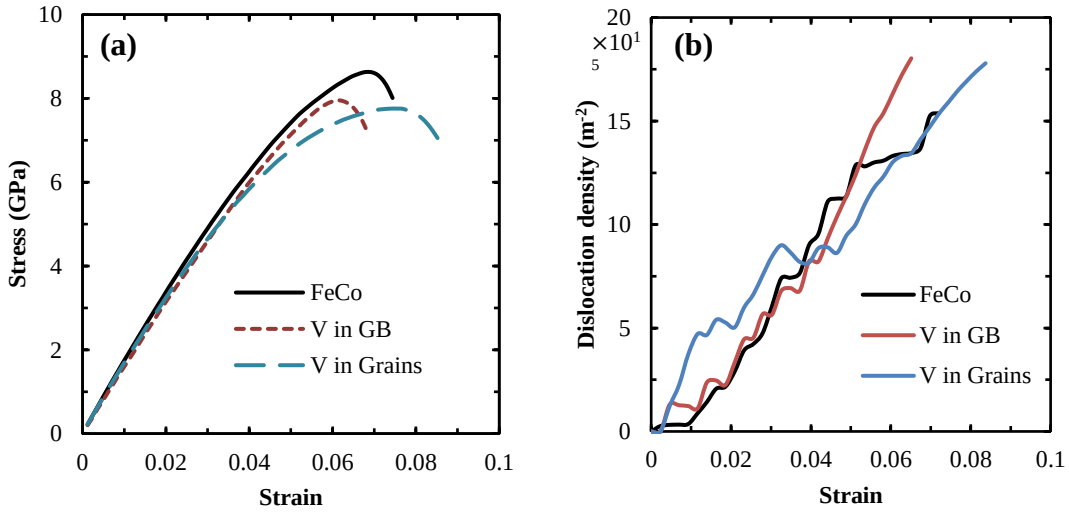

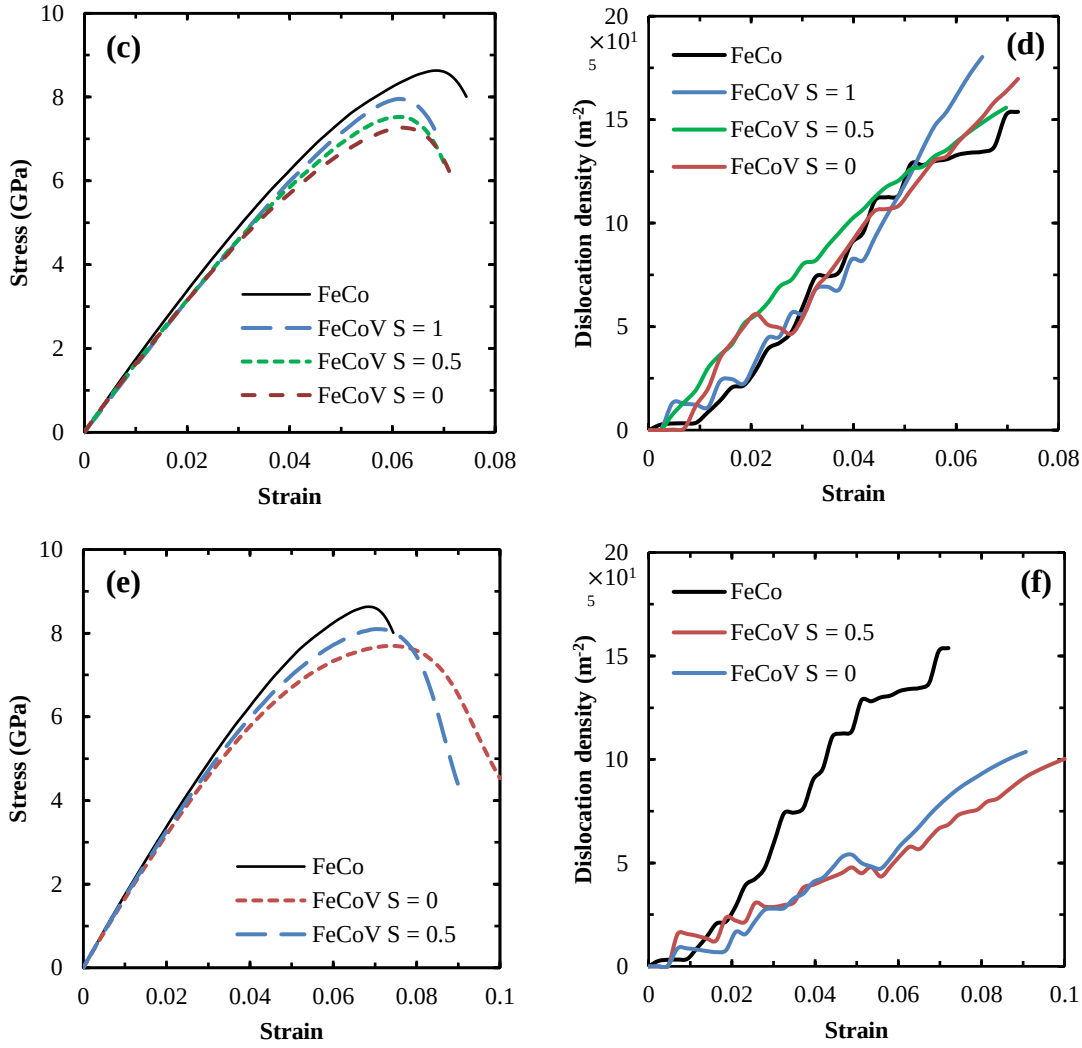

Figure 5.11 Stress strain curve and dislocation density evolution of FeCo-2V alloys when V is introduced into: **(a, b)** fully ordered GBs and grains, **(c, d)** only GBs with different ordering degrees and **(e, f)** only APBs in grains with different ordering degrees.

The effects of V in the disordered FeCo alloys were assessed by straining the models containing different ordering degrees at GBs and at grains separately. **Figure 5.11 (c)** shows the stress-strain curves when V is introduced to FeCo with GBs presenting full ordering (S=1), partial ordering (S=0.5) and full disordering (S=0). The stress and strain of the UTS point is reduced compared to the binary alloy. The ordering degree does not seem to have a major effect on the strain magnitude of the UTS. Nevertheless, it was observed that disordering reduces the UTS value. Disordering also increases the fracture point by promoting mobility at the GBs. This was observed in the binary alloy (**Figure 5.11 (a)**) but

the effect is maximized by V. Reducing the fracture stress but increasing the fracture point by ~3% and ~11% for the partially and fully disordered alloys, respectively. **Figure 5.11 (d)** shows a similar pattern as observed in **Figure 5.11 (b)** where an increased dislocation rate was observed, leading to a larger number of dislocations and eventually a faster development of the fracture point.

Figure 5.11 (e) shows the stress-strain curves when V is introduced at FeCo APBs with partially ordered (S = 0.5) and fully disordered (S = 0) grains. For both models, the stress builds up to yielding at ~3% strain, which is sooner than the previously tested models. The S = 0.5 and S = 0 models retarded the UTS point by ~3% and ~8% respectively. Moreover, the UTS was reduced by ~7% and ~11% compared to the ordered binary FeCo. Near the UTS point, crack nucleation begins at the GBs. The S = 0.5 model failed at 9.1% in an intergranular fashion. In the case of the S = 0, crack nucleation and propagation were observed but fracture was not achieved within 10% strain. For these cases, most stresses concentrate mainly at the GBs, the remaining stresses were dissipated through slippage at the APB. This is confirmed in **Figure 5.11 (f)** where a reduced dislocation rate is observed after the initial accommodation of stresses in the GBs. This was also observed in **Figure 5.11 (d)**, however the effect is maximized by the introduction of V promoting the mobility of the APBs delaying the appearance of the fracture point.

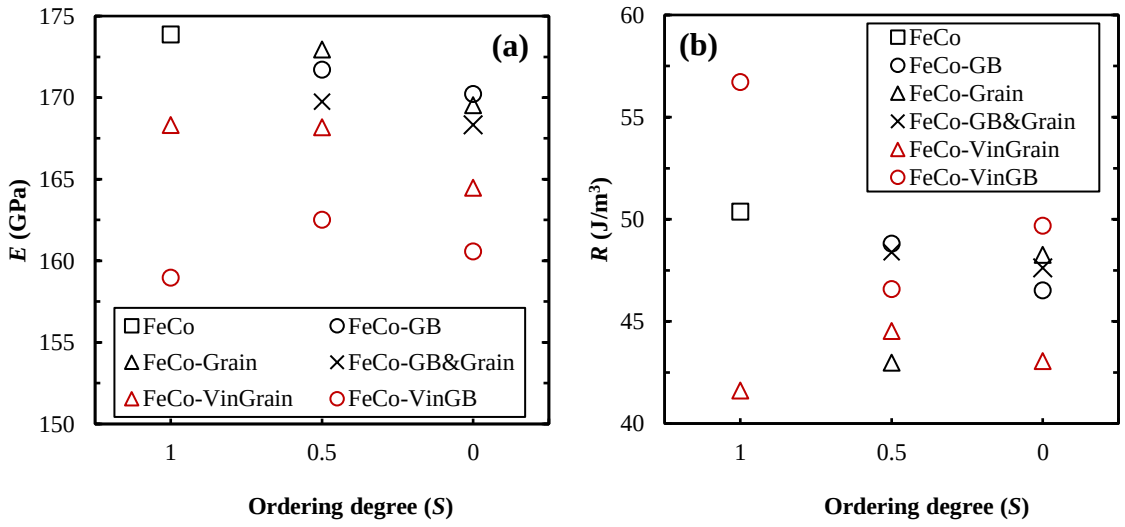

Figure 5.12 Determined values for the **(a)** Young's modulus (*E*) and **(b)** modulus of resilience (*R*), for FeCo (black) and FeCo-2V (red) when V is introduced in the GBs and/or grains displaying different ordering degrees (*S*).

In this study, Young's modulus (E) was derived from stress-strain curves, illustrated in **Figure 5.12**. The ordered binary alloy exhibited E values in close alignment with experimental data (~165 GPa [79]). Overall, the resulted *E* shows a proportional behavior to the ordering degree, showing that the ordered alloy possess a greater stiffness than the disordered counterparts. When V is introduced in the grains, a similar trend can be observed. However, when introduced in GBs, the ordered alloy seems to present a lower *E*. Subsequently, the yield strength (σ_y) was determined using the point of 0.2% residual strain (offset method), enabling the calculation of the modulus of resilience (*R*) via the following equation,

$$R = \frac{\sigma_y^2}{2E} \tag{36}$$

The results from these calculations are depicted in **Figure 5.12**. The highest resilience was observed in the ordered alloy with V introduced in the GBs, indicating enhanced deformability and energy absorption, which should bolster ductility. In contrast, the lowest resilience was found when V is present in the grains of the ordered alloy. Interestingly, when V is inserted in the GBs presenting a disordered state, this modulus is risen to nearly match the one presented by the binary alloy. While these results give a perspective on the relative behaviors within the elastic region, the deformation microstructural mechanisms may slightly swift the final results regarding the ductility and the fracture point as discussed previously.

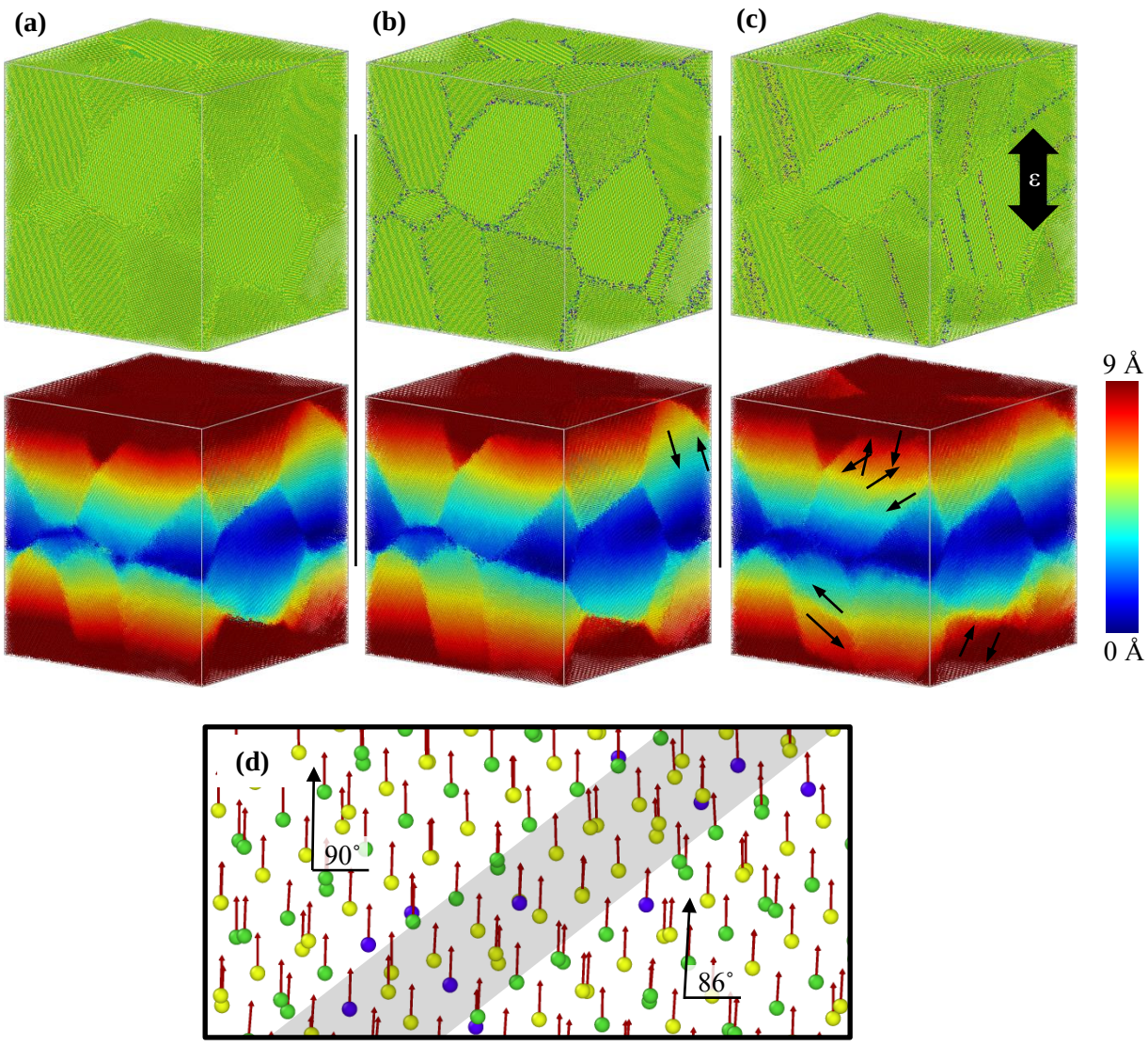

Figure 5.13 Representation of the straining model of **(a)** FeCo (S=1), **(b)** FeCo-2V with V introduced in the GBs (S=0) and **(c)** FeCo-2V with V introduced in the APBs (S=0). Green atoms represent Fe, yellow atoms stand for Co, and purple atoms are used for V. The corresponding image below is the visualization of the displacement per atom for each system at 0.06 strain. Arrows in **(c)** exhibit the relative movement of the APDs. **(d)** Snapshot of a boundary region between two APDs with the average angle of the atomic displacement, the shaded region denotes the APB.

The displacement per atom in the different models at 0.06 strain can be observed in **Figure 5.13**. The displacement gradient denotes that the atoms near the strained boundaries displaced a maximum value of ~9 Å. Atoms located in grains not being directly strained or

located closer to GBs display a minimum displacement. This reflects that stresses are mostly concentrated in the GBs, as observed in **Figure 5.9**. In the ordered FeCo (**Figure 5.8 (a)**) and FeCo-2V with V introduced in disordered GBs (**Figure 5.11 (b)**) the deformation is accommodated by stretching and rotation of grains. Grains not being directly strained rotated to a maximum of ~11 degrees. The rest of grains presented an average of ~1.5 degrees rotation for both systems. It can be observed that **Figure 5.11 (b)** presents sharper GBs than **Figure 5.11 (a)**, revealing that atoms at the grains are less likely to diffuse into the GBs containing V. This translates to less mobile GBs which increases the brittleness. APB slippage is observable for the $S = 0$ model in **Figure 5.11 (c)**. Here the arrows indicate the relative movement of the APD according to the displacement of the atoms. **Figure 5.11 (d)** shows a closeup snapshot of the atomic displacement surrounding one of the APBs. The upper section follows a displacement in average parallel to the straining direction whereas the lower section shows less displacement with an average deviation of ~4 degrees from the straining direction. Overall, the encounter of APDs with APBs results in slippage that ultimately leads to a high level of amorphization in the regions where the APD intersects the GBs. These regions slow down the crack propagation and extend the plastic deformation region and thus the ductility of the material.

We noticed that introducing V did not change the mechanism of fracture in FeCo alloys. Thus, our simulations partially agree with experiments, where the incorporation of V in ordered FeCo has been observed to lead to a mixture of transgranular and intergranular cleavage [2,9]. However, Li et al. [120] experimentally observed that the ordering degree might not be the only factor that governs the fracture morphology. This suggests that magnetic interactions and the presence of impurities play a key role in defining the fracture type of FeCo alloys, which will be considered in our future research.

5.5 Conclusions

We have developed a second nearest-neighbor modified embedded-atom method (2NN MEAM) interatomic potentials for the Fe-Co and Fe-V binary systems based on a Fe interatomic potential suitable for mechanical assessment. The potentials reproduce a large

frame of the binary properties compared with first principles calculations. These potentials were merged with an existing Co-V binary potential to describe the Fe-Co-V ternary system. Finally, we applied uniaxial tension on the equiatomic FeCo and FeCo-2V nanocrystalline (NC) bulks to study the mechanical response and fracture pathways. The conclusions are as follows:

1) The FeCo tensile test reveals that modifying the ordering degree of the grain boundaries (GB) and grains have a small impact on the ultimate tensile strength (UTS) and the fracture point. Disorder in the GBs slightly facilitates grain mobility which delays the crack nucleation. Whereas antiphase boundaries (APB) can better accommodate the initial stresses in the plastic regime. The concentration of stresses at the triple junction GBs initiates a crack nucleation and propagation leading to an intergranular fracture regardless of the ordering conditions.
2) The influence of V was assessed by incorporating 2 at. % V into the FeCo alloy. V was found to reduce the {112} and {110} APB energies. Hybrid grand canonical Monte Carlo – molecular dynamics (GCMC-MD) simulations reveal that V migrates to the GBs in the ordered alloy, preferring to replace Fe atoms in the vicinity of Co interactions. Introducing disordering in the grains, GCMC-MD simulations predict that V atoms prefer to migrate mainly to GBs while a few atoms to the anti-phase boundaries (APB).
3) V was exclusively introduced in the GBs of FeCo with different ordering degrees in the GBs. The tensile simulations reveal that this insertion promotes a stronger brittleness than the binary alloy disregarding the ordering conditions. Introducing V exclusively in the APBs highly promotes slippage in the inner grains. The increased mobility of the APDs decreases the UTS but greatly delays the fracture strain, thus increasing the ductility of the FeCo-V. We found that the addition of V does not modify the intergranular fracture mode.

Chapter 6

Modified Embedded Atom Method Interatomic Potentials for The Fe-Al, Fe-Cu, Fe-Nb, Fe-W, And Co-Nb Binary Alloys

In this study, we developed interatomic potentials for the Fe-Al, Fe-Cu, Fe-Nb, Fe-W, and Co-Nb binary systems using the second nearest-neighbor modified embedded-atom method (2NN MEAM) formalism. The interatomic potentials were parameterized through fitting to available data on essential physical properties such as enthalpies of formation, structural parameters, and elastic constants. The fitted interatomic potentials are capable of accurately reproducing these properties, demonstrating a satisfactory level of concordance with data collected through experimentation, CALPHAD evaluations, and first-principles calculations. These potentials can be merged with existing MEAM potentials to study the physical metallurgy of multicomponent and high entropy alloys (HEA), enabling deeper understanding of their unique properties at the atomic scale.

**This section is published substantially in Computational Materials Science, 2023. https://doi.org/10.1016/j.commatsci.2023.112488. Reprint with permission.

6.1 Introduction

Brittleness at room temperature has restricted a wider use of Iron-Cobalt (FeCo) alloys in more demanding applications. To enhance the ductility while keeping the magnetic properties virtually unaffected, it has been proposed to introduce minor amounts of alloying elements such as Al, Cu, Nb, and W [8–11]. The impact of these alloying elements on the microstructure remains unclear, as experimental studies face limitations in capturing the complexities of microstructural changes during thermal and deformation processes. Computational methods, such as atomistic-level approaches, can provide descriptions of microstructural phenomena. Given the hierarchical construction of interatomic potentials within the second nearest-neighbor modified embedded-atom method (2NN MEAM) [41], the utilization of corresponding unary potentials is crucial for the proper functioning of binary potentials. To accurately describe the binary and ternary interactions in FeCo-X (X=Al, Cu, Nb, and W) alloys, multiple interatomic potentials are required. In **Chapter 5**, an interatomic potential for FeCo was developed and effectively utilized to investigate microstructural changes during deformation. Furthermore, this potential was expanded to incorporate V additions into the FeCo microstructure, laying the foundation and enabling the exploration of other ternary and more complex multi-elemental systems [121]. The binary description for FeCo was developed using the unary Fe [98] and Co [76] interatomic potentials. Seeking to incorporate additional elements into the FeCo alloy, we have referenced descriptions from the literature for the individual interactions of Al [122], Cu [122], Nb [41], and W [41]. In terms of MEAM binary potentials, the literature provides ready-to-implement Co-Al [76], Co-Cu [123], and Co-W [124] interactions. Although interatomic potentials for the Fe-Al [125–128], Fe-Cu [126,129] and Fe-Nb [130] systems exist in the literature, they are based on a different Fe unary potential, making them incompatible with our intended study.

Thus, the purpose of this work is to develop the remaining binary interatomic potentials, namely Fe-Al, Fe-Cu, Fe-Nb, Fe-W, and Co-Nb. This study can be considered as a necessary foundation step towards understanding the effect of ternary interactions in FeCo-based systems. In the following section, we briefly outline the interatomic potential modeling and parameterizing process. In Section 3, we present the physical properties

predicted by the interatomic potentials. Finally, we summarize our findings in the conclusions.

6.2 Determination of Interatomic Potential Parameters

Within the context of the 2NN MEAM methodology, Lee et al. [41] formulated a comprehensive collection of interatomic potentials specifically tailored for the bcc transition metals, encompassing Cr, Mo, W, V, Nb, Ta, and an updated version for Fe. From their work, we have incorporated the W and Nb potentials. In the case of the Fe potential, an enhanced version was subsequently introduced [98], which has been implemented in this chapter. This Fe potential was specifically chosen for its enhanced mechanical capabilities, including the ability to predict non-degenerate core behavior within the bcc structure and enhanced phase stability. The latter attribute addresses the absence of magnetic effects in MD calculations, which do not account for electron spins and associated magnetic interactions. This proves particularly valuable when investigating magnetic alloys such as FeCo. In **Chapter 5**, we developed an in-house potential specifically tailored for FeCo, leveraging the Fe potential. This approach has showcased notable advancements in mechanical performance. The potential accurately captures the deformation behavior of FeCo, confirming the observations reported in the literature, where the behavior of FeCo alloys is typically characterized by a brittle intergranular fracture [121]. In contrast, our extensive testing of alternative FeCo potentials [49,131], including the one developed in **Chapter 4**, which are based on earlier versions of the Fe potential exhibit the formation of phase transitions under strain, leading to a more ductile behavior.

In the domain of fcc metals, Lee et al. [122] produced an updated suite of interatomic potentials tailored for Cu, Ag, Au, Ni, Pd, Pt, Al, and Pb. From their work, we have incorporated the Cu and Al potentials. The Co potential utilized in this study was originally developed by Dong et al. [76] with a specific focus on its suitability for investigating multicomponent alloys. In their study, the authors also incorporated the aforementioned Al potential, resulting in a binary potential that enables the exploration of the properties of the

Co-Al system. The parameterization details of the adopted elemental systems employed in this investigation are provided in **Table 6.1**.

In this study, we employed the $L1_2$ hypothetical structure as a reference for all the systems under consideration. The atomic potential optimization process uses a multi-objective optimization technique that combines the force matching method and the weighted sum method, as outlined by Kim et al. [60]. The 2NN MEAM potential parameters for each combination of elements were calibrated to reproduce the enthalpies of formation and mixing, lattice parameters, and elastic moduli of stable compounds and solid solutions as determined from experiments, CALPHAD assessments and first principles calculations. **Table 6.2** lists the parameters that were fitted for the binary interactions. Literature sources provide more information on the 2NN MEAM theory [41,59,60,67].

Table 6.1 Sets of 2NN MEAM parameters for the unary systems. E_c is reported in eV, while r_e and C_{min}/C_{max} are reported in Å. All other quantities are dimensionless.

	E_c	r_e	A	$\beta^{(0)}$	$\beta^{(1)}$	$\beta^{(2)}$	$\beta^{(3)}$	$t^{(1)}$	$t^{(2)}$	$t^{(3)}$	C_{min}	C_{max}	$d+/d-$
Al [122]	3.36	2.860	1.160	3.20	2.6	6.0	2.6	3.05	0.51	7.75	0.49	2.8	0.05/0.05
Fe [98]	4.28	2.469	0.585	3.80	2.0	0.9	0.0	-0.80	12.30	2.00	0.63	1.9	0.0/0.3
Co [76]	4.41	2.500	0.900	3.50	0.0	0.0	4.0	3.50	5.00	-1.00	0.49	2.0	0.0/0.0
Cu [122]	3.54	2.555	0.940	3.83	2.2	6.0	2.2	2.72	3.04	1.95	1.21	2.8	0.05/0.05
Nb [41]	7.47	2.860	0.760	5.08	1.0	2.5	1.0	1.70	2.80	-1.60	0.36	2.8	0.0/0.0
W [41]	8.66	2.740	0.400	6.54	1.0	1.0	1.0	-0.60	0.30	-8.70	0.49	2.8	0.0/0.0

Table 6.2 Sets of 2NN MEAM parameters for the binary systems. E_c is reported in eV, while r_e and C_{min}/C_{max} are reported in Å. All other quantities are dimensionless.

Alloy (A-B)	Fe-Al	Fe-Cu	Fe-Nb	Fe-W	Co-Nb
Ref. Structure	$L1_2$	$L1_2$	$L1_2$	L12	$L1_2$
Ec	-4.17	-3.90	-5.02	-5.15	-5.34
r_e	2.640	2.560	2.675	2.610	2.570
α	5.370	5.250	5.122	5.400	5.450
C_{min} *(A-B-A)*	0.58	0.70	1.20	0.16	0.40
C_{min} *(B-A-B)*	0.45	1.30	0.20	0.76	1.40
C_{min} *(A-A-B)*	0.55	1.60	0.60	0.76	1.50
C_{min} *(A-B-B)*	0.55	1.60	0.60	0.76	1.50
C_{max} *(A-B-A)*	2.38	2.10	1.90	2.05	2.30
C_{max} *(B-A-B)*	2.80	2.80	2.70	2.80	2.80
C_{max} *(A-A-B)*	1.90	1.90	2.70	1.90	2.80
C_{max} *(A-B-B)*	1.90	1.90	2.70	1.90	2.80

d+	0.05	0.05	0.01	0.00	0.00
d-	0.05	0.05	0.01	0.00	0.00
ρ_0^A: ρ_0^B	1:1	1:1	1:1	1:1	1:1

6.3 Calculation of Fundamental Physical Properties

To verify the reliability of the interatomic potentials, we compared their predicted fundamental properties with the published literature. This chapter examines the properties of several crystal structures, each of which corresponds to specific alloy compositions. The crystal structures under investigation include B2, C14, C15, D_{85}, D03, $L1_2$ and Nb_2Co_7. The B2 structure, discussed in preceding chapters, serves as the simplest ordered equiatomic configuration for binary alloys, featuring a bcc reference structure. Moving to the C14 and C15 structures, these are categorized as Laves phases and exhibit an AB2 intermetallic ratio. These phases manifest intricate architectures where the larger A-type atoms adopt cubic and hexagonal diamond-like ordering, while the smaller B-type atoms form tetrahedral arrangements around the A-type atoms. The unique stacking sequences within these phases give rise to various Laves structures [132]. The D_{85} structure, showcases a complex hexagonal close-packed lattice constructed from tetrahedral polyhedra. It features an A_7B_6 intermetallic ratio and involves atom distribution across five sublattices [133]. The D03 and $L1_2$ structures represent the ordered bcc- and fcc-derivative phases at the A_3B composition. Due to their structural similarities, diffusionless D03-$L1_2$ transitions can occur in select binary alloys, analogous to the B2-$L1_0$ transitions discussed in **Chapter 4**. Additionally, the Nb_2Co_7 composition demonstrates a crystal structure resembling that of the Zr_2Ni_7 compound. In this arrangement, larger Zr atoms are positioned within a hcp lattice, while smaller Ni atoms take up residence in octahedral sites within the hcp framework. This pseudo-hexagonal structure is categorized within the monoclinic C2/m space group. For a visual representation of these structures, please refer to **Figure 6.1**.

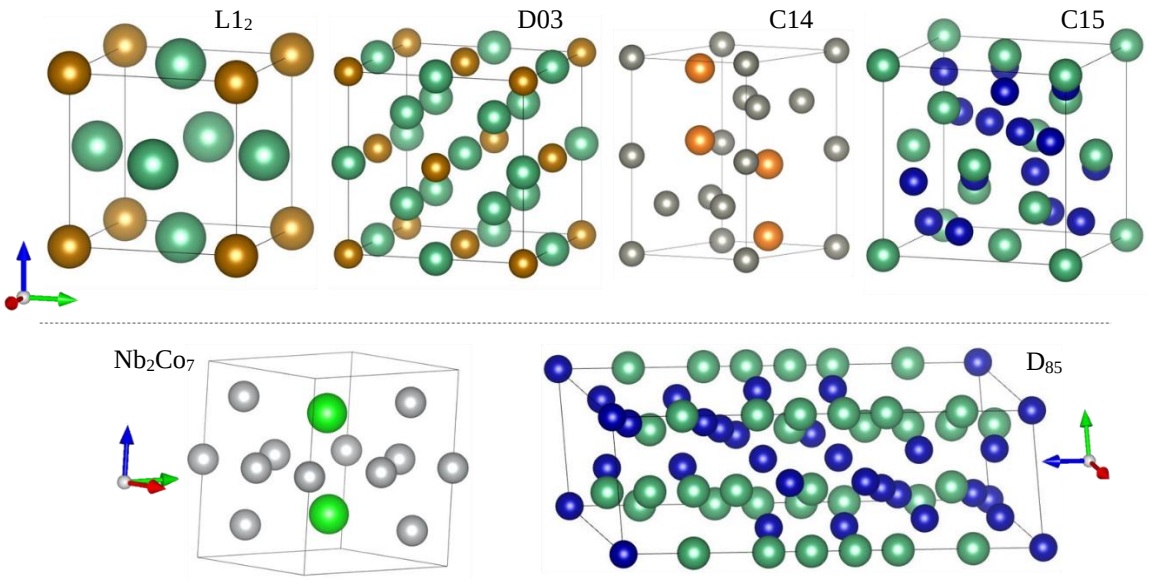

Figure 6.1 Crystal structures explored in this chapter. The axes indicators represent the alignment of the *a* (red), *b* (green) and *c* (blue) lattices.

To assess the suitability of the potentials to be used in other compositions, the thermodynamic properties were evaluated using solid solution phases throughout the stoichiometric range. To simulate the systems, we employed periodic boundary conditions and set the radial cutoff distance to 4.8 Å. The Large-scale Atomic/Molecular Massively Parallel Simulator (LAMMPS) [117] was utilized to perform the MD calculations.

6.3.1 Calculated Properties of The Fe-Al Binary System

The Fe-Al system has been extensively investigated in the field of MD, with several MEAM potentials developed in previous studies. Lee et al. [125] formulated a well-balanced potential with the aim of exploring the influence of aluminum on defect formation and plastic deformation behavior in high Al steels (Fe-Mn-Al-C). Jelinek et al. [126] utilized a generalized approach to develop a series of unary potentials for Al, Si, Mg, Cu, and Fe as well as their binary combinations. Mahata et al. [127] formulated interatomic potentials for Al-Cu, Al-Fe, and Al-Ni systems, with a specific emphasis on modeling the thermal nucleation-solidification effects. Chen et al. [128], developed an Fe-Al potential with the capability to predict the complex Fe_3Al_8 structure for the study of the effect of

galvanic coating on inhibition layers. While the motivation to develop this potential arises from the incompatibility of the unary systems, the objective is to create a binary potential that not only ensures the stability of the structures but also establishes agreement with the elastic properties. This distinguishes our approach from previous methods that may not have achieved the same level of success in simultaneously addressing these crucial aspects. In the Fe-Al system, experimental observations from the phase diagram reveal that in the region of up to 50 at.% Al, three bcc-based structures are prevalent depending on the temperature and composition, the ordered B2 and D03 and a disordered A2 [134–136]. Contrary to experimental observations, first principles studies have found that the $L1_2$ is slightly more stable than the D03 structure [137,138]. Thus, in this work the properties of the ordered B2, D03 and $L1_2$ structures are initially calculated. The results from the present study are compared with the available literature in **Table 6.3**.

Table 6.3 Calculated properties of Fe-Al intermetallic compounds at 0 K. Lattice parameters *a* and *c* (Å), enthalpy of formation ΔH (eV/atom), elastic constants C_{XX} and bulk modulus *B* (GPa).

	This Work	FP / CALPHAD	Exp.	Other Calculations
FeAl - B2				
a	2.92	2.87 [126], 2.83 [139], 2.87 [140], 2.90 [141]	2.90 [142]	2.95 [126], 2.91 [125], 2.90 [127]
ΔH	-0.381	-0.347 [126], -0.334 [140], -0.379 [143], -0.338 [144], -0.311 [138], -0.377 [145]	-0.250 [146], -0.280 [147], -0.423 [148]	-0.342 [126], -0.298 [125], -0.357 [128], -0.267 [127]
C_{11}	214	257 [126], 289 [139], 206 [141]	209 [149], 180 [150]	251 [126], 152 [125], 256 [151], 172 [127]
C_{12}	93	133 [126], 129 [139], 130 [141]	123 [149], 113 [150]	92 [126], 110 [125], 94 [151], 117 [127]
C_{44}	168	138 [126], 165 [139], 107 [141]	127 [149], 127 [150]	111 [126], 78 [125], 115 [151], 88 [127]
B	143	174 [126], 183 [139], 177 [140], 156 [141] , 160 [137]	152 [149], 136 [150]	145 [126], 124 [125], 135 [127]
Fe_3Al - D03				
a	5.76	5.73 [126], 5.72 [152], 5.69 [141], 5.75 [137]	5.79 [142]	5.77 [126], 5.74 [125], 5.764 [127]
ΔH	-0.325	-0.201 [126], -0.260 [152], -0.186 [137] , -0.201 [138]	-0.202 [146], -0.321 [147]	0.346 [126], -0.205 [125], -0.305 [128], -0.223 [127]
C_{11}	231	194 [126], 184 [141], 164 [137]	171 [149]	177 [126], 222 [125], 188 [151], 212 [127]
C_{12}	110	143 [126], 162 [141], 127 [137]	130 [149]	117 [126], 112 [125], 125 [151], 113 [127]
C_{44}	104	140 [126], 137 [141], 142 [137]	131 [149]	129 [126], 109 [125], 121 [151], 97 [127]
B	160	160 [126], 170 [141], 140 [137]	144 [149]	137 [126], 148 [125], 146 [127]

Fe_3Al - $L1_2$			
a	3.72	3.64 [126], 3.64 [140], 3.66 [138], 3.65 [137]	3.72 [126], 3.67 [125], 3.60 [127]
ΔH	-0.129	-0.200 [140], -0.222 [138], -0.199 [137], -0.196 [126], -0.210 [128]	0.274 [126], -0.179 [125], -0.097 [128], -0.177 [127]
C_{11}	191	181 [126], 184 [137]	251 [126], 174 [125], 181 [127]
C_{12}	152	158 [126], 145 [137]	83 [126], 137 [125], 127 [127]
C_{44}	137	125 [126], 160 [137]	97 [126], 76 [125], 72 [127]
B	168	166 [126], 158 [140] , 168 [138], 158 [137]	139 [126], 149 [125], 145 [127]

The lattice constants calculated for the reference structures are marginally larger compared with FP calculations. Nonetheless, they exhibit a high degree of concordance with both experimental results and other MD calculations. The enthalpies of formation for the B2 and D03 structures exhibit a high level of agreement with the reference values, while the $L1_2$ structure demonstrates a slightly elevated enthalpy. Notably, the present potential predicts a lower enthalpy of formation for the D03 structure than the $L1_2$ structure, consistent with experimental evidence that the D03 structure is more stable at this particular composition. The predicted elastic constants are generally within the bounds of the limits observed in the literature. While there are some deviations, the elastic constants support the relationships $C_{11}>C_{44}>C_{12}$ for the B2 structure and $C_{11}>C_{12}>C_{44}$ for the D03 and $L1_2$ structures as observed in both experiments and FP calculations. Other MEAM potentials are deviated from the outcomes outlined in the primary references, owing to their intended applications or the methodologies employed in their development. For instance, the B2 reference structure chosen by Jelinek et al. [126] offers precision for near equiatomic compositions but struggles to replicate the energetic and elastic traits of Fe-rich compounds, resulting in positive formation enthalpies. Conversely, Lee et al. [125], in their emphasis on high aluminum steels, have prioritized the Fe-rich compositions, leading to properties that are less precise for the B2 structure. The recent potential introduced by Mahata et al. [127] developed with a specific focus on the formation enthalpy and solid-liquid transition temperatures, exhibiting commendable accuracy in predicting the properties of the relevant compounds. Nevertheless, it deviates from the expected elastic constant trend for the B2 structure. Finally, in the study conducted by Chen et al. [128], their potential was specifically designed to investigate the intricate Fe_3Al_8 structure at low temperatures.

With the adjustment of the Al unary potential, the stability for the Fe_3Al_8 compound was improved, but the accuracy of the elastic constants was compromised.

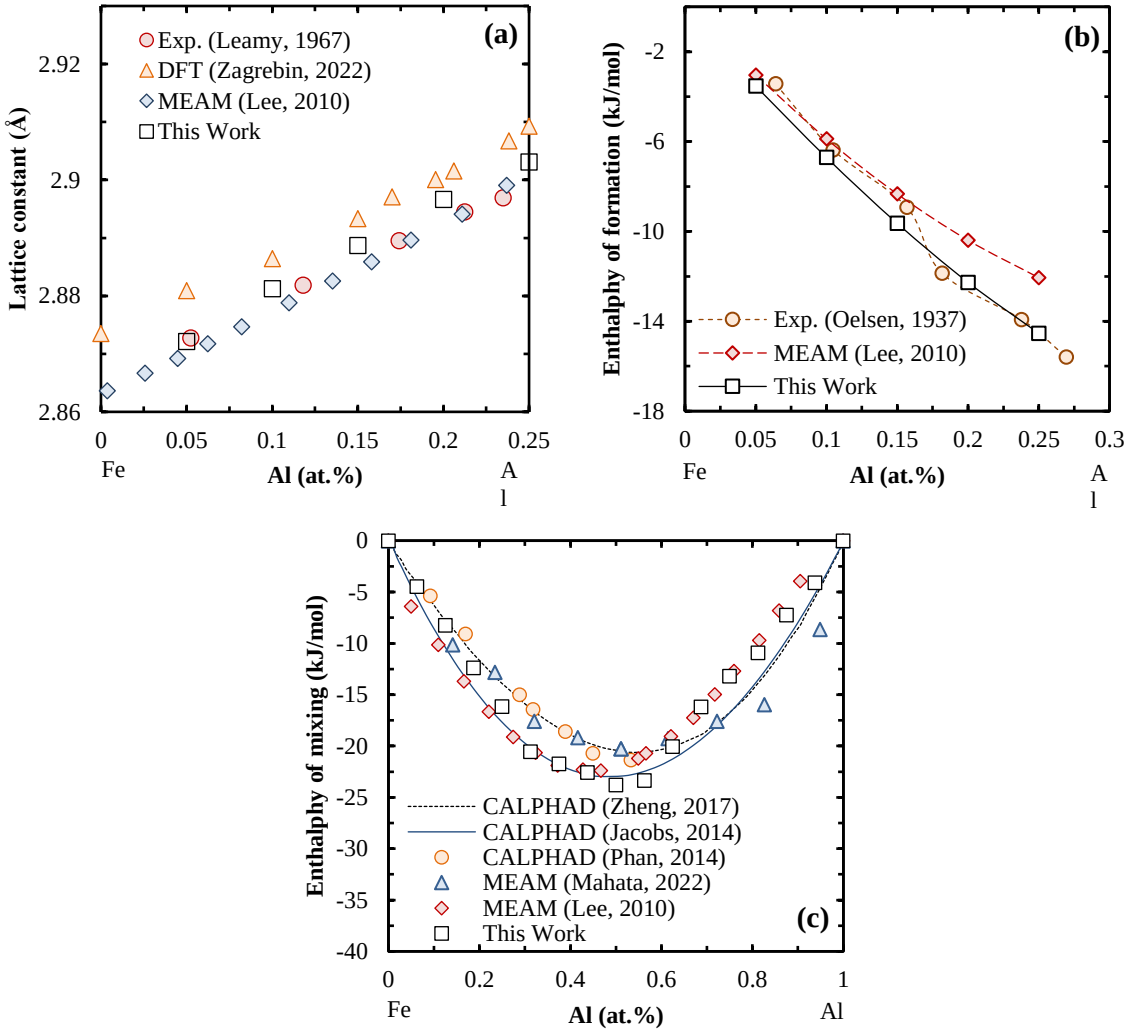

Figure 6.2 **(a)** Lattice parameter and **(b)** enthalpy of mixing for the Fe-rich bcc solid solution in the Fe-Al system at 0 K. **(c)** Enthalpy of mixing of the Fe-Al liquid alloys at 1873 K. In comparison with experimental data [153,154] and DFT [135], CALPHAD [155–157] and MD calculations [125,127].

The results of our calculations for solid solutions are presented in **Figure 6.2**, which shows the compositional lattice parameter and enthalpy of mixing curves for the Fe-rich region at 0 K, as well as the enthalpy of mixing curve for the entire compositional range of the solid solution at 1873 K. At 0 K, the present calculation shows that the lattice parameter presents a slightly larger compositional growth rate of ~0.16 compared to the ~0.15 Å/at.% Al shown by literature values. This is expected given the slight overestimation of the lattice

parameters observed in the ordered structures. The mixing enthalpy in the Fe-rich region closely aligns with the findings of the references, exhibiting a slope that is more in line with ab initio calculations. At 1873 K, the mixing enthalpy curve exhibits a miscibility gap showing a negative deviation to Vergard's law, which correctly reflects the thermodynamic stability of the liquid phase at elevated temperatures.

6.3.2 Calculated Properties of The Fe-Cu Binary System

To the best of our knowledge, two previous studies have utilized the MEAM to develop Fe-Cu interatomic potentials. Lee et al. [129] focused on studying defect formation in Fe-Cu alloys induced by irradiation, specifically investigating primary knock-on atom energies and defect properties. As mentioned earlier, Jelinek et al. [126] utilized a generalized approach to develop a series of unary and binary potentials, including a specific description for the Fe-Cu system as mentioned in the previous section. Owing to the incongruity of unary potentials, our primary focus is to develop a binary potential that overcomes the challenges observed in other potentials to achieve both structural stability and accurate elastic descriptions simultaneously.

According to phase diagrams, the Fe-Cu system displays a combination of bcc and fcc solid solutions at low temperatures [158–162]. Various processing techniques, including mechanical alloying and vapor deposition, have been utilized to create metastable Fe-Cu compounds [163–167]. The metastable phases under consideration have been the subject of comprehensive ab initio studies, with particular emphasis on the Fe-rich $L1_2$, D03, and the equiatomic B2 structures. Consequently, our investigation was centered on these structures. We have presented a comparison of the properties calculated in the present work with the ones in the literature in **Table 6.4**.

Table 6.4 Calculated properties of Fe-Cu intermetallic compounds at 0 K. Lattice parameters a and c (Å), enthalpy of formation ΔH (eV/atom), elastic constants C_{XX} and bulk modulus B (GPa).

	This Work	FP / CALPHAD	Other Calculations
Fe_3Cu - $L1_2$			
a	3.61	3.65 [168], 3.61 [126], 3.58 [169], 3.64 [129]	3.61 [126], 3.63 [129], 3.63 [170]
ΔH	0.182	0.125 [168], 0.133 [126], 0.125 [129]	0.267 [126], 0.158 [171], 0.183 [129]

C_{11}	168	141 [126], 163 [172]	263 [126]
C_{12}	158	127 [126], 155 [172]	127 [126]
C_{44}	94	100 [126], 98 [172]	80 [126]
B	162	132 [126]	172 [126]
Fe_3Cu - D03			
a	2.87	2.88 [173], 2.87 [174]	
ΔH	0.097	0.162 [174]	
C_{11}	183	215 [80]	
C_{12}	132	155 [80]	
C_{44}	86	141 [80]	
B	150	175 [80], 166 [174]	
FeCu - B2			
a	2.86	2.88 [174], 2.83 [126], 2.89 [169]	2.89 [126], 2.89 [169], 2.87 [170]
ΔH	0.232	0.281 [174], 0.264 [126], 0.262 [175], 0.275 [169]	0.217 [126], 0.325 [169]
C_{11}	135	142 [126]	222 [126]
C_{12}	144	246 [126]	131 [126]
C_{44}	127	108 [126]	105 [126]
B	140	134 [174], 211 [126], 190 [169], 148 [169]	161 [126], 151 [169]

Excellent agreement between predicted and FP-calculated lattice constants was observed for the metastable structures. The enthalpy of formation for the $L1_2$ structure is consistent with FP calculations, while the D03 and B2 structures exhibit slightly lower enthalpies. Nevertheless, the enthalpies of these compounds remain higher than those calculated for the solid solution, indicating that the disordered solution has a higher thermodynamic stability. The elastic parameters for the $L1_2$ phase fall within the range of values predicted by ab initio calculations with less than 10% error. The present potential underestimates the C_{44} for the D03 and the C_{12} for the B2 structures giving a maximum error of ~35%. Nonetheless, the elastic parameters predicted by FP calculations for the $L1_2$ and B2 structures show that $C_{11}>C_{12}>C_{44}$ and $C_{12}>C_{11}>C_{44}$, respectively, which is in line with our calculations. Compared to the prior Fe-Cu MEAM investigations, the potential proposed by Jelinek et al. [126] predicts a sequence of $C_{11}>C_{12}>C_{44}$ for the B2 structure, contrary to the findings of their FP calculations. On the other hand, Lee et al. [129] focused their study on the energetics of defects, but overlooked the assessment of the elastic moduli.

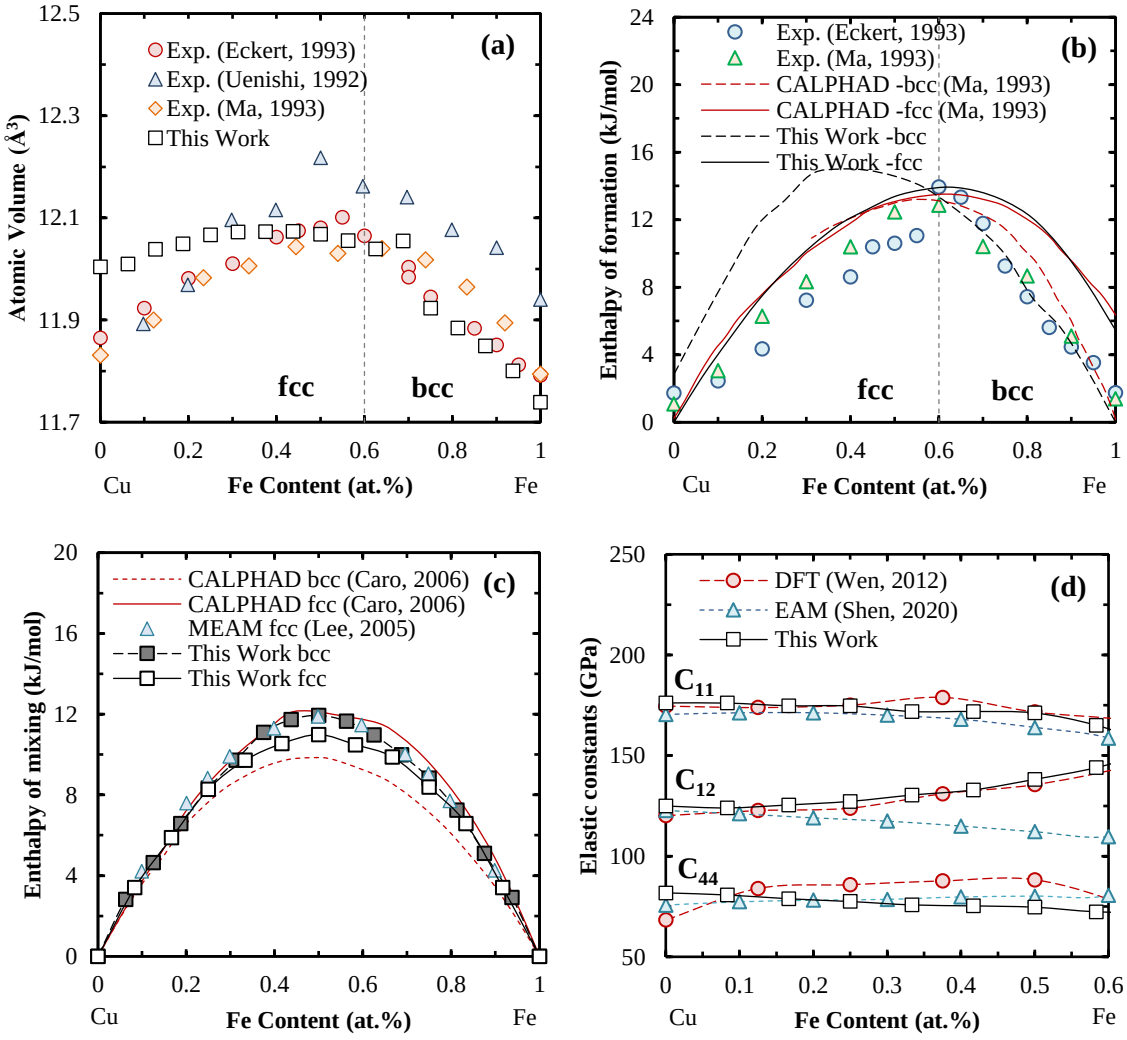

Figure 6.3 **(a)** Atomic volume and **(b)** enthalpy of formation for the solid solution in the Fe-Cu system at 298 K. **(c)** Enthalpy of mixing for the bcc and fcc structures, and **(d)** elastic constants for the fcc solid solutions at 0 K. In comparison with experimental data [164,165,167,176] at ~298 K and CALPHAD assessments [160,167] and MD calculations [129,170].

Experimental studies have demonstrated that an fcc structure can be observed in the Cu-rich region extending up to $Fe_{(1-x)}Cu_x$ concentrations of $60 \leq x \leq 70$ at.%. At lower Cu concentrations, the alloy presents a bcc structure [163,177]. The compositional dependence of the atomic volume, mixing enthalpies and elastic constants were measured for the corresponding phases at 0 and 298 K, these are compared with the literature in **Figure 6.3**. The experimental limit between the fcc and bcc phases is denoted by a vertical dashed line. The calculated atomic volumes agree with the trend observed in experiments with some

differences in the Cu-rich region due to an overestimation of the lattice constant by the implemented unary interatomic potential. The determined convex hulls for the formation enthalpy at room temperature align with the behavior observed in the literature. Specifically, the enthalpy curve for the fcc structure exhibits a lower value up to approximately ~55 at.% Cu, where it intersects with the bcc curve. This intersection suggests a theoretical fcc-bcc phase transition. In the remaining stoichiometric range, the bcc configuration displays a lower enthalpy compared to the fcc counterpart, indicating a higher degree of thermodynamic favorability. Notably, Ma et al. [167] performed CALPHAD calculations, which demonstrated a similar trend with an intersection at ~50 at.% Cu. However, it is worth mentioning that the authors later incorporated magnetic effects, leading to a prediction of the switching between fcc and bcc at ~60 at.% Cu.

At 0 K, a discrepancy exists in the literature regarding the enthalpy of mixing for the bcc and fcc structures. CALPHAD calculations conducted by Caro et al. [160] suggest that the bcc structure exhibits a lower enthalpy compared to the fcc structure, whereas calculations performed by Ma et al. [167] indicate the opposite trend. The present potential aligns with the latter findings, indicating that the fcc structure exhibits a lower energy state than the bcc structure, especially in the central region. Finally, the calculated elastic constants for the compositional fcc solid solution closely align with the results of FP calculations for the C_{11} and C_{12} constants. However, there is a slight deviation in the case of C_{44}, although it still exhibits a similar trend as observed in MD calculations.

6.3.3 Calculated Properties of The Fe-Nb Binary System

Based on available information, the Fe-Nb system has only been investigated in terms of the MEAM by Sa et al. [130]. In their study, the authors developed interatomic potentials for the Fe-Nb and Fe-Ti systems, specifically aiming at exploring binary carbides and their potential integration with other potentials for studying nitride systems. However, the interatomic potential lacks an elasticity description, crucial for mechanical testing. Thus, the development of a new potential is necessary not only to address the incompatibility of the unary systems but also to incorporate the elastic properties.

In the Fe-Nb binary system, two main intermetallic compounds have been confirmed to be stable, a lave phase identified as λ-Fe_2Nb with a C14 crystal structure ($MgZn_2$-like) and a μ-Fe_7Nb_6 phase with a trigonal $D8_5$ structure (Fe_7W_6-like) [178–182]. In this study we included these compounds while the D03 was taken to expand the assessment. The calculated properties are compared with the literature in **Table 6.5**.

Table 6.5 Calculated properties of Fe-Nb intermetallic compounds at 0 K. Lattice parameters *a* and *c* (Å), enthalpy of formation ΔH (eV/atom), elastic constants C_{XX} and bulk modulus *B* (GPa).

	This Work	FP / CALPHAD	Exp.	Other Calculations
Fe_2Nb - C14				
a	4.89	4.78 [173], 4.85 [183], 4.75 [152], 4.79 [184], -4.76 [185]	4.81 to 4.87 [180]	4.87 [130]
c	7.96	8.08 [173], 7.88 [183], 7.85 [152], 7.91 [184], -7.87 [185]	7.85 to 7.94 [180]	7.91 [130]
ΔH	-0.184	-0.189 [130], -0.122 [152], -0.150 [185]	-0.037 to -0.072 [186]	-0.175 [130]
C_{11}	285	303 [80], 283 [183], 268 [184]		
C_{12}	143	131 [80], 99 [183], 100 [184]		
C_{13}	145	132 [80], 70 [183], 116 [184]		
C_{33}	275	378 [80], 285 [183], 339 [184]		
C_{44}	65	78 [80], 82 [183], 59 [184]		
C_{66}	71	85 [80], 41 [184]		
B	190	196 [80], 147 [183], 185 [184]		
Fe_7Nb_6 - $D8_5$				
a	4.91	4.89 [184], 4.87 [185]	4.92 [182]	
c	27.20	26.77 [184], 26.64 [185]	26.8 [182]	
ΔH	-0.155	-0.130 [187], -0.120 [184], -0.167 [130], -0.140 [185]	-0.045 to -0.082 [186]	
C_{11}	181	313 [184]		
C_{12}	132	136 [184]		
C_{13}	130	122 [184]		
C_{33}	202	322 [184]		
C_{44}	24	44 [184]		
C_{66}	27	14 [184]		
B	190	256 [184], 190 [184]		
Fe_3Nb - D03				
a	5.98	5.95 [173], 5.89 [152], 5.89 [185]		
ΔH	-0.017	-0.050 [173], -0.053 [152], -0.069 [185]		

C_{11}	273	275 [80]
C_{12}	129	173 [80]
C_{44}	104	98 [80]
B	189	207 [80]

There is a close agreement between the calculated lattice parameters for the studied structures and the references, with small deviations observed. Concerning the enthalpy of formation, the present potential predicts that the enthalpy of C14 is 0.03 kJ/mol more negative than $D8_5$ structure. While FP calculations show a difference of ~0.01 kJ/mol, the references disagree on which structure has a more negative enthalpy of formation. The elastic constants calculated for the C14 structure are within the limits spanned by the references whereas the $D8_5$ and D03 structures show a maximum deviation of ~40% and ~25%, respectively. In this regard, the presented potential marks the inaugural MD attempt to replicate the elastic constants of these Fe-Nb compounds. The potential by Sa et al. [130] focuses solely on the enthalpy of formation of the C14 structure, along with the enthalpy of mixing within the Fe-rich bcc solid solution and the high-temperature liquid solution.

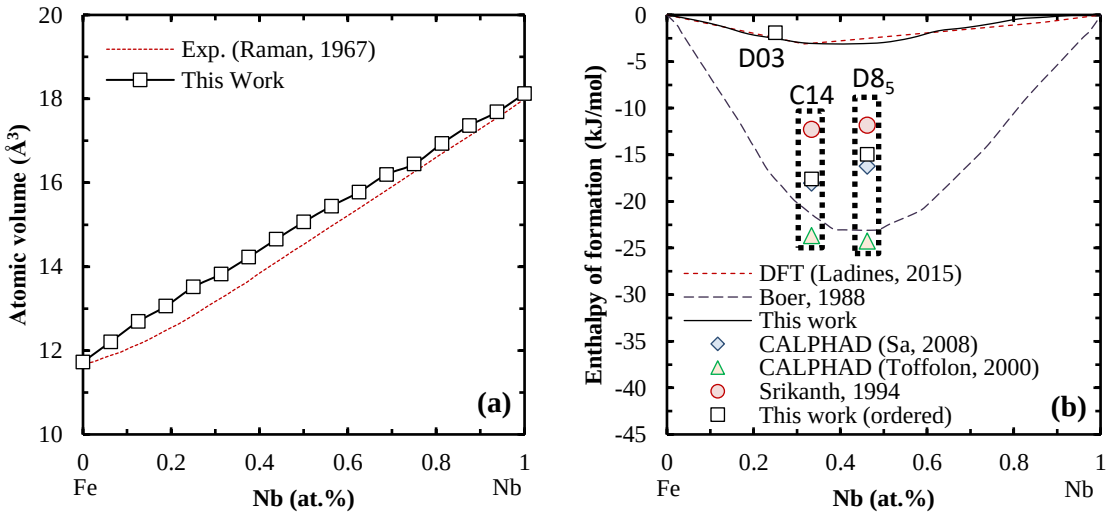

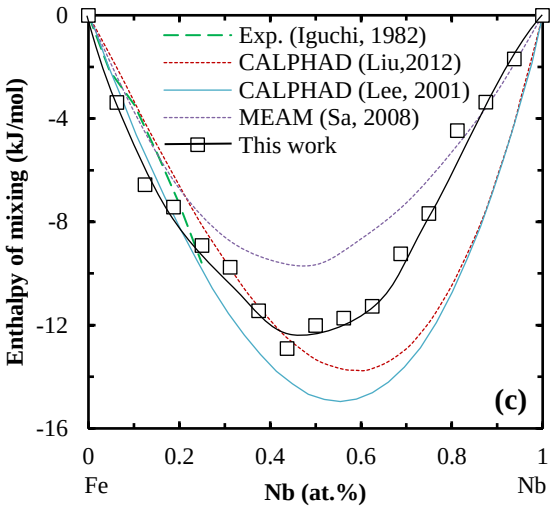

Figure 6.4 **(a)** Atomic volume for the bcc solid solution in the Fe-Nb system at 298 K. **(b)** Enthalpy of mixing for the bcc solid solution (lines) and enthalpy of formation for the principal structures (markers) in the Fe-Nb system at 0 K. **(c)** Enthalpy of mixing for the liquid solution at 2200 K. In comparison with experimental data [182,188], FP calculations [184], CALPHAD calculations [130,181,187,189], thermodynamic assessments [179,190] and MD calculations [130].

Figure 6.4 illustrates the atomic volume calculations and compares the enthalpy of formation and mixing at low and high temperatures. At 298 K, the calculated atomic volumes denote a compositional growth close to experiments. However, in the Fe-rich region a slight expansion is predicted by the present potential whereas a subtle contraction has been observed in experiments, showing a maximum deviation of 4% at 0.25 at.% Nb. The predicted convex hull for the enthalpy of mixing of the bcc solid solution at 0 K closely reproduces the behavior predicted by FP calculations. The potential correctly predicts a more negative enthalpy of formation for the main structures than for the bcc solid solution, suggesting a higher thermodynamic stability for C14 and $D8_5$ compounds. At 2200 K, the calculated enthalpy of mixing denotes a convex hull for the liquid solutions consistent with experimental observations and CALPHAD assessments for the Fe-rich region. However, from the near equiatomic composition to the rest of the stoichiometric range the mixing enthalpy is found to be overestimated. In the Nb-rich region, the present potential shows a behavior similar to the one predicted by another MEAM potential based on the same unary Nb potential [130].

6.3.4 Calculated Properties of The Fe-W Binary System

Similar as the Fe-Nb, the Fe-W system has been confirmed to form two intermetallic phases, a λ-Fe_2W with a C14 lave phase and a μ-Fe_7W_6 with a $D8_5$ structure [191–193]. Additionally, a bcc solid solution has been stabilized by experimental methods along the compositional range [194–197]. Fe-W has been previously studied from an MD perspective [198–200]. However, these approaches were concentrated on the bcc solid solution only without considering the intermetallic phases. Moreover, a thorough search of the literature finds that there is no MEAM potential for the Fe-W system. In this study, our focus is to accurately replicate the properties of the solid solutions and the confirmed phases. The predicted properties for the intermetallic compounds and the comparison with the literature can be observed in **Table 6.6**.

Table 6.6 Calculated properties of Fe-W intermetallic compounds at 0 K. Lattice parameters *a* and *c* (Å), enthalpy of formation ΔH (eV/atom), elastic constants C_{XX} and bulk modulus *B* (GPa).

	This Work	FP / CALPHAD
Fe_2W - C14		
a	4.75	4.71 [201], 4.71 [193], 4.66 [173], 4.69 [152]
c	7.73	7.66 [201], 7.72 [193], 7.92 [173], 7.59 [152]
ΔH	-0.064	-0.638 [201], -0.032 [193], -0.023 [173], -0.021 [152]
C_{11}	418	483 [201], 506 [193], 494 [80]
C_{12}	203	177 [201], 188 [193], 189 [80]
C_{13}	187	181 [201], 146 [193], 142 [80]
C_{33}	431	476 [201], 428 [193], 416 [80]
C_{44}	83	127 [201], 126 [193], 115 [80]
C_{66}	107	159 [193], 152 [80]
B	268	280 [201], 271 [193], 259 [80]
Fe_7W_6 - $D8_5$		
a	4.75	4.75 [193], 4.77 [173], 4.74 [152]
c	26.38	25.77 [193], 25.93 [173], 25.80 [152]
ΔH	-0.036	-0.026 [193], -0.016 [173], -0.020 [152]
C_{11}	231	433 [193], 469 [80]
C_{12}	124	175 [193], 210 [80]
C_{13}	107	129 [193], 149 [80]

C_{33}	268	434 [193], 483 [80]
C_{44}	63	118 [193], 116 [80]
C_{66}	64	129 [193], 130 [80]
B	156	266 [193], 270 [80]

The fitted potential predicts structural parameters consistent with the references. According to the FP calculations, the C14 structure exhibits a negative formation enthalpy. However, there is a significant deviation of approximately 0.6 eV/atom between the reported values. The fitted potential predicts a negative enthalpy of formation for the C14 structure that is closer to the mainstream values presented in the literature. The enthalpy of formation for the $D8_5$ structure in our calculations is slightly more negative than previously reported in the literature. The predicted elastic constants for the C14 structure exhibit an error of up to 29%, whereas those for the $D8_5$ structure are more inaccurate with an error of up to 50%.

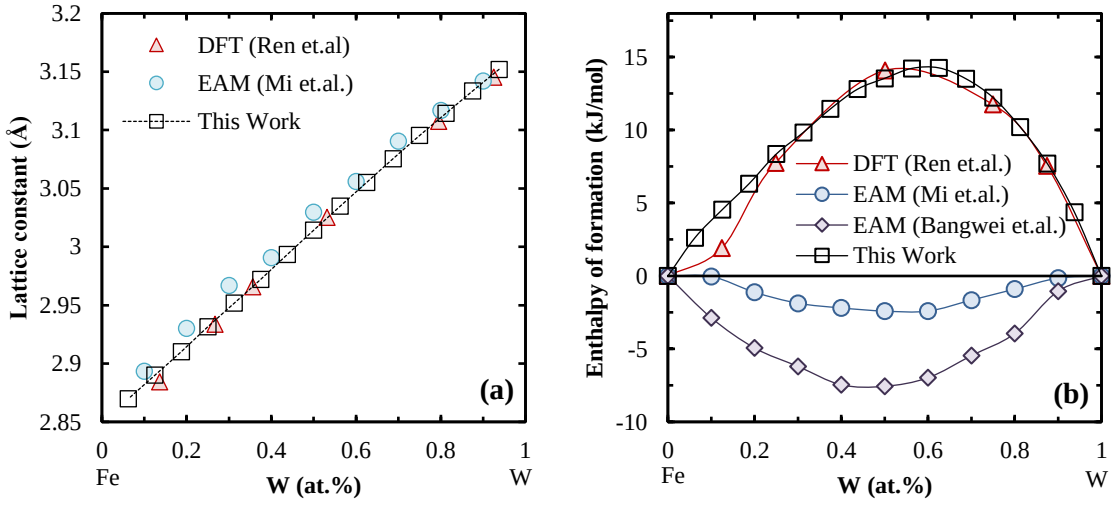

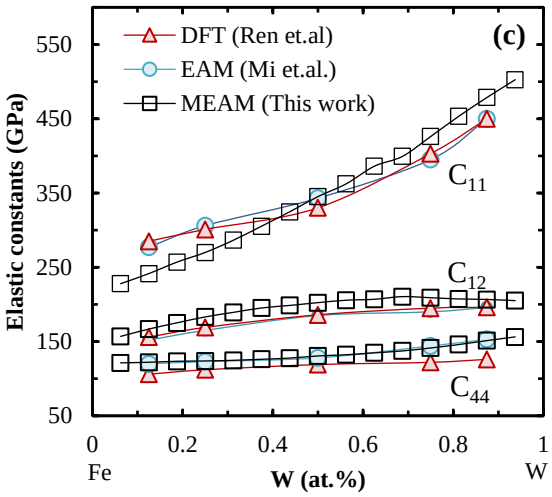

Figure 6.5 **(a)** Lattice constant, **(b)** enthalpy of formation and **(c)** elastic constants for the bcc solid solution in the Fe-W system at 0 K. In comparison with DFT [193] and EAM calculations [198,199]. The reference states are bcc Fe and bcc W.

In **Figure 6.5**, the predicted results for the bcc solid solutions are compared with those reported in the literature. The compositional lattice parameter follows the behavior shown by the references, similar as described by the Vergard's law. Controversially, MD calculations exhibit negative enthalpies of mixing, whereas a thermodynamic assessment predicts a zero enthalpy for the whole composition [202], both contradicting FP computations that denote a positive curve. The present potential predicts a concave hull similar to FP calculations with slightly larger formation enthalpies in the Fe-rich region. The compositional elastic constants follow a trend similar to the references, however, the potential slightly diverges in the compositional ends, especially regarding C_{11} due to the implemented unary potentials.

6.3.5 Calculated Properties of The Co-Nb Binary System

The equilibrium diagram of the system niobium-cobalt presents some controversies regarding the intermetallic phases. There is an agreement that at low temperatures a Co_7Nb_6 μ-phase with a $D8_5$ structure, and a C15 lave phase are stable whereas a metastable Co_7Nb_2 (Zr_2Ni_7-like) and an $L1_2$ structure can be obtained depending on the processing and heat-treatment [186,203–205]. Experimental data on the equilibrium Co-Nb compounds is

limited, leading to a reliance on computational approaches, particularly first principles calculations. In the field of MD, previous studies on the Co-Nb system have primarily focused on the EAM [206]. However, no MEAM potential for the Co-Nb system could be identified in the existing literature.

Table 6.7 Calculated properties of Co-Nb intermetallic compounds at 0 K. Lattice parameters *a* and *c* (Å), enthalpy of formation ΔH (eV/atom), elastic constants C_{XX} and bulk modulus *B* (GPa).

	This Work	FP / CALPHAD	Exp.	Other Calculations
Co_3Nb - $L1_2$				
a	3.63	3.64 [207], 3.63 [208], 3.64 [173]	3.66 [209]	3.60 [206]
ΔH	-0.164	-0.146 [207], -0.166 [208], -0.140 [173], -0.31 [186]	-0.056 to -0.096 [186]	
C_{11}	346	367 [207], 353 [208]		316 [206]
C_{12}	179	171 [207], 166 [208]		198 [206]
C_{44}	108	165 [207], 159 [208]		137 [206]
B	247	236 [207], 228 [208], 237 [80]		
Co_2Nb - C15				
a	6.69	6.77 [210], 6.74 [173]	6.70 [211]	
ΔH	-0.119	-0.29 [210], -0.14 [173], -0.16 [212]	-0.19 [213], -0.06 [186]	
C_{11}	370	349 [210], 353 [80]		
C_{12}	162	162 [210], 170 [80]		
C_{44}	110	130 [210], 126 [80]		
B	231	224 [210], 231 [80]		
Co_7Nb_6 - $D8_5$				
a	4.79	4.89 [214], 4.85 [152], 4.98 [173]	4.92 [215]	
c	25.99	26.09 [214], 26.02 [152], 26.12 [173]	26.28 [215]	
ΔH	-0.098	-0.17 [152], -0.16 [173], -0.11 [212]		
C_{11}	223	369 [214], 353 [80]		
C_{12}	130	156 [214], 143 [80]		
C_{13}	98	146 [214], 135 [80]		
C_{33}	226	369 [214], 385 [80]		
C_{44}	51	79 [214], 76 [80]		
C_{66}	58	106 [214], 105 [80]		
B	256	222 [214], 213 [80]		

The properties of the Co-Nb compounds have been calculated with the fitted potential and compared the results with existing literature in **Table 6.7**. The computed lattices and enthalpy of formation for the $L1_2$, C15 and $D8_5$ structures closely reproduce the literature data. The elastic constants for the studied structures present a maximum deviation of ~30% and ~12% compared with FP calculations for the $L1_2$ and C15 structures, respectively. Nonetheless, the predicted bulk moduli are in close agreement with the references, and the error does not exceed 5%. As observed with the potentials for the Fe-Nb and Fe-W systems, the $D8_5$ elastic constants for the Co-Nb system are underestimated with a maximum error of ~44%. Nonetheless, the correct hierarchy between the elastic constants is maintained for all the structures including the $D8_5$ structure where $C_{33}>C_{11}>C_{12}>C_{13}>C_{66}>C_{44}$.

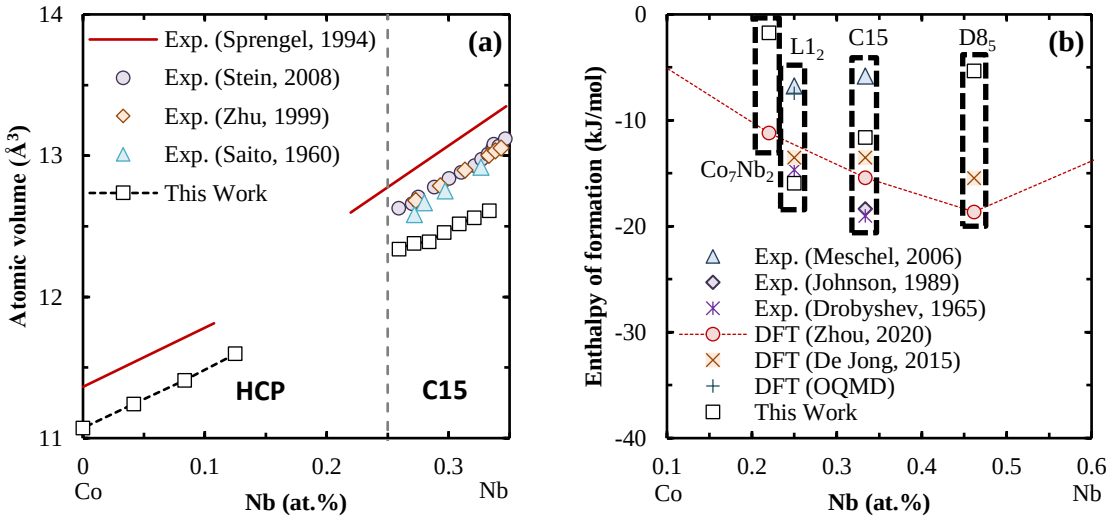

Figure 6.6 **(a)** Atomic volume for the Co-rich hcp and the C15-based solid solutions in the Co-Nb system and **(b)** enthalpy of formation for the experimentally confirmed Co-Nb compounds at 298 K. In comparison with experiments [186,204,213,216–219] and DFT calculations [152,173,212].

A comparison between the available literature and our calculations for the atomic volume of solid solutions and the enthalpy of formation of stable compounds at 298 K is depicted in **Figure 6.6**. In the Co-Nb system, the near Co compositions show a Co(Nb) solid solution based on the hcp structure. Moreover, the C15 homogeneity range is extended from a minimum Nb of ~26% to a maximum of ~35%. Thus, the atomic volumes were calculated for the solutions based on these structures at 298 K. The estimated atomic volumes are slightly lower (with a deviation of ~2.3%) than experimental data. This is expected as the

MD simulation assumes a perfect atomic composition without any impurities. Nonetheless, the volumes denote a correct growth rate compared to the experiments. The stability of the main compounds at this temperature was also tested and compared with the references. For the $L1_2$ and C15 structures the enthalpies are close to the references. However, the Co_7Nb_2 and $D8_5$ structures indicate a higher but still negative enthalpy.

6.4 Conclusions

In this study, we developed 2NN MEAM interatomic potentials for the Fe-Al, Fe-Cu, Fe-Nb, Fe-W, and Co-Nb systems. Structural, energetical, and elastic properties for the thermodynamically stable compounds and solid solutions are closely reproduced by these potentials, as demonstrated by their comparison with theoretical calculations and experimental data. The formulated Fe-Al and Fe-Cu potentials stand out for their ability to predict essential properties across the considered compounds and solid solutions. This distinction becomes more apparent when compared to other interatomic potentials that have been tailored for specific applications, encompassing studies of different crystal structures and phase transformations, among other objectives. In relation to the Fe-Nb system, even though another MEAM potential is available, this study presents a pioneer exploration from MD perspective into the elastic properties of the stable structures while concurrently considering the attributes of solid and liquid solutions. For the Fe-W and Co-W systems, this work serves as a first MEAM approach into comprehending the characteristics of stable compounds and solid solutions. The universality of the developed interatomic potentials allows further combinations with other binary potentials to describe FeCo-based systems as well as other alloys.

Chapter 7

Atomistic Investigation of Effect of Alloying on Mechanical Properties and Microstructural Evolution of Ternary FeCo-X (X = V, Nb, Mo, W)

This study delves into the impact of V, Nb, Mo, and W on the mechanical properties of equiatomic FeCo, employing the modified embedded atom method (MEAM). Analysis of individual effects on antiphase boundary (APB) energies reveals a consistent reduction along preferred slip planes, except for Nb. Monte Carlo-molecular dynamics (MC-MD) simulations were used to explore the diffusion behavior of these solutes, highlighting their dynamic interactions and preference to migrate into the grain boundaries (GB).

Tensile simulations on nanocrystalline (NC) models unveil comparable stress-strain curves, with V and Mo displaying continuous yielding. Nb and W exhibit a more humped yield curve, surpassing the ultimate tensile strength (UTS) of the binary FeCo alloy but at lower breakage strains. Microcrack nucleation patterns differ, occurring at GB triple junctions for binary FeCo and at the intersection of a slip band and a GB for V and W alloys, with limited propagation in both cases. In contrast, Nb and Mo additions show enhanced stress accommodation through slip band formation within grains, preventing microcrack development.

**This section is published substantially in Computational Materials Science, 2024. https://doi.org/10.1016/j.commatsci.2024.113030. Reprint with permission.

7.1 Introduction

The addition of elements like V, Nb, Mo and W has been found effective to improve the cold workability of FeCo alloys when combined with suitable heat treatment [3,24,28]. Among these additions, Nb and V have been found to limit the maximum degree of ordering within the alloy and to even provide a positive impact on the magnetic properties of the alloy. Several hypotheses have been proposed regarding the improved cold workability in FeCo-X alloys, including the retardation of the ordering process [26,220], the formation of strong vacancy-solute interactions due to a higher concentration of vacancies [221–223], the formation of ordered Co_3X clusters [2,24], and segregation of solutes to the common slip directions or antiphase boundaries (APB) [2,37,121].

This study aims to further explore the effects of V, Nb, Mo and W based on their documented improvement of the ductility of FeCo alloys [8–11]. Consequently, this investigation involves characterizing FeCo-X (X = V, Nb, Mo, W) alloys using interatomic potentials under the modified embedded atom method (MEAM). Interatomic potentials are available for the unary Co [76], Fe [41], V [41], Nb [41], Mo [224] and W [41] systems as well for the binary Co-Fe [52], Co-V [97], Co-Nb [225], Co-Mo [226], Co-W [124], Fe-V [104], Fe-Nb [130] and Fe-Mo [226]. The sole remaining binary interaction to elucidate is the Fe-W system. However, it is worth noting that the Fe interatomic potential adopted in this chapter is a recently developed potential enhanced for stability and mechanical description [41]. In the case of the previously adopted Fe potential [98] utilized in **Chapter 5**, challenges with stability arose when integrating this potential to describe certain ternary interactions. It was noticed that this happened when combining the Fe-Co potential, with potentials of elements displaying a larger radii than the FeCo constituents and a strong inclination to favor other ground state configurations. Thus, it is theorized that these additions possibly introduced high pressure and stress regions within the very robust FeCo microstructure, as described by the Fe-Co potential. This compromise may have resulted in a trade-off where the qualities that improved its mechanical description in binary state also compromised its miscibility capabilities. For example, an interatomic potential for Fe-W [225] was introduced in **Chapter 6**. Although, when merged to describe the Fe-Co-W interactions, structural instability was observed. This issue may stem from the strong

stability of the B2 structure by the FeCo potential, which contrasts with the tendency of the Fe-W potential to favor other structures due to its notably high enthalpy of formation associated with the bcc phase. Therefore, the outstanding task involves the development of a new Fe-W interatomic potential with the updated and more neutral Fe potential. The adopted Co-Fe [52] potential was further enhanced for a better mechanical description but maintaining the essential structural and elastic properties. Ternary interactions are lastly fitted to improve the energetical descriptions of solutes in FeCo APBs. After which, the impact of the ternary elements is measured on the stacking faults (SF) and the GB energies. Subsequently, MD combined with Monte Carlo (MC) simulations are employed to examine the diffusion of alloying elements in nanocrystalline (NC) FeCo systems. Furthermore, MD straining simulations are utilized to explore the evolution of the microstructure during deformation under high-rate deformation conditions representative of MD simulations. The findings are comprehensively compared and discussed in subsequent sections.

7.2 Interatomic Potentials

To establish a foundation for this computational approach, a description of the unary systems is first established using semi-empirical interatomic potentials, upon which subsequent binary and ternary interactions are built. A comprehensive understanding of the 2NN MEAM theory can be found in the literature [41,59,60,67] and has been discussed previously in **Chapter 3**.

7.2.1 Co-Fe Binary Potential

A Co-Fe potential with improved mechanical capabilities is available in the literature [52]. The potential represents an enhancement of a prior Co-Fe potential [49], specifically tailored for improved stability of the bcc-based microstructure. The potential was built on widely used unary potentials thus allowing to easily combine with a plethora of intermetallic potentials. However, this potential predicts low APB energies of ~70 mJ/m^2 for the known preferred slip planes for the FeCo system, namely the {110} and {112}

planes in the <111> slip direction. Whereas experimental data and FP calculations have found these energies to be in the 120-169 mJ/m^2 range [10,11,37–39].

In this work, the potential was further improved to closely reproduce the APB energies as described by the literature. Two screening parameters with a lesser impact on the properties of the bcc structure where modified, namely the C_{max} (*Co-Co-Fe*) and C_{max} (*Co-Fe-Fe*). Expanding the reach of these parameters from 2 Å to 2.73 Å proved sufficient to achieve reasonable APB energies. The predicted properties for the B2 structure after this improvement are shown in **Table 7.1**. The energy of the APB associated with a <111>/2 shift vector on a {110} plane has been found to be approximately 15% less than that of a {112} plane [149], which is reflected in the predictions. On the other hand, the modifications slightly increased the formation energy of the solid solution from ~-8 kJ/mol to ~-7 kJ/mol. Nevertheless, the structural and elastic properties of the B2 structure are predicted as described by the original potential [52].

Table 7.1 Analysis of physical properties for ground state B2 FeCo using the current 2NN MEAM potential and references. The cohesive energy E_c (eV), the lattice parameter a (Å), the elastic constants C_{11}, C_{12}, C_{44} and the bulk modulus B (GPa). The enthalpy of formation ΔH (kJ/mol), APB energies (mJ/m^2) and the formation energies (eV) for anti-site atoms (E_{Fe}^{β}, E_{Co}^{α}) and vacancies (E_v^{α}, E_v^{β}).

	This Work	Exp.	FP	MD/MC
a	2.855	2.857 [79]	2.843 [32,80], 2.840 [81], 2.862 [38]	2.840 [121], 2.839 [49] , 2.826 [47]
C_{11}	237		259 [80], 263 [81], 195 [38]	232 [121], 226 [49] , 231 [47]
C_{12}	206		154 [80], 152 [81], 137 [38]	167 [121], 168 [49] , 179 [47]
C_{44}	150		130 [80], 108 [81], 123 [38]	144 [121], 136 [49] , 138 [47]
B	217	165 [79]	189 [80,81], 196 [32]	189 [121], 196 [47]
ΔH	-10.93		-8.30 [16], -12.51 [77]	-11.04 [121], -9.79 [49], -11.61 [16]
$\gamma_{APB}^{(110)}$	131	120-160 [10,227]	129 [11], 126 [39], 126 [38]	141 [121], 128 [37], 127 [47]
$\gamma_{APB}^{(112)}$	151		169 [11], 168 [39], 157 [38]	176 [121], 159 [37], 140 [47]
E_{Fe}^{β}	0.14		0.7 [32], 0.17 [11]	0.14 [121], 0.25 [47]
E_{Co}^{α}	0.25		0.7 [32], 0.17 [11]	0.23 [121], 0.25 [47]
E_v^{α}	1.61	1.15 [34]	1.65 [32], 1.78 [11], 1.41 [38]	1.95 [121], 1.65 [47]
E_v^{β}	1.77	1.15 [34]	1.75 [32], 1.78 [11], 166 [38]	2.05 [121], 1.65 [47]

7.2.2 Fe-W Binary Potential

The Fe-W phase diagram at low temperatures is mainly dominated by a bcc solid solution, showing only two compositional intermetallic phases, a λ-Fe_2W with a C14 lave phase and a μ-Fe_7W_6 with a $D8_5$ structure [191–193]. Recently, a study employed the MEAM to explore the properties of these compounds for the first time within the MD framework [225]. However, the interatomic potential relies on distinct unary potentials, rendering it incompatible with the set of potentials currently adopted for this research.
In this study, our focus remains on the bcc solid solutions and the properties associated with the C14 structure. The energetics of the B2 phase are considered to evaluate the stability of the solid solution. The intricacies of the $D8_5$ compound have been excluded from our analysis due to its predominant stabilization through magnetism, an aspect not considered in the context of MD [130]. To construct the interatomic potential, we have employed the $L1_2$ structure as a reference point, while all other relevant parameters have been meticulously calibrated to replicate the physical properties exhibited by the compounds and solutions. A comprehensive overview of the predicted properties concerning the intermetallic compounds is available in **Table 7.2**. The optimized MEAM parameters tailored for the Fe-W system are presented in **Table 7.3**.

Table 7.2 Calculated properties of Fe-W intermetallic compounds at 0 K. Lattice parameters *a* and *c* (Å), enthalpy of formation ΔH (kJ/mol), elastic constants C_{XX} and bulk modulus *B* (GPa).

	This Work	Exp.	FP / CALPHAD	MD
Fe_2W - C14				
a	4.77	4.73 [191]	4.71 [201], 4.71 [193], 4.66 [173], 4.69 [152]	4.75 [225]
c	7.76	7.70 [191]	7.66 [201], 7.72 [193], 7.92 [173], 7.59 [152]	7.73 [225]
ΔH	-14.53		-61.56 [201], -3.08 [193], -2.21 [173], -2.02 [152]	-6.17 [225], -13.27 [198]
C_{11}	360		483 [201], 506 [193], 494 [80]	418 [225]
C_{12}	171		177 [201], 188 [193], 189 [80]	203 [225]
C_{13}	165		181 [201], 146 [193], 142 [80]	187 [225]
C_{33}	367		476 [201], 428 [193], 416 [80]	431 [225]
C_{44}	85		127 [201], 126 [193], 115 [80]	83 [225]
C_{66}	94		159 [193], 152 [80]	107 [225]

B	232	280 [201], 271 [193], 259 [80]	268 [225]
FeW - B2			
a	2.993	2.985 [193]	3.005 [198]
ΔH	17.58	18 [193]	18.33 [198]

Table 7.3 Optimized parameters for the Fe-W system. E_c is expressed in eV, while r_e and C_{min}/C_{max} are presented in Å. All other parameters are unitless.

Ec	r_e	α	C_{min} *(A-B-A)*	C_{min} *(B-A-B)*	C_{min} *(A-A-B)*	C_{min} *(A-B-B)*	C_{max} *(A-B-A)*	C_{max} *(B-A-B)*	C_{max} *(A-A-B)*	C_{max} *(A-B-B)*	*d+*	*d-*	ρ_0^A: ρ_0^B
-5.20	2.61	5.3	1.20	0.75	0.42	0.42	2.80	2.80	2.80	2.80	0.05	0.05	1:1

The properties of the λ-Fe_2W phase, characterized by the C14 structure, were initially investigated using an interatomic potential. The obtained lattice constants closely align with values reported in the literature, suggesting a *c/a* ratio of 1.626. This closely matches the experimentally measured ratio of 1.627, and falls within the range of FP values, approximately ranging from 1.618 to 1.699.

Consensus exists in the literature regarding the negative enthalpy of formation for the C14 structure. However, notable discrepancies emerge in FP calculations, exhibiting a wild variation of ~60 kJ/mol among the reported values. These variations may stem from differences in methodology and the consideration of ferromagnetism. Nonetheless, our predicted formation energy comfortably falls within this range, demonstrating similarities to estimates derived from a potential developed under the Embedded Atom Method (EAM) [198]. Deviations are observed for the elastic constants, consistently falling below the values presented in the references. The maximum error observed for these parameters is 38%.

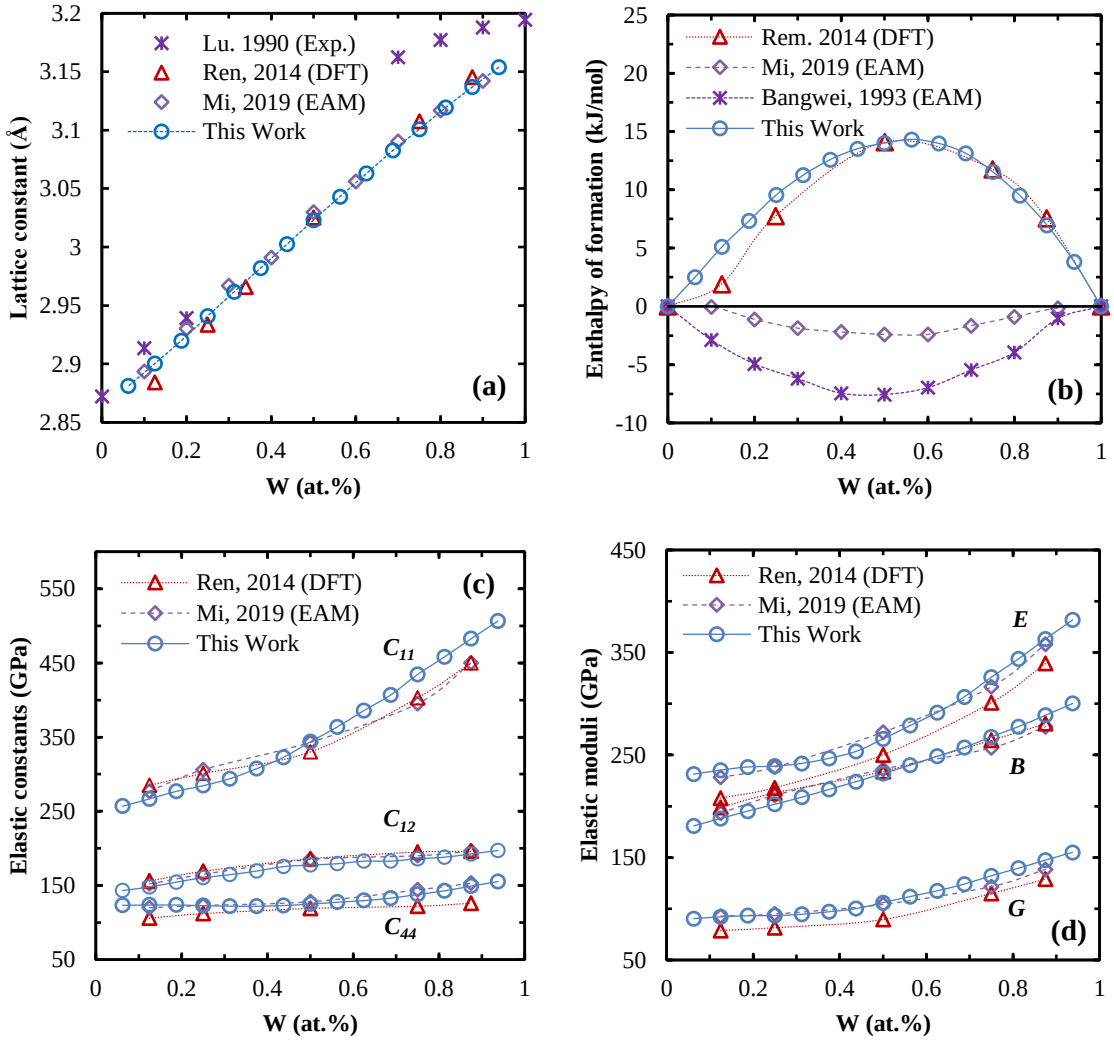

Figure 7.1 **(a)** Lattice constant, **(b)** enthalpy of formation, **(c)** elastic constants and **(d)** elastic moduli for the bcc solid solution in the Fe-W system at 0 K. In comparison with experimental data [228], DFT [193] and EAM calculations [198,199]. The reference states are bcc Fe and bcc W.

In **Figure 7.1**, the calculated properties of the bcc solid solutions are presented. First, the structural behavior across the compositional range was calculated. Notably, experimental values exhibit a substantial deviation from Vergard's law on the W-rich side, in contrast to the predictions derived from FP results. In this study, the lattice parameters are closely aligned with theoretical calculations, demonstrating a growth rate of approximately 0.31 Å/W at.%. The enthalpy of mixing has been assessed using the Miedema model, yielding an approximate value of 0 kJ/mol for the entire compositional range [202], whereas MD computations display a negative convex hull. In this work the enthalpy of mixing exhibits

a positive concave hull, in line with FP calculations. However, due to magnetic effects, the curve described by FP calculations present lower values for $Fe_xW_{(1-x)}$ compositions with x exceeding 0.75, which is not entirely replicated by the present potential. Furthermore, we explored the elastic constants and elastic moduli for the solid solutions, observing a generally good agreement in the overall behavior of the curves, particularly near the equiatomic composition. In this context, a maximum deviation of 19% was observed compared to FP calculations.

7.2.3 Interatomic Potentials

Ternary interatomic potentials for the Fe-Co-V and Fe-Co-Mo are available in the literature [52]. However, the Fe-Co-W and Fe-Co-Nb potentials have not been developed yet. Similar as with the existing ternary potentials, a concept of averaging is initially employed to combine the remaining binary parameters [229]. Considering the elements *A*, *B* and *C*, the interaction between atoms of *A* and *B* screening an atom of a *C* [$C_{min/max}$ (*A*-*C*-*B*)] can be approximated as the average of the *A*-*A* screening *C* [$C_{min/max}$ (*A*-*C*-*A*)] and *B*-*B* screening *C* [$C_{min/max}$ (*B*-*C*-*B*)]. This would translate the $C_{min/max}$(*A*-*C*-*B*) into the form $[0.5(C_{min/max}{}^{A\text{-}C\text{-}A})^{1/2} + 0.5(C_{min/max}{}^{B\text{-}C\text{-}B})^{1/2}]^2$. This is calculated for the C_{min} and C_{max} over the (*A*-*B*-*C*), (*B*-*A*-*C*) and (*A*-*C*-*B*) directions to completely describe the ternary system. Additionally, further optimization was undertaken to enhance the prediction of energy changes resulting from the presence of solutes in the APB. The screening directions with a substantial impact on the {110} and {112} planes were modified depending on the alloy. The resulting parameters are listed in **Table 7.4**.

Table 7.4 Sets of 2NN MEAM parameters for the ternary systems. The screening parameters C_{min}/C_{max} are given in Å.

Screening direction	Co-Fe-V	Co-Fe-Nb	Co-Fe-Mo	Co-Fe-W
C_{min} (*A*-*C*-*B*)	0.40	0.66	0.42	0.99
C_{min} (*A*-*B*-*C*)	1.10*	0.42	0.82*	0.61
C_{min} (*B*-*A*-*C*)	0.99	0.75*	0.85	0.20*
C_{max} (*A*-*C*-*B*)	2.80	2.54	2.59	2.80
C_{max} (*A*-*B*-*C*)	2.80*	2.06	2.80*	2.06

C_{max} (*B-A-C*)	2.38	2.80*	2.38	2.80*

* Fitted parameters

7.3 Effect of Solutes on the APBs, SFs and GBs

The behavior of FeCo alloys under deformation is strongly influenced by the presence of APBs. These play a pivotal role in dictating the alloy mechanical properties, with their energy levels serving as a critical parameter. The APB energy defines the separation distance between *a*/2<111> dislocations. Low APB energies allow wide separations of dislocations, permitting each to independently engage in cross-slip. Conversely, high APB energies hinders the separation of partial dislocations, causing them to remain coupled, which facilitates their collective cross-slip. However, FeCo APB energies fall in between these energy states. This restricts dislocations to intermediate separations, where partial dislocations necessitate higher energies to cross-slip and thus are constrained to slipping along their original slip plane [230]. Hence, it is anticipated that the addition of alloying elements, which lower the APB energies, will promote smoother dislocation movement and, consequently, enhance the ductility of the alloy. Prior research has demonstrated that incorporating V, Nb, W and Mo in low contents enhances the ductility of FeCo alloys [8–11]. These additions have proven effective in reducing the degree of long-range order (LRO). Moreover, recent studies utilizing ab initio calculations have further demonstrated their ability to decrease the energy associated with APBs [37,38].

In this work, APB energies are determined by assessing the disparities in energy levels between the initial state of the system and the state that emerges after the formation of an APB. Using the same methodology, we also computed the generalized stacking fault energy (GSFE) curves, varying the distances relative to the Burgers vector. From here the impact of solutes on three important energy values were drawn: the unstable stacking fault energy (γ_{usf}), which measures the energy required for temporary lattice defects that can lead to deformation; the intrinsic stacking fault energy (γ_{isf}), which is in fact the APB energy in FeCo alloys due to the A2/B2 structure configuration in the studied slip systems [48,114]; and the unstable twin fault energy (γ_{utf}), quantifying the energy needed for twin defects in the lattice.

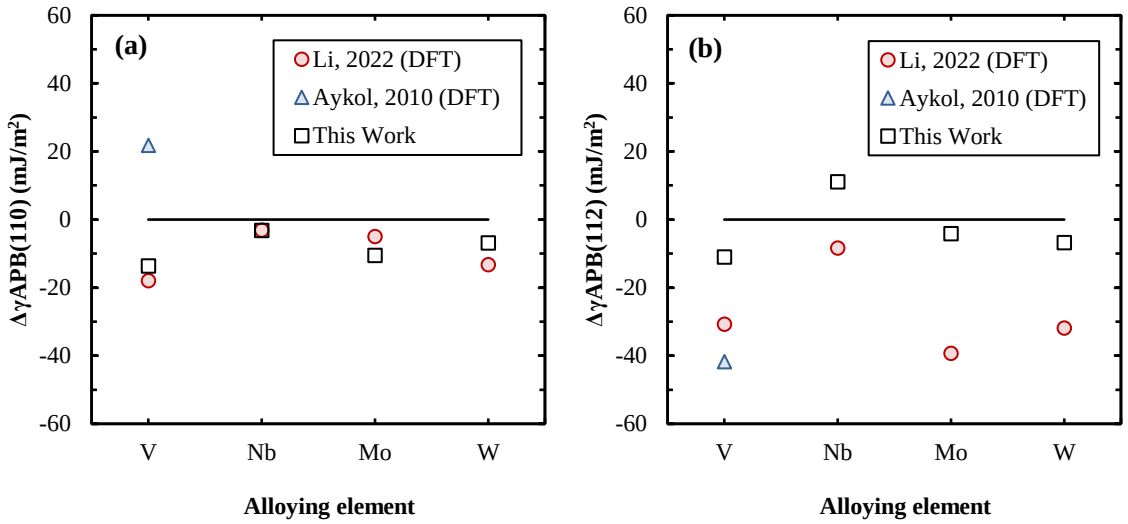

Figure 7.2 Variation in FeCo {110} **(a)** and {112} **(b)** APB energies in the <111> slip direction due to 4 at.% solute additions. In comparison with FP calculations [37,38].

The predicted APB energies for FeCo, at 131 mJ/m² for the <111> {110} and 151 mJ/m² for the <111> {112} slip systems, comfortably align with the moderate energy range typically observed in the literature, falling within the bracket of 120-169 mJ/m² [2,10,11,37]. The impact of V, Nb, W and Mo in the APBs is evaluated at 4 at.% for a proper comparison with the literature. The energy difference between the APB containing the solutes and the binary FeCo ($\Delta\gamma APB = \gamma APB_{FeCo\text{-}X} - \gamma APB_{FeCo}$) can be observed in **Figure 7.2**. It was observed that these transition metals reduce the APB energies on the {110} planes, consistent with recent FP calculations by Li et al. [38]. The energetical impact of these solutes have the relations: V > Mo > W > Nb, meaning that V is the most effective solute to reduce the {110} APB energy. However, it is worth noting that in the case of V, Aykol et al. [37] predicted an increase on the {110} APB energy, contradicting Li et al. [38] results. For the {112} APB energies, a reduction is observed for V, W and Mo additions but with a lower magnitude as shown by FP calculations. FP calculations decrease the energies on the {112} APB following the order of Mo > W > V > Nb whereas the present MD calculations predicts V > W > Mo. Despite our efforts fitting the ternary potential, Nb exhibited an unexpected increase in the predicted {112} APB energy. The data reveals that V exerts the most substantial influence in lowering APB energies, while Nb appears to be the least effective.

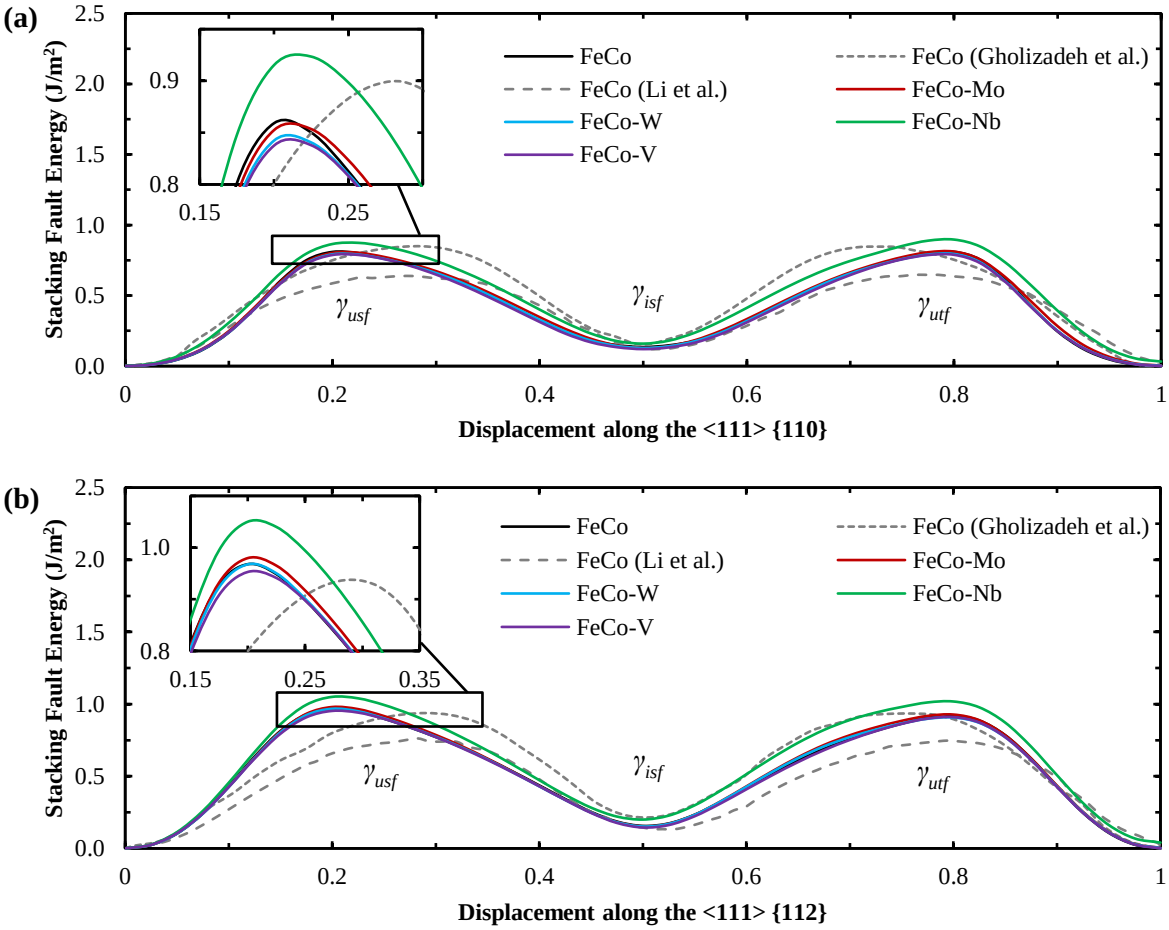

Figure 7.3 GSFE curves for FeCo in the {110} **(a)** and {112} **(b)** in the <111> slip direction due to 4 at.% solute additions. In comparison with FP and MD calculations [37,38].

The GSFE curves for the binary FeCo alloy in the <111> {110} and <111> {112} slip systems is depicted in **Figure 7.3**. The curves align with those predicted in existing literature [48,114], presenting higher accuracy near the γ_{isf}. In the region surrounding the γ_{isf}, introducing solutes into the alloy displayed marginal changes to the curve of the original alloy. These changes were shown previously in **Figure 7.2**, since γ_{isf} is equivalent to the $\Delta\gamma_{APB}$ in these slip systems. Differences for γ_{usf} are evident signified by a shifting in the displacement distance between the peaks; our interatomic potential shows a peak at ~0.2, while FP calculations place it at ~0.3 along the Burgers vector direction. For the γ_{utf}, FP calculations shows its maximum ~0.75 whereas MD calculations, including ours, predict the peak to appear ~0.8. These variations may stem from the stronger Fe-Fe interaction established by the low screening range in the 2NN MEAM parameters for this

interaction. From the perspective of γ_{usf}, as highlighted in **Figure 7.3**, introducing solutes in the <111> {110} plane reveals an energy sequence of Nb > FeCo > Mo > W > V, while in the <111> {112} plane, the order is Nb > Mo > FeCo > W > V compared to pure FeCo. Interestingly, Nb highly increases these energies, denoting a higher resistance to plastic deformation. The introduction of V and W suggests a marginally decrease in the energy needed for unstable stacking faults to develop within the alloy. This reduction in γ_{usf} might promote the movement and slipping of dislocations in the crystal lattice, potentially enhancing the plasticity and ductility of the material.

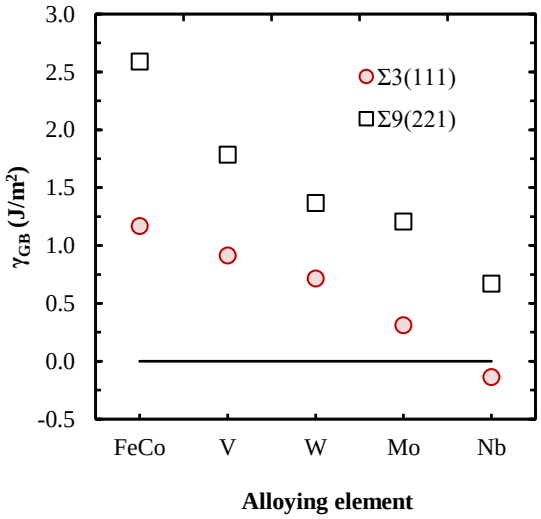

Figure 7.4 Calculated energies for the Σ3(111) and Σ9(221) GBs types as a function of the solute additions.

The Σ3 and Σ9 GB types, observed experimentally in FeCo alloys, represent a substantial portion of grain boundaries, comprising around 60% and 10%, respectively, based on misorientation distributions below the ODT [112,113]. The effect of disordering on these was already explored in this study in **Section 5.4.1**. In this section, the effect of solutes on the energies of the symmetric tilted Σ3(111) and Σ9(221) types of GBs were calculated. Interestingly, the solutes tend to lower the GB energies (γ_{GB}) following similar trends as observed with the APBs and SFEs. Elevated γ_{GB} are known to act as barriers to dislocation motion, consequently diminishing ductility and fracture resilience. Thus, the introduction of these solutes, which lower these energies, could potentially enhance the mechanical

response of FeCo by allowing better dislocation motion. Purely from the perspective of γ_{GB}, Mo should be more beneficial imparting ductility, followed by W and V. Interestingly, Nb displays a negative energy for the Σ3 GB type, indicating that the grain boundary is energetically unfavorable and unlikely to form. This is reflected in the following section where Nb shows a lower segregation to GBs than the other alloys.

7.4 Diffusion

This study investigates the individual preferred arrangement of V, Nb, W and Mo at 2 at.% within a FeCo NC model using MD-MC simulations. This approach accelerates the diffusion behavior, enabling the observation of solute drag effects within MD timescales. Here, the system achieves thermodynamic equilibrium periodically via MD, while stochastic atomic swap trials based on the interchange energies of atomic pairs are performed following the MC method. To enhance computational efficiency, opting for larger exchange attempts proves advantageous, without compromising the integrity of the sampling process, as long as the total number of MD/MC cycles remains sufficiently high [57]. In this study, the acceptance ratio of MC swaps was leveraged to enhance computational efficiency. This involved conducting preliminary simulations with varying MC swaps and MD times. We sought an initial acceptance ratio that facilitated the attainment of a nearly static final state with a low exchange rate at the end of the simulation time, ensuring both meaningful insights and computational feasibility. Due to the large size of the system with 300 Å per side (~2.4×10^6 atoms), 10,000 MC site exchanges were attempted every 10 timestep during 5.5 ns, with a timestep of 1 fs. The simulation took place under isothermal-isobaric conditions, maintaining a temperature of 300 K and zero pressure.

The solute atoms were initially distributed randomly within the FeCo system, constituting a replacement of 2 at.% of the total atoms while preserving the equiatomic distribution of Fe and Co atoms. Due to the random distribution, approximately 0.17 at.% of the solute atoms were initially located at the grain boundaries (GB). Upon conducting MD-MC simulations, a clear trend emerged: the solute atoms remaining in the grains displayed a preference for exchanging places with atoms located at the GBs. Known for their weaker

atomic bonds compared to the grains, GBs naturally attract alloying elements. The solute migration to the GBs can be observed in **Figure 7. 5**. Notably, V atoms exhibited the fastest diffusion, reaching a concentration of approximately 1.7 at.% out of the introduced 2 at.% in the NC model. Slightly lower concentrations were observed for W and Mo reaching ~1.64 and 1.53 at.%, respectively. In contrast, Nb displayed high stability within the ordered FeCo sublattices, diffusing at a much slower rate and concentrating at approximately ~0.30 at.% in the GBs from the initial ~0.16 at.% randomly placed in the GBs. Most of the remaining solute atoms in the grains preferred to stay in their initial site. The migration of V, Nb, Mo, and W atoms to the GBs indicates a preference for swapping sites with Fe atoms, followed to a lesser extent by Co, depending on the specific alloy. This preference to occupy the Fe sublattice has been observed experimentally with V additions [31]. In terms of diffusion ratio, solute atoms swapping with Fe follow the preference of V > Mo > W > Nb, while the sequence with Co atoms is Mo > V > W > Nb.

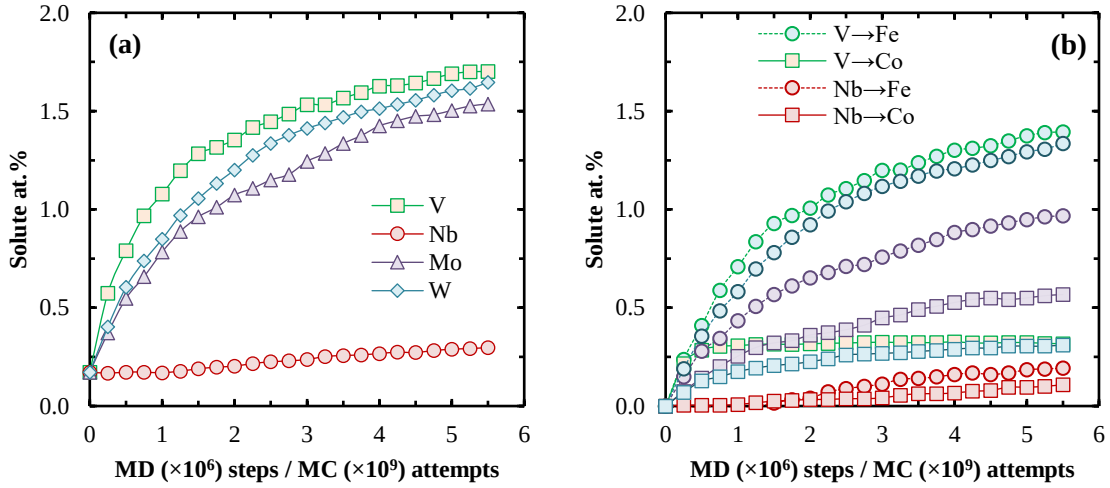

Figure 7.5 **(a)** Migration of solute atoms to the GBs under the MD-MC scheme. **(b)** Evolution of the exchange of solute atoms with Fe and Co atoms in the GBs. The MD steps and MC swap attempts throughout the diffusion process are accompanied by their respective multipliers.

The discussed elemental additives have proven experimentally to enhance the ductility and workability of near equiatomic FeCo alloys. This enhancement is characterized by the common trait of forming $L1_2$-Co3X precipitates, identified as the γ2 phase [24]. The ductility of the alloy is believed to increase due to disordered regions surrounding the γ2 precipitates [2,14,24,231]. In this scenario, the preference for atomic swapping with Fe

atoms indicates the potential formation of Co-rich compounds. As Fe and Co atoms exit the GBs, they redistribute within the grains, forming discrete clusters enriched in either Fe or Co. However, structural analysis under the polyhedral template matching (PTM) identified only a few atoms (>100) to be on an $L1_2$ compounds in the NC models. Nevertheless, the models exhibit a slightly higher quantity of atoms in an fcc-based configuration, predominantly $L1_0$. However, this configuration constitutes no more than 0.1% of the total atoms. Upon closer inspection, sporadic structures resembling a rhombohedral symmetry, reminiscent of the laves phases and μ-phase ($D8_5$ structure), were observed in the vicinity of GB in models containing Nb, Mo, and W. Experimental observations of the μ-phase have been documented in FeCo-Nb alloys, particularly those with a high Nb content [232]. This can be rationalized by the inherent formation of these compounds in the composing binary alloys, namely Fe-Nb [178–182], Fe-W [191–193], Fe-Mo [233,234], Co-Nb [186,203–205], Co-W [214,235], and Co-Mo [214,236].

7.5 Straining Simulations

In order to assess the influence of solutes on the mechanical behavior and microstructure of FeCo, the NC models that had been previously equilibrated through MD-MC simulations were subjected to uniaxial tensile straining. The systems were initially equilibrated at room temperature (300 K) using the Nose-Hoover thermostat within the isobaric-isothermal ensemble (NPT). The elevated strain rates inherent in MD simulations can lead to heightened disorder in atomic structures, promoting amorphization and impeding the formation of slip planes [237–239]. In our study, we have employed a relatively low strain rate of 2×10^8 s^{-1}, which is proven to be low enough to avoid amorphization and preserve the integrity of the model. Owing to the periodic conditions, directions perpendicular to the loading direction remained quasi-static, experiencing zero pressure.

Considering the limited size and the number of grains, the nanocrystalline system cannot achieve complete isotropy. Therefore, to assess result variability, straining tests were conducted along the principal directions of the Cartesian plane. This approach has been employed in both experimental and computational studies to evaluate elastic anisotropy in nanocrystalline systems [240–243]. A representation of the model strained along the [001]

axis can be observed in **Figure 7.6**. The stress-strain curves for all the alloys in the [001] direction and the individual response per alloy in different straining directions are presented within the same set of figures.

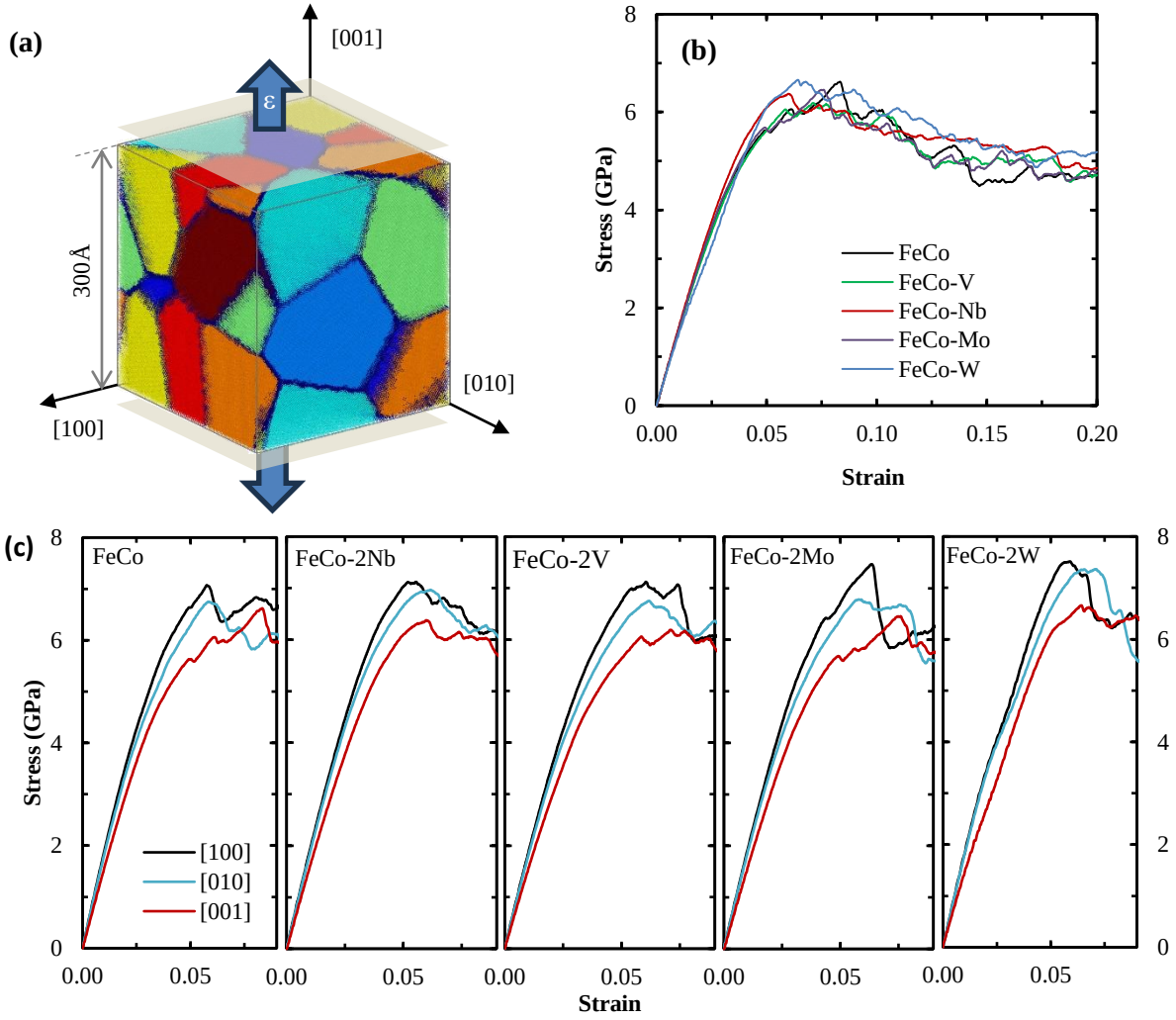

Figure 7.6 **(a)** Representation of the uniaxial straining test over the [001] axis on the NC model and **(b)** the stress-strain behavior of FeCo containing 2 at.% individual additions of V, Nb, Mo, and W over this direction. **(c)** Comparative response per alloy when strained in the [100], [010] and [001] directions.

The stress-strain curves exhibit a consistent pattern: stress builds up in an almost linear manner, followed by continuous yielding without a sudden shift from elastic to plastic deformation. This behavior has been observed in FeCo alloys with ultra-fine grains, with around ~100 nm in size [21,22]. However, differences in the theorized origin and the

subsequent occurrences after the elastic-plastic shifting are evident. The authors of the experimental study attributed the increased plasticity to a partially recrystallized and reordered structure, comprising approximately 70% of the material [22]. Moreover, a grain size of ~15 nm has been identified by a similar study as being within or close to the limits of the Hall-Petch effect without triggering the "inverse Hall-Petch effect" [244]. This choice makes the system more representative and linkable to larger scenarios, enhancing the validity and applicability of the simulation results.

In this study, the NC models feature smaller grain sizes of approximately ~15 nm, anticipating a similar yielding behavior. Additionally, the small size of the models contributes to notable fluctuations in the stress-strain curves, primarily driven by slippage, grain accommodations, and microcracking. After the onset of the yield, a relatively steady strain softening is developed. No significant differences in the stress-strain behavior were observed, regardless of the incorporated solute. It has been theorized that in smaller grain sizes, the stress-strain behavior relies more on GBs, possibly due to the limited extent of the LRO. Considering that the solutes in question have been proven effective in improving the ductility by reducing the LRO [8–11], it is conceivable that the impact of these additions is diminished in MD models due to their smaller size. A comprehensive depiction of the mechanical properties of FeCo, showcasing their variations based on different additions, is illustrated in **Figure 7.7**.

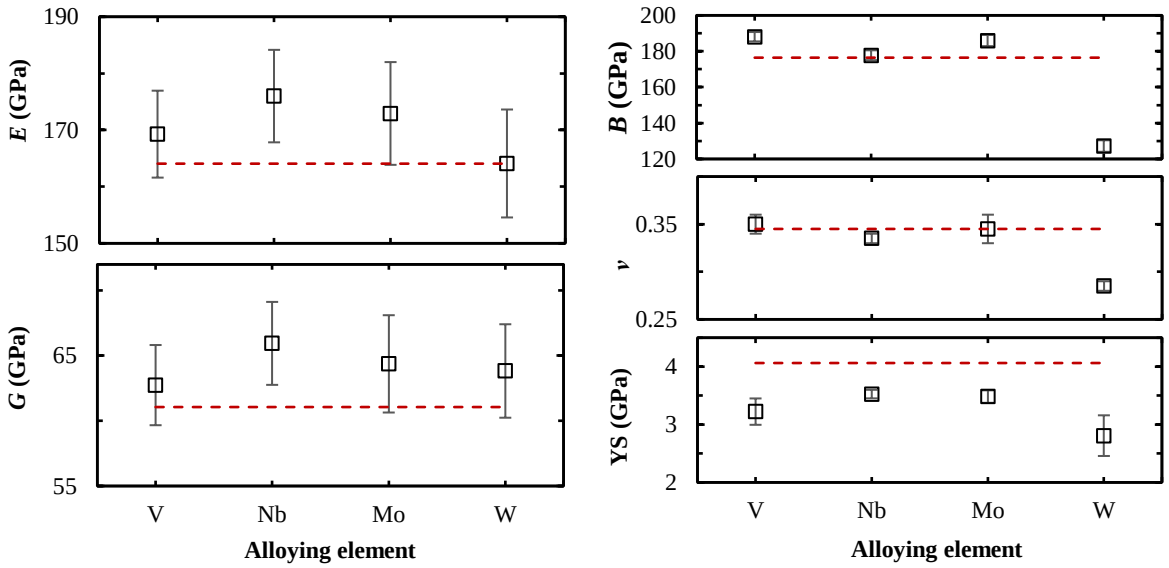

Figure 7.7 Determined averaged values and deviation observed for the elastic moduli: Young's

modulus (*E*), shear modulus (*G*), bulk modulus (*B*), Poisson's ratio (*v*) and yield strength (YS) compared with the averaged values predicted for the binary FeCo shown as a dotted red line.

A direct comparison of the elastic moduli with experimental results is difficult owing to the variability of results by different methods and sample conditions. For example, when V is added in FeCo, different heat treatments may result in an increase or decrease of the different elastic moduli [79,245]. Moreover, while the introduction of V has been extensively explored, investigations into other alloying elements remain limited. The ability of a material to resist elastic tensile deformation is determined by the Young's modulus (*E*). In this work, the predicted value for the binary FeCo alloy is 164 ± 7 GPa, intersecting the range described by experiments ranging from 167 to 197 GPa [79,115]. The addition of W exhibits an almost negligible impact, by slightly reducing the Young's modulus, while the other additions raise this parameter, with Nb showing the larger impact when compared to the binary alloy. Enhanced lateral deformation capability, reflected in a higher Poisson's ratio (*v*), signifies increased material flexibility under stress. The straining tests predict that W reduces lateral deformation, other additions denoted a minor impact yielding values close to the base alloy. Using the *E* and *v* the shear modulus (*G*) was calculated [65]. The results indicate that, within the elastic range, all the additions enhance the shear resistance, and Nb addition is the most effective. Considering the different elastic moduli, it can be inferred that, within the elastic region, W imparts greater ductility compared to the other additions. For the yield strength (YS), we define the YS point at 0.2% residual plastic strain. Our predicted impact on the YS is in partial agreement with experimental observations reported by Kawahara et al. [246], supporting the relationship V < Mo < Nb whereas W showed an even lower YS than V. However, the authors observed significant variability depending on the thermal treatment applied to the alloys, e.g., W exhibits a much lower yield strength when ageing is not applied. In addition, the bulk modulus (*B*) was calculated using the fundamental relationship

$$B = \frac{E}{3(1-2v)} \tag{37}$$

Results for the bulk modulus were incorporated in **Figure 7.7** revealing an increasing resistance to volumetric deformation in the order of Nb, Mo, and V. Conversely, W exhibits a significantly lower *B*, indicating greater stress accommodation in the nanocrystalline

model. Additionally, a comparison of bulk modulus values was conducted using the method proposed by Chonghe Li et al. [247,248], taking advantage of the Miedema model. The method relies in an empirical relationship between the electron density (η_{ws}) and the molar volume (V_{mol}), as shown in its basic expression in **Equation 38**. The authors have extended the same approach to describe binary and ternary alloys by incorporating enthalpies of formation (ΔH) to correct deviations in Vmol.

$$B = \eta_{ws}^2 V_{mol} \tag{38}$$

Taking a simplistic approach, the impact of the additional elements appears to be negligible probably due to their low content, with the calculated *B* for FeCo and its variants hovering ~209 ± 3 GPa. This value in close agreement with the ones calculated for the B2 FeCo in this work (217 GPa) and FP calculations (189-196 GPa) as shown in **Table 7.1**. However, it is important to acknowledge that a more thorough analysis is necessary to fully describe a nanocrystalline system. This includes precise atom counting with their respective enthalpy changes according to various orderings, presence in the grain boundaries (GBs), and secondary structures.

Unlike other MD studies on FeCo [47,121], the present simulations show that the stresses are not exclusively accommodated in the GBs. In the case of the binary FeCo and the alloys containing V and Mo, multiple slip bands emerge, promoting strain hardening until reaching the ultimate tensile strength (UTS). Conversely, the incorporation of Nb and W showcase a more pronounced stress accommodation in the GBs, leading to a delayed development of slip bands. These observations imply that the addition of Nb and W has a more substantial impact in extending the elastic region. The UTS showed variability with the straining orientation, resulting in findings that were not conclusive. However, it is evident from **Figure 7.6** that W consistently exhibited a higher UTS regardless of the orientation. Snapshots of the evolution of the NC models, showcasing sliced regions that encapsulate the most significant events during the deformation are shown in **Figure 7.8**.

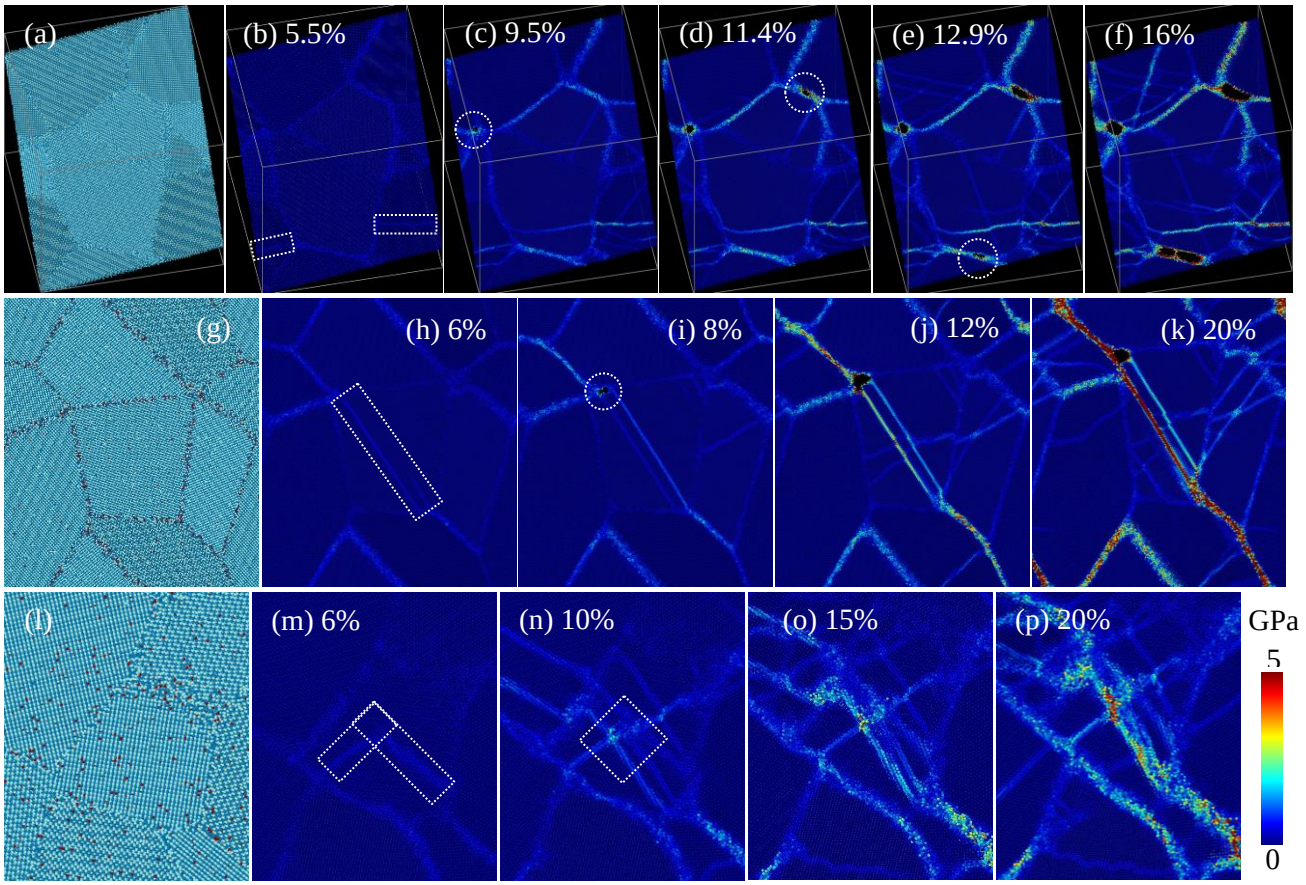

Figure 7.8 Sliced view presenting the relaxed model and the evolution of the straining process at various stages under atomic strain analysis for FeCo **(a-f)**, FeCo-2V **(g-k)**, and FeCo-2Nb **(l-p)**. Fe atoms are depicted in cyan, Co in blue, and V and Nb in dark red for the relaxed models. White squares indicate the initial slip and cross-slip development, while circles mark microcrack nucleation.

As discussed, all NC models exhibited slip bands as the primary cause of yielding during the straining process regardless of the solute introduced. The slip bands mainly developed on the {110} and {112}, typical of bcc and FeCo alloys. After yielding, the alloys exhibited different deformation pathways. In the case of the binary FeCo, multiple slip bands and cross slip appeared before void nucleation, initiated between ~7.6 to ~9.3% strain depending on the strain orientation at GB triple junctions. However, the microcrack exhibited growth confined within the GB region without propagating through the GBs. This led to further development of slippage and nucleation of other microcracks with a similar plastic behavior. Finally, void linkage was observed, contributing to the overall progression of damage within the material.

The addition of the solutes in FeCo is observed to influence the deformation-induced defects. For models with V and W additions, slip bands develop within the grains, eventually intersecting GBs and serving as points of stress concentration. One of these intersections gives rise to stress leading to the nucleation of a single microcrack. The model containing V reached an early microcrack development between ~6.5 to ~8% strain depending on the straining direction. Models with W and Mo displayed void nucleation occurring ~14.3% and ~6.9%, respectively. However, this was observed only in one orientation; no nucleation was observed in the remaining orientations. These microcracks are observed to grow slowly, propagating only to the nearest GB junction. This allows for significant grain accommodation, enhancing the compatibility of plastic deformation.

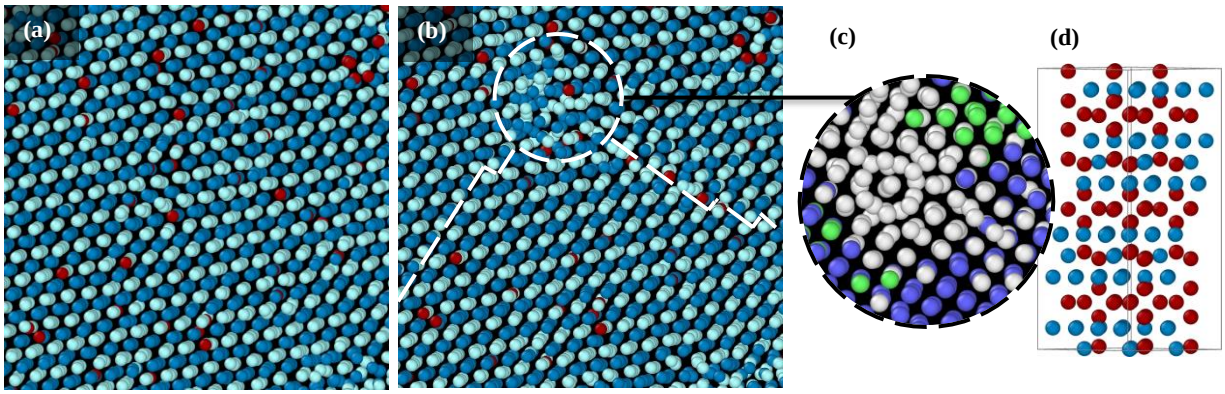

Figure 7.9 Sliced view featuring the FeCo-2Nb alloy at ~4.6% strain **(a)** and at ~6% strain **(b)**, showing slip bands intersecting a compound, highlighted in white lines. **(c)** Observation of the compound under the PTM analysis, showing bcc, fcc and unidentified atoms in blue, green and white respectively. **(d)** Representation of the μ-phase ($D8_5$ structure) as observed in the Co-Nb alloys. Fe atoms are represented in cyan and Co in blue, Nb is presented in dark red.

The NC model containing Nb exhibited an early onset of cross slippage. Interestingly, the higher concentration of Nb in the grains compared to the other alloys promotes scarce fcc-based compounds. One of the grains exhibited a cluster of Nb atoms promoting a small bcc-fcc region as observable in **Figure 7.9**. Under stress, this region transformed into a structure not identified by the PTM analysis. Examination of the compound coordinates uncovered a partial resemblance to a structure with a rhombohedral symmetry, reminiscent of the laves phases and μ-phase similar as observed in the vicinity of GBs of some of the additions, as described in **Section 7.4**. During the deformation process, a slip band

developed, encountering the compound, which acted as a pinning site for further cross slippage within the grain, as observable in **Figure 7.8 (l-p)**. As strain increased, this point served as a focal point for additional stresses, without developing microcracks, while minor slippage occurred in other grains. In total, the straining simulations were run up to 20% strain without reaching complete fracture in the models, similar as observed in FeCo by Li et al. [47]. In contrast, in experimental observations FeCo alloys usually do not exceed more than ~10% strain [3,79,249].

While these results provide insights into the behaviors observed in this study, it is important to note that they are specifically applicable to the nano-scale. At larger scales, complex fracture behaviors exhibited by materials with an ordered internal structure often require a more complex approach for an accurate description [251].

7.6 Conclusions

In this study, we utilized molecular dynamics (MD) simulations to investigate the influence of adding V, Nb, W, and Mo on the mechanical characteristics of the FeCo alloy. Within the framework of the modified embedded atom method (MEAM), we developed an interatomic potential that accurately accounts for the previously missing Fe-W interaction. Simultaneously, a Co-Fe potential was enhanced to accurately reproduce the antiphase boundary (APB) energies. These developments provided the essential potentials required to describe the FeCo-X alloys (X = V, Nb, W, Mo). Solute-influenced variations in the {110} and {112} APB energies were calculated, showing that V and Mo has the most pronounced impact in reducing these energies, respectively. In contrast, Nb showed limited effectiveness in the {110} and increasing the {112} APB energy. The energy levels associated with Σ3 and Σ9 grain boundaries indicate that Mo has a more positive effect on enhancing ductility, followed by W and V. Conversely, Nb exhibits a negative energy for the Σ3 GB type, making it unstable and unlikely to form.

The atomic distributions and analysis of sublattice preferences within a nanocrystalline (NC) system was conducted using a combination of MD and Monte Carlo simulations (MD-MC). Systems with 2 at.% V, W, and Mo predominantly segregated solute atoms to the grain boundaries (GB), while only a small fraction of Nb segregated there. The

swapping preference was primarily with Fe atoms, followed by Co atoms, with varying ratios depending on the specific alloy. Interestingly, models containing Nb, Mo, and W developed structures resembling a rhombohedral symmetry in the vicinity of GB.

The mechanical influence of these solutes was assessed by analyzing stress-strain responses and monitoring the microstructure evolution. Models with and without inclusions developed slip bands demarking the elastic-plastic transition and further showing cross slippage. Models incorporating Nb exhibited notable resistance to void formation, with no observed crack development. In the case of FeCo and the inclusions of V, all the NC models initiated microcracks at different strains whereas additions of Mo and W displayed void development depending on the straining orientation. Regardless of the addition, the developed microcracks grow slowly instead of propagating through the GBs. Overall, it was observed that W imparted a higher ductility by showing a lower Young's and bulk modulus which translated to later development of slip bands and delivering the higher ultimate tensile strength (UTS), however at a lower strains than other alloys probably due to the lower displayed Poisson's ratio and the intrinsic isotropy of the model.

Chapter 8

Conclusions and Recommendations

The concluding chapter offers a comprehensive synthesis of the study's progression throughout the PhD program, providing a clear overview of the methodologies and tools employed to investigate FeCo alloys. The study effectively demonstrates diverse approaches to probing FeCo alloys through molecular dynamics (MD), highlighting distinct physical behaviors influenced by variations in Fe-Co potentials. Utilizing three interatomic potentials, each tailored to excel in specific domains (thermal, mechanical, and solute stability), this study presents a chronological account of atomistic insights obtained from MD simulations and probabilistic modeling using Monte Carlo (MC) methods. The results significantly contribute to an enhanced understanding of the unique mechanical phenomena observed in FeCo alloys within the study's scope. Notably, a substantial focus of the thesis was dedicated to developing binary and ternary potentials, enabling a comprehensive evaluation of the impact of V, Nb, Mo, and W solutes in the FeCo system. These developed potentials are expected to be valuable tools for future investigations into various intermetallic systems.

8.1 Summary

In this research, molecular dynamics (MD) simulations were used to investigate mainly the mechanical behavior of FeCo alloys as well as the effects that ternary alloying elements have on the microstructure and the stress-strain behavior. Among these elements, the effects of V were first assessed since it is the most popular addition in FeCo alloys due to the enhance on the ductility and the magnetic properties. Subsequently, the incorporation of W, Nb and Mo were explored since these have been found to have a positive impact on the mechanical properties of the alloy.

Based on the Modified Embedded Atom Method (MEAM), this study required several interatomic potentials to correctly describe the unary, binary, and ternary intermetallic systems. Interatomic potentials were adopted from the literature when available. It has been found that the behavior of FeCo depends on the interatomic potentials. In the case of the Fe-Co interactions, different potentials were developed according to the needs, resulting in potentials with enhanced thermodynamics (Chapter 4), mechanical behavior (Chapter 5) and structural stability of solutes (Chapter 6). The development of interatomic potentials involved a Multi-Objective Optimization (MOO) process, fine-tuning MEAM parameters to accurately capture Fe-Co interactions and interactions with V, Nb, Mo, and W solutes (Chapter 7). Primarily, MD and Monte Carlo (MC) simulations were performed using the Large-scale Atomic/Molecular Massively Parallel Simulator (LAMMPS). Different simulations including straining and thermal ramping tests were executed under different thermodynamic ensembles to replicate diverse scenarios. Simulations requiring vast computational power were performed on the National Supercomputing Centre (NSCC) servers, specifically ASPIRE1 (now retired) and ASPIRE2.

The evolution and final state of studied systems were characterized graphically and numerically using different software packages. By the combination of these computational tools, we were able to explore different aspects of the FeCo alloys and the impact of V, Nb, Mo, and W solutes on the mechanical properties.

8.2 Conclusions

In this investigation different Fe-Co interatomic potentials were tested, developed and improved. The first improved interatomic potential was initially intended for mechanical applications, but due to limitations of the unary potentials, it presented challenges regarding the stability of the B2 structure. Consequently, during tensile straining tests, the potential led to the deterioration of the bcc-based structure, promoting the formation of fcc and hcp regions. Nonetheless, this interatomic potential presents improved thermal capabilities, reproducing an artefact B2-$L1_0$ phase transformation in the absence of disordering and predicting accurate temperatures for the melting point. The potential was employed to study the order-disorder transformation by introducing vacancies into the FeCo matrix. The bulk containing these vacancies was subjected to relaxation at various temperatures, allowing for the observation of vacancy diffusion and its impact on the long-range order (LRO). The results obtained are to some extent consistent with experimental findings based on the Bragg-Williams ordering parameter. The potential was finally used to stabilize $L1_0$ nanofilms using as a buffer fcc monolayers, reproducing experimental procedures. The energetical behavior of the monolayers closely aligned with predictions from first principles calculations.

The next step involved the comprehensive development of a novel Fe-Co interatomic potential, which was based on unary potentials optimized for mechanical applications. During the fitting process, not only the elastic constants were considered but also the antiphase boundary (APB) energies associated with the preferred slip planes, specifically the {110} and {112} planes. This potential was concurrently developed with a new Fe-V potential. These potentials were later integrated to provide a complete description of the FeCo-V alloy. To comprehensively study the deformation behavior, we constructed a nanocrystalline (NC) model and further tailored it to replicate various ordering degrees within grains and grain boundaries (GB).

Tensile tests performed on the binary FeCo consistently exhibited a comparable fracture behavior. Stresses primarily localized within the GBs, with particular emphasis on the triple junctions. Consequently, cracks typically initiated at these triple junctions and rapidly propagated along the adjoining GBs. The results indicated that the ordering degree within

both GBs and grains has a relatively minor impact on the deformation behavior. Disorder within the GBs appeared to slightly enhance grain mobility, delaying crack nucleation. In contrast, the presence of antiphase domains (APD) within the grains seemed to play a more substantial role in accommodating initial stresses within the plastic regime.

Following, FeCo supercells containing APBs underwent doping with a 2% content of V. This addition resulted in the expected reduction in the {112} and {110} APB energies, consistent with the established theoretical framework. Subsequently, V atoms were introduced randomly into the NC model, and their diffusion within the system was investigated using a hybrid grand canonical Monte Carlo – molecular dynamics (GCMC-MD) approach. The simulations revealed that V atoms exhibited a propensity to migrate towards GBs, irrespective of the ordering conditions. Due to differences in enthalpies, V preferred to exchange positions with Fe atoms, indicating a tendency to form Co-rich compounds. However, in this investigation Co_3V compounds with an $L1_2$ structure was not observed as hypothesized by some references.

Considering different scenarios, V was also introduced independently in GBs and APBs in grains. Tensile tests revealed that V in the GBs constrained grain mobility, resulting in increased brittleness in the alloy. Conversely, when V was introduced into the APBs, it significantly promoted slippage within the inner grains, leading to a delay in fracture strain. However, regardless of the ordering conditions and the presence of V, all simulations consistently exhibited crack nucleation and propagation along the GBs, ultimately resulting in an intergranular type of fracture. This behavior closely mimicked the macroscale behavior of the real alloy presenting relatively small grains.

To study the effect of other alloying elements, missing binary interatomic potentials from the literature were developed in order to describe the FeCo-X (X = Al, Cu, Nb, and W) alloys, namely the Fe-Al, Fe-Cu, Fe-Nb, Fe-W and Co-Nb. This study pioneers a comprehensive MD exploration of the elastic properties of stable structures in the Fe-Nb system. Similarly, this work sets an initial foray of MEAM methodologies into comprehending the Fe-W and Co-W systems. However, difficulties were encountered during the development of triple-element interactions. Instability was found when including Nb and W, being these the principal interest of this study due to the known enhancement on the mechanical properties of the FeCo alloy.

Alternatively, a newly developed Co-Fe interatomic potential from the literature was chosen, compatible with various intermetallic potentials from this study. Consequently, the focus shifted to proven ductility-enhancing solutes: V, Nb, Mo, and W. The Co-Fe potential was soft tunned to match the APB boundaries for the {112} and {110} planes. Additionally, the Fe-W interatomic potential and ternary interactions were addressed. Interatomic potentials for Fe-Co-V, Fe-Co-Nb, Fe-Co-Mo, and Fe-Co-W ternary alloys were fine-tuned to best capture the influence of these solutes on the APB energies of the FeCo alloy.

Diffusivity was studied using combined MD-Monte Carlo simulations (MD-MC). Systems containing 2 at.% of V, W, and Mo exhibited predominant segregation of solute atoms to GBs, while only a small fraction of Nb showed a similar tendency. Atomic exchange of solutes was primarily observed with Fe atoms, followed by Co atoms, with varying ratios depending on the alloy. Notably, some models developed structures with a rhombohedral symmetry in the proximity of GB, bearing resemblance to the laves- and μ-phases, naturally occurring in the combination of Fe or Co with Nb, W, and Mo.

Stress-strain tests revealed that models with and without additions developed slip bands within the grains mainly on the {110} planes. The beginning of the slippage denoted the beginning of yielding. Three different types of deformation pathways were observed: first, for the FeCo binary alloy, multiple microcracks appeared without propagating through the GBs leading to void linkage in some cases. Second, models containing V and W additions developed a single microcrack. V accelerated void development while W slowed it compared to FeCo, with microcracks showing slow growth without propagating through grain boundaries. Third, models with Nb and Mo exhibited slippage leading to cross slippage, demonstrating resistance to void formation.

In summary, tungsten (W) was found to be the more likely material to enhance ductility within the elastic region, attributed to its lower Young's and Bulk modulus. This unique combination led to a delayed emergence of slip bands and the attainment of a higher ultimate tensile strength (UTS). The distinctive mechanical behavior exhibited by W addition suggests its potential as a promising alloying element for improving the overall performance of FeCo-based materials.

8.3 Recommended Future Work

The series of interatomic potentials developed in this study sets a base to explore new alloys. The interatomic potentials can be merged with each other to describe other systems. In the case of Fe-Co, quaternary solute interactions require the development of ternary potentials, which are far simple to develop than the unary and binary counterparts. Investigating the interplay of multiple solutes can provide an enhanced understanding of how different elements influence the mechanical and structural properties of FeCo alloys. Moreover, these potentials can expand the scope of research beyond FeCo alloys, encompassing the description of other alloying systems. This is particularly pertinent for multielement systems, including multilayered systems and High Entropy Alloys (HEAs), which have garnered significant attention due to their unique properties and are increasingly being explored using MD techniques [46,104,252].

The integration of Spin-Dynamics (SD) into MD simulations is still at an early stage. While a few studies have utilized this combined methodology focusing on the Fe system [253,254], it was only in recent years that it became integrated into an MD code (LAMMPS) for universal compatibility with existing MD potentials [255]. Similar to MD, joint SD potentials require further tunning, introducing additional layers of complexity and variability. Moreover, it has been estimated that including magnetic spin interactions increases by 4-5 times the computational cost [255]. Despite this, MD-SD simulations have the capacity to open new perspectives on the magnetic properties and behaviors of FeCo alloys, including the ordering phenomena which is attributed to the magnetic interactions. Combining MD-SD simulations with an interatomic potential enhanced for mechanical capabilities as presented in this work, would theoretically offer the opportunity to observe the correct order-disorder transitions, phase transformations and crystal growth within grains while maintaining a good perspective on the mechanical behavior.

The current available computational power, although plenty for large systems within the MD scope, is not sufficient to replicate realistic atomic systems. Considering employing higher computational power in the future to simulate larger atomic systems would facilitate the observation of macroscopic size effects in FeCo alloys. This would provide insights

into the material's behavior under conditions that more closely resemble real-world applications.

These prospective directions intend to advance beyond the groundwork established in the current study, providing avenues for more detailed insights and broadening the application of the findings to diverse alloy systems and larger-scale scenarios.

REFERENCES

[1] B. Sarlioglu and C. T. Morris, *More Electric Aircraft: Review, Challenges, and Opportunities for Commercial Transport Aircraft*, IEEE Trans. Transp. Electrif. (2015).

[2] R. S. Sundar and S. C. Deevi, *Soft Magnetic FeCo Alloys: Alloy Development, Processing, and Properties*, Int. Mater. Rev. **50**, 157 (2005).

[3] T. Sourmail, *Near Equiatomic FeCo Alloys: Constitution, Mechanical and Magnetic Properties*, Prog. Mater. Sci. **50**, 816 (2005).

[4] Y. Ustinovshikov and S. Tresheva, *Character of Transformations in Fe–Co System*, Mater. Sci. Eng. A **248**, 238 (1998).

[5] A. H. Habib, C. L. Ondeck, P. Chaudhary, M. R. Bockstaller, and M. E. McHenry, *Evaluation of Iron-Cobalt/Ferrite Core-Shell Nanoparticles for Cancer Thermotherapy*, J. Appl. Phys. (2008).

[6] C.-W. CHEN, *METALLURGY OF SOFT MAGNETIC MATERIALS*, in *Magnetism and Metallurgy of Soft Magnetic Materials* (1977).

[7] J. Chen, D. Wang, S. Cheng, and J. Wang, *Influence of Manufacture Process on Magnetic Property of FeCoV Alloy*, in *2014 17th International Conference on Electrical Machines and Systems, ICEMS 2014* (2014).

[8] P. Moine, J. P. Eymery, and P. Grosbras, *The Effects of Short-Range Order and Long-Range Order on the Equilibrium Configuration of Superdislocations in Fe-Co : 2 At% V-Consequences on Flow Stress*, Phys. Status Solidi **46**, 177 (1971).

[9] N. S. Stoloff and R. G. Davies, *The Plastic Deformation of Ordered FeCo and Fe_3Al Alloys*, Acta Metall. **12**, 473 (1964).

[10] M. J. Marcinkowski and R. M. Fisher, *Theoretical Analysis of Plastic Deformation in Superlattices Based on the Body-Centered Cubic Structure*, J. Appl. Phys. **34**, 2135 (1963).

[11] C. Fu and M. Krčmar, *First-Principles Study of the Structural, Defect, and Mechanical Properties of B2 FeCo Alloys*, Phys. Rev. B **74**, 174108 (2006).

[12] M. Yalçin, A. Mekhrabov, and M. Akdeniz, *Effects of Nanoparticle Geometry and Temperature on the Structural Evolution in FeCo Nanoalloys*, Acta Phys. Pol. A **125**, 600 (2014).

[13] Z. Pei, M. Eisenbach, S. Mu, and G. Stocks, *Error Controlling of the Combined Cluster-Expansion and Wang-Landau Monte-Carlo Method and Its Application to FeCo*, Comput. Phys. Commun. **235**, 95 (2019).

[14] A. I. C. Persiano and R. D. Rawlings, *Effect of Niobium Additions on the Structure and Magnetic Properties of Equiatomic Iron-Cobalt Alloys*, J. Mater. Sci. **26**, 4026 (1991).

[15] T. Nishizawa and K. Ishida, *The Co-Fe (Cobalt-Iron) System*, Bull. Alloy Phase Diagrams **5**, 250 (1984).

[16] J. Wang, X. G. Lu, N. Zhu, and W. Zheng, *Thermodynamic and Diffusion Kinetic Studies of the Fe-Co System*, Calphad Comput. Coupling Phase Diagrams Thermochem. **58**, 82 (2017).

[17] S. Mahmood Shah, N. Ullah, B. Ullah, M. Shehzad Khan, and T. Usman, *Thermodynamic Analysis and Calculations of (Fe-Co) Alloy by Modeling and Simulation Using Thermo-Calc Software*, J. Heterocycl. **1**, 35 (2018).

[18] W. L. Bragg and E. J. Williams, *The Effect of Thermal Agitation on Atomic Arrangement in Alloys*, Proc. R. Soc. London. Ser. A, Contain. Pap. a Math. Phys. Character **145**, 699 (1934).

[19] S.-T. Fong, K. Sadananda, and M. J. Marcinkowski, *Effect of Strain, Temperature, and Atomic Order on Slip Deformation in FeCo*, Metall. Trans. **5**, 1239 (1974).

[20] L. Ren, S. Basu, R. Yu, and J. Q. Xiao, *Mechanical Properties of Fe-Co Soft Magnets*, J. Mater. Sci. **6**, 1451 (2001).

[21] K. R. Jordan and N. S. Stoloff, *Plastic Deformation and Fracture in FeCo--2 Pct V.*, Trans. Met. Soc. AIME **245**, 2027 (1969).

[22] A. Duckham, D. Z. Zhang, D. Liang, V. Luzin, R. C. Cammarata, R. L. Leheny, C. L. Chien, and T. P. Weihs, *Temperature Dependent Mechanical Properties of Ultra-Fine Grained FeCo-2V*, Acta Mater. **51**, 4083 (2003).

[23] L. Zhao and I. Baker, *The Effect of Grain Size and Fe:Co Ratio on the Room Temperature Yielding of FeCo*, Acta Metall. Mater. **42**, 1953 (1994).

[24] K. Kawahara, *Effect of Additive Elements on Cold Workability in FeCo Alloys*, J. Mater. Sci. **18**, 1709 (1983).

[25] R. A. Buckley, *Microstructure and Kinetics of the Ordering Transformation in Iron–Cobalt Alloys, FeCo, FeCo–0.4%Cr, FeCo–2.5%V*, Met. Sci. **9**, 243 (1975).

[26] C. M. Orrock, The Microstructure and Properties of Equiatomic Iron-Cobalt Magnetic Alloys with Alloying Additions., University of London, 1985.

[27] C. W. Chen, *Metallurgy and Magnetic Properties of an Fe-Co-V Alloy*, J. Appl. Phys. **32**, (1961).

[28] R. Sundar and S. Deevi, *Influence of Alloying Elements on the Mechanical Properties of FeCo–V Alloys*, Intermetallics **12**, 921 (2004).

[29] S. Hasani, A. Shafyei, M. Shamanian, P. Behjati, H. Mostaan, T. Juuti, and J. A. Szpunar, *Correlation between Magnetic Properties and Allotropic Phase Transition of Fe-Co-V Alloy*, Acta Metall. Sin. (English Lett. **28**, 1055 (2015).

[30] A. M. Glezer, D. V. Luzgin, L. F. Muradimova, S. O. Shirshikov, M. A. Libman, I. V. Schetinin, N. S. Perov, D. L. Dyakonov, and R. V. Sundeyev, *Structural Phase Changes during Deformation of FeCo-V Alloys by Torsion under High Pressure*, IOP Conf. Ser. Mater. Sci. Eng. **709**, (2020).

[31] A. I. C. Persiano and R. D. Rawlings, *A Mössbauer Investigation of Equiatomic FeCo with Vanadium and Niobium Additions*, Phys. Status Solidi **103**, 547 (1987).

[32] M. Neumayer and M. Fähnle, *Atomic Defects in FeCo: Stabilization of the Structure by Magnetism*, Phys. Rev. B - Condens. Matter Mater. Phys. **64**, 2 (2001).

[33] S. Assa Aravindh, S. Mathi Jaya, M. C. Valsakumar, and C. S. Sundar, *Compositional Variation of Magnetic Moment, Magnetic Anisotropy Energy and Coercivity in Fe(1−x)Mx (M = Co/Ni) Nanowires: An Ab Initio Study*, Appl. Nanosci. **2**, 409 (2012).

[34] M. Mizuno, H. Araki, and Y. Shirai, *First Principles Calculation of Defect and Magnetic Structures in FeCo*, Mater. Trans. 2464 (2006).

[35] M. Krcmar, C. L. Fu, and J. R. Morris, *First-Principles Study of Structural and Defect Properties in FeCo Intermetallics*, MRS Proc. **842**, S1.4 (2004).

[36] H. Zhang, M. P. J. Punkkinen, B. Johansson, S. Hertzman, and L. Vitos, *Single-Crystal Elastic Constants of Ferromagnetic Bcc Fe-Based Random Alloys from First-Principles Theory*, Phys. Rev. B - Condens. Matter Mater. Phys. **81**, 1 (2010).

[37] M. Aykol, A. Mekhrabov, and M. Akdeniz, *Effect of Vanadium on Atomic Ordering Characteristics and Anti-Phase Boundary Energies of B2-FeCo Alloys*, Intermetallics **18**, 893 (2010).

[38] Y. Li, D. Yang, and W. Qiang, *First-Principles Study of the Effects of Solutes on Long-*

Range Order Degree, Self-Diffusions and Antiphase Boundary Energies in Ordered FeCo Alloy, J. Magn. Magn. Mater. **562**, 169767 (2022).

[39] Y. Li and W. Qiang, *Ordered Structure and Solute-Suppressed Atomic Ordering in Iron-Cobalt Alloys*, Comput. Mater. Sci. **202**, 111005 (2022).

[40] M. S. Daw and M. I. Baskes, *Embedded-Atom Method: Derivation and Application to Impurities, Surfaces, and Other Defects in Metals*, Phys. Rev. B (1984).

[41] B. J. Lee, M. I. Baskes, H. Kim, and Y. K. Cho, *Second Nearest-Neighbor Modified Embedded Atom Method Potentials for Bcc Transition Metals*, Phys. Rev. B - Condens. Matter Mater. Phys. **64**, (2001).

[42] X. W. Zhou et al., *Atomic Scale Structure of Sputtered Metal Multilayers*, Acta Mater. **49**, 4005 (2001).

[43] X. W. Zhou, R. A. Johnson, and H. N. G. Wadley, *Misfit-Energy-Increasing Dislocations in Vapor-Deposited CoFe/NiFe Multilayers*, Phys. Rev. B - Condens. Matter Mater. Phys. **69**, 1 (2004).

[44] L. J. Meng, X. Y. Peng, K. W. Zhang, C. Tang, and J. X. Zhong, *Structural Phase Transitions of FeCo and FeNi Nanoparticles: A Molecular Dynamics Study*, J. Appl. Phys. **111**, (2012).

[45] L. J. Meng, X. Y. Peng, C. Tang, K. W. Zhang, G. M. Stocks, and J. X. Zhong, *A Quasicore-Shell Structure of FeCo and FeNi Nanoparticles*, J. Appl. Phys. **108**, 1 (2010).

[46] D. Farkas and A. Caro, *Model Interatomic Potentials and Lattice Strain in a High-Entropy Alloy*, J. Mater. Res. **33**, 3218 (2018).

[47] Y. L. Li, X. Cheng, W. H. Duan, and W. J. Qiang, *Improved Ductility by Coupled Motion of Grain Boundaries in Nanocrystalline B2-FeCo Alloys*, Comput. Mater. Sci. **198**, (2021).

[48] Y. Li, Z. Huang, K. Wang, D. Yang, F. Ding, and W. Qiang, *Abnormally Fast Crack Propagation Induced by Short-Range Ordering in Iron-Cobalt Alloys: A Combined Experiments and Molecular Dynamics Simulations*, J. Alloys Compd. **924[1] Y.**, 166649 (2022).

[49] W. M. Choi, Y. Kim, D. Seol, and B. J. Lee, *Modified Embedded-Atom Method Interatomic Potentials for the Co-Cr, Co-Fe, Co-Mn, Cr-Mn and Mn-Ni Binary Systems*, Comput. Mater. Sci. **130**, 121 (2017).

[50] W. M. Choi, Y. H. Jo, S. S. Sohn, S. Lee, and B. J. Lee, *Understanding the Physical Metallurgy of the CoCrFeMnNi High-Entropy Alloy: An Atomistic Simulation Study*, Npj Comput. Mater. **4**, 1 (2018).

[51] S. Firdosy et al., *Compositionally Graded Joints between Magnetically Dissimilar Alloys Achieved through Directed Energy Deposition*, Scr. Mater. **202**, 114005 (2021).

[52] J. Wang, H. Kwon, H. S. Kim, and B. J. Lee, *A Neural Network Model for High Entropy Alloy Design*, Npj Comput. Mater. **9**, 1 (2023).

[53] Y. Li, F. Xu, L. Hou, L. Sun, H. Su, X. Li, and W. Ren, *Molecular Dynamics Simulation of the Transformation of Fe-Co Alloy by Machine Learning Force Field Based on Atomic Cluster Expansion*, Chem. Phys. Lett. **826**, 140646 (2023).

[54] A. Egorov, A. Subramanyam, Z. Yuan, R. Drautz, and T. Hammerschmidt, *Magnetic Bond-Order Potential for Iron-Cobalt Alloys*, Phys. Rev. Mater. **7**, 44403 (2023).

[55] S. Goel et al., *Horizons of Modern Molecular Dynamics Simulation in Digitalized Solid Freeform Fabrication with Advanced Materials*, Mater. Today Chem. **18**, 100356 (2020).

[56] E. R. Smith, P. E. Theodorakis, R. V. Craster, and O. K. Matar, *Moving Contact Lines: Linking Molecular Dynamics and Continuum-Scale Modeling*, Langmuir (2018).

[57] S. Li and S. Urata, *An Atomistic-to-Continuum Molecular Dynamics: Theory, Algorithm, and Applications*, Comput. Methods Appl. Mech. Eng. (2016).

[58] J. A. Harrison, J. D. Schall, S. Maskey, P. T. Mikulski, M. T. Knippenberg, and B. H. Morrow, *Review of Force Fields and Intermolecular Potentials Used in Atomistic Computational Materials Research*, Appl. Phys. Rev. **5**, (2018).

[59] M. I. Baskes, *Modified Embedded-Atom Potentials for Cubic Materials and Impurities*, Phys. Rev. B **46**, 2727 (1992).

[60] S. Kim, M. F. Horstemeyer, M. I. Baskes, M. Rais-Rohani, S. Kim, B. Jelinek, J. Houze, A. Moitra, and L. Liyanage, *Semi-Empirical Potential Methods for Atomistic Simulations of Metals and Their Construction Procedures*, J. Eng. Mater. Technol. **131**, 0412101 (2009).

[61] M. I. Baskes, *Application of the Embedded-Atom Method to Covalent Materials: A Semiempirical Potential for Silicon*, Phys. Rev. Lett. **59**, 2666 (1987).

[62] J. H. Rose, J. R. Smith, F. Guinea, and J. Ferrante, *Universal Features of the Equation of State of Metals*, Phys. Rev. B **29**, 2963 (1984).

[63] J. P. Tavenner, M. I. Mendelev, and J. W. Lawson, *Molecular Dynamics Based Kinetic Monte Carlo Simulation for Accelerated Diffusion*, Comput. Mater. Sci. **218**, 111929 (2023).

[64] R. Kosloff, *Time-Dependent Quantum-Mechanical Methods for Molecular Dynamics*, J. Phys. Chem. **92**, 2087 (1988).

[65] W. D. Callister and D. G. Rethwisch, *Materials Science and Engineering 9th Edition* (2014).

[66] R. Hill, *The Elastic Behaviour of a Crystalline Aggregate*, Proc. Phys. Soc. Sect. A (1952).

[67] B. J. Lee and M. I. Baskes, *Second Nearest-Neighbor Modified Embedded-Atom-Method Potential*, Phys. Rev. B - Condens. Matter Mater. Phys. **62**, 8564 (2000).

[68] M. R. M. R. Hestenes, E. Stiefel, and others, *Methods of Conjugate Gradients for Solving Linear Systems*, J. Res. Natl. Bur. Stand. (1934). **49**, 409 (1952).

[69] B. J. Lee, W. S. Ko, H. K. Kim, and E. H. Kim, *The Modified Embedded-Atom Method Interatomic Potentials and Recent Progress in Atomistic Simulations*, Calphad Comput. Coupling Phase Diagrams Thermochem. **34**, 510 (2010).

[70] S. Paul, M. Muralles, D. Schwen, M. Short, and K. Momeni, *A Modified Embedded-Atom Potential for Fe-Cr-Si Alloys*, J. Phys. Chem. C acs. jpcc.1c07021 (2021).

[71] H. S. Jang, D. Seol, and B. J. Lee, *Modified Embedded-Atom Method Interatomic Potentials for Mg–Al–Ca and Mg–Al–Zn Ternary Systems*, J. Magnes. Alloy. **9**, 317 (2021).

[72] Y. K. Kim, W. S. Jung, and B. J. Lee, *Modified Embedded-Atom Method Interatomic Potentials for the Ni-Co Binary and the Ni-Al-Co Ternary Systems*, Model. Simul. Mater. Sci. Eng. **23**, 0 (2015).

[73] K. Momma and F. Izumi, *VESTA 3 for Three-Dimensional Visualization of Crystal, Volumetric and Morphology Data*, J. Appl. Crystallogr. **44**, 1272 (2011).

[74] H. Ito, M. Saito, T. Miyamachi, F. Komori, T. Koganezawa, M. Mizuguchi, and M. Kotsugi, *Fabrication of L 10-Type FeCo Ordered Structure Using a Periodic Ni Buffer Layer*, AIP Adv. **9**, (2019).

[75] T. Hasegawa, S. Kanatani, M. Kazaana, K. Takahashi, K. Kumagai, M. Hirao, and S. Ishio, *Conversion of FeCo from Soft to Hard Magnetic Material by Lattice Engineering*

and Nanopatterning, Sci. Rep. **7**, 1 (2017).

[76] W. Dong, H. Kim, W. Ko, B. Lee, and B. J. Lee, *Atomistic Modeling of Pure Co and Co-Al System*, Calphad **38**, 7 (2012).

[77] A. Díaz-Ortiz, R. Drautz, M. Fähnle, and H. Dosch, *First-Principles Modeling of Magnetism and Phase Equilibria in Binary Alloys*, in *Journal of Alloys and Compounds*, Vol. 369 (2004), pp. 27–32.

[78] G. A. Farnan, C. L. Fu, Z. Gai, M. Krcmar, A. P. Baddorf, Z. Zhang, and J. Shen, *Electronic Stability of Magnetic Fe = Co Superlattices with Monatomic Layer Alternation*, 1 (2003).

[79] O. K. Belousov and N. A. Palii, *Concentration and Temperature Dependences of the Elastic Properties of Quenched Fe-Co and FeCo-2V Alloys*, Russ. Metall. **2009**, 41 (2009).

[80] M. De Jong et al., *Charting the Complete Elastic Properties of Inorganic Crystalline Compounds*, Sci. Data **2**, 1 (2015).

[81] M. Rahaman, First-Principles Investigations of Ordering in Binary Alloys, Kungliga Tekniska Hogskolan, 2013.

[82] C. Niu, A. J. Zaddach, C. C. Koch, and D. L. Irving, *First Principles Exploration of Near-Equiatomic NiFeCrCo High Entropy Alloys*, J. Alloys Compd. **672**, 510 (2016).

[83] T. G. Woodcock, R. Hermann, and W. Löser, *Development of a Metastable Phase Diagram to Describe Solidification in Undercooled Fe-Co Melts*, Calphad Comput. Coupling Phase Diagrams Thermochem. (2007).

[84] J. E. Rodriguez and D. M. Matson, *Thermodynamic Modeling of the Solidification Path of Levitated Fe-Co Alloys*, Calphad Comput. Coupling Phase Diagrams Thermochem. (2015).

[85] J. Rodgers and W. Maddok, Second Report of the Alloy Steels Research Commitee, 1939.

[86] A. Díaz-Ortiz, R. Drautz, M. Fähnle, H. Dosch, and J. M. Sanchez, *Structure and Magnetism in Bcc-Based Iron-Cobalt Alloys*, Phys. Rev. B **73**, 224208 (2006).

[87] L. M. Pike, Y. A. Chang, and C. T. Liu, *Point Defect Concentrations and Hardening in Binary B2 Intermetallics*, Acta Mater. **45**, 3709 (1997).

[88] R. M. Bozorth, *Ferromagnetism* (1993).

[89] D. I. Bardos, *Mean Magnetic Moments in Bcc FeSingle Bond SignCo Alloys*, J. Appl.

Phys. (1969).

[90] F. Arslan, H. B. Bell, and D. B. Downie, *Enthalpies of Formation of Ordered Iron–Cobalt Alloys*, Met. Sci. **12**, 198 (1978).

[91] I. Ohnuma, H. Enoki, O. Ikeda, R. Kainuma, H. Ohtani, B. Sundman, and K. Ishida, *Phase Equilibria in the Fe-Co Binary System*, Acta Mater. **50**, 379 (2002).

[92] K. Harada, H. Ishibashi, and M. Kogachi, *Defect Properties and Magnetism in B2-Type CoFe Alloys*, Mater. Res. Soc. Symp. Proc. **753**, 1 (2002).

[93] Y. Zhang and E. J. Maginn, *A Comparison of Methods for Melting Point Calculation Using Molecular Dynamics Simulations*, J. Chem. Phys. **136**, (2012).

[94] P. M. Piaggi and M. Parrinello, *Entropy Based Fingerprint for Local Crystalline Order*, J. Chem. Phys. **147**, (2017).

[95] R. J. Hawkins and J. M. Sanchez, *Ferromagnetism and Chemical Ordering in Cobalt-Iron*, J. Phys. F Met. Phys. **18**, 767 (1988).

[96] Y. Tahara and O. Kensuke, Kinetic Behavior of Ordering in B2-Type Alloys, 1988.

[97] S. H. Oh, D. Seol, and B. J. Lee, *Second Nearest-Neighbor Modified Embedded-Atom Method Interatomic Potentials for the Co-M (M = Ti, V) Binary Systems*, Calphad Comput. Coupling Phase Diagrams Thermochem. **70**, 101791 (2020).

[98] T. Lee, M. I. Baskes, S. M. Valone, and J. D. Doll, *Atomistic Modeling of Thermodynamic Equilibrium and Polymorphism of Iron*, J. Phys. Condens. Matter **24**, (2012).

[99] M. D. Stanislaw and J. Cieslak, *Sigma-Phase in Fe-Cr and Fe-V Alloy Systems and Its Physical Properties*, Crit. Rev. Solid State Mater. Sci. **36**, 191 (2011).

[100] S. Plimpton, P. Crozier, and A. Thompson, *LAMMPS-Large-Scale Atomic/Molecular Massively Parallel Simulator*, http://lammps.sandia.gov.

[101] A. Stukowski, *Visualization and Analysis of Atomistic Simulation Data with OVITO-the Open Visualization Tool*, Model. Simul. Mater. Sci. Eng. (2010).

[102] V. L. Moruzzi and P. M. Marcus, *Total Energies and Magnetic Moments in Fe, V, and Ordered FeV*, Phys. Rev. B **45**, 2934 (1992).

[103] R. Wang, S. Wang, X. Wu, and J. Yang, *Pressure Induced Structural Instability of FeV Intermetallic Compound with B2 Ordering*, J. Alloys Compd. **650**, 537 (2015).

[104] W. M. Choi, J. S. Kim, W. S. Ko, D. G. Kim, Y. H. Jo, S. S. Sohn, S. Lee, and B. J. Lee, *Computational Design of V-CoCrFeMnNi High-Entropy Alloys: An Atomistic Simulation*

Study, Calphad Comput. Coupling Phase Diagrams Thermochem. **74**, 102317 (2021).

[105] J. J. Donegan and J. R. Neighbours, *Elastic Constants of Vanadium Iron-Alloys*, Acta Metall. **21**, 821 (1973).

[106] J. Cieslak, J. Tobola, and S. M. Dubiel, *Formation Energy in σ-Phase Fe-V Alloys*, J. Phys. Chem. Solids **74**, 1303 (2013).

[107] E. O. Hall and S. H. Algie, *The Sigma Phase*, Metall. Rev. **11**, 61 (1966).

[108] E. Kabliman, A. V. Ruban, P. Blaha, O. Peil, and K. Schwarz, *Ab Initio Study of Lattice Site Occupancies in Binary Sigma Phases Using a Single-Site Mean Field Model*, Appl. Sci. **2**, 654 (2012).

[109] P. Hirel, *Atomsk: A Tool for Manipulating and Converting Atomic Data Files*, Comput. Phys. Commun. **197**, 212 (2015).

[110] J. M. Cowley, *Short-Range Order and Long-Range Order Parameters*, Phys. Rev. **138**, (1965).

[111] I. Baker and E. M. Schulson, *On Grain Boundaries in Nickel-Rich Ni3Al*, Scr. Metall. **23**, 1883 (1989).

[112] V. Semenov, E. Rabkin, E. Bischoff, and W. Gust, *The Effect of the Grain Boundary Misorientation on the Kinetics of the Discontinuous Ordering Reaction in Fe-50 at.%Co*, Acta Mater. **46**, 2289 (1998).

[113] S. Hasani, M. Shamanian, A. Shafyei, P. Behjati, H. Mostaan, P. Sahu, and J. A. Szpunar, *Electron Microscopy Study on Grain Boundary Characterizations of Fe-Co-V Alloy during Annealing*, Vacuum **114**, 1 (2015).

[114] H. Gholizadeh and S. Hasani, *Ab-Initio Calculation of the γ-Surface and Cleavage Energy in the B2 FeCo Intermetallic Compound*, Comput. Mater. Sci. **143**, 515 (2018).

[115] S. Baco, Q. A. Abbas, T. J. Hayward, and N. A. Morley, *An Investigation on the Mechanical Properties of Soft Magnetostrictive FeCoCr Films by Nanoindentation*, J. Alloys Compd. **881**, 160549 (2021).

[116] D. Frenkel, B. Smit, and M. A. Ratner, *Understanding Molecular Simulation: From Algorithms to Applications*, Phys. Today **50**, 66 (1997).

[117] A. P. Thompson et al., *LAMMPS - a Flexible Simulation Tool for Particle-Based Materials Modeling at the Atomic, Meso, and Continuum Scales*, Comput. Phys. Commun. **271**, 108171 (2022).

[118] A. Williams, G. H. Kwei, A. T. Ortiz, M. Karnowski, and W. K. Warburton, *Combined Neutron and X-Ray Powder Diffraction Study of Fe0.50Co0.48V0.02*, J. Mater. Res. **5**, 1197 (1990).

[119] K. Kawahara, *Structures and Mechanical Properties of an FeCo-2V Alloy*, J. Mater. Sci. **18**, 3427 (1983).

[120] Z. Li, V. Gill, A. Lambourne, Z. Dong, M. Avdeev, J. T. Oh, and Z. Chen, *Mechanical Properties and Fractographic Analyses of FeCo-2V Alloy Heat-Treated around Order-Disorder Transition Temperature*, J. Mater. Res. Technol. 1 (2022).

[121] M. Muralles, J. T. Oh, and Z. Chen, *Influence of V Addition on the Mechanical Properties of FeCo Alloys: A Molecular Dynamics Study*, Materialia **27**, 101670 (2023).

[122] B. J. Lee, J. Shim, and M. I. Baskes, *Semiempirical Atomic Potentials for the Fcc Metals Cu, Ag, Au, Ni, Pd, Pt, Al, and Pb Based on First and Second Nearest-Neighbor Modified Embedded Atom Method*, Phys. Rev. B **68**, 144112 (2003).

[123] J. Wang, S. H. Oh, and B. J. Lee, *Second-Nearest-Neighbor Modified Embedded-Atom Method Interatomic Potential for Cu-M (M = Co, Mo) Binary Systems*, Comput. Mater. Sci. **178**, 109627 (2020).

[124] W. Dong, Z. Chen, and B.-J. Lee, *Modified Embedded-Atom Interatomic Potential for Co-W and Al-W Systems*, Trans. Nonferrous Met. Soc. China **25**, 907 (2015).

[125] E. Lee and B. J. Lee, *Modified Embedded-Atom Method Interatomic Potential for the Fe-Al System*, J. Phys. Condens. Matter **22**, (2010).

[126] B. Jelinek, S. Groh, M. F. Horstemeyer, J. Houze, S. Kim, G. J. Wagner, A. Moitra, and M. I. Baskes, *Modified Embedded Atom Method Potential for Al, Si, Mg, Cu, and Fe Alloys*, Phys. Rev. B - Condens. Matter Mater. Phys. **85**, 245102 (2012).

[127] A. Mahata, T. Mukhopadhyay, and M. Asle Zaeem, *Modified Embedded-Atom Method Interatomic Potentials for Al-Cu, Al-Fe and Al-Ni Binary Alloys: From Room Temperature to Melting Point*, Comput. Mater. Sci. **201**, 110902 (2022).

[128] K. Chen, S. Mun, M. Baskes, M. Horstemeyer, and B. Li, *Development of 2NN MEAM Potential for Fe-Al and Atomistic Investigation of Surface and Interface Properties of the Inhibition Layer in Galvanized Fe*, Model. Simul. Mater. Sci. Eng. **30**, 0 (2022).

[129] B. J. Lee, B. D. Wirth, J. H. Shim, J. Kwon, S. C. Kwon, and J. H. Hong, *Modified Embedded-Atom Method Interatomic Potential for the Fe-Cu Alloy System and Cascade*

Simulations on Pure Fe and Fe-Cu Alloys, Phys. Rev. B - Condens. Matter Mater. Phys. **71**, 1 (2005).

[130] I. Sa and B. J. Lee, *Modified Embedded-Atom Method Interatomic Potentials for the Fe-Nb and Fe-Ti Binary Systems*, Scr. Mater. **59**, 595 (2008).

[131] M. Muralles, J. T. Oh, and Z. Chen, *Molecular Dynamics Study of FeCo Phase Transitions and Thermal Properties Based on an Improved 2NN MEAM Potential*, J. Mater. Res. Technol. **19**, 1102 (2022).

[132] Z. Xie, D. Chauraud, E. Bitzek, S. Korte-Kerzel, and J. Guénolé, *Laves Phase Crystal Analysis (LaCA): Atomistic Identification of Lattice Defects in C14 and C15 Topologically Close-Packed Phases*, J. Mater. Res. **36**, 2010 (2021).

[133] A. L. Udovsky and D. A. Vasilyev, *Application of New Method in Quantum-Mechanical Calculations of the Structural Properties and the Formation Energy of the Ordered Mu - Phase in the Fe - Mo System*, J. Phys. Conf. Ser. **2052**, 012048 (2021).

[134] B. Sundman, I. Ohnuma, N. Dupin, U. R. Kattner, and S. G. Fries, *An Assessment of the Entire Al-Fe System Including D03 Ordering*, Acta Mater. **57**, 2896 (2009).

[135] M. A. Zagrebin, M. V. Matyunina, A. B. Koshkin, V. V. Sokolovskiy, and V. D. Buchelnikov, *Structural and Magnetic Properties of Fe-Al Alloys: Ab Initio Studies*, J. Magn. Magn. Mater. **557**, 169437 (2022).

[136] O. Ikeda, I. Ohnuma, R. Kainuma, and K. Ishida, *Phase Equilibria and Stability of Ordered BCC Phases in the Fe-Rich Portion of the Fe–Al System*, Intermetallics **9**, 755 (2001).

[137] D. Connétable and P. Maugis, *First Principle Calculations of the κ-Fe_3AlC Perovskite and Iron-Aluminium Intermetallics*, Intermetallics **16**, 345 (2008).

[138] F. Lechermann, M. Fähnle, and J. M. Sanchez, *First-Principles Investigation of the Ni-Fe-Al System*, Intermetallics **13**, 1096 (2005).

[139] C. L. Fu and M. H. Yoo, *Deformation Behavior of B2 Type Aluminides: FeAl and NiAl*, Acta Metall. Mater. **40**, 703 (1992).

[140] P. Maugis, J. Lacaze, R. Besson, and J. Morillo, *Ab Initio Calculations of Phase Stabilities in the Fe-Al-C System and CALPHAD-Type Assessment of the Iron-Rich Corner*, Metall. Mater. Trans. A **37**, 3397 (2006).

[141] L. Shaojun, D. Suqing, and M. Benkun, *First-Principles Calculation of Vibrational*

Entropy for Fe-Al Compounds, Phys. Rev. B **58**, 9705 (1998).

[142] W. B. Pearson, *A Handbook of Lattice Spacings and Structures of Metals and Alloys: International Series of Monographs on Metal Physics and Physical Metallurgy, Vol. 4*, Vol. 4 (Elsevier, 2013).

[143] P. G. Gonzales-Ormeño, H. M. Petrilli, and C. G. Schön, *Ab-Initio Calculations of the Formation Energies of BCC-Based Superlattices in the Fe-Al System*, Calphad **26**, 573 (2002).

[144] M. Friák and J. Neugebauer, *Ab Initio Study of the Anomalous Volume-Composition Dependence in Fe–Al Alloys*, Intermetallics **18**, 1316 (2010).

[145] J. Breuer, A. Grün, F. Sommer, and E. J. Mittemeijer, *Enthalpy of Formation of B2-$Fe_{1-x}Al_x$ and B2-$(Ni,Fe)_{1-x}Al_x$*, Metall. Mater. Trans. B **32**, 913 (2001).

[146] R. Hultgren, P. D. Desai, D. T. Hawkins, M. Gleiser, and K. Kelley, Selected Values of the Thermodynamic Properties of the Elements, 1973.

[147] C. J. Smithells and E. A. Brandes, *Contributors*, in *Smithells Metals Reference Book* (Elsevier, 2004), pp. xix–xxi.

[148] C. Vailhé and O. Farkas, *Shear Faults and Dislocation Core Structures in B2 CoAl*, J. Mater. Res. **12**, 2559 (1997).

[149] M. H. Yoo, T. Takasugi, S. Hanada, and O. Izumi, *Slip Modes in B2-Type Intermetallic Alloys*, Mater. Trans. JIM **31**, 435 (1990).

[150] G. Simmons and H. Wang, *Single Crystal Elastic Constants and Calculated Aggregate Properties. A Handbook* (MIT Press, Cambridge, Mass, 1971).

[151] M. Z. Khalid, J. Friis, P. H. Ninive, K. Marthinsen, I. G. Ringdalen, and A. Strandlie, *Modified Embedded Atom Method Potential for Fe-Al Intermetallics Mechanical Strength: A Comparative Analysis of Atomistic Simulations*, Phys. B Condens. Matter **618**, (2021).

[152] J. E. Saal, S. Kirklin, M. Aykol, B. Meredig, and C. Wolverton, *Materials Design and Discovery with High-Throughput Density Functional Theory: The Open Quantum Materials Database (OQMD)*, JOM **65**, 1501 (2013).

[153] H. J. Leamy, E. D. Gibson, and F. X. Kayser, *The Elastic Stiffness Coefficients of Iron-Aluminum Alloys-I Experimental Results and Thermodynamic Analysis*, Acta Metall. **15**, 1827 (1967).

[154] W. Oelsen, *The Heats of Formation of Binary and Ternary Alloys and Their Importance in Metallurgical Reactions*, Z. Electrochem **43**, 530 (1937).

[155] W. Zheng, S. He, M. Selleby, Y. He, L. Li, X. G. Lu, and J. Ågren, *Thermodynamic Assessment of the Al-C-Fe System*, Calphad Comput. Coupling Phase Diagrams Thermochem. **58**, 34 (2017).

[156] A. T. Phan, M. Paek, and Y. Kang, *Phase Equilibria and Thermodynamics of the Fe-Al-C System: Critical Evaluation, Experiment and Thermodynamic Optimization*, Acta Mater. **79**, 1 (2014).

[157] M. H. Jacobs and R. Schmid-Fetzer, *Phase Behavior and Thermodynamic Properties in the System Fe-Al*, Calphad **33**, 170 (2009).

[158] P. Lindqvist and B. Uhrenius, *On the Fe-Cu Phase Diagram*, Calphad **4**, 193 (1980).

[159] J. He and J. Zhao, *Behavior of Fe-Rich Phase during Rapid Solidification of Cu-Fe Hypoperitectic Alloy*, Mater. Sci. Eng. A **404**, 85 (2005).

[160] A. Caro, M. Caro, E. M. Lopasso, P. E. A. Turchi, and D. Farkas, *Thermodynamics of Fe-Cu Alloys as Described by a Classic Potential*, J. Nucl. Mater. **349**, 317 (2006).

[161] M. Hasebe and T. Nishizawa, *Calculation of Phase Diagrams of the Iron-Copper and Cobalt-Copper Systems*, Calphad **4**, 83 (1980).

[162] O. K. von Goldbeck, *Iron-Copper Fe-Cu*, in *Iron-Binary Phase Diagrams* (Springer Berlin Heidelberg, Berlin, Heidelberg, Heidelberg, 1982), pp. 35–37.

[163] A. R. Yavari, P. J. Desré, and T. Benameur, *Mechanically Driven Alloying of Immiscible Elements*, Phys. Rev. Lett. **68**, 2235 (1992).

[164] J. Eckert, J. C. Holzer, C. E. Krill, and W. L. Johnson, *Mechanically Driven Alloying and Grain Size Changes in Nanocrystalline Fe-Cu Powders*, J. Appl. Phys. **73**, 2794 (1993).

[165] K. Uenishi, K. F. Kobayashi, S. Nasu, H. Hatano, K. N. Ishihara, and P. Hideo Shingu, *Mechanical Alloying in the Fe-Cu System*, Int. J. Mater. Res. **83**, 132 (1992).

[166] C. L. Chien, S. H. Liou, D. Kofalt, W. Yu, T. Egami, and T. R. McGuire, *Magnetic Properties of FexCu100−x Solid Solutions*, Phys. Rev. B **33**, 3247 (1986).

[167] E. Ma, M. Atzmon, and F. E. Pinkerton, *Thermodynamic and Magnetic Properties of Metastable Fe_xCu_{100-x} Solid Solutions Formed by Mechanical Alloying*, J. Appl. Phys. **74**, 955 (1993).

[168] G. J. Ackland, D. J. Bacon, A. F. Calder, and T. Harry, *Computer Simulation of Point*

Defect Properties in Dilute Fe-Cu Alloy Using a Many-Body Interatomic Potential, Philos. Mag. A **75**, 713 (1997).

[169] H. R. Gong, L. T. Kong, and B. X. Liu, *Structural Stability and Magnetic Properties of Metastable Fe-Cu Alloys Studied by Ab Initio Calculations and Molecular Dynamics Simulations*, Phys. Rev. B - Condens. Matter Mater. Phys. **69**, 1 (2004).

[170] Y. J. Shen, L. C. Liu, S. T. Mi, H. R. Gong, and S. F. Zhou, *Construction of an n -Body Fe-Cu Potential and Its Application in Atomistic Modeling of Fe-Cu Solid Solutions*, J. Appl. Phys. **127**, (2020).

[171] M. Ludwig, D. Farkas, D. Pedraza, and S. Schmauder, *Embedded Atom Potential for Fe-Cu Interactions and Simulations of Precipitate-Matrix Interfaces*, Model. Simul. Mater. Sci. Eng. **6**, 19 (1998).

[172] K. Choudhary et al., *The Joint Automated Repository for Various Integrated Simulations (JARVIS) for Data-Driven Materials Design*, Npj Comput. Mater. **6**, 173 (2020).

[173] A. Jain et al., *Commentary: The Materials Project: A Materials Genome Approach to Accelerating Materials Innovation*, APL Mater. **1**, 011002 (2013).

[174] J. Z. Liu, A. Van De Walle, G. Ghosh, and M. Asta, *Structure, Energetics, and Mechanical Stability of Fe-Cu Bcc Alloys from First-Principles Calculations*, Phys. Rev. B - Condens. Matter Mater. Phys. **72**, 40 (2005).

[175] M. Mihalkovic, M., Widom, *Quasicrystal Approximants with Novel Compositions and Structures*, in *MRS Online Proceedings Library*, Vol. 805 (2003), pp. 3–8.

[176] Y. F. Wen and J. Sun, *Theoretical Prediction of Mechanical Stability of Ferromagnetic Fcc Fe-Cu Alloys from First Principles*, J. Appl. Phys. **111**, (2012).

[177] E. Ma and M. Atzmon, *Phase Transformations Induced by Mechanical Alloying in Binary Systems*, Mater. Chem. Phys. **39**, 249 (1995).

[178] H. Okamoto, *Fe-Nb (Iron-Niobium)*, J. Phase Equilibria **23**, 112 (2002).

[179] S. Srikanth and A. Petric, *A Thermodynamic Evaluation of the Fe-Nb System*, Zeitschrift Für Met. **85**, 164 (1994).

[180] E. Paul and L. J. Swartzendruber, *The Fe−Nb (Iron-Niobium) System*, Bull. Alloy Phase Diagrams **7**, 248 (1986).

[181] C. Toffolon and C. Servant, *Thermodynamic Assessment of the Fe-Nb System*, Calphad Comput. Coupling Phase Diagrams Thermochem. **24**, 97 (2000).

[182] A. Raman, *Structural Study of Niobium-Iron Alloys*, Proc. Indian Acad. Sci. - Sect. A **65**, 256 (1967).

[183] J. J. Qi, Y. Zhou, W. Wang, L. H. Qian, Z. Q. Lv, and W. T. Fu, *Electronic, Magnetic and Mechanical Properties of (Fe,Ni)$_2$Nb from Density Functional Theory*, J. Magn. Magn. Mater. **452**, 219 (2018).

[184] A. N. Ladines, T. Hammerschmidt, and R. Drautz, *Structural Stability of Fe-Based Topologically Close-Packed Phases*, Intermetallics **59**, 59 (2015).

[185] D. Connétable, M. Mathon, and J. Lacaze, *First Principle Energies of Binary and Ternary Phases of the Fe–Nb–Ni–Cr System*, Calphad **35**, 588 (2011).

[186] S. V. Meschel and O. J. Kleppa, *The Standard Enthalpies of Formation of Some Intermetallic Compounds of Transition Metals by High Temperature Direct Synthesis Calorimetry*, J. Alloys Compd. **415**, 143 (2006).

[187] S. Liu, B. Hallstedt, D. Music, and Y. Du, *Ab Initio Calculations and Thermodynamic Modeling for the Fe-Mn-Nb System*, Calphad Comput. Coupling Phase Diagrams Thermochem. **38**, 43 (2012).

[188] Y. Iguchi, S. Nobori, K. Saito, and T. Fuwa, *A Calorimetric Study of Heats of Mixing of Liquid Iron Alloys*, Tetsu-to-Hagane **68**, 633 (1982).

[189] B.-J. Lee, *Thermodynamic Assessment of the Fe-Nb-Ti-C-N System*, Metall. Mater. Trans. A **32**, 2423 (2001).

[190] F. R. de Boer, R. Boom, W. C. Mattens, and A. R. Miedema, *Cohesion in Metals. Transition Metal Alloys*, Vol. 1 (Amsterdam, Netherlands; North-Holland, Netherlands, 1988).

[191] C. S. Smith, *Precipitation Hardening in the Fe-W System*, J. Appl. Phys. **12**, 817 (1941).

[192] A. Antoni-Zdziobek, T. Commeau, and J. M. Joubert, *Partial Redetermination of the Fe-W Phase Diagram*, Metall. Mater. Trans. A Phys. Metall. Mater. Sci. **44**, 2996 (2013).

[193] Q. Q. Ren, J. L. Fan, Y. Han, and H. R. Gong, *Structural, Thermodynamic, Mechanical, and Magnetic Properties of FeW System*, J. Appl. Phys. **116**, (2014).

[194] M. Lu and C. L. Chien, *Structural and Magnetic Properties of Fe-W Alloys*, J. Appl. Phys. **67**, 5787 (1990).

[195] K. Sumiyama, H. Masashi, and T. Wataru, *Magnetic and Electrical Properties of Nonequilibrium Fe-W Alloys Produced by Sputter Deposition*, Jpn. J. Appl. Phys. **30**,

2839 (1991).

[196] A. A. Novakova, T. Y. Kiseleva, V. V. Lyovina, D. V. Kuznetsov, and A. L. Dzidziguri, *Low Temperature Formation of Nanocrystalline Fe–W and Fe–Mo Compounds*, J. Alloys Compd. **317**–**318**, 423 (2001).

[197] T. D. Shen, K. Y. Wang, M. X. Quan, and J. T. Wang, *Amorphous Phase Transition Mechanism by the Mechanical Alloying of the Fe–W System*, J. Appl. Phys. **71**, 1967 (1992).

[198] S. T. Mi, H. R. Gong, and J. L. Fan, *Structural Stability and Mechanical Property of Fe-W Solid Solutions from a Constructed Fe-W Potential*, J. Appl. Phys. **126**, (2019).

[199] Z. Bangwei and O. Yifang, *Theoretical Calculation of Thermodynamic Data for Bcc Binary Alloys with the Embedded-Atom Method*, Phys. Rev. B **48**, 3022 (1993).

[200] G. Bonny, N. Castin, J. Bullens, A. Bakaev, T. Klaver, and D. Terentyev, *On the Mobility of Vacancy Clusters in Reduced Activation Steels: An Atomistic Study in the Fe–Cr–W Model Alloy*, J. Phys. Condens. Matter **25**, 315401 (2013).

[201] Z. Q. Lv, Z. F. Zhang, Q. Zhang, Z. H. Wang, S. H. Sun, and W. T. Fu, *Structural, Electronic and Elastic Properties of the Laves Phases WFe2, MoFe2, WCr2 and MoCr2 from First-Principles*, Solid State Sci. **56**, 16 (2016).

[202] A. R. Miedema, P. F. de Châtel, and F. R. de Boer, *Cohesion in Alloys - Fundamentals of a Semi-Empirical Model*, Phys. B+C **100**, 1 (1980).

[203] C. He, F. Stein, and M. Palm, *Thermodynamic Description of the Systems Co-Nb, Al-Nb and Co-Al-Nb*, J. Alloys Compd. **637**, 361 (2015).

[204] F. Stein, D. Jiang, M. Palm, G. Sauthoff, D. Grüner, and G. Kreiner, *Experimental Reinvestigation of the Co-Nb Phase Diagram*, Intermetallics **16**, 785 (2008).

[205] K. C. Hari Kumar, I. Ansara, P. Wollants, and L. Delaey, *Thermodynamic Optimisation of the Co-Nb System*, J. Alloys Compd. **267**, 105 (1998).

[206] R. F. Zhang, Y. Kong, and B. X. Liu, *Construction of N-Body Potentials for Hcp-Bcc Metal Systems within the Framework of Embedded Atom Method*, Phys. Rev. B - Condens. Matter Mater. Phys. **71**, 1 (2005).

[207] M. Jin, N. Miao, W. Zhao, J. Zhou, Q. Du, and Z. Sun, *Structural Stability and Mechanical Properties of $Co_3(Al, M)$ (M = Ti, V, Cr, Zr, Nb, Mo, Hf, Ta, W) Compounds*, Comput. Mater. Sci. **148**, 27 (2018).

[208] C. Wang, C. Zhang, Y. Wang, J. Han, W. Xu, and X. Liu, *Effects of Transition Elements on the Structural, Elastic Properties and Relative Phase Stability of $L1_2$ Γ′-Co_3Nb from First-Principles Calculations*, Metals (Basel). **11**, (2021).

[209] V. S. Skorodziyevskii, A. D. Rood', A. I. Ustinov, and K. V. Chuistov, *The Crystalline Structure of α -Martensite in Co-Based Alloys*, Scr. Metall. **22**, 307 (1988).

[210] S. Chen, Y. Sun, Y. H. Duan, B. Huang, and M. J. Peng, *Phase Stability, Structural and Elastic Properties of C15-Type Laves Transition-Metal Compounds MCo_2 from First-Principles Calculations*, J. Alloys Compd. **630**, 202 (2015).

[211] v. Blavina and R. Trojko, *Structural Investigations of the $Nb_{1-x}Si_xT_2$ and $Nb_{1-x}Al_xT_2$ (T, Cr, Mn, Fe, Co, Ni) Systems*, J. Less Common Met. **119**, 297 (1986).

[212] C. Zhou, C. Guo, J. Li, C. Li, and Z. Du, *Key Experiments and Thermodynamic Description of the Co-Nb-Ni System*, Metall. Mater. Trans. A Phys. Metall. Mater. Sci. **51**, 5892 (2020).

[213] E. Johnson, *Cohesion in Metals*, Nucl. Instruments Methods Phys. Res. Sect. B Beam Interact. with Mater. Atoms **42**, 403 (1989).

[214] P. Li, J. Zhang, S. Ma, Y. Zhang, H. Jin, and S. Mao, *First-Principles Investigations on Structural Stability, Elastic and Electronic Properties of Co_7M_6 (M= W, Mo, Nb) μ Phases*, Mol. Simul. **45**, 752 (2019).

[215] A. K. Shurin, K. PI, and G. EI, *Crystal Structure of NbCo*, SOVIET PHYSICS CRYSTALLOGRAPHY, USSR.

[216] W. Sprengel, M. Denkinger, and H. Mehrer, *Multiphase Diffusion in the CoNb and NiNb Systems: Part II. Interdiffusion*, Intermetallics **2**, 137 (1994).

[217] J. H. Zhu, L. M. Pike, C. T. Liu, and P. K. Liaw, *Point Defects in Binary Laves Phase Alloys*, Acta Mater. **47**, 2003 (1999).

[218] S. Saito and P. A. Beck, *Co-Rich Intermediate Phases In The Cb-Co System*, Trans. Met. Soc. AIME **218**, (1960).

[219] V. N. Drobyshev and T. N. Rezukhina, *Thermodynamic Properties of Cobalt-Niobium Alloys*, Zh. Fiz. Khim. **39**, 151 (1965).

[220] R. V. Major and V. Samadian, *Physical Metallurgy and Properties of a New High Saturation Co-Fe Alloy*, J. Mater. Eng. **11**, 27 (1989).

[221] J. P. Eymery, P. Grosbras, and P. Moine, *Ordering Kinetics of Various FeCo Alloys*, Phys.

Status Solidi **21**, 517 (1974).

[222] P. Grosbras, J. P. Eymery, and P. Moine, *Nature de La Transformation Desordre-Ordre Dans Les Alliages Fer-Cobalt. Influence de l'addition de Vanadium*, Acta Metall. **24**, 189 (1976).

[223] A. W. Smith and R. D. Rawlings, *A Neutron Diffraction Study of Ordering in an Iron–Cobalt–1.8% Vanadium Alloy*, Phys. Status Solidi **34**, 117 (1976).

[224] G. U. Jeong, C. S. Park, H. S. Do, S. M. Park, and B. J. Lee, *Second Nearest-Neighbor Modified Embedded-Atom Method Interatomic Potentials for the Pd-M (M = Al, Co, Cu, Fe, Mo, Ni, Ti) Binary Systems*, Calphad Comput. Coupling Phase Diagrams Thermochem. **62**, 172 (2018).

[225] M. Muralles, J. T. Oh, and Z. Chen, *Modified Embedded Atom Method Interatomic Potentials for the Fe-Al, Fe-Cu, Fe-Nb, Fe-W, and Co-Nb Binary Alloys*, Comput. Mater. Sci. **230**, 112488 (2023).

[226] S. H. Oh, J. S. Kim, C. S. Park, and B. J. Lee, *Second Nearest-Neighbor Modified Embedded-Atom Method Interatomic Potentials for the Mo-M (M = Al, Co, Cr, Fe, Ni, Ti) Binary Alloy Systems*, Comput. Mater. Sci. **194**, 110473 (2021).

[227] M. J. Marcinkowski and H. Chessin, *Relationship between Flow Stress and Atomic Order in the FeCo Alloy*, Philos. Mag. **10**, 837 (1964).

[228] M. Lu and C. L. Chien, *Structural and Magnetic Properties of Fe-W Alloys*, J. Appl. Phys. **67**, 5787 (1990).

[229] H. S. Jang, D. Seol, and B. J. Lee, *Modified Embedded-Atom Method Interatomic Potential for the Mg–Zn–Ca Ternary System*, Calphad Comput. Coupling Phase Diagrams Thermochem. **67**, 101674 (2019).

[230] I. Baker, *A Review of the Mechanical Properties of B2 Compounds*, Mater. Sci. Eng. A **192**–**193**, 1 (1995).

[231] E. P. George, A. N. Gubbi, I. Baker, and L. Robertson, *Mechanical Properties of Soft Magnetic FeCo Alloys*, Mater. Sci. Eng. A **329**–**331**, 325 (2002).

[232] M. T. Raposo, J. D. Ardisson, and A. I. C. Persiano, *Magnetic Study of the Fe-Co-Nb μ and Nbss Phases*, J. Magn. Magn. Mater. **272**–**276**, 2003 (2004).

[233] H. Kleykamp and V. Schauer, *Phase Equilibria and Thermodynamics in the Fe-Mo and Fe-Mo-O Systems*, J. Less Common Met. **81**, 229 (1981).

[234] V. B. Rajkumar and K. C. Hari Kumar, *Thermodynamic Modeling of the Fe–Mo System Coupled with Experiments and Ab Initio Calculations*, J. Alloys Compd. **611**, 303 (2014).

[235] A. Magneli and A. Westgren, *Röntgenuntersuchung von Kobalt–Wolframlegierungen*, Zeitschrift Für Anorg. Und Allg. Chemie **238**, 268 (1938).

[236] J. B. Forsyth and L. M. d'Alte da Veiga, *The Structure of the μ-Phase Co 7 Mo 6*, Acta Crystallogr. **15**, 543 (1962).

[237] M. Muralles, D. Choi, and B. Lee, *A Comparative Study of Mechanical Properties of Ni <001> Nanowires from Atomistic Calculations*, J. Mech. Sci. Technol. **31**, 4887 (2017).

[238] M. Zhou, *A New Look at the Atomic Level Virial Stress: On Continuum-Molecular System Equivalence*, Proc. R. Soc. London. Ser. A Math. Phys. Eng. Sci. **459**, 2347 (2003).

[239] H. Ikeda, Y. Qi, T. Çagin, K. Samwer, W. L. Johnson, and W. A. Goddard, *Strain Rate Induced Amorphization in Metallic Nanowires*, Phys. Rev. Lett. **82**, 2900 (1999).

[240] D. C. Hurley, R. H. Geiss, M. Kopycinska-Müller, J. Müller, D. T. Read, J. E. Wright, N. M. Jennett, and A. S. Maxwell, *Anisotropic Elastic Properties of Nanocrystalline Nickel Thin Films*, J. Mater. Res. **20**, 1186 (2005).

[241] R. Babicheva, Atomistic Simulation of Mechanical Behaviours of Nanocrystalline AI Alloys with Grain Boundary Segregation, Nanyang Technological University, 2017.

[242] M. Tonks, P. Millett, W. Cai, and D. Wolf, *Analysis of the Elastic Strain Energy Driving Force for Grain Boundary Migration Using Phase Field Simulation*, Scr. Mater. **63**, 1049 (2010).

[243] D. V. Bachurin and P. Gumbsch, *Elastic and Plastic Anisotropy after Straining of Nanocrystalline Palladium*, Phys. Rev. B **85**, 085407 (2012).

[244] L. Zhang and Y. Shibuta, *Inverse Hall-Petch Relationship of High-Entropy Alloy by Atomistic Simulation*, Mater. Lett. **274**, 128024 (2020).

[245] Z. Li, V. Gill, A. Lambourne, Z. Dong, M. Avdeev, J. T. Oh, and Z. Chen, *Mechanical Properties and Fractographic Analyses of FeCo-2V Alloy Heat-Treated around Order-Disorder Transition Temperature*, J. Mater. Res. Technol. **22**, 3302 (2023).

[246] K. Kawahara and M. Uehara, *A Possibility for Developing High Strength Soft Magnetic Materials in FeCo-X Alloys*, J. Mater. Sci. **19**, 2575 (1984).

[247] C. Li, Y. L. Chin, and P. Wu, *Correlation between Bulk Modulus of Ternary Intermetallic Compounds and Atomic Properties of Their Constituent Elements*, Intermetallics **12**, 103

(2004).

[248] C. Li and P. Wu, *Correlation of Bulk Modulus and the Constituent Element Properties of Binary Intermetallic Compounds*, **37**, 4642 (2001).

[249] B. Song, B. Sanborn, D. Susan, K. Johnson, J. Dabling, J. Carroll, A. Brink, S. Grutzik, and A. B. Kustas, *Dynamic Tensile Response of a Fe–49Co–2V Alloy at Various Strain Rates and Temperatures*, J. Dyn. Behav. Mater. **6**, 224 (2020).

[250] A. A. Griffith, *VI. The Phenomena of Rupture and Flow in Solids*, Philos. Trans. R. Soc. London. Ser. A, Contain. Pap. a Math. or Phys. Character **221**, 163 (1921).

[251] S. Stach, *Modelling Fracture Processes in Orthopaedic Implants*, in *Computational Modelling of Biomechanics and Biotribology in the Musculoskeletal System* (Elsevier, 2014), pp. 331–368.

[252] Y. Lin, T. Yang, L. Lang, C. Shan, H. Deng, W. Hu, and F. Gao, *Enhanced Radiation Tolerance of the Ni-Co-Cr-Fe High-Entropy Alloy as Revealed from Primary Damage*, Acta Mater. (2020).

[253] P.-W. Ma, C. H. Woo, and S. L. Dudarev, *Large-Scale Simulation of the Spin-Lattice Dynamics in Ferromagnetic Iron*, Phys. Rev. B **78**, 024434 (2008).

[254] S. L. Dudarev and P. M. Derlet, *A 'Magnetic' Interatomic Potential for Molecular Dynamics Simulations*, J. Phys. Condens. Matter **17**, 7097 (2005).

[255] J. Tranchida, S. J. Plimpton, P. Thibaudeau, and A. P. Thompson, *Massively Parallel Symplectic Algorithm for Coupled Magnetic Spin Dynamics and Molecular Dynamics*, J. Comput. Phys. **372**, 406 (2018).

APPENDIX

In this thesis appendix, the essential scripts utilized for training the 2NN MEAM interatomic potentials are presented taking as a subject the Fe-Co interactions in a B2 structure. These scripts are prepared to work with the LAMMPS package. The scripts serve as foundational tools, supporting the computational methodologies integral to the comprehensive exploration and analysis of interatomic behaviors, thereby contributing significantly to the overall framework of this research endeavor.

The subsequent script attains the ground structure of the alloy by employing Conjugate Gradient minimization of forces and energies. From the resultant system, one can derive both the cohesive energy and lattice parameters.

```
# --- Initialize Simulation ---
units metal
dimension 3
boundary p p p
atom_style atomic
atom_modify map array
# --- Define minimization parameters ---
variable etol equal 0.0
variable ftol equal 1.0e-10
variable maxiter equal 5000
variable maxeval equal 5000
variable dmax equal 1.0e-2
# --- Create Atoms ---
# generate the box and atom positions using a bcc
lattice
variable a equal 2.84
# Fe atoms
lattice    custom 1 a1 $a 0 0 a2 0 $a 0 a3 0 0 $a &
                    basis 0 0 0
region              supercell block 0 1 0 1 0 1 units
lattice
create_box          3 supercell
create_atoms        1 region supercell
# Co atoms
lattice    custom 1 a1 $a 0 0 a2 0 $a 0 a3 0 0 $a &
                    basis 0.5 0.5 0.5
create_atoms        3 region supercell
variable b equal 3
replicate           $b $b $b
# --- Interatomic Potential ---
pair_style          meam
pair_coeff * * library.meam Fe Co
PotentialFile.meam Fe Co
# --- Define Settings ---
compute eng all pe/atom
compute eatoms all reduce sum c_eng
# --- Minimize ---
reset_timestep 0
change_box all triclinic
#fix 1 all box/relax aniso 0.0
fix 1 all box/relax tri 0.0 vmax 0.001
thermo 1000
thermo_style custom step pe lx ly lz xy xz yz press
c_eatoms
min_style cg
dump 1 all custom 1000 visual.xyz id type x y z
minimize ${etol} ${ftol} ${maxiter} ${maxeval}
# --- Energies ---
variable natoms equal "count(all)"
variable teng equal "c_eatoms"
variable ecoh equal "v_teng/v_natoms"
variable xleng equal "lx/v_b"
variable yleng equal "ly/v_b"
variable zleng equal "lz/v_b"
# --- Export to screen ---
print "======================"
print "FeCo-B2 Properties"
print "Cohesive Energy = ${ecoh} eV/atom"
print "a lattice = ${xleng} Ang"
print "b lattice = ${yleng} Ang"
print "c lattice = ${zleng} Ang"
```

The following set of four scripts collaboratively achieves the ground state of the system and introduces a micro-strain to calculate the elastic constant tensors. The **main script** outlines the fundamental process, with **script 2** specifying simulation conditions and generating the atomic system. **Script 3** serves as the input for the interatomic potential, and **script 4** is responsible for applying directional micro-strains while resetting the system for an accurate measurement of various elastic constants.

Main Script

```
Include Script 2
include Script 3
# --- Compute initial state ---
change_box all triclinic
fix 3 all box/relax  aniso 0.0
minimize ${etol} ${ftol} ${maxiter} ${maxeval}
variable tmp equal pxx
variable pxx0 equal ${tmp}
variable tmp equal pyy
variable pyy0 equal ${tmp}
variable tmp equal pzz
variable pzz0 equal ${tmp}
variable tmp equal pyz
variable pyz0 equal ${tmp}
variable tmp equal pxz
variable pxz0 equal ${tmp}
variable tmp equal pxy
variable pxy0 equal ${tmp}
variable tmp equal lx
variable lx0 equal ${tmp}
variable tmp equal ly
variable ly0 equal ${tmp}
variable tmp equal lz
variable lz0 equal ${tmp}
# --- Define the derivatives of the strain components
---
# Constants uses $, variables use v_
variable d1 equal -(v_pxx1-
${pxx0})/(v_delta/v_len0)*${cfac}
variable d2 equal -(v_pyy1-
${pyy0})/(v_delta/v_len0)*${cfac}
variable d3 equal -(v_pzz1-
${pzz0})/(v_delta/v_len0)*${cfac}
variable d4 equal -(v_pyz1-
${pyz0})/(v_delta/v_len0)*${cfac}
variable d5 equal -(v_pxz1-
${pxz0})/(v_delta/v_len0)*${cfac}
variable d6 equal -(v_pxy1-
${pxy0})/(v_delta/v_len0)*${cfac}
# Write restart
unfix 3
write_restart restart.equil
# uxx Perturbation
variable dir equal 1
include  Script 4
# uyy Perturbation
variable dir equal 2
include  Script 4
# uzz Perturbation
variable dir equal 3
include  Script 4
# uyz Perturbation
variable dir equal 4
include  Script 4
# uxz Perturbation
variable dir equal 5
include  Script 4
# uxy Perturbation
variable dir equal 6
include  Script 4
# --- Output final values ---
variable C11all equal ${C11}
variable C22all equal ${C22}
variable C33all equal ${C33}
variable C12all equal 0.5*(${C12}+${C21})
variable C13all equal 0.5*(${C13}+${C31})
variable C23all equal 0.5*(${C23}+${C32})
variable C44all equal ${C44}
variable C55all equal ${C55}
variable C66all equal ${C66}
variable C14all equal 0.5*(${C14}+${C41})
variable C15all equal 0.5*(${C15}+${C51})
variable C16all equal 0.5*(${C16}+${C61})
variable C24all equal 0.5*(${C24}+${C42})
variable C25all equal 0.5*(${C25}+${C52})
variable C26all equal 0.5*(${C26}+${C62})
variable C34all equal 0.5*(${C34}+${C43})
variable C35all equal 0.5*(${C35}+${C53})
variable C36all equal 0.5*(${C36}+${C63})
```

```
variable C45all equal 0.5*(${C45}+${C54})
variable C46all equal 0.5*(${C46}+${C64})
variable C56all equal 0.5*(${C56}+${C65})
# --- Average moduli for cubic crystals ---
variable C11cubic equal
(${C11all}+${C22all}+${C33all})/3.0
variable C12cubic equal
(${C12all}+${C13all}+${C23all})/3.0
variable C44cubic equal
(${C44all}+${C55all}+${C66all})/3.0
variable bulkmodulus equal
(${C11cubic}+2*${C12cubic})/3.0
variable shearmodulus1 equal ${C44cubic}
variable shearmodulus2 equal (${C11cubic}-
${C12cubic})/2.0
variable poissonratio equal
1.0/(1.0+${C11cubic}/${C12cubic})
print "======================"
print "Average properties for FeCo-B2"
print "======================"
print "C11 = ${C11cubic} ${cunits}"
print "C12 = ${C12cubic} ${cunits}"
print "C44 = ${C44cubic} ${cunits}"
print "Bulk Modulus = ${bulkmodulus} ${cunits}"
print "Shear Modulus 1 = ${shearmodulus1}
${cunits}"
print "Shear Modulus 2 = ${shearmodulus2}
${cunits}"
print "Poisson Ratio = ${poissonratio}"
print "======================"
print "Components of the Elastic Constant Tensor"
print "======================"
print "Elastic Constant C11all = ${C11all}
${cunits}"
print "Elastic Constant C22all = ${C22all}
${cunits}"
print "Elastic Constant C33all = ${C33all}
${cunits}"
print "Elastic Constant C12all = ${C12all}
${cunits}"
print "Elastic Constant C13all = ${C13all}
${cunits}"
print "Elastic Constant C23all = ${C23all}
${cunits}"
print "Elastic Constant C44all = ${C44all}
${cunits}"
print "Elastic Constant C55all = ${C55all}
${cunits}"
print "Elastic Constant C66all = ${C66all}
${cunits}"
print "Elastic Constant C14all = ${C14all}
${cunits}"
print "Elastic Constant C15all = ${C15all}
${cunits}"
print "Elastic Constant C16all = ${C16all}
${cunits}"
print "Elastic Constant C24all = ${C24all}
${cunits}"
print "Elastic Constant C25all = ${C25all}
${cunits}"
print "Elastic Constant C26all = ${C26all}
${cunits}"
print "Elastic Constant C34all = ${C34all}
${cunits}"
print "Elastic Constant C35all = ${C35all}
${cunits}"
print "Elastic Constant C36all = ${C36all}
${cunits}"
print "Elastic Constant C45all = ${C45all}
${cunits}"
print "Elastic Constant C46all = ${C46all}
${cunits}"
print "Elastic Constant C56all = ${C56all}
${cunits}"
```

Script 2

```
units                   metal
variable cfac equal 1.0e-4
variable cunits string GPa
# --- Define minimization parameters---
variable etol equal 0.0
variable ftol equal 1.0e-10
variable maxiter equal 5000
variable maxeval equal 5000
variable dmax equal 1.0e-2
# --- Generate the box and atom positions ---
variable a equal 2.84
boundary                p p p
# Fe atoms
lattice    custom 1 a1 $a 0 0 a2 0 $a 0 a3 0 0 $a &
                        basis 0.0 0.0 0.0
region                  supercell block 0 1 0 1 0 1 units
lattice
create_box              3 supercell
create_atoms            1 region supercell
# Co atoms
lattice    custom 1 a1 $a 0 0 a2 0 $a 0 a3 0 0 $a &
                        basis 0.5 0.5 0.5
create_atoms            2 region supercell
replicate               3 3 3
# Set mass, just to satisfy LAMMPS
mass 1 1.0e-20
```

Script 3

```
# --- Choose potential ---
pair_style              meam
pair_coeff * * library.meam Fe Co
PotentialFile.meam Fe Co
# --- Setup neighbor style ---
neighbor 1.0 nsq
neigh_modify once no every 1 delay 0 check yes
# --- Setup minimization style ---
min_style               cg
min_modify              dmax ${dmax} line quadratic
# --- Setup output ---
thermo                  1
thermo_style custom step temp pe press pxx pyy pzz
pxy pxz pyz lx ly lz vol
thermo_modify norm no
```

Script 4

```
if "${dir} == 1" then &
  "variable len0 equal ${lx0}"
if "${dir} == 2" then &
  "variable len0 equal ${ly0}"
if "${dir} == 3" then &
  "variable len0 equal ${lz0}"
if "${dir} == 4" then &
  "variable len0 equal ${lz0}"
if "${dir} == 5" then &
  "variable len0 equal ${lz0}"
if "${dir} == 6" then &
  "variable len0 equal ${ly0}"
# --- Reset box and simulation parameters ---
clear
read_restart restart.equil
include Script 3
# --- Negative deformation ---
variable delta equal -${up}*${len0}
if "${dir} == 1" then &
  "change_box all x delta 0 ${delta} remap units box"
if "${dir} == 2" then &
  "change_box all y delta 0 ${delta} remap units box"
if "${dir} == 3" then &
  "change_box all z delta 0 ${delta} remap units box"
if "${dir} == 4" then &
  "change_box all yz delta ${delta} remap units box"
if "${dir} == 5" then &
  "change_box all xz delta ${delta} remap units box"
if "${dir} == 6" then &
  "change_box all xy delta ${delta} remap units box"
# --- Relax atoms positions ---
minimize ${etol} ${ftol} ${maxiter} ${maxeval}
# --- Obtain new stress tensor ---
 variable tmp equal pxx
variable pxx1 equal ${tmp}
variable tmp equal pyy
variable pyy1 equal ${tmp}
variable tmp equal pzz
variable pzz1 equal ${tmp}
variable tmp equal pxy
variable pxy1 equal ${tmp}
variable tmp equal pxz
variable pxz1 equal ${tmp}
variable tmp equal pyz
variable pyz1 equal ${tmp}
# -- Compute elastic constant from pressure tensor --
variable C1neg equal ${d1}
variable C2neg equal ${d2}
variable C3neg equal ${d3}
variable C4neg equal ${d4}
variable C5neg equal ${d5}
variable C6neg equal ${d6}
# --- Reset box and simulation parameters ---
clear
read_restart restart.equil
include Script 3
# --- Positive deformation ---
variable delta equal ${up}*${len0}
if "${dir} == 1" then &
  "change_box all x delta 0 ${delta} remap units box"
if "${dir} == 2" then &
  "change_box all y delta 0 ${delta} remap units box"
if "${dir} == 3" then &
  "change_box all z delta 0 ${delta} remap units box"
if "${dir} == 4" then &
  "change_box all yz delta ${delta} remap units box"
if "${dir} == 5" then &
  "change_box all xz delta ${delta} remap units box"
if "${dir} == 6" then &
  "change_box all xy delta ${delta} remap units box"
# --- Relax atoms positions ---
minimize ${etol} ${ftol} ${maxiter} ${maxeval}
# --- Obtain new stress tensor ---
 variable tmp equal pe
variable e1 equal ${tmp}
variable tmp equal press
variable p1 equal ${tmp}
variable tmp equal pxx
variable pxx1 equal ${tmp}
variable tmp equal pyy
variable pyy1 equal ${tmp}
```

```
variable tmp equal pzz
variable pzz1 equal ${tmp}
variable tmp equal pxy
variable pxy1 equal ${tmp}
variable tmp equal pxz
variable pxz1 equal ${tmp}
variable tmp equal pyz
variable pyz1 equal ${tmp}
# -- Compute elastic constant from pressure tensor --
variable C1pos equal ${d1}
variable C2pos equal ${d2}
variable C3pos equal ${d3}
variable C4pos equal ${d4}
variable C5pos equal ${d5}
variable C6pos equal ${d6}
# --- Combine positive and negative ---
variable C1${dir} equal 0.5*(${C1neg}+${C1pos})
variable C2${dir} equal 0.5*(${C2neg}+${C2pos})
variable C3${dir} equal 0.5*(${C3neg}+${C3pos})
variable C4${dir} equal 0.5*(${C4neg}+${C4pos})
variable C5${dir} equal 0.5*(${C5neg}+${C5pos})
variable C6${dir} equal 0.5*(${C6neg}+${C6pos})
# --- Delete dir to make sure it is not reused ---
variable dir delete
```

The following script introduces a point defect, specifically a vacancy, into the Fe sublattice of the FeCo system. The simulation captures the energy of the ground state for both the initial system and the system after removing the Fe atom, yielding valuable insights into the vacancy formation energy. Furthermore, this script can be readily adapted to calculate formation energies for the other types of vacancies and antisites.

```
units               metal
dimension           3
boundary            p           p    p
atom_style          atomic
# --- Atom & Box definition ---
variable ao equal 2.84
          #lattice constant/2
variable b equal 4                          #box  side  size
     in unit cells
variable c equal "v_ao * v_b"                       #box
     side size in Angstroms
# --- Create Atoms ---
region simbox       block -$c $c -$c $c -$c $c
create_box 3        simbox
     # --- Fe ---
lattice    custom 1 a1 ${ao} 0 0 a2 0 ${ao} 0 a3 0 0
     ${ao} &
                basis 0.0 0 0.0
create_atoms 1 region simbox
     # --- Co ---
lattice    custom 1 a1 ${ao} 0 0 a2 0 ${ao} 0 a3 0 0
     ${ao} &
                basis 0.5 0.5 0.5
create_atoms 2 region simbox
# --- POTENTIAL ---
pair_style          meam
pair_coeff * * library.meam Fe Co V FeCoV.meam Fe
     Co V
# --- Settings ---
compute csym all centro/atom bcc
compute eng all pe/atom
compute eatoms all reduce sum c_eng
# --- Minimization ---
reset_timestep      0
thermo 10
thermo_style custom step pe lx ly lz press pxx pyy
     pzz c_eatoms
min_style cg
minimize 1e-15 1e-15 5000 5000
variable N equal count(all)
variable No equal $N
variable E equal "c_eatoms"
variable Ei equal $E

# --- Atom removal ---
variable r2 equal sqrt(${ao}^2+${ao}^2)/4
region select sphere 0 0 0 ${r2} units box
delete_atoms region select compress yes
# --- Minimization ---
reset_timestep      0
thermo 10
thermo_style custom step pe lx ly lz press pxx pyy
     pzz c_eatoms
dump 1 all custom 500 VacancyFe.ovi id type xs ys
     zs c_csym c_eng
min_style cg
minimize 1e-15 1e-15 5000 5000
variable Ef equal "c_eatoms"
variable Ev equal (${Ef}-((${No}-1)/${No})*${Ei})
print "==================="
```

```
print "Results for vacancy in Fe(alpha) sublattice"
print "=================="
print "Total number of atoms = ${No}"
print "Initial energy of atoms = ${Ei} eV"
print "Final energy of atoms = ${Ef} eV"
print "Formation energy = ${Ev} eV"
```

The subsequent script divides the nano system in two sections and following introduces a displacement size of *a*/2 in one of the sections, reproducing a {110} <111> antiphase boundary (APB). The simulation assesses the energy of the ground state for both the initial system and the system post-displacement, providing valuable insights into the APB energy.

```
units               metal
dimension           3
boundary            p p s
atom_style          atomic
# --- Structure Definition ---
variable a equal 2.8712
variable x equal 10
variable y equal 10
variable z equal 8
variable zl equal ($z/2)-0.05
variable zu equal ($z/2)-0.04
variable x_displace equal ${a}*0.5
variable y_displace equal ${a}*sqrt(2)*0.5
# --- Fe atoms ---
lattice    custom 1.0 a1 $a 0 0 a2 0 $a 0 a3 0.0 0.0 $a
&
                    orient x 1 0 0 orient y 0 1 1 orient
z 0 -1 1 &
                  basis 0.0 0.0 0.0
region              whole block -0.01 ${x} -0.01 ${y}
-0.01 ${z} units lattice
create_box          3 whole
region              1 block INF ${x} INF ${y} INF
${zl} units lattice
create_atoms        1 region 1
# --- Co atoms ---
lattice    custom 1.0 a1 $a 0 0 a2 0 $a 0 a3 0.0 0.0 $a
&
                    orient x 1 0 0 orient y 0 1 1 orient
z 0 -1 1 &
                  basis 0.5 0.5 0.5
create_atoms        2 region 1
region              2 block INF ${x} INF ${y} ${zu}
INF units lattice
# --- Fe atoms ---
lattice    custom 1.0 a1 $a 0 0 a2 0 $a 0 a3 0.0 0.0 $a
&
                    orient x 1 0 0 orient y 0 1 1 orient
z 0 -1 1 &
                  basis 0 0 0
create_atoms        1 region 2
# --- Co atoms ---
lattice    custom 1.0 a1 $a 0 0 a2 0 $a 0 a3 0.0 0.0 $a
&
                    orient x 1 0 0 orient y 0 1 1 orient
z 0 -1 1 &
                  basis 0.5 0.5 0.5
create_atoms        2 region 2
# --- Potential ---
pair_style          meam
pair_coeff * * library.meam Fe Co V FeCoV.meam Fe
Co V
# --- Settings ---
change_box all triclinic
compute peratom all pe/atom
compute eatoms all reduce sum c_peratom
thermo 25
thermo_style custom step pe c_eatoms xlat ylat zlat
# --- 1st Minimization ---
min_style cg
minimize 1e-10 1e-10 10000 10000
variable E equal "c_eatoms"
variable Eo equal $E
variable boxx equal lx
variable boxy equal ly
group bot region 1
group top region 2
displace_atoms      top     move     ${x_displace}
${y_displace} 0.0 units box
# --- 2nd Minimization ---
fix 1 all setforce 0 0 NULL
min_style cg
minimize 1e-10 1e-10 1000 1000
variable Ef equal "c_eatoms"
variable Cf equal 1.60217657e-16 #eV to mJ
variable A equal (${boxx}*${boxy})*1e-20 #Ang^2
to m^2
variable Eapb equal ((${Ef}-${Eo})*${Cf})/(${A})
print "===================="
print "Result FeCo {110} APB "
print "===================="
print "{110} APB Energy = ${Eapb} mJ/m^2
```